

A Non-syn-gas Catalytic Route to Methanol Production

By

Mr. Cheng-Tar Wu (BS, MS)

454756

University College

A dissertation submitted for the degree of Doctor of Philosophy at the Inorganic Chemistry Laboratory, Department of Chemistry, University of Oxford

2013

A Non-syn-gas Catalytic Route to Methanol Production

By

Mr. Cheng-Tar Wu (BS, MS)

454756

University College

Supervisor

Prof. S. C. Edman Tsang

Internal Assessor

Prof. George Smith, FRS

A dissertation submitted for the degree of Doctor of Philosophy at the Inorganic Chemistry Laboratory, Department of Chemistry, University of Oxford

2013

TABLE OF CONTENTS

TABLE OF CONTENTS i

DECLARATION v

DEDICATION vi

ACKNOWLEDGEMENTS vii

ABSTRACT ix

LIST OF FIGURES xi

LIST OF TABLES xx

LIST OF SYMBOLS AND ABBREVIATIONS xxii

LIST OF PUBLICATIONS xxv

CHAPTER 1 - INTRODUCTION 1

1.1 CATALYSIS 3

1.2 PRINCIPLE OF HETEROGENEOUS CATALYSIS 11

1.3 PREPARATION OF CATALYSTS 18

1.4 THE METHANOL ECONOMY 25

1.5 A NON-SYN-GAS CATALYTIC ROUTE FOR METHANOL PRODUCTION 30

1.6 AIMS AND OBJECTIVES 46

1.7 OVERVIEW OF THE THESIS 48

1.8 REFERENCES 49

CHAPTER 2 - ANALYTICAL TECHNIQUES 58

2.1 INTRODUCTION 59

2.2 X-RAY DIFFRACTION 61

2.3 ELECTRON MICROSCOPY 65

2.4 X-RAY PHOTOELECTRON SPECTROSCOPY 69

2.5 EXTENDED X-RAY ABSORPTION FINE STRUCTURE 72

2.6 THERMOGRAVIOMETRIC ANALYSIS 75

2.7 TEMPERATURE PROGRAMMED DESORPTION REDUCTION AND OXIDATION 77

2.8 GAS CHROMATOGRAPHY 80

2.9 HIGH PERFORMANCE LIQUID CHROMATOGRAPHY 83

2.10 REFERENCES 88

CHAPTER 3 - EXPERIMENTAL AND CHARACTERISATION 90

3.1 MODIFIED RANEY CATALYSTS 92

3.2 BIMETALLIC CATALYSTS 93

3.3 SUPPORTED OXIDE CATALYSTS 95

3.4 PALLADIUM-IRON ALLOY 97

3.5 HYDROGENOLYSIS OF ETHYLENE GLYCOL 98

3.6 OXIDATION OF METHANE 100

3.7 CHARACTERISATIONS 102

3.8 REFERENCES 106

CHAPTER 4 - RANEY CATALYSTS FOR HYDROGENOLYSIS OF ETHYLENE GLYCOL 107

4.1 INTRODUCTION 108

4.2 EXPERIMENTAL METHODS 110

4.3 CATALYST CHARACTERISATION 113

4.4 HYDROGENOLYSIS TESTING 115

4.5 DISCUSSION 121

4.6 CONCLUSION 130

4.7 REFERENCES 132

CHAPTER 5 – SUPPORTED OXIDE CATALYSTS FOR HYDROGENOLYSIS OF ETHYLENE GLYCOL 135

5.1 INTRODUCTION 137

5.2 OBJECTIVES 139

5.3 SYNTHESIS OF CATALYSTS 139

5.4 CHARACTERISATIONS OF METAL SUPPORTED OXIDE CATALYSTS 141

5.5 CATALYTIC TESTING 159

5.6 DISCUSSION 173

5.7 CONCLUSION 175

5.8 REFERENCES 176

CHAPTER 6 – OXIDATION OF METHANE FOR HYDROGEN AND CARBON DIOXIDE PRODUCTION....179

6.1 INTRODUCTION....180

6.2 OBJECTIVES....184

6.3 CHARACTERISATIONS OF CATALYSTS....185

6.4 THERMODYNAMIC CALCULATIONS....190

6.5 CATALYTIC TESTING....193

6.5 DISCUSSION....201

6.6 CONCLUSION....205

6.7 REFERENCES....206

CHAPTER 7 - CONCLUSION AND FUTURE PERSPECTIVE....210

7.1 CONCLUSION AND FUTURE WORK....211

7.2 FUTURE PERSPECTIVE....212

CHAPTER 8 – APPENDIX....214

8.1 DENSITY FUNCTIONAL THEORY OF METAL SURFACES....215

8.2 A SIMPLE MODEL FOR d-BAND THEORY[2]....216

8.3 REFERENCES....219

DECLARATION

I confirm that this is my own work and the use of all material from other sources has been properly and fully acknowledged.

Cheng-Tar Wu

DEDICATION

To my wife Yu-Ting and parents.

ACKNOWLEDGEMENTS

First I would like to thank Prof. S.C. Edman Tsang my supervisor for the opportunity to work in his laboratory, for his advice, help and guidance throughout my research project. I gratefully acknowledge the funding received towards my D.Phil. from the Swire D.Phil. Scholarship (provided by the Swire Educational Trust). I like to thank University of Oxford, Johnson Matthey, Engineering and Physical Science Research Council for the chemicals, precious metals and testing equipment during my D.Phil.

My research documented herein would not have been possible without their expert assistance on the experimental techniques which I greatly relied on. I like to thank Dr Kai Man Kerry Yu (Intrinsiq Materials) for his great technical expertise on analytical instruments, general advice, and his help on testing and analysis of new catalysts and reactions, who saved me a lot of man hours in the lab. Dr Jingping Hu and Prof. John Foord (PTCL, University of Oxford) for their assistance in XPS analysis. Dr Andrew Dent and Dr Anna Kroner (Diamond Light Source, UK) for EXAFS analysis. Dr Neil Young and Prof. Peter Nellist (Materials, University of Oxford) for TEM characterisations. Dr Phil Wiseman (ICL, University of Oxford) for training on the XRD. Mr Ashleigh Hewson for lab and equipment service. Mr Tom Bradshaw and Mr Keith Waters for IT support. Mrs Terri Adams for glassblower service. Mr Charlie Evans for workshop service. Mr Bill Thompson, Mr Leigh Bennett and Mr Levi Dash for stores assistance. Mrs Pam Cox, Mrs Trish Traynor and Ms Hazel Osborne for administrative assistance. D.Phil student Ms Fenglin Liao for her collaborations to my catalyst testing. Jin Qu (East China University of Science & Technology, China) for his collaborations to the theoretical calculation. Part II

student Mr Joseph Elliott and Mr Ben Lo for their collaborations to my Rh/Fe_3O_4 work. Dr Karaked Tedsree (Burapha University, Thailand), Dr C.W. Aaron Chan (Intrinsiq Materials) and Mr Simon Jones for general discussions. Finally the Tsang group of past and present: Dr Chih-Hao Yu, Dr Jiahui Xu, Dr Katarzyna Morawa, Vivian Chang, Prof. Yun Zhao, Dr Gordon Lee, Tom Chapman, Steven Zhou, Bee Pengsawang, Abdullah Khan, Amy Kolpin, Clive Eley, Serena Jia, Prof. Min Liu, Aaron Lau, Hanif Mahadi, Ieuan Ellis, Dr Qin Lu, Prof. Qingkun Shang, Dr Weiyi Tong, Dr Hongwei Yang, Feng Xu, Molly Li, Weiran Zheng, Prof. Keizo Nakagawa, Yaling Xie, Adam West, Kevin Cheung, Mary Burkitt-Gray, Matthew Powell, Lusha Fu, Sharon He.

ABSTRACT

At present, more than 80% of the world's energy consumption and production of chemicals is originated from the use of fossil resources. There is a tremendous growing interest in utilising biomass molecules for energy provision due to their carbon neutrality. Lower alcohols such as methanol and ethanol if produced from biomass as transportation fuels as well as platform chemicals, can become strategically important for many energy/chemically starved countries. Currently, they are synthesised by indirect and inefficient processes. We show *for the first time* in this thesis study that ethylene glycol, the simplest representative of biomass-derived polyols, can be directly converted to these two lower alcohols by selective hydrogenolysis over modified Raney Ni and Cu catalysts in hydrogen atmosphere. This work provides essential information that may lead to the development of new catalysts for carbohydrate activation to methanol, a novel but important reaction concerning the important biomass conversion to transportable form of energy. Modification of electronic structure and the adsorption properties of Raney catalysts have therefore been achieved by blending with second metal(s). It is found that the activity and selectivity of this reaction can be significantly affected by this approach. In contrast, there is no subtle effect on methanol selectivity despite a great variation in the d-band centre positions of metal catalysts which show a distinctive effect on other products. Our result suggests that methanol is produced on specific surface sites independent from the other sites at an intrinsic rate and will not be converted to other products by the d-band alteration. On the other hand, it is reported in this thesis that a dramatic improvement in the combined selectivity to methanol/ethanol reaching 80% can be obtained over a Pd/Fe_3O_4 catalyst under relatively milder conditions (20 bar

and 195 ^{o}C). This direct production of the non-enzymatic bio-alcohols is established over a carefully prepared co-precipitated Pd/Fe_3O_4 catalyst which gives a metallic phase of unexpectedly high dispersion ranging from small clusters to individual metal adatoms on defective iron oxide to give the required metal-support interaction for the novel synthesis. It is demonstrated that the small PdFe clusters on iron oxide surface provide the active species responsible for methanol production. In addition, a related Rh/Fe_3O_4 catalyst synthesised by co-precipitation is also shown to be selective for CO_2 and H_2 production from a direct methane-oxygen oxidation reaction. As a result, 2.7% conversion of methane with selectivity ratio of CO_2/H_2 = 4 in a mixed gas feed stream of CH_4/O_2 = 30 at 300 ^{o}C is obtained. The reaction is operated in a kinetically controlled regime at 300^{o}C, where the CO formation from reverse water gas shift reaction is greatly suppressed. It is evident that the Rh/Fe_3O_4 acts as an interesting bifunctional catalyst for this reaction. This catalyst firstly gives a high dispersion of Rh which is expected to deliver a higher surface energy with enhanced activity. The Rh metal surface provides catalytically active sites for dissociation of methane to adsorbed hydrogen and carbon atoms effectively, and active oxygen on metal surface readily catalyses the carbon atoms to CO. Following these elementary reactions, the surface oxygen from Fe_3O_4 subsequently converts it to CO_2 selectively at the metal-support interface. As a result, the novel study of catalytic biomass conversion and the discoveries of new catalysts are reported in this thesis.

Key words: Heterogeneous catalysis, Ethylene glycol, Hydrogenolysis, Methanol production, Methane oxidation.

LIST OF FIGURES

Fig. 1-1 An estimated publications in the last 30 years (from 1980 to 2011) by searching the term 'catalysis' and 'heterogeneous catalysis' on Thomson Reuters Web of Knowledge.

Fig. 1-2 An estimated patents in the last 30 years (from 1980 to 2011) by searching the term 'catalysis' and 'heterogeneous catalysis' on the website of (a) the United States Patent and Trademark Office; (b) European Patent Office.

Fig. 1-3 A different energy pathway for a reaction with or without the assistance of a catalyst.

Fig. 1-4 Catalysis deals with the transition between reactants and products. It does not affect the overall reaction thermodynamics.

Fig. 1-5 Individual steps of a heterogeneously catalysed gas-phase reaction.

Fig. 1-6 General effects of temperature on catalytic activity. The intrinsic activation energy is equal to Ea, and R is the gas constant.

Fig. 1-7 The relation between catalytic activity and the strength of chemisorption of the reactant in a unimolecular reaction.

Fig. 1-8 The two main mechanisms in gas/solid heterogeneous catalysis: a Langmuir–Hinshelwood; b Eley–Rideal.

Fig. 1-9 Types and examples of solid catalysts, grouped by preparation method.

Fig. 1-10 Preparation routes for technical catalysts.

Fig. 1-11 The Raney process, in which a metal/aluminum alloy is prepared by fusion, and subsequently the aluminum is dissolved by aqueous NaOH, leaving a metallic sponge.

Fig. 1-12 SEM micrographs of the catalysts used in this study: (a) Raney-nickel 4200, (b) Raney-nickel 3202, (c) ruthenium on alumina, (d) ruthenium on carbon, (e) Raneycopper, and (f) Raney-cobalt.

Fig. 1-13 The relation between the homogeneous nucleation rate (nuclei per ml/second) and the degree of supersaturation. s = actual concentration/solubility.

Fig. 1-14 Hot-injection method for the synthesis of monodisperse nanoparticles.

Fig. 1-15 Conventional routes for manufacturing synthesis gas: (a) steam reforming; (b) partial oxidation.; Improved partial oxidation processes for manufacturing synthesis gas: (c) autothermal reformer; (d) catalytic partial oxidation; (e) oxygen-permeable catalytic membrane reformer; Combination of steam reforming and partial oxidation can comprise (f) mass integration for: (i) improved synthesis gas quality as well as (ii) mass and heat integration; (g) for improved energy efficiency.

Fig. 1-16 The flow chart of methanol production process.

Fig. 1-17 A schematic representation of a number of possible reaction pathways of the hydrogenolysis of glycerol.

Fig. 1-18 A scheme outlining the hydrogenolysis of glycerol on Ru- / Pt-based catalyst. M denotes either Ru or Pt.

Fig. 2-1 Catalyst characterisation techniques.

Fig. 2-2 A PANalytical X'Pert Pro X-ray diffractometer.

Fig. 2-3 Atomic levels involved in copper Kα and Kβ emission

Fig. 2-4 Diffraction of X-rays from crystal lattice planes illustrating Bragg's law

Fig. 2-5 Schematic 3D view of a traditional flat-plate diffraction setup (top); Typical laboratory powder diffraction setups (bottom).

Fig. 2-6 Cross section of a TEM microscope.

Fig. 2-7 Scheme of a scanning transmission electron microscope with bright- and dark-field detectors. ADF: annular dark field; HAADF: high-angle annular dark field.

Fig. 2-8 Photoemission and the Auger process. Left: An incident X-ray photon is absorbed and a photoelectron emitted. Binding energy of the photoelectron can be determined from the measurement of its kinetic energy. The atom stays behind as an unstable ion with a hole in one of the core levels. Right: The excited ion relaxes by filling the core hole with an electron from a higher shell. The energy released by this transition is taken up by another electron, the Auger electron, which leaves the sample with an element-specific kinetic energy. In Auger spectroscopy, a beam of energetic (2–5 keV) electrons creates the initial core holes.

Fig. 2-9 Absorption of X-rays as a function of photon energy E = h by a free atom and by atoms in a lattice. The fine structure represents the extended X-ray absorption fine structure (EXAFS) function. XANES: X-ray absorption near edge spectroscopy.

Fig. 2-10 A TA instrument Q50 (top); Schematic for the TGA Q50 (bottom).

Fig. 2-11 A CE instrument TPD/R/O 1100 (top); Diagram for the reactor assembly (bottom).

Fig. 2-12 A Perkin Elmer Autosystem XL Arnel Gas phase GC-FID (top); Working illustration of a GC (bottom).

Fig. 2-13 A Perkin Elmer series 200 HPLC system (top); Schematic of an HPLC system (bottom).

Fig. 3-1 A Hettich Universal 320 Centrifuge.

Fig. 3-2 A Fisher Scientific FB 15051 ultrasonic bath.

Fig. 3-3 A Carbolite type MTF 12/38/400 tube furnaces.

Fig. 3-4 A Vacuum Atmospheres HE-63-P glove box.

Fig. 3-5 Temperature profile for the calcination of $Pd/Fe(OH)_x$ catalyst.

Fig. 3-6 Temperature profile for the reduction of PdO/Fe_2O_3 catalyst.

Fig. 3-7 A Parr 160 mL pressure vessel.

Fig. 3-8 A schematic diagram showing the high pressure reactor designed for the catalyst testing: 1, inlet valve; 2, pressure gauge; 3, motor; 4, heater; 5, extractor; 6, pressure detector; 7, temperature controller; 8, thermocouple; 9, safety rupture disk;10, internal string system; 11, inlet tube; 12, sample bottle; 13, cooling coil; 14, outlet valve.

Fig. 3-9 A self-built reactor setup for methane oxidation. A, inlet valve; B, pressure gauge; C, D and E, mass flow controller; E, extractor; F, furnace; G, 6-mm-diameter stainless steel reactor; H, thermocouple; I, powder mixture was sandwiched between quartz wool plugs; J, furnace temperature controller; K and L, ice bath; M, GC with a TCD; N, GC with a FID; O, computer.

Fig. 3-10 An Agilent 7890A GC system.

Fig. 4-1 TEM images of a typical Raney Ni2800 catalyst.

Fig. 4-2 Typical XRD patterns of Raney Ni impregnated with various surface elements showing no new phases (isomorphic deposition) but differences in Ni lattice strains (65^o and 78^o are holder peaks).

Fig. 4-3 The effect of reaction time (a) and catalyst amount (b) on selectivity and conversion at 175 ^oC and 20 bar of H_2

Fig. 4-4 A simple schematic diagram for adsorbed ethylene glycol for the hydrogenolysis of C-C on a transition metal M site (top); Typical pathway for the hydrogenolysis of ethylene glycol (bottom).

Fig. 4-5 Diagrams showing the calculated electron difference of adsorbed ethylene glycol on a Ni(211) step site with adsorption energy of -1.02 eV compared to the free state. (a) side view of adsorption; (b) top view of adsorption.

Fig. 5-1 PXRD profiles for a series of metal oxide (Fe_3O_4, ZnO, Ga_2O_3, CeO_2 and Al_2O_3) supported Pd catalysts which have been calcined in air at 300 ^oC followed by reduction in dilute H_2 (at H_2:N_2 molar ratios of 1:2) at 200 ^oC.

Fig. 5-2 (a) PXRD profiles for Fe_2O_3 and Fe_2O_3 supported metal oxides (including Pd, Rh, Ni, Pt and Ag) calcined in air at 300 ^oC; (b) PXRD profiles for Fe_3O_4 and Fe_3O_4 supported metals (including Pd, Rh, Ni, Pt and Ag) reduced in dilute hydrogen (at H_2:N_2 molar ratios of 1:2) at 200 ^oC.

Fig. 5-3 (a) PXRD patterns for Pd/Fe_2O_3 before and after hydrogenolysis of ethylene glycol at 195 ^oC, 20 bar H_2 (RT) (the high and broad peak at 17^o in Pd/Fe_2O_3 before reaction was derived from the air-tight sample holder); (b) Enlarged XRD region to show two small peaks formed after reaction corresponding to PdFe rather than Pd.

Fig. 5-4 The envisaged co-precipitated network of -Pd-O-Fe- created after hydrolysis and cross-condensation between Pd and Fe precursors in water.

Fig. 5-5 In-situ XRD profile for 5% PdO/Fe_2O_3 in dilute H_2.

Fig. 5-6 (a) H_2–TPR profiles for Fe_2O_3 and PdO/Fe_2O_3; (b) 1st and 2nd repeated TPR profiles for PdO/Fe_2O_3 in H_2 after temperature programmed heating was terminated at 200 ^oC as compared to the TPR profile for PdO/Al_2O_3.

Fig. 5-7 TEM micrographs of 5% Pd/Fe_3O_4 obtained by: (a) precipitation of palladium nitrate on commercial Fe_3O_4; (b) co-precipitation of palladium and iron nitrate; both samples were reduced in 33% H_2/N_2 at 200 °C.

Fig. 5-8 (a) HAADF-STEM image showing an aggregate of nanoscale Pd/Fe_3O_4 catalyst particles. (b) Higher magnification HAADF-STEM image of a thin area, revealing the catalyst surface is covered in nanoscale clusters of metal atoms. (c) Histogram reporting the size distribution of particles in (b). Features such as irregular monolayer clusters and single atoms have not been included here due to ambiguity in defining their size due to mobility under the beam and varying background contrast from the uneven underlying support.

Fig. 5-9 HAADF-STEM imaging of the Pd/Fe_3O_4 catalyst. (a) Typical area of the specimen containing irregular atomic clusters with three distinctive surface adatoms. (b) The same raw data as Fig. 5-9a with the image contrast enhanced to highlight the three single adatoms. The circle highlights the three single adatoms on the Fe_3O_4 surface. (c) Line profile along the line marked in Fig. 5-9a, showing three distinct isolated atoms, each with a half peak width of 1.1 Å. (d) and (e) represent typical irregular groups of atom clusters found in the catalyst material.

Fig. 5-10 XPS spectra of Pd/Fe_3O_4 catalyst at different hydrogen pre-reduction times (1, 5 and 48 h). The spectra are evaluated at 195 °C for 24 h (corresponding to different alcohol selectivities). All spectra were calibrated to an adventitious C 1s peak at 284.5 eV with the application of electron shower gun to reduce charging effects of the samples. (a) Fe $2p_{3/2}$ region. The dash lines correspond to literature values for the binding

energies of Fe $2p_{3/2}$ (red) and the Fe $2p_{3/2}$ in a PdFe alloy (black) (NIST database); (b) Pd $3d_{5/2}$ region. The dash lines correspond to literature values for the binding energies of Pd $3d_{5/2}$ (red) and Pd $3d_{5/2}$ in a PdFe alloy (black) (NIST database).

Fig. 5-11 (a) Catalytic performances of 5% Pd supported on different oxides (prepared by co-precipitation) for hydrogenolysis of ethylene glycol (pure 4.0 nm Pd and 4.6 nm PdFe showed no activity for alcohol production); (b) Comparison of 5% Pd and 5% Rh on iron oxide for hydrogenolysis of ethylene glycol.

Fig. 5-12 (a) Change of gross selectivity over 5% Pd/Fe_2O_3 versus time in batch-wise hydrogenolysis of ethylene glycol; (b) Time-fraction selectivity over 5% Pd/Fe_2O_3 at different periods in batch-wise hydrogenolysis of ethylene glycol.

Fig. 5-13 Catalytic performance for hydrogenolysis of ethylene glycol over fresh (pre-reduced in H_2 at 200 ^oC for 1 h) and spent Pd catalysts under different temperatures.

Fig. 5-14 Catalytic performance for hydrogenolysis of ethylene glycol over Pd/Fe_3O_4 with different Pd metal loadings.

Fig. 5-15 Plot of selectivities for ethylene glycol hydrogenolysis over different metal catalysts supported on iron oxide.

Fig. 5-16 Plot of selectivities for ethylene glycol hydrogenolysis over different metal catalysts (supported on iron oxide). A volcano relationship between product selectivity and *d*-band centre position can be clearly seen.

Fig. 5-17 A schematic diagram describing the adsorbed ethylene glycol for the hydrogenolysis of ethylene glycol on a transition metal M.

Fig. 5-18 A kinetic study to evaluate the orders of reaction with respect to substrates with derived apparent activation energy over Pd/Fe_3O_4: (a) A plot showing the decrease in methanol production at increasing hydrogen pressure; (b) A plot showing the increase in methanol production at increasing ethylene glycol concentration; (c) A plot of ln *k* against 1/T for the Pd/Fe_3O_4 catalyst.

Fig. 6-1 Proved reserves of NG, reserved growth, estimated undiscovered resources, and unconventional resources in the US and elsewhere in the world.

Fig. 6-2 PXRD patterns of the 5% Rh/C catalyst before and after oxidation of methane.

Fig. 6-3 H_2-TPR profiles of calcined Fe_2O_3 and 5% M/Fe_2O_3 (M = Rh, Pd, Ag, Ni or Pt).

Fig. 6-4 CH_4-TPR profiles of calcined Fe_2O_3 and M/Fe_2O_3 (M = Rh, Pd, Ag, Ni or Pt).

Fig. 6-5 Methane-TPR profiles of calcined Fe_2O_3, Rh/Fe_2O_3, Rh/C, Pt/graphite, Pd/graphite and Rh/graphite (all metal loadings are 5%).

Fig. 6-6 HAADF-STEM imaging of Rh/Fe_3O_4 catalyst. (a) Typical morphology of Rh/Fe_3O_4 catalyst; (b) Higher magnification image of Rh particles distributed on the surface of iron oxide. The lattice fringes of the iron oxide are clearly demonstrated.

Fig. 6-7 Thermodynamic equilibrium product compositions. A plot of thermodynamic equilibrium product compositions as a function of temperature. (a) $CH_4:O_2$ = 30:1; (b) $CH_4:O_2$ = 18.6:1; (c) $CH_4:O_2$ = 10:1;

(d) CH_4:O_2 = 3:1; (calculations performed with the HSC Chemistry 5.11 software).

Fig. 6-8 Temperature-dependent catalytic performance with different feed ratios of CH_4/O_2 over 5%Rh/Fe_2O_3 catalysts. (a) CH_4:O_2 = 30:1; (b) CH_4:O_2 = 10:1; (c) CH_4:O_2 = 1:3; (left) full scale gas composition change with temperature; (right) enlarged region to show a clear gas composition of H_2, CO and CO_2.

Fig. 6-9 A schematic diagram to describe the adsorbed methane for the production of H_2 and CO_2 on a iron oxide supported Rhodium.

Fig. 6-10 Temperature-dependent catalytic performance over 5%Rh/C, 5%Rh/Fe_2O_3, 5%Rh/CeO_2, 5%Rh/Al_2O_3 and 5%Rh/Co_2O_3 catalysts at a gas feed ratio of CH_4/O_2 = 30. (a) H_2 content; (b) CO_2 content; (c) CO content.

Fig. 8-1 Illustration of bond formation between an adsorbate and the *s* and *d* states on a metal surface.

Fig. 8-2 Schematic illustration of the DOS of a transition metal, showing the broad *s* band and the narrow *d* bands (width *W*) around the Fermi level, ε_F.

Fig. 8-3 The local DOS at an adsorbate for: (a) a broad surface band; (b) a narrow metal band. (a) corresponds to the interaction with a metal *s* band and (b) is representative of the interaction with a transition metal *d* band.

Fig. 8-4 The local DOS projected onto an adsorbate state interacting with the *d* bands at a surface. The strength of the adsorbate–surface coupling matrix element *V* is kept fixed as the center of the *d* bands ε_d is shifted up toward the Fermi energy (ε_F = 0) and the width *W* of the *d* bands is decreased to

keep the number of electrons in the bands constant. As ε_d shifts up, the antibonding states are emptied above ε_F and the bond becomes stronger.

LIST OF TABLES

Table 1-1 Historical development of catalysis and industrial processes.

Table 1-2 Examples of major industrial processes using heterogeneous catalysis. (Reproduced from reference 15).

Table 1-3 Some industrially relevant catalysts and supports obtained by precipitation and coprecipitation techniques.

Table 1-4 Methanol production techniques with operating temperatures and pressures.

Table 2-1 List of characterisation techniques, source of agitation energy and the requisite information derived from the technique.

Table 2-2 Polarities for different types of experiments.

Table 4-1 Lattice constants for different metals on Raney Ni catalysts.

Table 4-2 Catalyst specifications according to supplier.

Table 4-3 The catalytic performances of Raney catalysts for ethylene glycol hydrogenolysis; the last column represents the summation of iso-propanol, formaldehyde and acetone.

Table 4-4 Catalytic performance of modified Raney Ni 2800 catalyst for hydrogenolysis of ethylene glycol.

Table 4-5 Catalytic performance of modified Raney Cu catalysts for hydrogenolysis of ethylene glycol.

Table 4-6 d-band centre values (relative to Fermi level) for clean metals and metals with a surface impurity (in brackets).

Table 4-7 Correlating d-band centre of (211) with methanol selectivity.

Table 4-8 Comparison between the catalytic performance of Cu, Ni and Rh metal catalyst for ethylene glycol hydrogenolysis.

Table 5-1 CO adsorption characteristics for Pd/Fe_3O_4 catalysts with different Pd loading. Particle size measurement taken from CO chemisorption was estimated by applying the formula $d = (1.12/D)$ nm and assuming a stiochiometric CO/Pd ratio.

Table 5-2 EXAFS characterisation of Pd/Fe_2O_3 before and after pre-reduction

Table 5-3 Specific catalytic activity and per gram based catalytic activity for the hydrogenolysis of ethylene glycol over Pd/Fe_3O_4 with different Pd metal loadings.

Table 6-1 Catalytic performances for methane activation over Rh/Fe_2O_3 catalysts at different methane to oxygen ratios.

Table 6-2 Catalytic performances for methane activation over a range of Fe_2O_3-supported metal catalysts at a methane to oxygen ratio = 30.

Table 6-3 Catalytic performances for methane activation over different supported Rh catalysts at a methane to oxygen ratio = 30.

LIST OF SYMBOLS AND ABBREVIATIONS

A	Arrhenius prefactor
C	Concentration
D	Dispersion measured by CO chemisorption
E	Activation Energy
ΔG	Change in Gibbs free energy
ΔH	Change in enthalpy
T	Temperature
r	Rate
k	Rate constant
R	Ideal gas constant
λ	wavelength
Fe_xO_y	Non-stiochiometric iron oxide
BET	Brunauer−Emmett−Teller
BF	Bright field
CCD	Charged couple device
CN	Coordination number
DFT	Density functional theory
EDX	Energy dispersive x-ray spectroscopy
E_F	Fermi level
EG	Ethylene glycol
EtOH	Ethanol
EXAFS	Extended x-ray absorption fine structure
FID	Flame ionisation detector
FTIR	Fourier transform infrared spectroscopy

FWHM	Full width half maximum
GC	Gas chromatography
HAADF	High angle annular dark field
HPLC	High performance liquid chromatography
MeOH	Methanol
Pd/C	Palladium supported on carbon (commercial catalyst)
$Pd/Fe(OH)_x$	Precipitate of palladium nitrate and iron nitrate
PdO/Fe_2O_3	Calcination product of $Pd/Fe(OH)_x$
Pd/Fe_3O_4	Reduction product of PdO/Fe_2O_3
ppm	Parts per million
PXRD	Powder x-ray diffraction
rpm	rotations per minute
Rh/Cu	Rhodium and copper alloy produced via polyol process
RT	Room temperature
RWGSR	Reverse water gas shift reaction
STEM	Scanning transmission electron microscopy
TCD	Thermo conductivity detector
TEM	Transmission electron microscopy
TGA	Thermogravimetric analysis
TOF	Turnover frequency
TON	Turnover number
TPD/R/O	Temperature programmed desorption/reduction/oxidation
TPR-MS	Temperature programmed reduction mass spectrometry
UV-Vis	Ultraviolet-Visible spectroscopy
WGSR	Water gas shift reaction

XAS	X-ray absorption spectroscopy
XANES	X-ray absorption near edge structure
XPS	X-ray photoelectron spectroscopy
XRD	X-ray diffraction

LIST OF PUBLICATIONS

1. C.-T. Wu, J. Qu, J. Elliott, K.M.K. Yu and S.C.E. Tsang "Hydrogenolysis of Ethylene Glycol to Methanol over Modified Raney® Catalysts," *Physical Chemistry Chemical Physics*, 15, 9043 (2013).

2. C.-T. Wu, K.M.K. Yu, F. Liao, N. Young, P. Nellist, A. Dent, A. Kroner and S.C.E. Tsang "A Non-syn-gas Catalytic Route to Methanol Production," *Nature Communications*, 3, 1050, (2012).

CHAPTER 1 - INTRODUCTION

CHAPTER 1 - INTRODUCTION....1

1.1 CATALYSIS....3

1.1.1 HISTORY OF CATALYSIS....6

1.1.2 DEFINITION OF CATALYSIS....8

1.1.3 TYPES OF CATALYSIS....9

1.2 PRINCIPLE OF HETEROGENEOUS CATALYSIS....11

1.2.1 STEPS IN A HETEROGENEOUS CATALYTIC REACTION....13

1.2.2 KINETICS AND MECHANISMS OF CATALYTIC REACTIONS 15

1.2.3 ACTIVITIES AND SELECTIVITIES....17

1.2.4 DEACTIVATION....18

1.3 PREPARATION OF CATALYSTS....18

1.3.1 HIGH-TEMPERATURE FUSION AND ALLOY LEACHING....19

1.3.2 PRECIPITATION AND CO-PRECIPITATION....21

1.3.3 IMPREGNATION OF POROUS SUPPORTS....23

1.3.4 POLYOL SYNTHESIS....24

1.4 THE METHANOL ECONOMY....25

1.4.1 GENERAL ASPECTS....25

1.4.2 HISTORICAL BACKGROUND....27

1.4.3 PRESENT USES OF METHANOL....29

1.5 A NON-SYN-GAS CATALYTIC ROUTE FOR METHANOL PRODUCTION

....30

1.5.1 METHANOL FROM FOSSIL RESOURCES: PRODUCTION VIA SYN-GAS 30

1.5.2 METHANOL FROM BIOMASS WITHOUT SYN-GAS 33

1.5.3 METHANOL FROM METHANE PARTIAL OXIDATION 42

1.5.4 METHANOL FROM CO_2 HYDROGENATION 45

1.6 AIMS AND OBJECTIVES 46

1.7 OVERVIEW OF THE THESIS 47

1.8 REFERENCES 49

1.1 CATALYSIS

Catalysts have been widely used in modern chemical, petrochemical, energy production, and environmental protection industries. In 1948, Alwin Mittasch said ''*Chemistry without catalysis would be a sword without handle, a light without brilliance, a bell without sound*'' which still holds true today.[1-2] More than 80% of commercial productions of chemicals involve catalytic processes. Therefore, catalytic science and technology is a key component of modern life and society, helping to drive the economy, and protecting the environment and public health.[3-4] As a consequence, the continuing investment in catalysis research by the public sectors has been recognised as one of the key technologies in many nations.

In the United States (US), the total support by governmental agencies, e.g. the US National Science Foundation (NSF), the Department of Energy (DOE), etc., for catalysis research is reaching $45m per year.[5-6] The Fritz Haber Institute (FHI) in Germany secures more than $35m funding, mainly from the German Science Foundation each year for fundamental research focusing on catalysis and related subjects. Catalysis has been highlighted as an important field for the United Kingdom (UK) industry. £28.5m has been granted by the UK's Engineering and Physical Sciences Research Council (EPSRC), funding 167 projects in catalysis research area on April 2011, on average around £9.5m grant each year.[7] Moreover, the UK is investing £12.9m to create a technology hub researching catalysts, aiming to reduce carbon dioxide emissions and producing cleaner water.[8] These investments are providing a promising development of catalytic science and technology in the future.

In recent decades, there has been a rapid growth in journal publications relating to catalysis, demonstrating the importance of catalysis among scientific research communities (Fig. 1-1). The rapid growth in knowledge has subsequently increased

the activity of patent filing in the US and Europe over the last 30 years (Fig. 1-2).

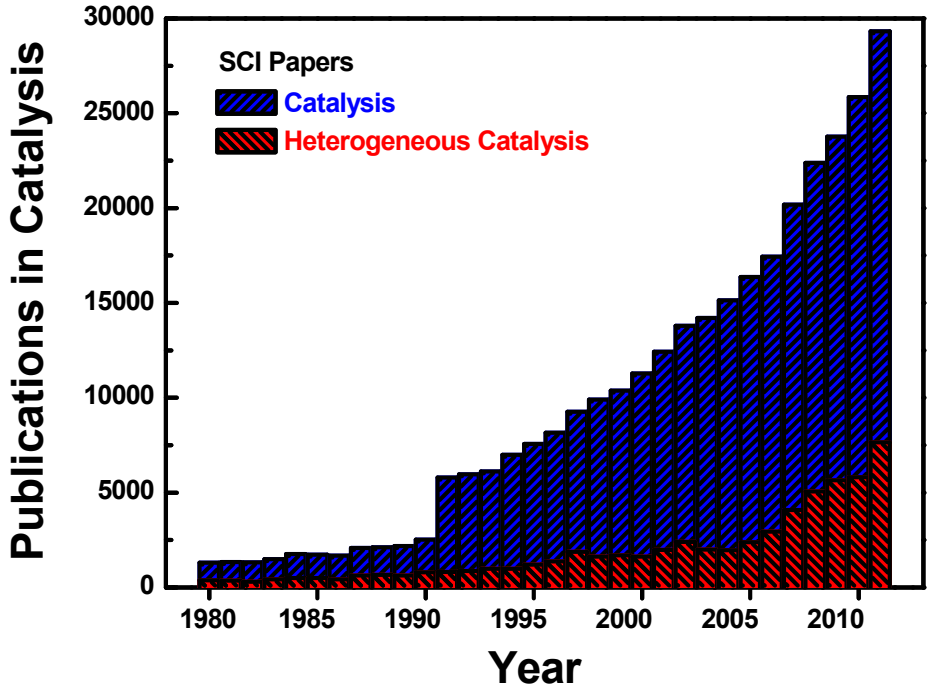


Fig. 1-1 An estimated publications in the last 30 years (from 1980 to 2011) by searching the term 'catalysis' and 'heterogeneous catalysis' on Thomson Reuters Web of Knowledge.

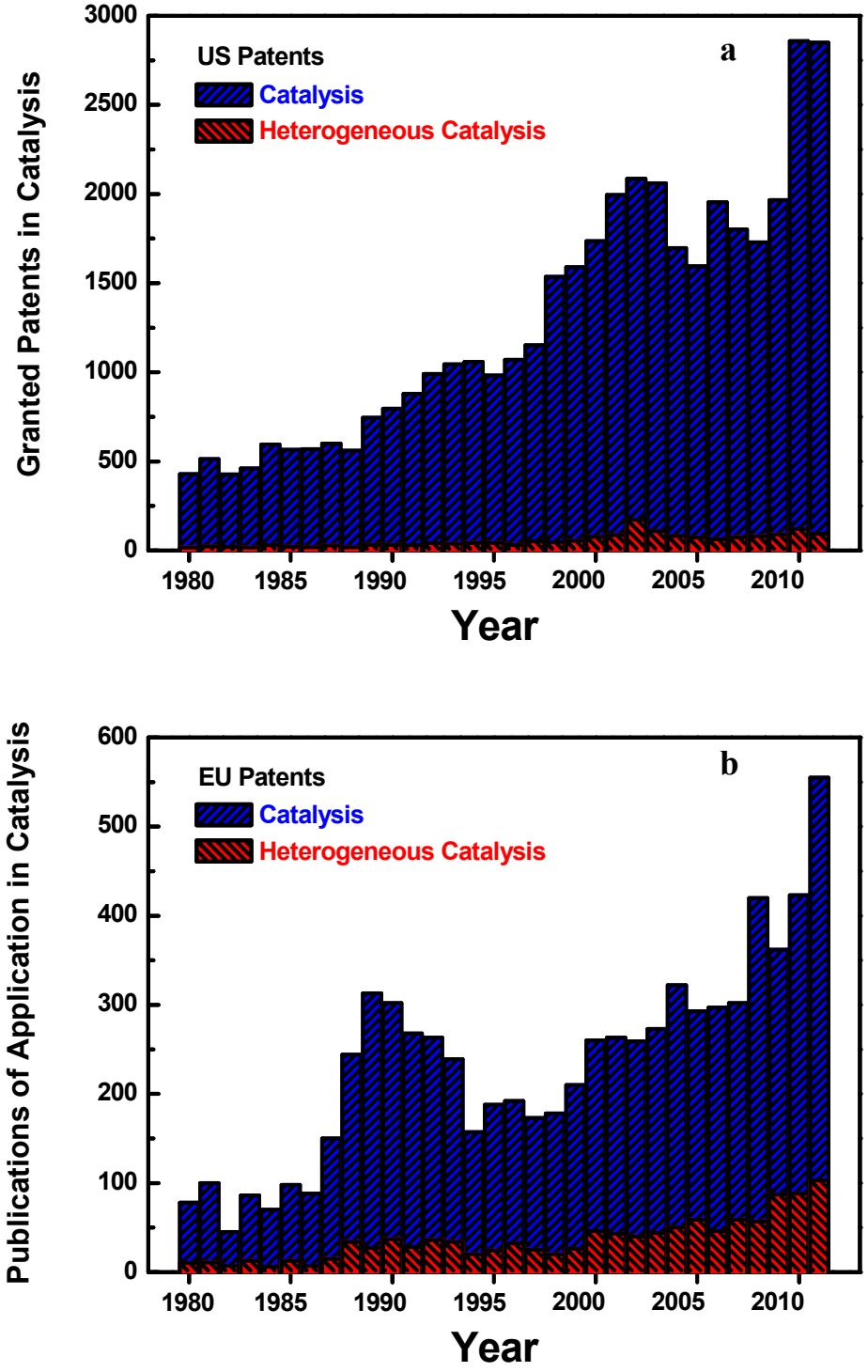


Fig. 1-2 An estimated patents in the last 30 years (from 1980 to 2011) by searching the term 'catalysis' and 'heterogeneous catalysis' on the website of (a) the United States Patent and Trademark Office; (b) European Patent Office.

Catalysis itself is a complex and a multi-disciplinary subject which contains chemistry, engineering, physics, materials science, biology and biochemistry.

Nowadays scientists possess many powerful techniques to characterise catalysts, some of which provide macro-level information whilst others provide micro-level information to precisely define the numbers and structures of active sites down to atomic/molecular level and probe the physics and chemistry of the interactions.

1.1.1 HISTORY OF CATALYSIS

Catalysis has a long history, dating back thousands of years. A typical case is fermentation which utilises enzymes contained in microorganisms (molds, yeasts, or bacteria) to transform organic substances into simpler compounds.[9] Mankind has been using yeast to convert carbohydrate (sugar) contained in wheat to ethyl alcohol. A good example of this was in Ancient Egyptian and Mesopotamia, where beer was produced through fermentation, which perhaps was the first example to demonstrate a homogeneous catalytic process.[10] However, the first scientific reports of catalysis was not unveiled until 1800. Joseph Priestley, an English scientist, and Martinus van Marum, a Dutch chemist, both observed the dehydrogenation of ethyl alcohol over metal catalysts.[11] In 1813, the decomposition of ammonia into hydrogen and nitrogen when passed over red-hot metals had been reported by Professor Louis Jacques Théard at the École Polytechnique in Paris, which has been recognised as the first report of a pattern of catalytic activity. A few years later, the first example of catalytic oxidation was reported by Humphrey Davy and published by the Royal Society (London) in 1817.[11-12] He found that heated platinum could catalyse the combination of coal gas (largely CO and H_2), and air (oxygen) without a flame, resulting in the development of the miner's safety-lamp, which is the earliest recorded patterns of selectivity in catalysis.[10]

The real concept of catalysis was proposed by the Swedish chemist Jöns Jakob Berzelius in an annual report on the progress of the whole of chemistry for the

Stockholm Academy of Sciences in 1835. He summarised a number of isolated observations made by various investigators in the early nineteenth century[11] and concluded that these early investigations could be due to a new force, namely "Catalytic Force", occurring by catalytic contact.[13] The word "catalysis" originates from Greek term (κατα and λνσιζ): "kata" means down and "lyein" means loosen.[13-14]

Except for the fermentation process for producing wine or beer, the first practice of industrial catalytic processes was reported in 1831. Peregrine Phillips patented certain improvements in manufacturing sulphuric acid commonly called Oil of Vitriol (British Patent No. 6069).[12] Another important practice at that time was the catalytic oxidation of ammonia for the production of nitric acid over platinum reported by C.F. Kuhlmann to the Lille Scientific Society in France in 1838. In 1895 Wilhelm Ostwald, Nobel Laureate in chemistry in 1909, recognised the functions of a catalyst and further gave the first modern definition of a catalyst: "A catalyst accelerates a chemical reaction without affecting the position of the equilibrium."[4, 12] Since then the research of catalysis started to take off. The notable developments in catalysis since 1900 are summarised in the following table:

Table 1-1 Historical development of catalysis and industrial processes.[4, 10, 15]

Year	Investigators	Milestones	Contributions
1902	Paul Sabatier J.B. Senderens		Methane from syngas over Ni catalyst
1909	Fritz Haber	Haber-Bosch Process	Obtained significant yields of ammonia using catalysts based on finely divided osmium
1913	Carl Bosch		Developed the first industrial-scale, commercially viable, synthesis of ammonia
1915	Irving Langmuir	Langmuir Isotherm	Quantitative theory of adsorption of gases on surfaces (to describe chemisorption on surfaces and also ultimately to the kinetic description of the bimolecular catalytic process)
1921	Lindemann		Mechanism of unimolecular reactions – activation by collisions
1923	Carl Bosch Alwin Mittasch		Commercialised the process for the production of methanol from water gas derived from coal using a ZnO/Cr_2O_3 catalyst at 300-400 ^oC and 300 atm
1927	Irving Langmuir Cyril Hinshelwood	Langmuir-Hinshelwood kinetics	Proposed the mechanism of the reaction between two molecules over a heterogeneous catalyst surface
1938	Franz Fischer Hans Tropsch	Fischer-Tropsch process	The synthesis of synthetic fuels (the production of liquid hydrocarbons from coal-derived syn-gas)
1940s	Vladimir Haensel	Naphtha reforming	The development of the steam reforming of naphthas over Pt
1970	Blasiak		Methanol synthesis (low pressure, ICI) over Cu-Zn-Al oxide
1985	P.B. Weisz and C.D. Chang	Methanol to gasoline (MTG) process	Gasoline from methanol process (Mobil) over HZSM-5 Zeolite

1.1.2 DEFINITION OF CATALYSIS

As detailed the history of catalysis in the previous section, the first concept/definition of catalysis and a catalyst were proposed (defined) by Berzelius in 1835 and Ostwald in 1895, respectively. Since then the definition of a catalyst has been discussed many times.[1, 16] For example, a catalyst is a substance that is involved in the progress of the reaction, affecting the kinetics (lowering the activation energy barrier and accelerating the reaction rate) but without changing the thermodynamics

of a reaction. At the end of the reaction, the catalyst returns to its original form through a series of elementary steps.[1, 17] Fig. 1-3 shows a schematic diagram which illustrates a different energy pathway for a reaction with or without the help of a catalyst. Catalysts can be atoms, molecules, enzymes or even solid surfaces. Therefore, in the following section, different types of catalysis reactions (homogeneous, heterogeneous and bio-catalysis) will be briefly discussed.

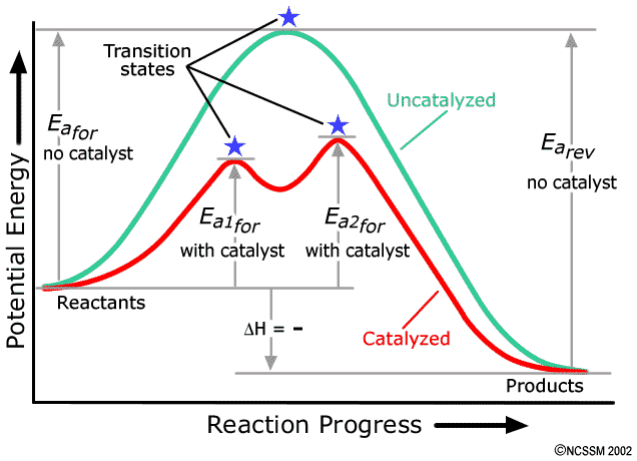


Fig. 1-3 A different energy pathway for a reaction with or without the assistance of a catalyst.[18-19]

Figure reproduced from ref. 19.

1.1.3 TYPES OF CATALYSIS

Catalysis can be customarily classified into three categories: homogeneous catalysis, heterogeneous catalysis and biocatalysis (enzyme). Each groups of catalysis will be briefly discussed below.

i) Homogeneous catalysis – In homogeneous catalysis, the catalyst, the reactants, and the products are all in the same phase. In most cases, the active site of a homogeneous catalyst is known and the reaction is quite selective. However, the homogeneous catalyst complexes are typically very sensitive to temperature, air, and moisture, and are normally very difficult to separate from the reaction products without destroying the expensive ligands, which is the major disadvantage.[1] Homogeneous catalysis is often aimed for the production of delicate

pharmaceuticals.[20] The market share of homogeneous catalysts is estimated to be only ca. 10–15 %.[4]

ii) Heterogeneous catalysis – Heterogeneous catalysis refers to catalysis taking place between several phases. The active centre of a heterogeneous catalyst is normally vague. Most often systems use solid catalyst with reactants in gaseous or liquid phase. As the reaction occurs at the gas-solid or liquid-solid interface, the reactants, the products and the catalysts can be separated easily, which offers one major advantage. Therefore, heterogeneous catalysts are the majority of the bulk-chemicals and petrochemicals industry and contains 80% of the catalyst market.[1, 20] Since the main scope of this dissertation is focused on heterogeneous catalysis more detail examples of heterogeneous catalysis, such as kinetics and preparation methods will be given in the next section.

iii) Biocatalysis – Biocatalysis, by enzymes or cells, is the use of natural catalysts to perform in the liquid phase.[1] Typically, an enzyme can complete 1000 catalytic cycles a second which is 400 times higher than conventional homogeneous/heterogeneous catalysts (normally range from 100–10,000 cycles per hour). It is, however, not the only advantage of biocatalysis. Enzymes can offer the unique enantiomeric selectivity to produce the enantiomer which has the desired activity for the pharmaceutical and food industries. One hindering factor of enzymes is that they are organisms and therefore reactions can often only take place under milder conditions.[15, 21]

The development of heterogeneous catalyst research encompasses three core areas: i) development of a suitable catalyst; ii) elucidation of reaction mechanism; iii) implementation of catalytic process in an industrial scale. Of the three core areas, technical implementation of applied catalysts remains at the heart of catalyst research.

A multi-disciplinary approach between chemistry and engineering is required. For these reasons, it is not surprising that the implementation of a new catalyst requires high capital input and take years from research to production on an industrial scale.

1.2 PRINCIPLE OF HETEROGENEOUS CATALYSIS

As discussed in the previous section, heterogeneous catalysis has been influencing our lives greatly in the 20th century and makes vital contributions to the world's economy. It covers a wide range of industrial applications ranging from petrochemical industries to food and pharmaceutical production.[1, 22-24] Moreover, heterogeneous catalysts make up 80% of all chemical processes worldwide. New applications of heterogeneous catalysis have also been investigated in green chemistry[25], fuel cells[26-28], and nanotechnology[29-31]. Let us elaborate more about the history of heterogeneous catalysis (Table 1-1 in section 1.1.1), tracing back the history to a hundred years ago, Fritz Haber, a German physical chemist, successfully produced ammonia by nitrogen gas and hydrogen gas over an osmium catalyst in 1908.[15] Based on Haber's finding, Carl Bosch with the help from Alwin Mittasch, systematically screened thousands of catalysts and finally discovered an efficient and a cheaper iron-based catalyst. The process and catalyst they found is still in used nowadays. Today, the Haber-Bosch process contributes millions of tonnes of ammonia each year for the fertiliser industry by catalytic hydrogenation of nitrogen gas over a catalyst at around 450°C and 300 bar.[32]

Fischer–Tropsch process probably is another great achievement in the history of heterogeneous catalysis. During the World War II, Germany had a high demand on fuels. However, Germany's lack of natural gas and fossil fuel but rich in coal meant the Fischer–Tropsch process produced liquid hydrocarbons (C5-C11 synthetic fuel)

from coal-derived syngas over iron and cobalt catalysts, contributing 90% of Germany's fuel consumption for aviation and motor industry at that time.[33] Since 1955, Sasol implemented and commercialised the production of synthetic fuel through Fischer–Tropsch process in South Africa, where also has abundant coal reserves. The process is still in used today to supply around 30% fuel demand in South Africa.[34]

Not surprisingly, heterogeneous catalysis governs the whole petrochemicals and bulk chemicals industry.[15] The total sales of refinery catalysts reached $2.7 billion in 2005[35] and is expected to expand to $4.3 billion by 2018,[36] with an annual growth about 3.6%. Table 1-2 shows some key processes and their basic information in the heterogeneous catalysis implemented in the last two decades.

Table 1-2 Examples of major industrial processes using heterogeneous catalysis.[15] Table reproduced from ref. 15.

Process	Catalyst	Reactants	Products	End usage
Haber–Bosch NH_3 synthesis	magnetite (Fe)	H_2, N_2	NH_3	fertilizer, gunpowder, explosives
Methanol synthesis	$Cu/ZnO/Al_2O_3$	CO, CO_2, H_2	CH_3OH	bulk chemicals, fuel
Fischer–Tropsch	Co, Fe	coal, natural gas	C5-C11 hydrocarbons	automotive fuel
Cracking	clays	long alkanes, C_{12+}	C_7-C_9 alkanes	fuel, detergents
Alkylation	zeolites, clays, silicates	C_3-C_5 alkanes	C_7-C_9 isoalkanes	high-octane fuel
Dehydrogenation/reforming	Pt/Al_2O_3	alkanes	alkenes	polymers, bulk chemicals
Hydrodesulfurisation	Co/Mo sulfides	diesel fuel	sulfur-free diesel	automotive fuel
Hydrocracking	Pt on zeolites or aluminosilicates	aromatics mixture	saturated hydrocarbons	automotive/aviation fuel
Isomerisation	H-ZSM-5 zeolites	xylenes, toluene	p-xylene	polymers, bulk chemicals
Polymerisation	Ti, Ziegler–Natta	ethene	poly(ethylene)	polymers, bulk chemicals
Oxidation	Vanadium oxide	xylenes	phthalic acids	polymers

According to the definition of catalysis, a catalyst changes the mechanism of the reaction but cannot alter the position of thermodynamic equilibrium. For example, as illustrated in Fig. 1-4, if we travel from A to B, no matter which route (pathway) we take (either left or right), we can reach point B eventually. The route we take will change the kinetics of the reaction whilst the level of thermodynamic equilibrium of destination B will not change. In the following sections, we will introduce steps which have undergone catalysis reaction and the kinetics of catalytic reactions.

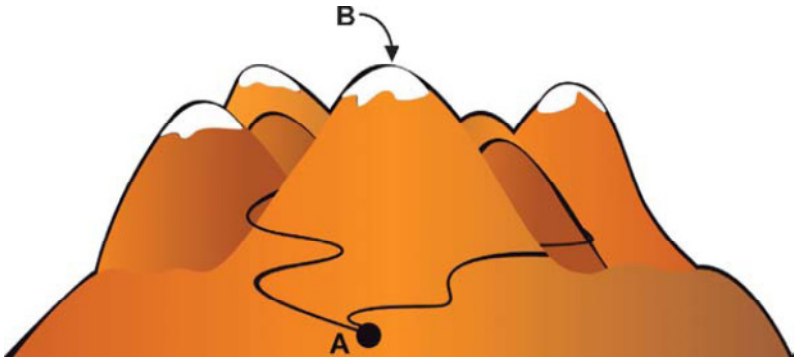


Fig. 1-4 Catalysis deals with the transition between reactants and products. It does not affect the overall reaction thermodynamics.[15] Figure reproduced from ref. 15.

1.2.1 STEPS IN A HETEROGENEOUS CATALYTIC REACTION

A heterogeneous catalysis can be separated as a combination of successive elementary steps during an overall catalytic process which are described elsewhere[1, 4, 37] and shown as following steps:

1. External diffusion of the reactants from bulk phase through the boundary layer to the external catalyst surface.
2. Intraparticle (internal) diffusion of the reactants to the active sites on catalyst surface
3. Adsorption of the reactants on active sites.
4. Surface reactions, including formation or conversion of various adsorbed intermediates.

5. Desorption of products from the active sites.
6. Intraparticle (internal) diffusion of the products from the active sites on catalyst surface to the external catalyst surface.
7. Diffusion of the products from the external catalyst surface across the boundary layer to the bulk phase.

All aforementioned steps are illustrated in Fig. 1-5 and generally can be categorised into three different regimes according to the reaction rate: (a) film diffusion (Steps 1 and 7); (b) intraparticle (pore) diffusion (Steps 2 and 6); and (c) intrinsic reaction kinetics (Steps 3 to 5) of catalyst performance. Among which, the reaction rate of the intrinsic kinetics region (c) is the slowest compared to film and pore diffusion. Therefore, rate determining steps usually occur in steps 3 to 5. This rate determining step can also help us to determine the reaction order.

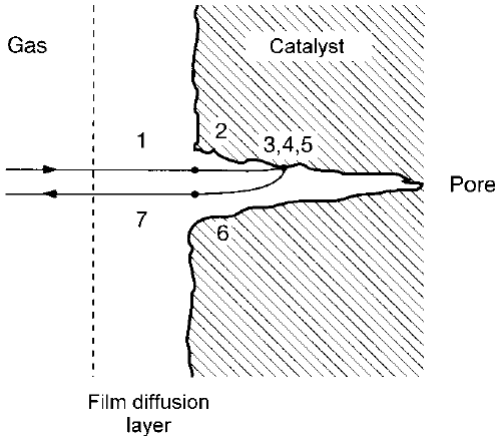


Fig. 1-5 Individual steps of a heterogeneously catalysed gas-phase reaction.[4] Figure reproduced from ref. 4.

In addition, a change in the reaction temperature also affects the reaction rate due to heat transfer effects, especially the rate in the kinetic region increases rapidly with increasing temperature as shown in Fig. 1-6. Moreover, as the temperature is further increased to a higher temperature, a rate change is observed in diffusion (film

and pore) regions. The changes in diffusion in film and pore regions are less rapid and less temperature dependent compared to the kinetic region.

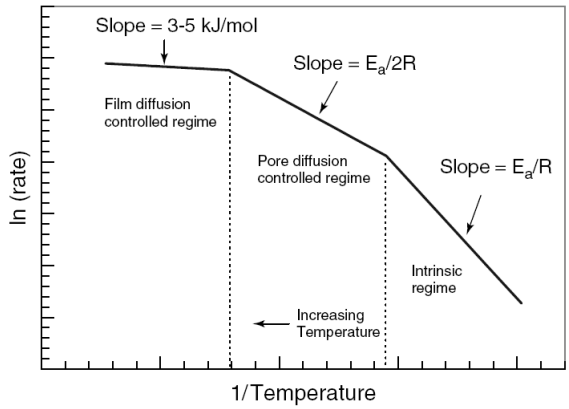


Fig. 1-6 General effects of temperature on catalytic activity. The intrinsic activation energy is equal to Ea, and R is the gas constant.[1] Figure reproduced from ref. 1.

1.2.2 KINETICS AND MECHANISMS OF CATALYTIC REACTIONS

In the following sections, we will describe three common kinetic models based on the Langmuir isotherm.[10] All of these models reduce the complex situations we encountered in real experiments.

1.2.2.1 Unimolecular Reaction -The Langmuir Isotherm

As we mentioned in the previous section, in a heterogeneous catalysis reaction the first step is the adsorption of reactants on the surface of the catalyst. Here we focus on gases reacting on solid catalysts. The relationships between the coverage of a gas adsorbent and its partial pressure above the surface are called isotherms, which are the components of the kinetics of catalytic reactions.[20]

Irving Langmuir developed the first quantitative theory of gas adsorption on surfaces, the well-known Langmuir adsorption isotherm (or Langmuir equation), describing the adsorption of a gas molecule (A) on a clean metal surface (M) at a constant temperature:[10]

$$M + A_{(g)} = \mathrm{A} - \mathrm{M}$$

The resultant equation is:

$$\theta_A = \frac{\alpha \cdot P_A}{1 + \alpha \cdot P_A}$$

where θ_A is the fractional coverage of the surface, P_A is the gas pressure or concentration of A, α is the adsorption constant, so-called Langmuir adsorption constant, which increases with an increase in the binding energy of adsorption and with a decrease in temperature. In addition, the catalytic activity is inversely related to the strength of the chemisorption of the reactant in a unimolecular reaction, as illustrated in Fig. 1-7, that is to say the higher the coverage of adsorbent, the lower the catalytic activity due to the sites being gradually covered until there are no empty sites remaining.

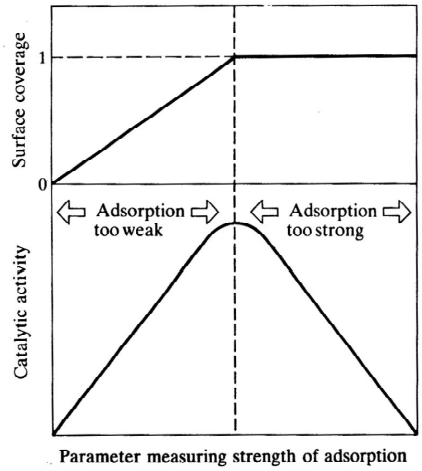


FIG. 6.1. The volcano curve: dependence of catalytic activity upon strength of reactant adsorption (lower part) and the corresponding variation in surface coverage (upper part).

Fig. 1-7 The relation between catalytic activity and the strength of chemisorption of the reactant in a unimolecular reaction.[38-39] Figure reproduced from ref. 38-39.

1.2.2.2 Bimolecular Reactions – Langmuir-Hinshelwood Kinetics

In 1926, Sir Cyril Hinshelwood published a book entitled "The Kinetics of

Chemical Change," where he expanded an earlier idea of Langmuir from 1921. The new model he proposed is known as Langmuir-Hinshelwood kinetics which explains the reaction between two molecules over a heterogeneous catalyst surface.[10] This model expressed the most common situation we encounter in the heterogeneous catalysis because many reactants are activated after adsorbing on the catalyst surface.[15, 40-41] It explains the reaction between two molecules (A and B) over the catalyst surface, which assumed that all species are on the surface before they take part in further reactions. Therefore, adsorbed species react with each other in the chemisorbed state on the surface, as illustrated in Fig. 1-8a.

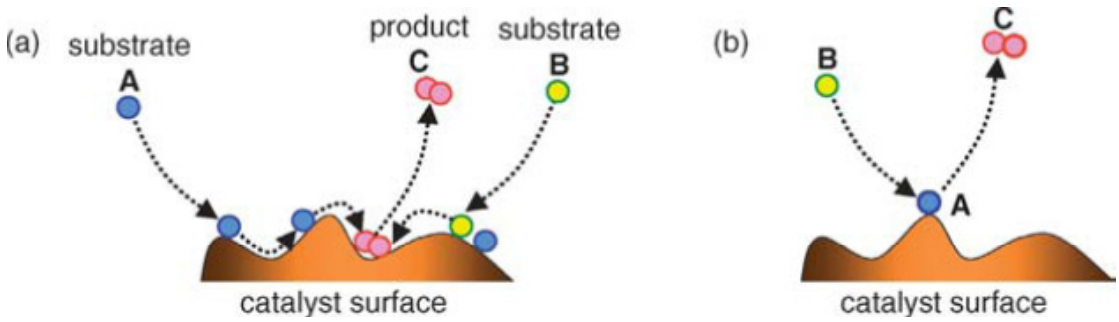


Fig. 1-8 The two main mechanisms in gas/solid heterogeneous catalysis: a Langmuir–Hinshelwood; b Eley–Rideal. [15] Figure reproduced from ref. 15.

1.2.2.3 Bimolecular Reactions - Eley-Rideal Kinetics

As compared to Langmuir-Hinshelwood kinetics, another possible mechanism is Eley-Rideal Kinetics (Fig. 1-8b). The Eley-Rideal Kinetics describes the situation occurring in a bimolecular catalysis, in which one of the reactant A adsorbed on the surface of the catalyst and directly interacts with B (from the gas phase) to form the product C.

1.2.3 ACTIVITIES AND SELECTIVITIES

Catalytic activity and selectivity are two important indices to identify the efficiency of a catalyst. However, in recent decades the scientific community tends to lean to improve the selectivity of a catalytic reaction rather than to increase the

activity. The rapid development of engineering techniques provides solutions for a catalytic reaction with a lower activity by removing the product promptly and recycling the unreacted reactant. However, the disadvantage in a lower selectivity reaction is the production of large quantities of unwanted side products resulting in additional separation cost.[1, 15]

For a typical catalysis reaction, the activity of a catalyst given in units of turnover number (TON), is defined by the number of passes through the catalytic cycle per unit of certain time (e.g. second, minute, etc.) before the catalyst dies (becomes deactivated). Some people may use the turnover frequency (TOF) simply divide the TON by time, which means the number of "reactant" molecules that one molecule of catalyst can convert into "product" molecules in a certain of time. The TON and TOF in heterogeneous catalysis are usually defined per active site, or per gram catalyst.[1, 15]

1.2.4 DEACTIVATION

In reality, the catalyst activity (reaction rate) decreases due to the deactivation of the catalyst. There are different many types of deactivation, however, we can make distinction between them based on the different deactivation mechanisms, described by the following: i) sintering or aging (loss of active surface area); ii) fouling (physical deposition of material such as coke on active surface); iii) poisoning (irreversible binding of an impurity, reactant or product species to the active catalyst site).[37]

1.3 PREPARATION OF CATALYSTS

Production of technical catalysts can be very complicated depending on the intended application. For the production of existing technical catalysts, the process

could be separated into two main categories: bulk and impregnated catalysts, as shown in Fig. 1-9, among which precipitation and impregnation/coating routes, which accounts for more than 80% for the production of industrial catalysts, are illustrated in Fig. 1-10.[1] In the following sections, we will only introduce the preparation methods, which will be carried out throughout this thesis, in more detail.

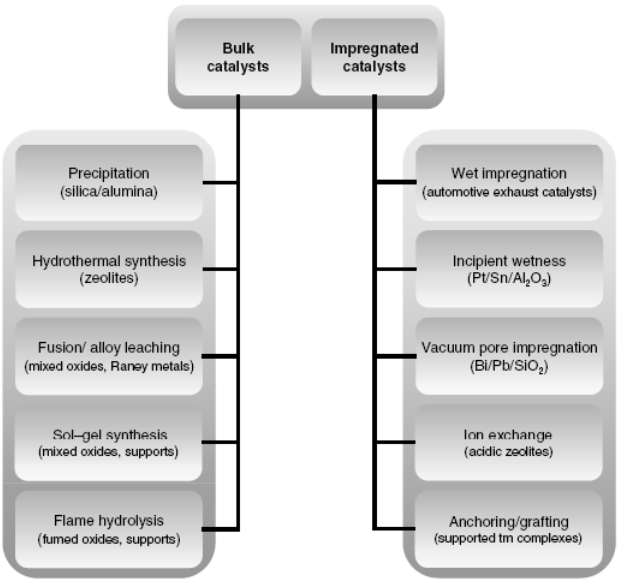


Fig. 1-9 Types and examples of solid catalysts, grouped by preparation method. [15] Figure reproduced from ref. 15.

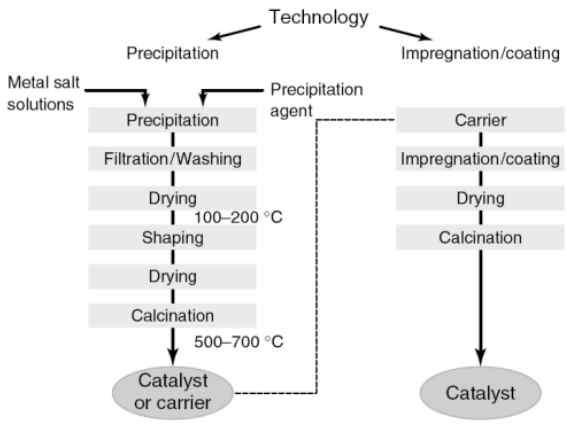


Fig. 1-10 Preparation routes for technical catalysts.[1] Figure reproduced from ref. 1.

1.3.1 HIGH-TEMPERATURE FUSION AND ALLOY LEACHING

A small number of heterogeneous catalysts are prepared by the fusion of

mixtures of oxidic or metallic precursors. The major advantage for fused catalysts is that it allows a mixing of compounds which are not miscible in solution, such as metal oxides or metals. Co-melting and fusion processes of the metal (oxide) precursors at high temperatures enables an intimate mixing down to atomic level. The melting enables the precursors and clusters to create highly pure, well dispersed solids. Furthermore, different phases can be obtained by controlling the cooling of the melt.[15] However, the melting/fusion process has the disadvantage of being an intensive amount of energy and also requires special equipment.

The most importantly practical use of melting/fusion is skeletal Raney series catalysts.[42-43] In 1924, Murray Raney, an American mechanical engineer, produced a 50 wt% nickel–silicon alloy that when treated with aqueous NaOH which resulted in gray metal slurry. This slurry provided an excellent activity, five times more active than the other catalyst at the time, for cottonseed oil hydrogenation.[44] Based on this finding, he made another batch of 50 wt.% nickel-aluminium alloy by fusion and leached out the Al with aqueous NaOH (the process is shown in Fig. 1-11) which surprisingly gave much higher activity than previous reactions. This resulted in a patent in 1926, and the catalyst is known as Raney nickel.[45] Materials with high temperature fusion/melting are then treated with aqueous NaOH to leach out the Al called ‘‘skeletal’’ or ‘‘sponge’’ metal catalysts. Based on Raney’s discovery, a subsequent development of other alloy leaching catalysts had been produced, including iron, cobalt, copper, ruthenium, and palladium.[1, 46-48] Afterwards, Raney’s patents and trademarks were purchased by W. R. Grace & Co. in 1963. Today the two most common skeletal metal (sponge-like) catalysts are nickel and copper for the use in hydrogenation, ammonolysis, and reductive alkylation.[49] These commercial catalysts are ready to use without further reduction. Fig. 1-12 shows the typical SEM

images of Raney nickel and Raney copper. Due to the fusion and leaching process, the Raney metals have a very high metal surface area and are not soluble in aqueous solution; they are easily separated from the products by settling or decantation. However, Raney metals are highly pyrophoric (can active oxygen molecule), and are therefore stored under water.[50]

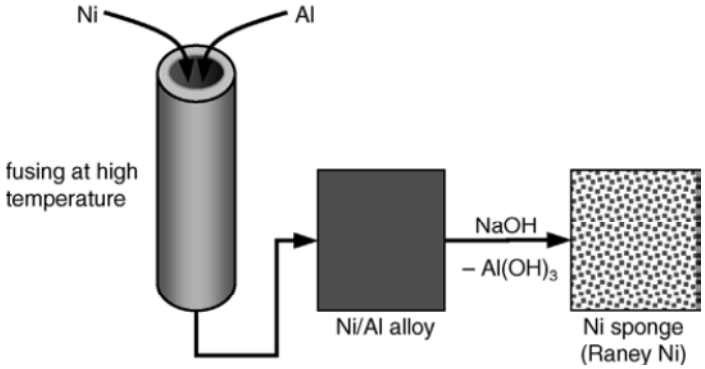


Fig. 1-11 The Raney process, in which a metal/aluminum alloy is prepared by fusion, and subsequently the aluminum is dissolved by aqueous NaOH, leaving a metallic sponge. [15] Figure reproduced from ref. 15.

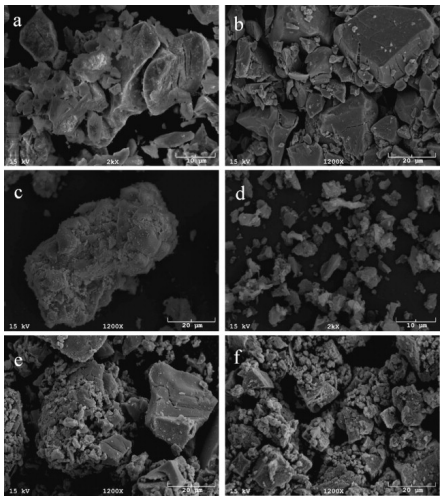


Fig. 1-12 SEM micrographs of the catalysts used in this study: (a) Raney-nickel 4200, (b) Raney-nickel 3202, (c) ruthenium on alumina, (d) ruthenium on carbon, (e) Raneycopper, and (f) Raney-cobalt.[51] Figure reproduced from ref. 51.

1.3.2 PRECIPITATION AND CO-PRECIPITATION

Precipitation (or co-precipitation) is one of the two most important preparation methods for the synthesis of solid catalysts. When more than one salt are precipitated together called co-precipitation. This technique produces a large number of common

commercial catalysts, such as $Cu/ZnO/Al_2O_3$ and Pd/Al_2O_3, which are used for methanol production, hydrogenation, steam reforming and water gas shift reaction. [52-53] More examples of practical catalysts prepared by precipitation/co-precipitation are listed in Table 1-3. Precipitation is unlike the simple mixing of precursors or metals at a high temperature for preparing fused catalysts. The precipitation contains three stages: liquid mixing to supersaturation, nucleation and crystal growth to form primary particles, and growth (aggregation) of the primary particles. The resulting gel is then aged, filtered, washed, dried, and finally calcined. Overall, for producing a catalyst by the precipitation requires following steps:

1) Mixing metal precursors in solution

2) Precipitating the salt by adjusting the pH (usually by adding an acid/base) in the aforementioned precursors in solution (supersaturation, nucleation, and growth occur at this step)

3) Aging the resulting precipitate followed by filtration, washing, drying and finally calcination.

Precipitation has the advantage of synthesising a high-purity material whilst co-precipitation can provide a stoichiometric mixture with well-defined mixed crystallites. This is also viewed as a more difficult method because the particle size, shape, and structure are all formed simultaneously. These particle characteristics are highly dependent on the conditions, such as the concentrations of precursors, temperatures, stirring rate, aging time and so on. Moreover, the nucleation process is strongly depends on the concentration of starting salts and synthesis temperature. Fig. 1-13 shows a typical relationship between nucleation and supersaturation. Moreover, it has been denounced that a great amount of salt solutions is generated after precipitation and also a large quantity of solution is consumed for washing and

filtration the resulting precipitated.

Table 1-3 Some industrially relevant catalysts and supports obtained by precipitation and coprecipitation techniques.[1] Table reproduced from ref. 1.

Material	Use	Important examples
Al_2O_3, mostly γ, in special cases α or η	Support, catalyst	Claus process, dehydration of alcohols to alkenes and ethers, support of hydrotreating catalysts, support for three-way catalyst
SiO_2	Support	Noble metal/SiO_2 for hydrogenation reactions, Ni/SiO_2 for hydrogenation reactions, V_2O_5/SiO_2 for sulfuric acid production, support for Ziegler catalysts
Al_2O_3/SiO_2	Catalyst	Acid-catalysed reactions, such as isomerisation, component of FCC catalysts
Fe_2O_3	Catalyst, catalyst Component	Fischer–Tropsch reactions, major component of catalyst for ethylbenzene dehydrogenation to styrene
TiO_2	Support, catalyst, catalyst component	Major component of DeNO*x* catalyst, photocatalyst
ZrO_2	Catalyst, support	Acid catalyst after sulfate modification, component of three-way catalyst support
Cu/ZnO	Catalyst	Methanol synthesis, methanol steam reforming
$(VO)_2P_2O_7$	Catalyst	Selective oxidation (e.g., butane to maleic anhydride)
Cu–Cr-oxides	Catalyst	Combustion reactions, hydrogenations
$AlPO_4$	Support, catalyst	Polymerization, acid-catalysed reactions
Sn–Sb-oxides	Catalyst	Selective oxidation (e.g., isobutene to methacrolein)
Bi-molybdates	Catalyst	Selective oxidation (e.g., propene to acrolein), mostly supported in thin-layer on non-porous carriers

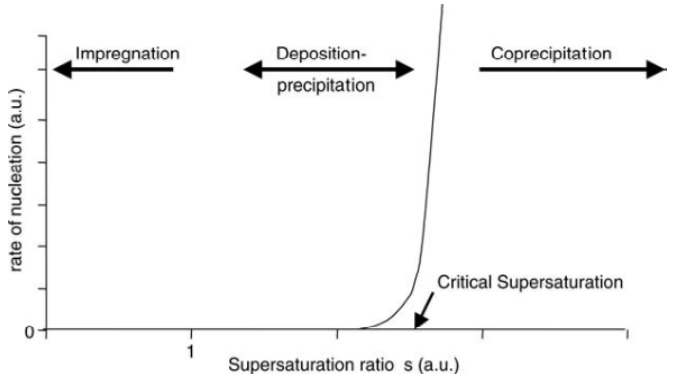


Fig. 1-13 The relation between the homogeneous nucleation rate (nuclei per ml/second) and the degree of supersaturation. s = actual concentration/solubility. [54] Figure reproduced from ref. 54.

1.3.3 IMPREGNATION OF POROUS SUPPORTS

Impregnation is another common method of making supported catalysts.[55]

According to the volume of solution added, impregnations can be classified in two categories: wet impregnation and incipient impregnation. In impregnation, the support usually has a porous structure where the catalyst precursor can fill the pores of the support by immersing into the precursor solution, so called wet impregnation. However, large volumes of aqueous waste are produced during the process. This technique can be improved by the incipient impregnation. This works by a solution of catalyst precursor being dropped on the powder of support until the pores of the support are filled with the liquid. This is followed by drying and calcination. Incipient impregnation has the advantage that it can achieve a high loading by repeating the impregnation process.

1.3.4 POLYOL SYNTHESIS

Despite the fact that conventional methods for the preparation of catalysts are quite convenient and can be produced in large scales, some advanced preparation methods have been investigated and executed in order to understand how we can further modify the properties of catalysts and understand the active sites for catalytic reactions. One of these advanced approaches is the "polyol process". The polyol process has been reported as a fascinating and promising technique for the preparation of colloidal nanoparticle.[56] For a typical polyol process, as illustrated in Fig. 1-14, several metallic nanoparticles/nanocatalysts can be synthesised by the reduction of metal salts with high boiling-point solvents such as ethylene glycol for polar reagents and diphenyl ether for non-polar reagents; in some cases (if a solvent with no reducing power is used), additional reductants such as 1,2-hexadecanediol is used for reducing metal precursors.[57]

It is evident that the catalytic activity is highly dependent on the size and dispersity of catalysts.[58] The polyol process provides an approach to synthesise

catalysts down to nano scale level. Moreover, the size of nanocatalysts can be controlled by varying several parameters, such as the ratio of metal precursors to surfactants, heating rate or even stirring rate of the reduction process.[59] Therefore, monodisperse nanoparticles can be obtained through this process.[60] Bimetallic nanoparticles, alloy or core-shell, can also be obtained by the polyol process. Sun and coworkers have successfully demonstrated the synthesis of monodisperse FePt (alloy) nanoparticles tunable from 3 to 10 nm diameter and with less than 5% size distribution by reducing metal precursors simultaneously.[61] For core-shell structure nanoparticles, a two-step reduction is used to reduced core metal and shell metal consecutively.[62]

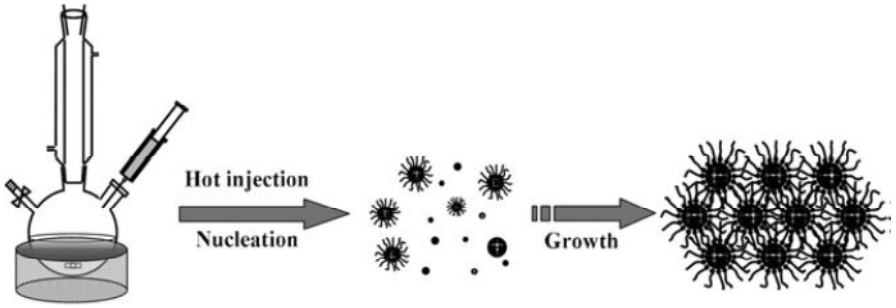


Fig. 1-14 Hot-injection method for the synthesis of monodisperse nanoparticles.[57] Figure reproduced from ref. 57.

1.4 THE METHANOL ECONOMY

1.4.1 GENERAL ASPECTS

The main energy sources, coal, oil and natural gas, are unlikely to provide us for another few centuries. We should not play down the consequences of the world's growing demand for energy and the demands on natural reserves, especially as the world population has reached 7 billion as of 2012.

The global trend is shifting away from the dependence on fossil fuel to alternative renewable resources, such as sun, wind, hydropower and biomass which offer cleaner alternatives to fossil fuels. It is believed that the utilisation of these

alternative energy sources will produce little pollution or no greenhouse gases emission. Although these energy sources could potential substitute fossil fuels, the current infrastructure is not quite established for these sources. Thus within the short term alternative source fossil fuels or routes to similar structures are of keen interest. Nobel laureate George Olah and his colleagues have advocated the Methanol Economy[63-64] which suggested that using methanol to replace fossil fuels as the next generation of energy source and fuels. It is well known that methanol is a basic building block of a wide variety of chemicals and is important for synthetic dyestuffs, resins, drugs, and perfumes. Methanol, in terms of energy source, is liquid therefore can be easily transported. Methanol can directly blend with gasoline for internal combustion engines and fits well with existing energy infrastructure when compared to hydrogen or natural gas. Moreover, for some countries that have abundant natural reserves other than oil (natural gas for Russia, coal for China, wood for Malaysia) but do not want to rely on importing oil from Middle East to feed their high energy demands, methanol is a perfect candidate due to the fact that methanol can be converted from coal, natural gas or even wood (biomass). A good example of a changing reliance on energy is China's in which the boosting economy has put an expanding demand for methanol of about 28 million metric tons (MMT) in 2011, almost half the world's demand, and expected to increase to 55 MMT by 2016.[65] China has successfully demonstrated coal-base methanol production: In 2009, more than 75% of methanol in China was produced from coal whilst with the rest was predominantly from natural gas.[66] The coal-based methanol industry is expected to substitute more than half of China's gasoline (blending methanol with conventional fuel) supply by 2015[66] which reflects Olah' version of the methanol economy. Furthermore, 4% of the world's methanol was used for fuel purposes in 2005 and this

increased to 11% in 2011.[65] This ratio is anticipated to further increase to 16% (around 14.8 MMT) by 2016.[65-66] It is clearly suggested that as petroleum prices rise due to growing global demand, the economics of methanol as an alternative fuel will become increasingly attractive.

Overall, the concept of Olah's "Methanol Economy" suggested that methanol can be used as: (i) a convenient energy storage and carrier medium; (ii) a readily transported and dispensed fuel, including uses in methanol fuel cells; and (iii) as a raw material for synthetic hydrocarbons and their products, including polymers and single-cell proteins (for animal feed and/or human consumption).[64] Moreover, according to Olah's proposal there should not be any restriction for choosing which is the best way to produce methanol and encouraged the discovery of alternative ways for methanol synthesis. The "Methanol Economy", rather than just a slogan, is a feasible approach and offers us insights into departing the dependence from fossil fuel and switching our thinking about how we can use and synthesise methanol smartly. Therefore, we will provide more flexible options/approaches in the following sections of this chapter.

1.4.2 HISTORICAL BACKGROUND

Methanol, known as methyl alcohol, wood alcohol or wood spirits, has a chemical formula CH_3OH and was first isolated by an Irish chemist Robert Boyle in 1661 whilst distilling boxwood, thus is also called wood alcohol or wood spirits. Later in 1905 Sabatier and co-workers used CO and H_2 for producing methanol. Here, methanol was founded as the byproduct when producing ammonia at high pressure and temperature (Haber and Bosch process) which contributed to the development of methanol synthesis.

The commercial process for methanol production was firstly introduced by BASF in 1923. The methanol was produced from syn-gas (the hydrogenation of CO) over a ZnO/Cr_2O_3 catalyst at severe conditions at 300-400 ^oC and 250-350 bar.[64, 67] A major breakthrough was made by Imperial Chemical Industries (ICI) in 1960s, the methanol was synthesised over Cu/ZnO catalysts at much lower pressure of 50-100 bar and 220-300 ^oC, so called ICI process. However, the initial conversion was only about 15%, therefore, recycled unreacted gases were required to improve the reaction efficiency. Lurgi launched the improved process in which natural gas was fed in steam saturated form and operated at much lower pressure.[64]

Table 1-4 Methanol production techniques with operating temperatures and pressures.[64, 68]

	Catalyst	Temperature (^oC)	Pressure (bar)
BASF/DuPont	$CuO/ZnO/Al_2O_3$	300-400	100 - 250
ICI	$CuO/ZnO/Al_2O_3$	250-300	50 - 100
Lurgi	$CuO/ZnO/(Al_2O_3)$	230-250	40- 50

It is evident that natural gas and coal are the two major feedstocks for methanol synthesis. The advantage of using natural gas as the feedstock, as compared to coal, is that natural gas is hydrogen rich and contains less sulphur (sulphur could poison the catalyst). Consequently, using natural gas for methanol synthesis can reduce the purification steps. Although, currently natural gas-based methanol still accounts for more than 90% in the methanol industry with the rest being produced from coal-based and biomass. We could expect a reverse situation in the near future as the natural gas reserve declines. Additionally, due to the limitation of natural reserves, as we stated earlier, coal-based methanol accounts for greater than 75% of overall methanol production in China in 2009.[66] Furthermore, Vancouver-based Methanex Corp. is going to move a methanol plant from Chile to Louisiana (US) to take advantage of North America's abundant shale gas reserve.[69] With the shifting trends in the

methanol production industry, continuous developments in (new) catalysts with better catalytic performance are necessary, not least because large amount of catalysts required to achieve the "Methanol Economy". For example, China requires 3000 tonnes of catalyst for its methanol industry.[70]

1.4.3 PRESENT USES OF METHANOL

At the present time, methanol is mainly used as the feedstock for the chemical industry. It is most commonly used for producing formaldehyde, acetic acid, methyl tertiary butyl ether (MTBE), methacrylate, dimethyl ether, olefins, amongst other petrochemical products. The total demand of the methanol market is 55.4 MMT in 2011 and expected to grow to 92.3 MMT by 2016 where more than half are consumed in Asia. If we divide the intended application of methanol into two categories: energetic and non-energetic, the ratio of energetic application is roughly 21% (11% for fuel and gasoline, and 10% for MTBE) with the rest for non-energetic usage. The role of methanol as the transportation fuel to power the future for next generations is clear. There are several provinces in China that introduced and adopted methanol as a transportation fuel, ranging from M5 (5% methanol blended with gasoline) to M100 (100% methanol). It was estimated that about 1.5 to 2 billion gallons of methanol was consumed in China's transportation sector in 2011.[66, 70] In the US, the consumption for methanol in fuel is about 0.3 MMT per year (1 metric ton ~ 330 gallons). A white paper in the US written by a fellow of MIT also proposed to use methanol as the alternative transportation fuel. It revealed that if natural reserves (natural gas and coal) in the US are dedicated for producing methanol and assume 10% of the gasoline consumed in the US is replaced by methanol, the existing natural gas and coal reserves can still last for 121 and 1000 years, respectively. Overall, the growing global economy contributes to the gradual increase in demand

for methanol in chemical feedstock. It is, however, a more striking feature that we can expect booming demand for methanol in fuel for the transportation sector in the next decades.

1.5 A NON-SYN-GAS CATALYTIC ROUTE FOR METHANOL PRODUCTION

Methanol, as the basic building block of a wide variety of chemicals, has been a remarkably global commodity over past few decades resulting in the world's vibrant methanol industry.[71] In the previous section, we have summarised the history of methanol synthesis dated back from 1900's and it has been used in transportation fuel and fuel cells. The wide applications of methanol are expected to boost its global demand from about 61 MMT in 2012 to twice this amount within 10 years time[72] which imposes the important position of methanol. Considering the fact that long-term energy security is a key global challenge, due to the general decline in fossil fuel reserves it is expected that methanol will be synthesised directly from different carbon-containing resources without any unnecessary atomic reorganisation. In addition, methanol is synthesised using natural gas from an energy-inefficient process currently. The conventional process for methanol production will be briefly described in the following section. Moreover, three alternative non-syn-gas routes for methanol synthesis will also be proposed.

1.5.1 METHANOL FROM FOSSIL RESOURCES: PRODUCTION VIA SYN-GAS

The Syn-gas process for producing methanol is most predominant over other approaches. Syn-gas is majorly manufactured from methane steam reforming so called gas to chemicals (GTC) process which is shown as following equation (Eq. 1-

1)[73],

$$CH_4 + H_2O \rightleftharpoons CO + 3H_2 \qquad \Delta H_{298K} = 206 \text{ kJ mol}^{-1} \qquad \text{Eq. 1-1}$$

Due to the strongly endothermic process for syn-gas production, which requires a high thermal energy input resulted in a pricey heat transfer cost, the process has been modified and can be categorised into three main types with the view to cost reduction:[74]

(1) Basic processes: steam reforming and partial oxidation

(2) Improvements in partial oxidation

(3) Combining steam reforming and partial oxidation

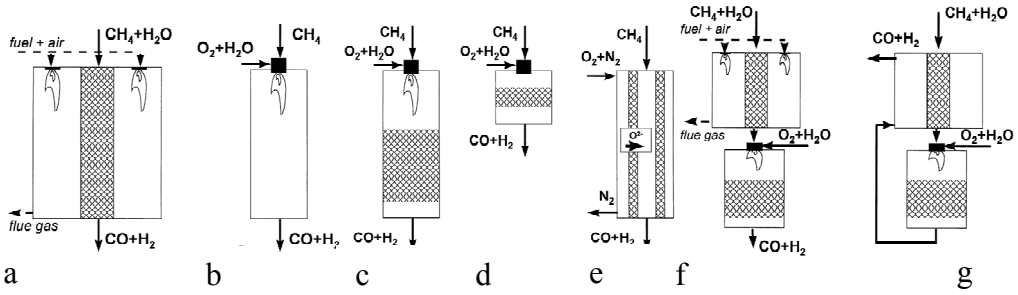


Fig. 1-15 Conventional routes for manufacturing synthesis gas: (a) steam reforming; (b) partial oxidation.; Improved partial oxidation processes for manufacturing synthesis gas: (c) autothermal reformer; (d) catalytic partial oxidation; (e) oxygen-permeable catalytic membrane reformer; Combination of steam reforming and partial oxidation can comprise (f) mass integration for: (i) improved synthesis gas quality as well as (ii) mass and heat integration; (g) for improved energy efficiency. [74] Figure reproduced from ref. 74.

The advances in syn-gas production has made the process complicated, nevertheless, a typical syn-gas process (GTC) can be simply illustrated as follows,

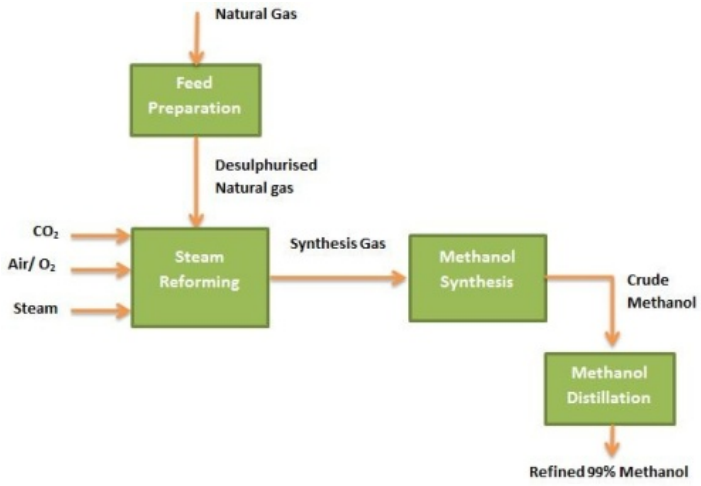


Fig. 1-16 The flow chart of methanol production process.

The overall reaction for methanol production via syn-gas pathway involves following equations,

$CO + 2H_2 \rightleftharpoons CH_3OH$ ΔH_{298K} = -90.7 kJ mol^{-1} Eq. 1-2

$CO_2 + 3H_2 \rightleftharpoons CH_3OH + H_2O$ ΔH_{298K} = -50.0 kJ mol^{-1} Eq. 1-3

$CO_2 + H_2 \rightleftharpoons CO + H_2O$ ΔH_{298K} = 41.0 kJ mol^{-1} Eq. 1-4

Notice that one mole of methane can be converted to three moles hydrogen (Eq. 1-1) which still has one mole excess hydrogen for the following methanol synthesis (Eq. 1-2), therefore, CO_2 is injected into the stream to react with the excess hydrogen to improve the efficiency of methanol production (Eq. 1-4).

Since the production of methanol from syn-gas is a continuous process, control of the composition of the feed stream is highly related to the methanol production efficiency. Here, a stoichiometry number is introduced to quantify the efficiency of methanol production that has been described elsewhere[64, 74]:

$$\text{Stoichiometry number} = \frac{\textbf{moles } H_2 - \textbf{moles } CO_2}{\textbf{moles } CO + \textbf{moles } CO_2}$$

The stoichiometry number is derived from the stoichiometric ratio of CO/H_2 (= 2 presented in Eq. 1-2) and the H_2 consumption which reacts with injected CO_2 in Eq.

1-4 is also taken into account. Therefore within an ideal stream, the stoichiometry number should be maintained at 2 or slightly above.

1.5.2 METHANOL FROM BIOMASS WITHOUT SYN-GAS

1.5.2.1 BACKGROUND

Currently, more than 80% of the world's energy consumption and production of chemicals is originated from the use of fossil resources. This non-renewable route is likely to be continued for a long period of time[75] with ever increasing energy demands predominated by fossil burning as a fuel for both mobile and stationary energy needs. However, there is a decline in the world's fossil fuel reserves, which is also associated with the popular concern in CO_2 emission and its relation with global warming.

One of the greatest trends of this century's global economy is trying to move away from the dependence on fossil fuel resources to sustainable and renewable energy resources for our energy needs.[76] The need for an alternative source of energy supply from renewable resources has become increasingly urgent over the last decade for a number of reasons. First, the global economy and many conflicts between countries have been increasingly related to the region and location for primary energy supply - petroleum. Governments are motivating the utilisation of renewable and locally available energies resources such as solar, wind, hydroelectricity and biomass. Secondly, there is a growing international concern on greenhouse gas emission and its national allowance and relations to the recent climate changes and climate related natural disasters.

Here, most governments' energy strategy is to seek for a new source of supply from renewable resources. It is however, the transport sector (vehicles), one of the most important areas in national energy consumption that has a limited choice for the

type of biomass sources. First, the biomass source is preferably to be in liquid form carrying high energy density with sufficient vapour pressure to fit the current infrastructure (to supply internal combustion engines and can be easily distributed to filling stations). Here, unlike fossil fuel resources, the energy density of most our harvestable biomasses (cellulose, lignin, hemicelluloses and vegetable oils) are relatively low due to their high oxygen content. On top of this, the high molecular weight raw biomasses with very low or even no vapour pressure puts a limitation on any direct application. Therefore, chemical processes like pyrolysis, gasification and transesterification are employed to upgrade these biomasses into more energy condensed forms.[77]

Thus, there is an urgent need for research in the chemistry of biomass to unlock the energy content in the biomass and to open up a wider usage of renewable biomass as a greener energy resource in the future.

1.5.2.2 GLYCEROL AS A RESOURCE OF BIORENEWABLE FEEDSTOCK

Non-food based biomass is an important energy resource in this challenge to generate a greener energy.[78] By applying a suitable catalyst, triacylglycerol can be converted into a bulk chemical having a higher vapour pressure (ethyl or methyl esters) with a greater suitability to be used as a fuel in the transportation sector.

Fatty acid methyl ester (FAME, also known as biodiesel), is made from transesterification of vegetable oils and animal fats with methanol, which has shown a lot of promise as an alternative diesel fuel. Here, glycerol is an unavoidable byproduct of the transesterification process.[79] Indeed, for every 9 kg of vegetable oil processed, 1 kg of glycerol is produced in mass terms.

With the current market of glycerol standing at around 1 million tonnes p.a., the declining market value of glycerol combined with relatively high cost of purification of crude glycerol has meant much of the glycerol produced in biodiesel plants is disposed of as waste. An increase in utilisation of glycerol would make glycerol separation profitable and could make biodiesel production process more efficient. From a molecular point of view, glycerol is an interesting chemical as it is highly functionalised compared to fossil derived hydrocarbons, giving it a strong potential as a biorenewable platform chemical.

1.5.2.3 HETEROGENEOUS CATALYTIC CONVERSION OF GLYCEROL

Over the past decades, many reports in the literature were concerned with catalytic conversions of glycerol.[76, 80-85] As energy crop cultivation has dramatically increased, the related oleochemistry researches have actually taken off. A number of previous works have focused on using heterogeneous catalyst systems, usually supported noble metal nanoparticles, to achieve a good conversion of glycerol. Thus, the catalytic conversion of glycerol into value added products has been the subject of many articles and reviews in recent times and has contributed to the emerging area of green chemistry. The emphasis has, however, varied from oxidation and partial oxidation to gasification and reforming of glycerol for the production of synthesis gas – CO and H_2.[76, 80-85]

1.5.2.3.1 CATALYTIC OXIDATION OF GLYCEROL

In the catalytic oxidation of glycerol, the emphasis has mainly been on the selective oxidation of the primary or secondary hydroxyl group. There is also a considerable interest in the oxidative polymerisation of glycerol to polyketomalonate, which is an important building block in the detergent industry.[76, 80]

1.5.2.3.2 CATALYTIC GASIFICATION OF GLYCEROL

In a catalytic reforming reaction over metal catalysts, particularly using platinum on alumina support catalyst, oxygenated hydrocarbons from biomass are used to produce hydrogen at high temperatures (~ 700 ^{o}C). Glycerol is proposed as an important starting material with a high selectivity to hydrogen formation. The gasification reaction of glycerol proceeds in two steps and with the overall reaction represented are shown as follows:

Steam reforming reaction: $C_3H_8O_3 \rightarrow 3CO + 4H_2$

Water gas shift reaction: $CO + H_2O \rightleftharpoons CO_2 + H_2$

Overall reaction: $C_3H_8O_3 + 3H_2O \rightleftharpoons 3CO_2 + 7H_2$

Even though CO_2 is generated as a by-product, this process is considered as a greener process for hydrogen production since glycerol comes from a renewable sources thus a nearly carbon neutral process.[82]

1.5.2.3.3 CATALYTIC HYDROGENOLYSIS OF GLYCEROL

Hydrogenolysis of glycerol is the main focus of this project. Hydrogenolysis is a breaking of chemical bonding in an organic molecule with a simultaneous addition of a hydrogen atom to each of the resulting molecular fragments. Here, the main challenge lies in the product selectivity from different degrees of C-C bond and C-O bond cleavages where activation energy barriers of these two fundamental reactions could be very similar. The proposed reaction scheme is shown in Figure 1-17.

In general, a possible route for producing methanol from biomass can be obtained by the selective cleavage of C-C bonds to form intermediate fragments which are further hydrogenated to form methanol under mild reaction (where the C-O bond must be preserved). Most hydrogenolysis reactions require high temperatures (between 200-350 ^{o}C) and pressures (between 20-250 bar) over supported noble

metal catalysts.[71, 76] Under such extreme reaction conditions, rupture of C-C bonds can take place but with simultaneously cleavage of C-O bonds. Thus, the reported hydrogenolysis reactions tend to drive glycerol to the end product, methane (a fully hydrogenated product). By promoting the catalyst with a base e.g. NaOH or CaO, it can cause basic sites for dehydration reaction. Thus, the reaction will proceed towards diols, including 1,2-propanediol, 1,3-propanediol or ethylene glycol formation. These compounds are considered as high-value chemicals with specfic applications in the polymer, pharmaceuticals, food, and cosmetics industries. They are also useful functional fluids (e.g. anti-freezing agents).

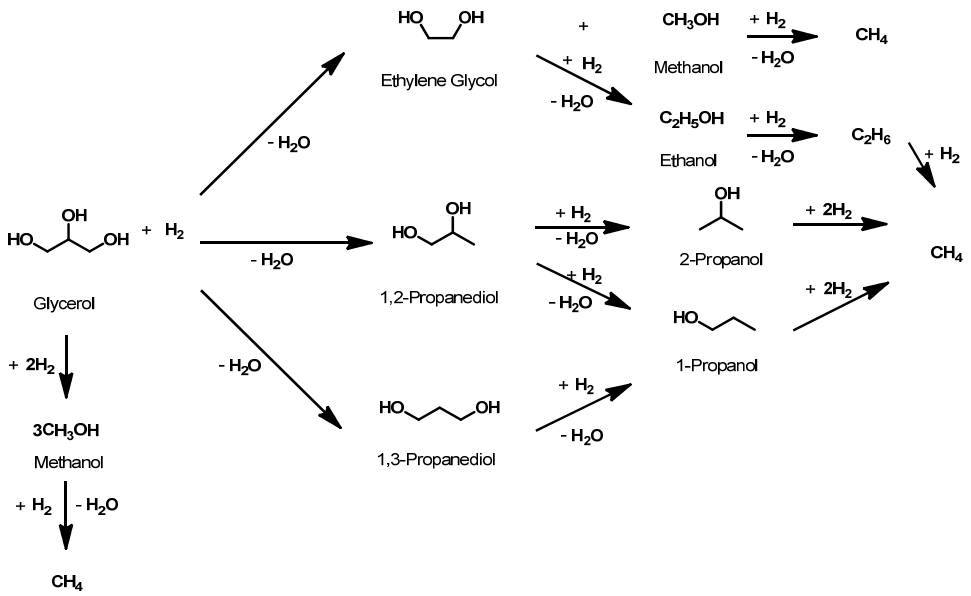


Fig. 1-17 A schematic representation of a number of possible reaction pathways of the hydrogenolysis of glycerol.

Montassier et al. reported a high activity over a number of transition metal catalysts for this reaction, most notably Cu/C which offered a 84% selectivity to 1,2-propanediol under 260 ^{o}C and 40 bar H_2.[86] Subsequently, Cu has been further refined as a hydrogenolysis catalyst using a zinc oxide support.[87-88] Also, a 94% selectivity towards to 1,2-propanediol under 205 ^{o}C has been achieved by using Raney Cu catalyst in a fixed bed reactor.[89] The effectiveness of Raney nickel has also been

reported for a higher selectivity to 1,2-propanediol (93%) under a low hydrogen pressure (10 bar) without any solvent or additives.[90] A number of heterogeneous catalysis reactions were focused, on the other hand, on breaking the primary C-O bond either by using a mixed-metal oxide catalyst[91] or by using a Ru (or Pt) catalyst in the presence of a solid acid promoters.[83, 92-93] Furikado et al. reported a good selectivity towards 1,2-propanediol and propanol using a silica supported Rh catalyst which gave a higher activity for glycerol hydrogenolysis than the Ru catalyst.[94] Although 1,3-propanediol has a higher market value than 1,2-propanediol, only a few reports have shown good selectivity to 1,3-propanediol as most of the reported noble metal catalysts exhibit preferential primary alcohol cleavage.

Some attempts have been made to understand the mechanism within glycerol hydrogenolysis. Montassier proposed a two branch mechanism with pathways that split between ethylene and propylene glycol formation.[95] He suggested that a bifunctional nature of their catalyst with an active metal surface for both dehydrogenation and subsequent hydrogenation. It was proposed that a common initial step for both reactions involved dehydration of glycerol to glyceraldehyde, with the subsequent step involving either a retro-aldol reaction followed by hydrogenation to give ethylene glycol and methanol, or a dehydration to give 1,2-propanediol. This paper also speculated that adsorbed hydroxyl radical species may play a key role in the reaction mechanism, possibly acting as a Brønsted base. This mechanism was later modified by Maris et al.[85] who compared a ruthenium catalyst and a platinum catalyst at a neutral and a basic pH. This study showed that both the C-C and C-O cleavage pathways were significant over the Pt catalyst while only the C-O cleavage pathway was dominant over the Ru catalyst when NaOH was used as the basic promoter. This work clearly supports Montassier's hypothesis that adsorbed

hydroxyls play a role in both of the reaction pathways. Regarding selective C-C cleavage, the adsorbed hydroxyl may impose a negative impact on the C-C cleavage step which would compete with the base catalysed C-O cleavage. A proposed mechanism is shown in Fig. 1-18 detailing the Maris modified Montassier pathway in the presence of base addition.

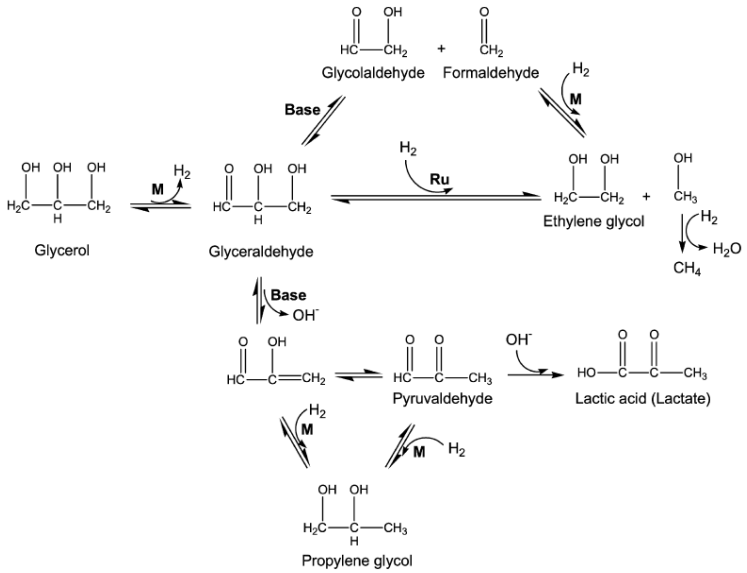


Fig. 1-18 A scheme outlining the hydrogenolysis of glycerol on Ru- / Pt-based catalyst. M denotes either Ru or Pt.[86] Figure reproduced from ref. 86.

It is noted that the economic demand for chemicals derived from glycerol is small and there still remains a challenge of converting of glycerol to energy products. The largest demand of products from the hydrogenolysis of glycerol is for the production of 1,2-propanediol. However, the global demand of 1,2-propanediol is far behind the surplus supply of glycerol as a result of the growing biodiesel industry. However, methanol has a huge demand and an increasing importance for the green energy economy. Therefore, there is a demand for any possible process of catalytic hydrogenolysis of glycerol to methanol with high selectivity. This has the potential not only be economically viable itself but will also increase the overall viability of biofuel plants.

1.5.2.3.4 NEW ENERGY SOURCE FROM GLYCEROL

Compared to glycerol its hydrogenolysis products, 1,2-propanediol, 1,3-propanediol[96] or ethylene glycol are all useful and valuable[97], but do not solve the energy issue. In this project, we are focusing on products with a higher vapour pressure, such as methanol and ethanol, which are considered as potential candidates to fill the energy needs.

Methanol is an excellent fuel for the transportation sector and is well adapted to existing internal combustion engines. The idea of using lower homologue alcohols (methanol and ethanol) as a fuel for internal combustion engines has been known and practiced for some time. There was, however, resurgence in interest in the 1970s when Thomas Reed of the Massachusetts Institute of Technology advocated that a 10% methanol blended gasoline improved the performance of a vehicle, gave better mileage and also acted as an octane booster. Methanol contains about half the energy density of gasoline. However, it has a higher octane rating which means that the fuel/air mixture can be compressed to a smaller volume before it is ignited by the spark plug, allowing the engine to run at a higher compression ratio and hence higher efficiency. Furthermore, methanol engines are low in overall emitters of air pollutants and particulates. Also, methanol is a fuel that can be used in fuel cells and is capable of producing electric energy by reacting with atmospheric oxygen. Noticeably, the Nobel Prize winner, George Olah proposed the use of green methanol in his recent publication entitled “Beyond Oil and Gas: The Methanol Economy”.[63] He advocated a future methanol economy, where methanol would be used as a convenient energy-storage material, a fuel, and a feedstock for the synthesis of hydrocarbons and their products.

The production of methanol from biomass thus offers an exciting means to utilise renewable bioresources. This research is focussed on the catalytic conversion of biomass for methanol production.

1.5.2.4 CHALLENGE

Using hydrogenolysis catalysis, it is possible to further process the poly-alcohols to alcohols with a lower molecular weight for use as a fuel. It has also been documented that both C-C and C-O bonds of polyols can be activated to produce various diols, with methane and carbon dioxide as by-products at a high temperature (200 ^{o}C) and a high pressure of hydrogen (40 bar).[81-82] Therefore, high methanol selectivity from catalytic conversion of biomass depends on the identification of an efficient catalyst in breaking only C-C bond without the C-O bond in hydrogen. The lack of understanding of the fundamental selective cleavage of the C-C bond on surface poses problems and provides motivation for this work since both reactions are thermodynamically favourable to take place. However, bond breaking step generally requires high activation energy. Thus, the C-C cleavage may require high temperature. On the other hand, the bond energies of both C-C bond and C-O bond are very similar (ΔH_{C-C} 348 kJ mol^{-1} and ΔH_{C-O} 360 kJ mol^{-1}), therefore, if the hydrogenolysis reaction is carried out in harsh conditions, it is less likely to achieve a higher selectivity where rupture of C-O bonds is unavoidable.

As aforementioned, the hydrogenolysis of glycerol gives us a range of products over conventional catalysts. Previous attempts from our research group were not quite successfully due to complexity in molecular rearrangement. To reduce the complexity in analysing products and understanding reaction mechanism, ethylene glycol was used as a model molecule to replace glycerol in this early stage. In addition, ethylene glycol as substance has also shown economical importance. Recently, it has been

reported a complete conversion of cellulose with impressive selectivity (61%) towards ethylene glycol over Ni-W_2C/AC catalyst.[98] This suggests that further processing of the biomass derived ethylene glycol could be an exciting direction.

1.5.3 METHANOL FROM METHANE PARTIAL OXIDATION

The synthesis of methanol from methane can simply be categorised in one of two routes: direct or non-direct route as shown in follows.

1) Direct route

$CH_4 + \frac{1}{2}O_2 \rightleftharpoons CH_3OH$ ΔG_{298K} = -111 kJ mol^{-1}, ΔH_{298K} = -126.4 kJ mol^{-1} Eq. 1-5

2) Non-direct route

$CH_4 + H_2O \rightleftharpoons CO + 3H_2$ ΔG_{298K} = 142 kJ mol^{-1}, ΔH_{298K} = 206.2 kJ mol^{-1} Eq. 1-6

$CO + 2H_2 \rightleftharpoons CH_3OH$ ΔG_{298K} = -25.1 kJ mol^{-1}, ΔH_{298K} = -90.7 kJ mol^{-1} Eq. 1-7

The conventional non-direct route (via syn-gas) has dominated the methanol industry for a long period which we have briefed in the previous section. The utilisation of biomass as feedstock of carbon source to produce bio-syn-gas has also been reported. However, it has been criticised that the non-direct route (via syn-gas) requires the methane to completely break down to CO/H_2 before it is re-assembled to methanol by the ex-ICI process. Moreover, the first endothermic step is thermally intensive and energy-consuming. It was estimated that the reforming process accounts for some 70% of entire cost.[99]

Therefore, much effort has been made to improve the thermal efficiency, such as improvement in; the partial oxidation to reach thermodynamic equilibrium, combination of steam reforming and partial oxidation, etc., which contribute to reductions in heat transfer duty and in investment cost. However, according to Lange's economic analysis on several process of methanol production, these

improvements do not seem to provide a significant reduction in capital cost – there is roughly 10% saving in capital cost when taking into account the thermal efficiency as compare to the conventional process[100], showing the limitation for improving current process. Although the techniques to build up commercial plants are becoming mature, the intensive investment cannot be prevented.

1.5.3.1 FROM CATALYSTS FREE APPROACH TO CATALYSIS

The directly partial oxidation of methane (POM) to methanol has been known for 80 years. In 1932, Newitt and Haffner reported that control of the oxidation rate of methane is crucial to synthesis methanol at a high pressure (10-150 bar, 330-400 ^{o}C) with methane/oxygen ratio of 8. A few years later, Boomer and coworkers demonstrated the catalytic conversion of methane over a copper catalyst in a flow system in 1937.[101] It was shown however that this route presented difficulties in providing high conversions of methane together with a high selectivity towards methanol. Due to these difficulties and the also the cheap price of crude oil and natural gas (the main source for methanol synthesis via syn-gas) in that era, less attention has been paid to the POM process to methanol synthesis. Gesser and Hunter summarised research on methanol synthesis from POM have been conducted during that period.[102] It is not until the first energy crisis in 1970s, the interest in this direct process awakened the scientific community to continue the research in methane chemistry.

1.5.3.2 RECENT ADVANCES OF HETEROGENEOUS CATALYTIC PARTIAL OXIDATION OF METHANE

In 1984, Liu et al. used molybdenum on silica as a catalyst at 570 ^{o}C under atmospheric pressure to catalyse POM which achieved 20.5% selectivity and at a 1.6

% conversion of methane.[103] Hutchings' group comprehensively studied a series of metal oxides and proposed the POM over Ga_2O_3/MoO_3 was the best catalyst. However, the yield was less than 1% per pass.[104] Utilising POM to produce methanol is always associated with formaldehyde, the overoxidised product of POM, as the main product.

Since the POM for the direct production of methanol is reduced in volume (Eq. 1-6), high pressure is more favourable according to Le Chatelier's principle. Given the fact that most previous works documented by Otsuka and Wang were carried out with the POM at ambient pressure,[105] the absence of methanol production was reasonable. On the other hand, a reasonable methanol selectivity (~25%) was observed in pressurised reaction which matched Le Chatelier's principle.

Many reviews have discussed the mechanism and aspects of POM,[106] however, as far as we are aware, no process on the direct POM to methanol has yet succeeded in achieving the combination of reasonable conversion and high selectivity over a solid catalyst. This is very challenging because the bond enthalpy (bond dissociation energies) of the C-H bond of methane is 438 kJ mol^{-1}, which is one of the strongest bonds in organic compounds and therefore, requires a high temperature to activate this bond. However, the dissociation energies of the C-H and O-H bonds of CH_3OH are 437 and 385 kJ mol^{-1} respectively which are lower than C-H bond.[107] Thus, if the reaction is operated in harsh conditions, it is unlikely to prevent the cleavage of the C-H and O-H bonds of methanol to be decomposed or overoxidised into HCHO and COx.[74, 105, 108] It is necessary to control the reaction in the kinetic region. Consequently, a lower temperature approach in POM for methanol synthesis has been investigated recently using hydrogen peroxide as oxidant.[109] Although a high

selectivity towards methanol (about 50%) was obtained over a AuPd/TiO_2 catalyst, the conversion was merely less than 0.02% per pass.

1.5.4 METHANOL FROM CO_2 HYDROGENATION

The concern of global warming has been raised for decades which is caused by the emission of greenhouse gases, among which CO_2 amount accounts for greater than 70%. As a result, how to reduce or recycle atmospheric CO_2 has been researched for years, especially the dramatic increase in CO_2 concentration, from 280 to 400 ppm,[110] in the atmosphere over last two centuries. Some attention has been paid to CO_2 fixation by biological and physical processes, such as pumping CO_2 into the ground or in the sea. However, this uptake of atmospheric CO_2 is relatively slow in geological terms. An onsite direct utilisation of the CO_2 emission from fossil-fuel power stations, petrochemical plants, and other industrial plants would be a better alternative and a promising approach if we can convert CO_2 to useful chemicals or liquid fuels (methanol) would be an attractive approach.

The industrial process for methanol synthesis from hydrogenation of CO_2 (Eq. 1-3) was known and applied in the early 20th century. Recent advances show that the hydrogenation of CO_2 to methanol can be carried out effectively over Cu/ZnO-based catalysts.[111-112] In addition, it was recently shown that CO_2 is the key intermediate for methanol formation via syn-gas.[113] In this case a sustainable supply of H_2 is required as seen in equation 1-8 and 1-3

$CH_4 + O_2 \rightleftharpoons CO_2 + 2H_2$ ΔG_{298K} = -343.56 kJ mol^{-1}, ΔH_{298K} = -318.56 kJ mol^{-1} Eq. 1-8

$CO_2 + 3H_2 \rightleftharpoons CH_3OH + H_2O$ ΔG_{298K} = -9.41 kJ mol^{-1}, ΔH_{298K} = -40.96 kJ mol^{-1} Eq. 1-3

Therefore, we are thus interested in exploring an alternative route that does not require extra hydrogen input, in which we propose using natural gas (mainly methane)

as the main source (a self-sustained approach). The combination of the oxidation of methane and the hydrogenation of CO_2 process (above Eqs. 1-8 & 1-3) seems possible approach since the thermodynamics are known to be feasible. Here, the idea is to produce CO_2 and H_2 as the intermediates followed by the hydrogenation of CO_2. This combination could provide solutions for: 1) reducing the intensive energy input for syn-gas production from methane (CH_4 + steam), and 2) providing a self-sustained hydrogen source.

$$CH_4 + \frac{1}{2}O_2 \rightleftharpoons CH_3OH \qquad \Delta G_{298K} = -111 \text{ kJ mol}^{-1}, \Delta H_{298K} = -126.4 \text{ kJ mol}^{-1} \quad \text{Eq. 1-5}$$

Comparing the overall Gibbs free energy between these two-step processes (Eqs. 1-8 & 1-3) and POM (Eq. 1-5), the former approach seems to be more viable for scientific community to continuing research than the direct POM, because the CO_2 hydrogenation technique is quite mature.

1.6 AIMS AND OBJECTIVES

The aim of this research is concerned with development of a non-syn-gas catalytic route to methanol production that could make a meaningful impact to petrochemical industry. In particular, the focus is on the formation of methanol from selective catalytic hydrogenolysis of ethylene glycol, a biomass derived polyol, over a new class of catalysts. Moreover, we also put an effort to conduct a preliminary research on partial oxidation of methane.

We seek to develop a new class of catalysts, where the metal is dispersed at the atomic level through metal-support interaction. In which the modifier may offer ligand or electronic effects to the metal which can offer the efficient C–C cleavage of a robust ethylene glycol molecule followed by C–H formation to form methanol in a hydrogenolysis process. Equally, work will be conducted to activate methane,

containing the strongest bond among hydrocarbons over this new class of catalysts. It is anticipated that this generic approach could offer a new catalytic route for methanol production. In the course of the project, our objectives are shown as follows:

- To synthesis a bi-metallic catalyst by modifying commercial catalysts, such as Raney Ni, Raney Cu and supported Rh with larger quantities of metal sites on a gram basis, using the modified polyol proces**.**
- To investigate the ligand or electronic effect of a second metal on the base metals (as aforementioned commercial catalysts) in the hydrogenolysis of ethylene glycol to lower alcohols.
- To develop a new class of metal oxide supported metal catalysts using a coprecipitation method for the hydrogenolysis of ethylene glycol.
- To study the catalytic effect over the new class of metal oxide supported metal catalysts and to optimise the reaction conditions by tuning the reaction parameters, for example temperature, pressure of hydrogen, concentration of substrate and resident time.
- To examine the activation energy and kinetics of the novel catalyst in the hydrogenation of ethylene glycol.
- To develop a new route of methanol synthesis by the partial oxidation of methane at low reaction temperatures over the new class of heterogeneous nanocatalysts.

1.7 OVERVIEW OF THE THESIS

This thesis comprises seven chapters, with three chapters outlining the research that I had done over the three and a half years of my D.Phil study.

CHAPTER ONE – Introduces the background of heterogeneous catalysis including its history, market, kinetics and the preparation of solid catalysts, conventional and non-traditional ways for methanol synthesis, the main challenges, and recent advances.

CHAPTER TWO – Introduces the most common analytical tools to characterise solid catalysts developed in the thesis.

CHAPTER THREE – Gives a detailed description of the materials and experimental methods used in the synthesis and catalytic testing of nanocatalysts involved in this thesis.

CHAPTER FOUR – Describes the synthesis and characterisation of modified nickel and copper catalysts using a polyol process. These materials were tested in hydrogenolysis of ethylene glycol in the liquid phase.

CHAPTER FIVE – Describes the synthesis and characterisation of metal oxide supported palladium catalysts using coprecipitation. These materials were tested in hydrogenolysis of ethylene glycol in the liquid phase in a pressurised reactor.

CHAPTER SIX – Describes the work on the partial oxidation of methane. These materials were tested in a mixed stream of oxygen, methane and nitrogen in a flow reactor.

CHAPTER SEVEN – Concludes the overall work based on the objectives set for the thesis and proposes perspectives on the future directions of the research

1.8 REFERENCES

1. G. Ertl, *Handbook of heterogeneous catalysis*, 2nd, completely rev. and enl. edn., Wiley-VCH, Weinheim, 2008.
2. S. D. Jackson, *Catal Sci Technol*, 2011, **1**, 855-855.
3. R. L. Augustine, *Catal Today*, 1997, **37**, 419-440.
4. J. Hagen, *Industrial catalysis : a practical approach*, 2nd, completely rev. and extended edn., Wiley-VCH, Weinheim, 2006.
5. National Research Council (U.S.). Committee on the Review of the Basic Energy Sciences Catalysis Science Program., National Research Council (U.S.). Board on Chemical Sciences and Technology. and National Research Council (U.S.). Division on Earth and Life Studies., National Academies Press, Washington, D.C., 2009, pp. 1 online resource (x, 128 p.).
6. R. J. Davis, *International assessment of research and development in catalysis by nanostructured materials / Robert Davis, editor*, Imperial College Press ; Distributed by World Scientific Publishing, London Singapore ; Hackensack, NJ, 2011.
7. The Engineering and Physical Sciences Research Council. (2013). *Catalysts*. Retrieved November 10, 2013, from http://www.epsrc.ac.uk/research/ourportfolio/researchareas/Pages/catalysis.aspx.
8. Centaur Communications Ltd. (2013). Retrieved November 10, 2013, from http://www.theengineer.co.uk/energy-and-environment/news/uk-technology-hub-aims-to-develop-improved-catalysts/1015406.article
9. P. S. Bisen, M. Debnath and G. B. K. S. Prasad, *Microbes : concepts and applications*, Wiley-Blackwell, Hoboken, N.J., 2012.

10. J. R. H. Ross, *Heterogeneous catalysis : fundamentals and applications*, Elsevier, Amsterdam, 2012.
11. A. J. B. Robertson, *Platin Met Rev*, 1975, **19**, 64-69.
12. M. W. Roberts, *Catal Lett*, 2000, **67**, I-I.
13. R. A. v. Santen, *Catalysis : an integrated approach*, 2nd, rev. and enl. edn., Elsevier, Amsterdam ; New York, 1999.
14. K. W. Kolasinski, *Surface science : foundations of catalysis and nanoscience*, 2nd edn., Wiley, Chichester, 2008.
15. G. Rothenberg, *Catalysis : concepts and green applications*, Wiley-VCH, Weinheim ; Chichester, 2008.
16. E. K. Rideal and H. S. Taylor, *Catalysis in theory and practice*, Macmillan and Co., limited, London,, 1919.
17. J. M. Thomas, K. I. Zamaraev, CHEMRAWN Committee of IUPAC. and International Union of Pure and Applied Chemistry., *Perspectives in catalysis*, Blackwell Scientific Publications, Oxford ; Boston, 1991.
18. About.com. (2013). *Catalysts and Catalysis*. Retrieved June 10, 2013, from http://chemistry.about.com/od/chemicalreactions/a/catalysts-catalysis.htm.
19. North Carolina School of Science and Mathematics. (2013). Retrieved November 10, 2013, from http://chemistry.about.com/od/chemicalreactions/a/catalysts-catalysis.htm.
20. I. Chorkendorff and J. W. Niemantsverdriet, *Concepts of modern catalysis and kinetics*, Wiley-VCH, Weinheim, 2003.
21. S. Truesdell, *Chem Eng Prog*, 2005, **101**, 44-47.
22. J. M. Thomas and W. J. Thomas, *Principles and practice of heterogeneous catalysis*, VCH, New York, 1997.

23. J. N. Armor, *Appl Catal a-Gen*, 2001, **222**, 407-426.

24. I. Chorkendorff and J. W. Niemantsverdriet, *Concepts of modern catalysis and kinetics*, 2nd, rev. and enlarged edn., Wiley-VCH, Weinheim, 2007.

25. A. Corma and H. Garcia, *Chem Rev*, 2003, **103**, 4307-4365.

26. S. D. Park, J. M. Vohs and R. J. Gorte, *Nature*, 2000, **404**, 265-267.

27. P. Luksirikul, K. Tedsree, M. G. Moloney, M. L. H. Green and S. C. E. Tsang, *Angewandte Chemie International Edition*, 2012, **51**, 6998-7001.

28. K. Tedsree, A. T. S. Kong and S. C. Tsang, *Angew Chem Int Edit*, 2009, **48**, 1443-1446.

29. J. E. Herrera, L. Balzano, A. Borgna, W. E. Alvarez and D. E. Resasco, *J Catal*, 2001, **204**, 129-145.

30. K. Tedsree, T. Li, S. Jones, C. W. A. Chan, K. M. K. Yu, P. A. J. Bagot, E. A. Marquis, G. D. W. Smith and S. C. E. Tsang, *Nat Nanotechnol*, 2011, **6**, 302-307.

31. K. Tedsree, C. W. A. Chan, S. Jones, Q. A. Cuan, W. K. Li, X. Q. Gong and S. C. E. Tsang, *Science*, 2011, **332**, 224-228.

32. Ceresana. (2012). *Market Study: Ammonia*. Retrieved May 18, 2013, from http://www.ceresana.com/en/market-studies/agriculture/ammonia/.

33. D. Leckel, *Energ Fuel*, 2009, **23**, 2342-2358.

34. Sasol. (2005). *Sasol counters factual inaccuracies by the Democratic Alliance in its call for a proposed supertax petrol levy on Sasol.* Retrieved May 25, 2013, from http://www.sasol.com/media-centre/media-releases/sasol-counters-factual-inaccuracies-democratic-alliance.

35. M. Bryner and A. Scott, *Chem Week*, 2006, **168**, 19-21.

36. Market Research.com. (2012). *Refinery Catalyst Market Shares, Strategies, and Forecasts, Worldwide, 2012 to 2018.* Retrieved May 22, 2013, from http://www.marketresearch.com/Wintergreen-Research-v739/Refinery-Catalyst-Shares-Strategies-Forecasts-6858844.
37. R. Klaewkla, M. Arend and W. F. Hoelderich, ed. H. Nakajima, InTech, 2011.
38. G. C. Bond, *Heterogeneous catalysis : principles and applications*, 2nd edn., Clarendon Press, Oxford; New York, 1986.
39. C. N. Satterfield, *Heterogeneous catalysis in industrial practice*, 2nd edn., McGraw-Hill, New York, 1991.
40. D. Y. Murzin, *Ind Eng Chem Res*, 2005, **44**, 1688-1697.
41. A. V. Petukhov, *Chem Phys Lett*, 1997, **277**, 539-544.
42. Y. Xu, S. Kameoka, K. Kishida, M. Demura, A. P. Tsai and T. Hirano, *Intermetallics*, 2005, **13**, 151-155.
43. Y. Xu, S. Kameoka, K. Kishida, M. Demura, A. P. Tsai and T. Hirano, *Mater Trans*, 2004, **45**, 3177-3179.
44. M. Raney, *United States Pat.*, 1,563,587, 1925.
45. M. Raney, *United States Pat.*, 1628190, 1927.
46. M. Raney, *United States Pat.*, 1915473, 1933.
47. B. V. Aller, *Journal of Applied Chemistry*, 1957, **7**, 130-134.
48. K. Urabe, T. Yoshioka and A. Ozaki, *J Catal*, 1978, **54**, 52-56.
49. N. I. Onuoha and M. S. Wainwright, *Chem Eng Commun*, 1984, **29**, 1-12.
50. A. J. Smith and D. L. Trimm, *Annu Rev Mater Res*, 2005, **35**, 127-142.
51. P. Azadi, K. M. Syed and R. Farnood, *Applied Catalysis A: General*, 2009, **358**, 65-72.

52. B. Delmon, P. A. Jacobs and G. Poncelet, *Preparation of catalysts I : scientific bases for the preparation of heterogeneous catalysts : proceedings of the first international symposium held at the Solvay Research Centre, Brussels, October 14-17, 1975*, Elsevier Scientific Pub. Co., Amsterdam ; New York, 1976.

53. M. V. Twigg and Imperial Chemical Industries PLC. Agricultural Division., *Catalyst handbook*, 2nd edn., Manson, London, 1996.

54. K. P. d. Jong, *Synthesis of solid catalysts*, Wiley-VCH Verlag, Weinheim, 2009.

55. M. Komiyama, *Catal Rev*, 1985, **27**, 341-372.

56. R. Harpeness, Z. Peng, X. S. Liu, V. G. Pol, Y. Koltypin and A. Gedanken, *J Colloid Interf Sci*, 2005, **287**, 678-684.

57. J. Park, J. Joo, S. G. Kwon, Y. Jang and T. Hyeon, *Angew Chem Int Edit*, 2007, **46**, 4630-4660.

58. Z. L. Liu, L. Hong, M. P. Tham, T. H. Lim and H. X. Jiang, *J Power Sources*, 2006, **161**, 831-835.

59. Y. Chen, K. Y. Liew and J. L. Li, *Mater Lett*, 2008, **62**, 1018-1021.

60. S. H. Sun and C. B. Murray, *J Appl Phys*, 1999, **85**, 4325-4330.

61. S. H. Sun, C. B. Murray, D. Weller, L. Folks and A. Moser, *Science*, 2000, **287**, 1989-1992.

62. N. Toshima and T. Yonezawa, *New J Chem*, 1998, **22**, 1179-1201.

63. G. A. Olah, *Angew Chem Int Edit*, 2005, **44**, 2636-2639.

64. G. A. Olah, A. Goeppert and G. K. S. Prakash, *Beyond oil and gas : the methanol economy*, Wiley-VCH ; John Wiley, Weinheim Chichester, 2006.

65. IHS. (2012). *Global Methanol*. Retrieved May 28, 2013, from http://www.ihs.com/products/chemical/market/methanol/global.aspx.

66. C. J. Yang and R. B. Jackson, *Energ Policy*, 2012, **41**, 878-884.

67. BASF. (2013). *The Haber-Bosch process and the era of fertilizers*. Retrieved May 17, 2013, from http://www.basf.com/group/corporate/en/about-basf/history/1902-1924/index.

68. S. Lee, *Methanol synthesis technology*, CRC Press, Boca Raton, 1990.

69. Thomson Reuters. (2013). Retrieved November 10, 2013, from http://www.reuters.com/article/2013/01/24/idUSnMKW544a+70+MKW20130124.

70. L. Bromberg and W. K. Cheng, *Methanol as an alternative transportation fuel in the US: Options for sustainable and/or energy-secure transportation*, Cambridge, 2010.

71. The Methanol Institute. (2011). *The Methanol Industry*. Retrieved April 24, 2013, from http://www.methanol.org/Methanol-Basics/The-Methanol-Industry.aspx.

72. Platts, McGraw Hill Financial. (2011). *Global methanol demand poised to rise on China demand growth: report*. Retrieved May 23, 2013, from http://www.platts.com/latest-news/petrochemicals/Houston/Global-methanol-demand-poised-to-rise-on-China-7610091.

73. A. Holmen, *Catal Today*, 2009, **142**, 2-8.

74. J. P. Lange, *Catal Today*, 2001, **64**, 3-8.

75. N. Dimitratos, J. A. Lopez-Sanchez and G. J. Hutchings, *Top Catal*, 2009, **52**, 258-268.

76. P. Gallezot, *Catal Today*, 2007, **121**, 76-91.

77. A. Behr, J. Eilting, K. Irawadi, J. Leschinski and F. Lindner, *Green Chem*, 2008, **10**, 13-30.

78. G. Taylor, *Energ Policy*, 2008, **36**, 4383-4389.

79. B. D. Wahlen, B. M. Barney and L. C. Seefeldt, *Energ Fuel*, 2008, **22**, 4223-4228.

80. M. Pagliaro, R. Ciriminna, H. Kimura, M. Rossi and C. Della Pina, *Angew Chem Int Edit*, 2007, **46**, 4434-4440.

81. C. H. C. Zhou, J. N. Beltramini, Y. X. Fan and G. Q. M. Lu, *Chem Soc Rev*, 2008, **37**, 527-549.

82. R. D. Cortright, R. R. Davda and J. A. Dumesic, *Nature*, 2002, **418**, 964-967.

83. J. Chaminand, L. Djakovitch, P. Gallezot, P. Marion, C. Pinel and C. Rosier, *Green Chem*, 2004, **6**, 359-361.

84. D. G. Lahr and B. H. Shanks, *J Catal*, 2005, **232**, 386-394.

85. E. P. Maris, W. C. Ketchie, M. Murayama and R. J. Davis, *J Catal*, 2007, **251**, 281-294.

86. C. Montassier, J. M. Dumas, P. Granger and J. Barbier, *Appl Catal a-Gen*, 1995, **121**, 231-244.

87. M. Balaraju, V. Rekha, P. S. S. Prasad, R. B. N. Prasad and N. Lingaiah, *Catal Lett*, 2008, **126**, 119-124.

88. L. Huang, Y. L. Zhu, H. Y. Zheng, Y. W. Li and Z. Y. Zeng, *J Chem Technol Biot*, 2008, **83**, 1670-1675.

89. S. R. Schmidt, S. K. Tanielyan, N. Marin, G. Alvez and R. L. Augustine, *Top Catal*, 2010, **53**, 1214-1216.

90. A. Perosa and P. Tundo, *Ind Eng Chem Res*, 2005, **44**, 8535-8537.

91. L. C. Meher, R. Gopinath, S. N. Naik and A. K. Dalai, *Ind Eng Chem Res*, 2009, **48**, 1840-1846.

92. M. Balaraju, V. Rekha, P. S. S. Prasad, B. L. A. P. Devi, R. B. N. Prasad and N. Lingaiah, *Appl Catal a-Gen*, 2009, **354**, 82-87.

93. T. Kurosaka, H. Maruyama, I. Naribayashi and Y. Sasaki, *Catal Commun*, 2008, **9**, 1360-1363.

94. I. Furikado, T. Miyazawa, S. Koso, A. Shimao, K. Kunimori and K. Tomishige, *Green Chem*, 2007, **9**, 582-588.

95. M. Guisnet, *Heterogeneous catalysis and fine chemicals : proceedings of an International Symposium, Poitiers, March 15-17, 1988*, Elsevier, Amsterdam ; Oxford, 1988.

96. T. Miyazawa, Y. Kusunoki, K. Kunimori and K. Tomishige, *J Catal*, 2006, **240**, 213-221.

97. J. van Haveren, E. L. Scott and J. Sanders, *Biofuel Bioprod Bior*, 2008, **2**, 41-57.

98. N. Ji, T. Zhang, M. Y. Zheng, A. Q. Wang, H. Wang, X. D. Wang and J. G. G. Chen, *Angew Chem Int Edit*, 2008, **47**, 8510-8513.

99. J. Haggin, *Chem Eng News*, 1990, **68**, 27-31.

100. J. P. Lange, *Ind Eng Chem Res*, 1997, **36**, 4282-4290.

101. E. H. Boomer and V. Thomas, *Canadian Journal of Research*, 1937, **15**, 401-413.

102. H. D. Gesser, N. R. Hunter and C. B. Prakash, *Chem Rev*, 1985, **85**, 235-244.

103. H. F. Liu, R. S. Liu, K. Y. Liew, R. E. Johnson and J. H. Lunsford, *J Am Chem Soc*, 1984, **106**, 4117-4121.

104. G. J. Hutchings, J. S. J. Hargreaves, R. W. Joyner and S. H. Taylor, in *Studies in Surface Science and Catalysis*, eds. R. L. E. C. P. N. J. H. S. M. de Pontes and M. S. Scurrell, Elsevier, 1997, vol. 107, pp. 41-46.

105. K. Otsuka and Y. Wang, *Appl Catal a-Gen*, 2001, **222**, 145-161.

106. T. J. Hall, J. S. J. Hargreaves, G. J. Hutchings, R. W. Joyner and S. H. Taylor, *Fuel Process Technol*, 1995, **42**, 151-178.

107. S. J. Blanksby and G. B. Ellison, *Accounts Chem Res*, 2003, **36**, 255-263.

108. Q. Zhang, D. He and Q. Zhu, *J Nat Gas Chem*, 2003, **12**, 81-89.

109. M. H. Ab Rahim, M. M. Forde, R. L. Jenkins, C. Hammond, Q. He, N. Dimitratos, J. A. Lopez-Sanchez, A. F. Carley, S. H. Taylor, D. J. Willock, D. M. Murphy, C. J. Kiely and G. J. Hutchings, *Angew Chem Int Edit*, 2013, **52**, 1280-1284.

110. R. Monastersky, *Nature*, 2013, **497**, 13-14.

111. M. Saito, T. Fujitani, M. Takeuchi and T. Watanabe, *Appl Catal a-Gen*, 1996, **138**, 311-318.

112. J. G. Wu, S. C. Luo, J. Toyir, M. Saito, M. Takeuchi and T. Watanabe, *Catal Today*, 1998, **45**, 215-220.

113. G. C. Chinchen, P. J. Denny, J. R. Jennings, M. S. Spencer and K. C. Waugh, *Appl Catal*, 1988, **36**, 1-65.

CHAPTER 2 - ANALYTICAL TECHNIQUES

CHAPTER 2 - ANALYTICAL TECHNIQUES 58

2.1 INTRODUCTION 59

2.2 X-RAY DIFFRACTION 61

2.3 ELECTRON MICROSCOPY 65

2.3.1 TRANSMISSION ELECTRON MICROSCOPY 65

2.3.2 SCANNING TRANSMISSION ELECTRON MICROSCOPY 67

2.4 X-RAY PHOTOELECTRON SPECTROSCOPY 69

2.5 EXTENDED X-RAY ABSORPTION FINE STRUCTURE 72

2.6 THERMOGRAVIOMETRIC ANALYSIS 75

2.7 TEMPERATURE PROGRAMMED DESORPTION REDUCTION AND OXIDATION 77

2.8 GAS CHROMATOGRAPHY 80

2.9 HIGH PERFORMANCE LIQUID CHROMATOGRAPHY 83

2.10 REFERENCES 88

2.1 INTRODUCTION

Catalysis itself is a complex and a multi-disciplinary subject. In a catalytic reaction, the properties of a working catalyst, such as activity, selectivity and stability, are of paramount importance. However, the catalytic properties of a catalyst surface are determined by its composition and structure on the atomic scale.[1] Nowadays scientists are able to gain access to many powerful techniques to characterise catalysts, some provide macro-level information and others provide micro-level information of their surface, composition and structure. Some key areas that could guide us to gain understanding catalysis on a fundamental level are shown schematically in Figure 2.1.[1] Furthermore, we are keen to understand the physicochemical properties of a catalyst, and define the numbers and structures of active sites in atomic/molecular level. A wide variety of diffraction, spectroscopy, microscopy, adsorption, desorption and surface reactions techniques is readily available to characterise a working catalyst and provide the essential information of the catalyst surface. This information can lead us to design a catalyst for a selected reaction.

Thus, we aim at characterising the catalyst to evaluate its composition, structure, and feature at the atomic level. Several spectroscopic, microscopic and diffraction techniques can be used to investigate solid catalysts (Fig. 2-1). These techniques are based on how the catalyst responds to external simulations subjected to intense light irradiation (X-ray), electrons bombardment (TEM), reactive molecule treatments (TPR/TPO) or heat applications (temperature programmed analysis).

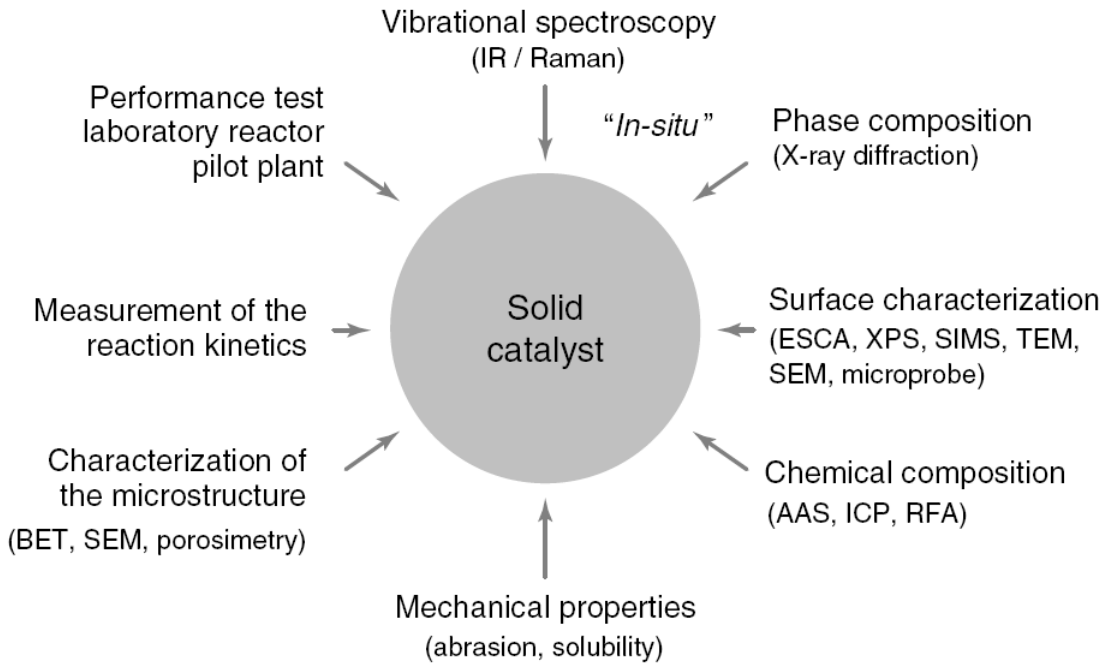


Fig. 2-1 Catalyst characterisation techniques.[2] Figure reproduced from ref. 2.

In this chapter, some of the most important techniques applied in catalyst characterisation or catalysis products analysis, such as transmission electron microscopy, scanning transmission electron microscopy, X-ray diffraction, X-ray photoelectron spectroscopy, temperature programmed analysis, pulse chemisorptions, gas chromatography, and high performance liquid chromatography will be briefly introduced. In addition, it will cover basic principles, applications and the derived information.

Table 2-1 List of characterisation techniques, source of excitation energy and the requisite information derived from the technique.[3] Table reproduced from ref. 3.

Acronym	Full name	In	Out	Information
AES	Auger electron spectroscopy	Electron	Electron	Surface composition
AFM	Atomic force microscopy	-	-	Surface morphology
EELS	Electron energy loss spectroscopy	Electron	Electron	Molecular vibrations
EDX	Energy dispersive X-ray analysis	Electron	X-ray	Composition
EXAFS	Extended X-ray absorption fine structure	X-rays	X-rays	Local structure
FEM	Field emission microscopy	Electric field	electron	Surface morphology
FIM	Field ion microscopy	Electric field	Ion	Surface morphology
IR	Infrared spectroscopy	Photon	Photon	Molecular vibrations
LEED	Low energy electron diffraction	Electron	Electron	Surface structure
LEIS	Low energy ion scattering	Ion	Ion	Surface composition
MAS	Mössbauer absorption and emission	γ-rays	γ-rays	Oxidation state, Lattice
MES	spectroscopy			symmetry, Magnetic properties
	Raman spectroscopy	Light	Light	Molecular vibrations
RBS	Rutherford backscattering	Ion	Ion	Concentration
SEM	Scanning electron microscopy	Electron	Electron	Morphology
SIMS	Secondary ion mass spectroscopy	Ion	Ion	Composition, local structure
SNMS	Secondary neutron mass spectroscopy	Ion	Neutron	Composition
STM	Scanning tunneling microscopy	Electric field	Current	Morphology
TDS	Thermal desorption spectroscopy	Heat	Gas	Coverage, adsorption energy
TEM	Transmission electron microscopy	Electron	Electron	Size, structure
TPDRO	Temperature programmed desorption, reduction and oxidation	Heat	Gas	Mechanism of bulk and surface reactions
TPRS	Temperature programmed Reaction spectroscopy	Heat	Gas	Mechanism of bulk and surface reactions
TPS	Temperature programmed sulfidation	Heat	Gas	Mechanism of bulk and surface reactions
UPS	UV photoelectron spectroscopy	UV Light	Electron	Chemical bonding
XPS	X-ray photoelectron spectroscopy	X-ray	Electron	Composition, oxidation state, dispersion
XRD	X-ray diffraction	X-ray	X-ray	Bulk structure, crytallite size

2.2 X-RAY DIFFRACTION

X-rays have wavelengths in the Ångström range which are sufficiently energetic to penetrate solids, and are well suited to probe their internal structure.[1] X-Ray diffraction (XRD), as seen in Fig. 2-2, is one of the most powerful and applied techniques in catalyst characterisation via a non-destructive examination. The technique is used to identify crystalline phases inside a catalyst and to estimate particle size of a catalyst by obtaining a pattern of its structural lattice parameters.



Fig. 2-2 A PANalytical X'Pert Pro X-ray diffractometer.

Conventional X-rays are generated by accelerating electrons emitted from a heated tungsten filament (cathode) bombarding a copper (anode) at high voltage inside a device known as the x-ray tube. The continuous spectrum is then produced by the deceleration of the charged particles bombarding the anode. At the same time, a line spectrum characteristic of the target material is produced and superimposed on the background radiation. These discrete lines are caused by the incoming electrons having enough energy to remove an electron from the K, L, or M shells of the target copper atoms and then this hole is filled by an outer electron falling back into the hole (Fig. 2-3). Here, the transition of electrons from the L shell to the innermost K shell produce 'K alpha' emissions called the Cu K_α line. The energy and wavelength of the Cu Kα line are 8.04 keV and 0.154 nm, respectively. Similarly, a less intense K_β line is emitted when the K-hole filled from the M-shell.[1]

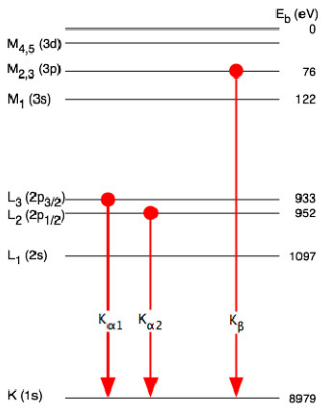


Fig. 2-3 Atomic levels involved in copper Kα and Kβ emission.

X-ray diffraction is based on constructive interference of the scattered monochromatic X-rays and atoms in a periodic lattice (or a crystalline sample). Figure 2.4 illustrates X-rays diffracted from crystal planes and to derive lattice spacings by using the Bragg's law which is expressed as:

$$n\lambda = 2d \sin\theta \,;\; n = 1, 2, \ldots$$

where n is the integer corresponds to the order of reflection; λ is the wavelength of the X-rays; d is the distance between two lattice planes; θ, known as the Bragg angle, is the angle between the incoming X-rays and the normal to the reflecting lattice plane.

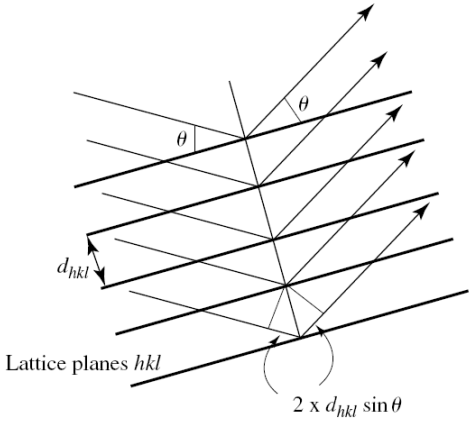


Fig. 2-4 Diffraction of X-rays from crystal lattice planes illustrating Bragg's law.[4] Figure reproduced from ref. 4.

The most commonly used geometry for obtaining XRD data is shown in Fig. 2-5. XRD data is measured with a static X-ray arm attached with a movable detector. This type of powder diffractometer called Bragg-Brentano setup as seen in Fig. 2-5 (bottom), which has an X-ray line source at 3. A flat-plate sample is mounted at 4 and a point detector at 6. The sample is scanned through an angle θ as the detector is moved through 2θ.

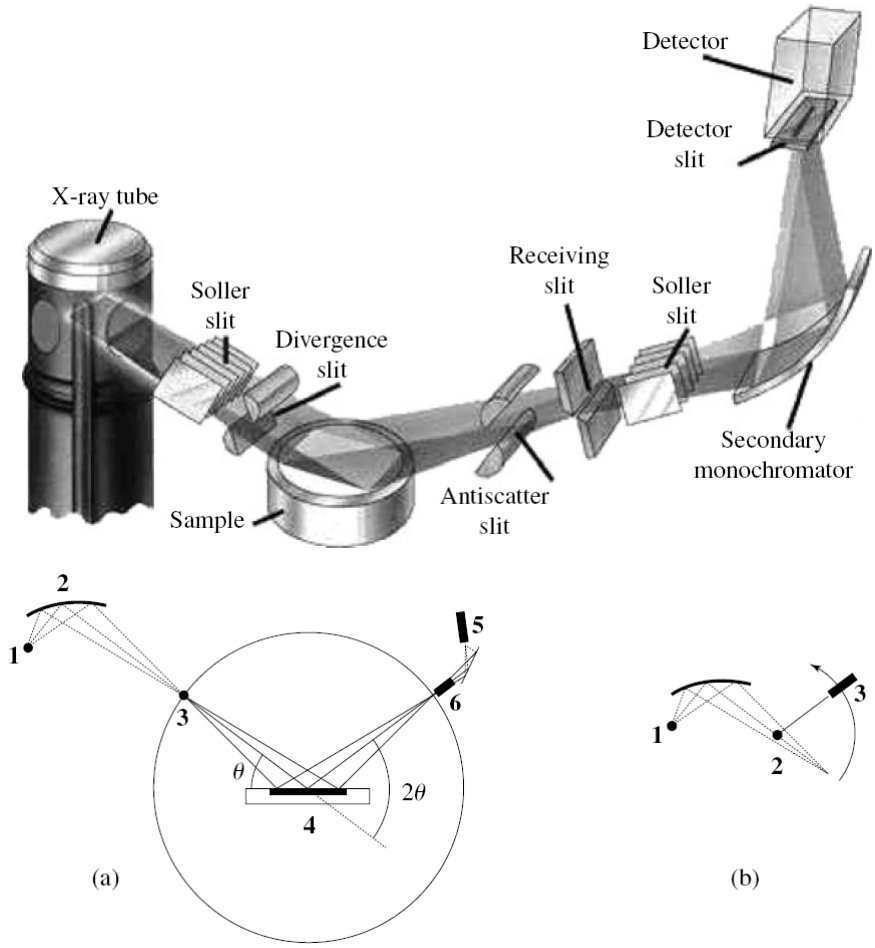


Fig. 2-5 Schematic 3D view of a traditional flat-plate diffraction setup (top); Typical laboratory powder diffraction setups (bottom).[4] Figure reproduced from ref. 4.

An important limitation applied to XRD is that we can only observe clear diffraction peaks when the sample possesses sufficient long-range order and symmetry. This can guide us to determine the dimensions of the reflecting planes by obtaining the width of diffraction peaks. For most nanocatalysts which have

crystallite sizes below 100 nm, line broadening occurs due to incomplete destructive interference in scattering directions where the X-rays are out of phase.[1] Therefore particle size can be predicted based on the simplest expression for peak broadening due to the sample by using the Scherrer equation:

$$L = \frac{K\lambda}{\beta \cos\theta}$$

where L is the is the averaged dimension of crystallites of the particles; λ is the wavelength of the incident X-ray; β is the line broadening at half the maximum intensity (FWHM) in radians; θ is the angle between the beam and normal to the reflecting plane; K is a constant which falls in the range 0.87-1.0 (it is usually assumed to be 1).

2.3 ELECTRON MICROSCOPY

2.3.1 TRANSMISSION ELECTRON MICROSCOPY

Two different types of electron microscope are shown schematically in Figure 2-6. Transmission electron microscopy (TEM) can reveal information about the finest details of the internal structure, including the composition, size, and shape of a specimen. TEM is theoretically similar to an optical microscope. The major difference is that TEM uses transmitted and diffracted electrons instead of light to obtain information about the structure and composition of the specimen. Moreover, electromagnetic lenses are used to focus electron beam in TEM instead of optical lenses in an optical microscope. A primary electron beam of high energy and high intensity firstly passes through a condenser to produce parallel rays, which then impinge on the specimen. After the electron beam interacts and passes the specimen, the beam is then refocused and expanded through sets of projector lenses onto the phosphor screen or a charge coupled device (CCD).[1]

The Rayleigh criterion, the generally accepted criterion for the minimum resolvable distance between two points of equal brightness,[5] defines the resolution of light microscope (δ_d) as:

$$\delta_d = \frac{0.61\,\lambda}{n\,\sin\beta}$$

where λ is the wavelength of the radiation; n is the refractive index of the view medium; β is the semi-angle of collection of the magnifying lens (unclear). As a result, the corresponding resolution limit δ_d is of the order of the wavelength. Typical operating conditions of a TEM instrument are 100 to 200 keV electrons (λ = 2.5 to 3.7 pm), 10^{-6} mbar vacuum, 0.3 nm resolution, and a magnification of 3 x 10^5 to 10^6.[1] The resolution of the electron microscope is limited by aberrations (imperfection in image formation) inherent in electromagnetic lenses.

For electrons to travel through the specimen, powdered samples must be 100 nm or less in diameter. Powdered samples are dusted onto a holey carbon grid of a few millimetres thickness, alternatively they can be dispersed in a solvent and a drop of suspension added onto the grid and dried. Liquid samples are diluted and several drops added onto the grid. Fig. 2-6 shows a typical cross section of a TEM microscope. The electron gun (a tungsten filament, LaB_6 crystal or a field emission tip) produces a monochromatic electrons beam at the top. The beam of electrons is then focused into a small and coherent beam by the double condenser lenses. The first and second lenses are used for controlling spot size and brightness, respectively. The coherent beam passes through the condenser aperture (usually user selectable) to filter out higher angle electrons far from the optical axis (the dotted line down the centre). The beam strikes the specimen and the transmitted beam is refocused by the objective lens into an image. The objective aperture restricts high angle electrons while selected

area diffraction aperture enables the user to interrogate diffraction patterns of electrons by the arrangements of atoms in the specimen. Intermediate and projector lenses enlarge the image passed through the column to a higher magnification. Finally the image is projected onto a phosphor screen for user investigation. In bright field mode, dark areas of the image represent areas with fewer electrons being transmitted either due to thinner regions of the sample or heavier atoms and vice versa. In contrast, dark field images can be obtained when the electron beam is slightly off angle from the bright beam.

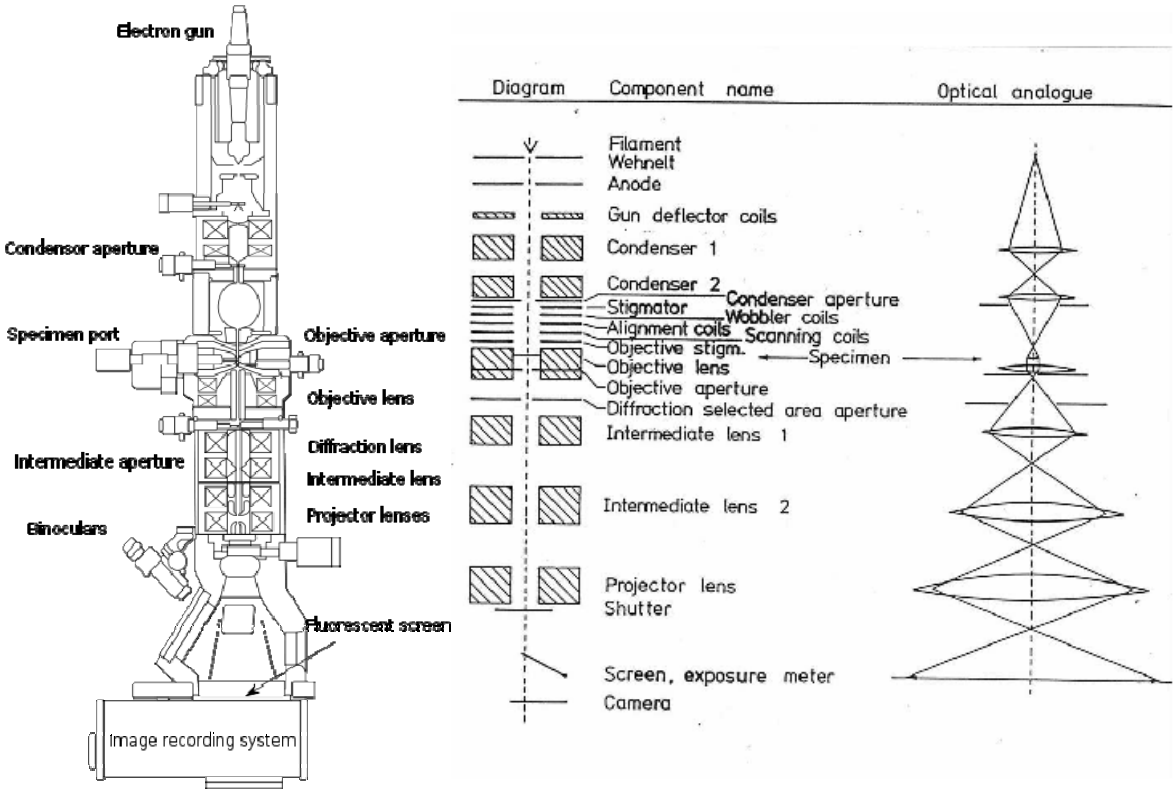


Fig. 2-6 Cross section of a TEM microscope. Figure reproduced from ref. 4.

2.3.2 SCANNING TRANSMISSION ELECTRON MICROSCOPY

Scanning transmission electron microscopy (STEM) combines the TEM and SEM modes of operation, providing a range of different imaging modes with the

ability to provide information on elemental composition and electronic structure at the ultimate sensitivity, that of a single atom.[6] The scanning coils are used to illuminate a small area of the sample, from which either bright- or dark-field images are obtained. Secondary or backscattered electrons can be used for imaging in STEM like in a SEM. On the other hand, higher signal levels and better spatial resolution are available if the primary beam is generated with a field emission gun; the resolution is comparable to that in TEM, with the advantage that selected regions of the sample can be investigated separately.[1, 6]

The contrast of imaging supported metal particles can be greatly enhanced by collecting images in dark-field mode, where the image is formed by collecting scattered electrons that are diffracted by the metal particles with an annular dark-field (ADF) detector, as shown in Fig. 2-7. In addition, the transmitted electrons at high scattering angle (larger than those under which Bragg diffraction occurs) can be collected to form high-resolution, chemically sensitive, atomic number (Z-) dependent contrast images. This high-angle annular dark field (HAADF) detection mode is also called Z-contrast microscopy.[1]

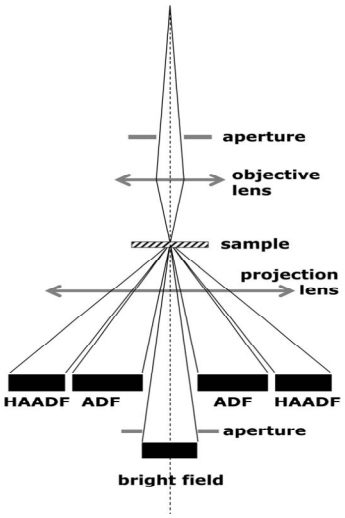


Fig. 2-7 Scheme of a scanning transmission electron microscope with bright- and dark-field detectors. ADF: annular dark field; HAADF: high-angle annular dark field.[1] Figure reproduced from ref. 1.

2.4 X-RAY PHOTOELECTRON SPECTROSCOPY

X-ray photoelectron spectroscopy (XPS) is one the most frequently used techniques in catalysis and an extremely sensitive spectroscopy with regard to surface of a specimen, providing information on the elemental composition, empirical formula and the oxidation state of the elements that exist on or near the surface of a material in a quantitative manner.[7-8] The generation of X-rays is similar to the aforementioned process in section 2.2. However, lower energies Mg K_α (1253.6 eV) and Al K_α (1486.3 eV) are often used X-ray sources in XPS measurements.

XPS is based on the photoelectric effect, whereby an atom absorbs a photon of energy, hn, after which a core or valence electron with binding energy E_B is ejected with kinetic energy (Fig. 2-8):

$$E_k = h\nu - E_B - \varphi$$

where E_k is the kinetic energy of the photoelectron; h is Planck's constant; υ is the frequency of the exciting radiation; E_B is the binding energy of the photoelectron with respect of the Fermi level of the sample; φ is the work function of the spectrometer. The XPS spectrum is usually plotted using the number of photoelectrons (N(E)) versus their binding energy (E_B). The kinetic energy (E_k) of the photoelectron is the experimental quantity measured by the spectrometer, but this is dependent on the photon energy of the X-rays employed and is therefore not an intrinsic material property.[9] The binding energy of the electron (E_B) is the parameter which identifies the electron specifically, both in terms of its parent element and atomic energy level.[10] In a typical XPS measurement, the X-ray is directed at the sample. The sample atom then absorbs the photon energy and a photoelectron is emitted. Photoelectrons are collected using an electron energy analyser (as seen in Fig. 2-8 (left)).

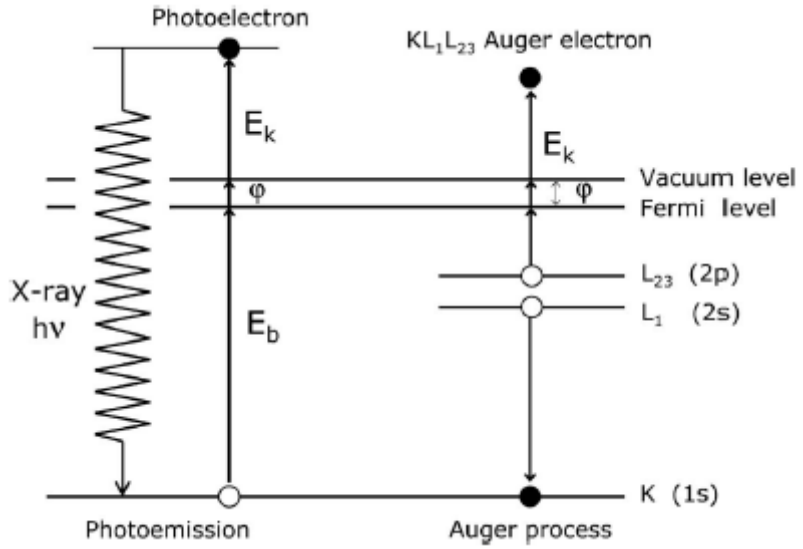


Fig. 2-8 Photoemission and the Auger process. Left: An incident X-ray photon is absorbed and a photoelectron emitted. Binding energy of the photoelectron can be determined from the measurement of its kinetic energy. The atom stays behind as an unstable ion with a hole in one of the core levels. Right: The excited ion relaxes by filling the core hole with an electron from a higher shell. The energy released by this transition is taken up by another electron, the Auger electron, which leaves the sample with an element-specific kinetic energy. In Auger spectroscopy, a beam of energetic (2–5 keV) electrons creates the initial core holes.[1] Figure reproduced from ref. 1.

In addition, the expected photoelectron peaks observed in the XPS spectrum, which may contain extra peaks due to Auger electrons. The Auger electrons cause by de-excitation (relaxation) of the photo ion by an Auger transition (Fig. 2-8). The Auger electrons are emitted with kinetic energies that are only dependent on the electronic state of the element responsible for the ejected electron. That is to say, Auger electrons have fixed kinetic energies, which are independent of the X-ray energy. Moreover, Auger peaks can be recognised by recording the spectrum at two different X-ray energies: XPS peaks appear at the same binding energies, while Auger peaks will shift on the binding energy scale. This can explain why X-ray sources often contain a dual anode of Mg and Al.[1] Auger peaks are easily identified

by varying the X-ray energy, and an overlap between XPS and Auger peaks can be avoided.

Photoelectron peaks in the XPS spectrum are labelled in line with the quantum numbers of the level from which the electron originates. An electron with orbital momentum l (0, 1, 2, 3, . . . indicated as s, p, d, f, . . .) and spin momentum s (spin up = +1/2 or spin down = –1/2) has a total momentum $j = l + s$ when the orbital momentum is $l \geq 1$. Thus each level has two sublevels, with an energy difference called the spin-orbit splitting.[1] For example, the Pd 3d level gives two photoemission peaks, the $3d_{5/2}$ ($l = 2$ and $j = 2 + 1/2$) and $3d_{3/2}$ ($l = 2$ and $j = 2 – 1/2$). The Fe 2p level gives rise to two peaks, the $2p_{3/2}$ ($l = 1$ and $j = 1 + 1/2$) and $2p_{1/2}$ ($l = 1$ and $j = 1 – 1/2$). It is noted that the intensity ratio of the two peaks of a spin-orbit doublet is determined by the multiplicity of the corresponding levels, equal to $2j + 1$. Hence, the intensity ratio of the j = 5/2 and j = 3/2 components of the Pd 3d doublet is 3:2, and that of the 3/2 and 1/2 peaks of the Fe 2p doublet is 2:1.

For the XPS measurements of conducting samples, the photoelectron energies can be referenced to the Fermi level energy of the spectrometer. Therefore, an absolute energy scale can be established, aiding the identification of species. On the other hand, non-conducting (or electrically insulating) specimens may charge up during measurement due to photoelectrons leaving the sample, therefore, the problem of energy calibration is significant. The potential that the sample acquires is determined by the photoelectric current of electrons leaving the sample, the current through the sample holder towards the sample, and the flow of Auger and secondary electrons from the source window onto the sample. Due to the positive charge on the sample, all XPS peaks in the spectrum shift by the same amount to higher binding energies.[1] Fortunately this can easily be corrected by using an element with a binding energy

that can be referenced. The carbon contamination is often used with a C 1s binding energy of 284.5 eV. In a typical XPS measurement, all spectra are calibrated to the adventitious C 1s peak at 284.5 eV with the application of an electron shower gun to reduce charging effect of the samples.

2.5 EXTENDED X-RAY ABSORPTION FINE STRUCTURE

Extended X-Ray Absorption Fine Structure (EXAFS) is an X-ray Absorption Spectroscopy (XAS) technique that uses synchrotron radiation as the X-ray source. EXAFS is caused by the interference of electron waves between atoms, providing local structure information that is limited to a few interatomic distances. For catalyst characterisation, the distance and the number of nearest and next-nearest neighbors of atoms are able to be investigated. The more uniform the environment is through the catalyst, the more meaningful is the EXAFS information. EXAFS deals with the interference effects visible in the absorption spectrum beyond the edge, and provides detailed information on the distance, number, and type of neighbors of the absorbing atom.[1, 11]

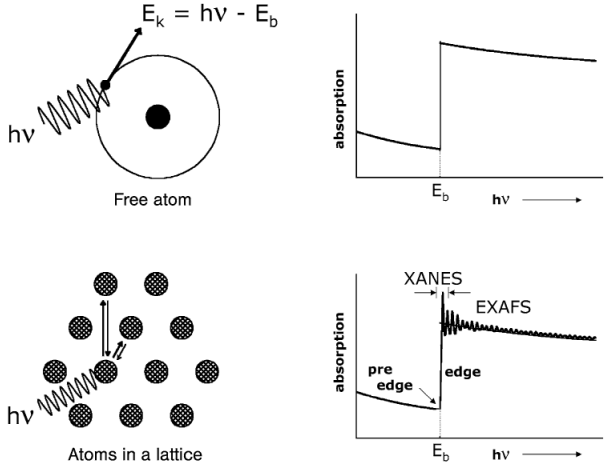


Fig. 2-9 Absorption of X-rays as a function of photon energy E = hν by a free atom and by atoms in a lattice. The fine structure represents the extended X-ray absorption fine structure (EXAFS) function. XANES: X-ray absorption near edge spectroscopy.[11] Figure reproduced from ref. 11.

As illustrated in Fig. 2-9, fine structure arises due to neighbors that surround the absorbing atom. The photoelectron, having both particle and wave character, can be scattered back from a neighboring atom. Because of its wave character, the outgoing and the backscattered electrons interfere. Depending on the wavelength of the electron, the distance between the emitting and scattering atom, and also the shift in phase caused by the scattering event, the two waves either enhance or destroy each other. As a result, the cross-section for X-ray absorption is modulated by the interference between the photoelectron waves, such that it is enhanced at energies where constructive interference occurs. As indicated in Fig. 2-9, the X-ray absorption spectrum exhibits fine structure, which extends to several hundred eV above the absorption edge. The absorption around the edge arises from electrons with low kinetic energies which interact with valence electrons.[1, 11]

The intensity of the wiggles goes up as the number of neighbors increases, the number of oscillations depends inversely on interatomic distances (as in any scattering or diffraction experiment), and the step height of the edge is proportional to the concentration of atoms in the sample.[1]

The EXAFS function, $\chi(k)$, is extracted from the X-ray absorption spectrum in Fig. 2-9 by removing first the approximately parabolic background and next the step, that is, the spectrum of the free atom in Fig. 2-9. As in any scattering experiment, it is customary to express the signal as a function of the wave number, k, rather than of energy. The relationship between k and the kinetic energy of the photoelectron is:

$$k = \frac{2\pi}{h}\sqrt{(2m_e E_{kin})} = \frac{2\pi}{h}\sqrt{2m_e(h\nu - E_b)} = m_e v$$

where k is the wavenumber of the photoelectron; h is Planck's constant; me is the mass of an electron; E_k is the kinetic energy of the photoelectron; n is the X-ray frequency; Eb is the binding energy of the photoemitted electron. $hk/2\pi$ is the

momentum of a wave quantum, whereas $\sqrt{(2m_eE_{kin})} = m_ev$ is the classical momentum of the electron when considered as a particle. It is impossible to explain EXAFS properly without theoretical formulae. In a mono atomic solid, the EXAFS function χ(k) is the sum of the scattering contributions of all atoms in neighboring coordination shells:

$$\chi(k) = \sum_{\mathrm{j}} A_{\mathrm{j}}(k)\sin\left(2kr_{\mathrm{j}} + \phi_{\mathrm{j}}(k)\right)$$

where χ(k) is the EXAFS function; j is the label of the coordination shells around the electron-emitting atom; A_j(k) is the amplitude, the scattering intensity due to the j^{th} coordination shell; r_j is the distance between the central atom and atoms in the j^{th} shell; ϕ(k) is the total phase shift, equal to the phase shift of the backscattering atom plus twice that of the absorbing atom.

The EXAFS function becomes understandable if we examine the Fourier transform of χ(k), which resembles a radial distribution function:

$$\theta_{\mathrm{n}}(r) = \frac{1}{\sqrt{2\pi}}\int_{k_{\mathrm{min}}}^{k_{\mathrm{max}}} k^n\chi(k)e^{2ikr}\mathrm{d}k$$

where θ_n(r) is the Fourier transform of the EXAFS signal; n is an integer, usually chosen as 1, 2, or 3; The function θ_n(r) represents the probability of finding an atom at a distance r, modified by the two r-dependent terms in the amplitude, which progressively decrease the intensity of distant shells. The transform is often weighted with either k or k^3, to emphasize the role of light or heavy atoms, respectively.

In summary, the analysis of an EXAFS spectrum is a time-consuming and expertise demanding venture which requires: i) Extract the EXAFS function χ(k) from measured data; ii) Select a k-interval and compute the k- or k^3-weighted Fourier transform; iii) Identify individual contributions to the Fourier transform and use these

to construct a set of parameters that gives acceptable fits to the spectrum $\chi(k)$, the magnitude, and the imaginary part of the Fourier transforms.

2.6 THERMOGRAVIOMETRIC ANALYSIS

Thermogravimetric Analysis (TGA) is a thermal analysis technique that measures the weight of a sample as a function of temperature and time as the temperature is varied in a controlled atmosphere.[12] The TGA measurement is principally used to determine the thermal stability and composition of a material. TGA relies on a high degree of precision in three measurements: mass change, temperature, and temperature change.[13] A TGA consists of two basic instrumental components: a precision balance with a pan loaded with the sample, and a programmable furnace. The pan is located in a furnace and heated or cooled during the experiment. A thin layer of sample is then loaded onto either a platinum, ceramic (alumina) or aluminium pan. The furnace can be programmed either for a constant heating rate, or for heating to acquire a constant mass loss with time. A sample purge gas (either inert or a reactive gas) controls the sample environment. The gas flows over the sample and exits through an exhaust (Fig. 2-10, bottom). The TGA can be used for measuring a sample's weight loss or gain due to decomposition, oxidation, or dehydration depend on the type of gas used in the experiment.

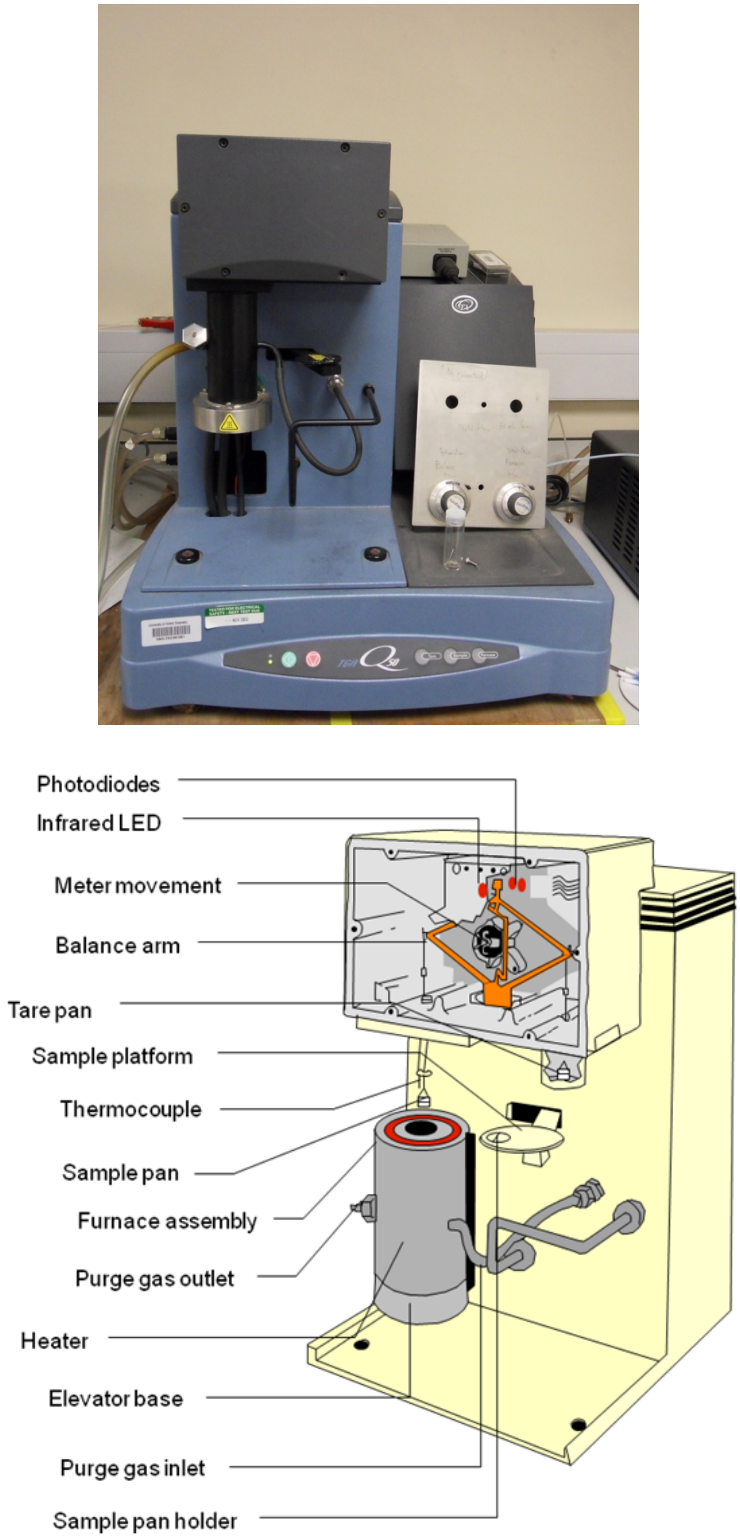


Fig. 2-10 A TA instrument Q50 (top); Schematic for the TGA Q50 (bottom).[14] Figure reproduced from ref. 14.

2.7 TEMPERATURE PROGRAMMED DESORPTION REDUCTION AND OXIDATION

Temperature programmed desorption/reduction/oxidation (TPD/R/O) is a technique which consists of passing a continuous gas stream (in most cases, a reactive gas is used, e.g. H_2, O_2, CO, etc) to the quartz tube and reactor under a user pre-defined temperature ramp (Fig. 2-11, top). Three types of temperature programmed experiments can be performed here: i) reduction (TPR); ii) oxidation (TPO); iii) desorption (TPD). These methods are useful to determine the type and number of active sites, determine thermodynamic or kinetic parameters as well as quantitative measurements of acid/base properties of the catalyst. In a typical measurement, catalysts are loaded between a bed of quartz wool (like a sandwich structure) and in turn is packed between the internal quartz tube and internal quartz reactor (Fig. 2-11, bottom). The internal tubes are placed inside the external quartz tube where it is merged with the stainless steel holder and sealed by a rubber o-ring. We can allow reactive gas to either flow into or by-pass the reactor by twisting the metal head.[14]



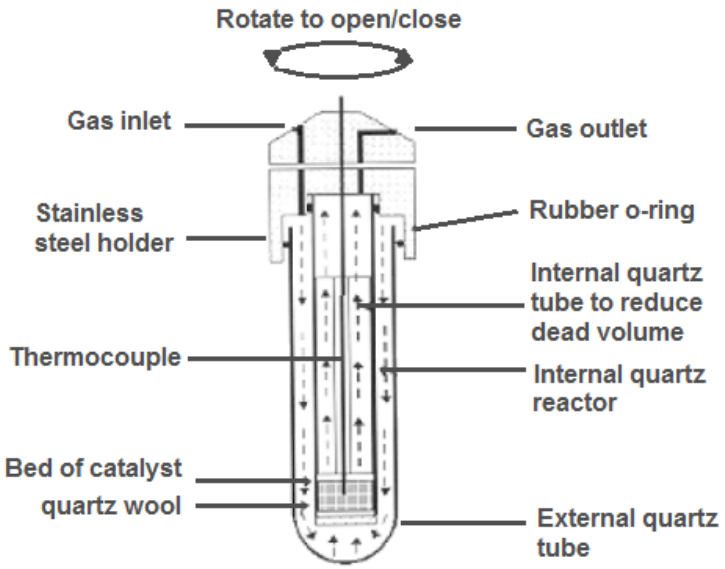


Fig. 2-11 A CE instrument TPD/R/O 1100 (top); Diagram for the reactor assembly (bottom).[14]

TPR analysis is dependent on the amount of sample, temperature ramping rate of quartz reactor, the composition of reactive gas, and the flow rate of the reactive gas. Based on TPR analysis, we can obtain a lot of information, including the percentage of reducible species and at what temperature its reduction takes place. More detailed experimental conditions will be introduced in Chapter 3. In a typical TPR experiment, a catalyst sample is dried in an oven to make sure the sample is pre-oxidised and then loaded into the quartz reactor for a pretreatment run under a He gas to remove any contaminants that may contain in the sample. A dilute H_2 gas is used to pass through the sample and then the effluent gas is detected by a thermo conductivity detector (TCD) which can indicate the consumption of H_2 gas after the sample starts to reduce. Signals are detected according to change in polarity compared to a reference gas (see Table 2-2). High sensitivity TCD provides liner response factors allowing for very accurate calibrations, which can be used to calculate the uptake of H_2 by integration of peak area to calculate the number of reactive sites reduced, reduction degree of active sites, and activation energy related to reduction using the correct reaction

stiochiometry. Overall, this technique is particularly useful and powerful when looking at different oxidation states in the sample. Moreover, the high sensitivity TCD can also allow for analysing low metal content samples. In TPO testing, the sample is typically pre-treated under H_2 to form a reduced form and then a constant gas mixture of 5% O_2/He is passed through the sample at increasing temperatures. Similar to TPR, total oxygen consumption can be calculated by integrating the overall area from the TCD signal and calculates the number of reactive sites oxidised. For a TPD analysis which provides an evaluation of binding strength, the number and types of reactive site on a catalyst by measuring the amount of gas desorbed (from the TCD) at an increasing temperature. Likewise, pretreatment and degassing are required to remove adsorbed water and any contaminants on the sample. Typically, a reactive gas is passed through the sample to allow surface adsorption/chemisorption to take place. Any gas, except H_2 or O_2, can be used to calculate acid/basic sites in a sample. Desorption is performed by gently increasing the temperature with a constant flow of inert gas such as N_2, Ar or He acting as a carrier gas for the desorbed (for the removal of the adsorbed) reactive gas. The desorbed gas is also detected by a TCD detector. By incorporating with a mass spectrometer, the exact chemical nature of effluent gas can be detected by these TPD/R/O techniques.

Table 2-2 Polarities for different types of experiments.[15] Table reproduced from ref. 15.

Analysis	Carrier	Detected gas	Polarity
TPD	Nitrogen	Hydrogen	-
	Argon		
	Helium	Oxygen	++
		Water vapor	
		Ammonia	
		Carbon monoxide	
TPR	Nitrogen + X% Hydrogen	Hydrogen	+
	Argon + X% Hydrogen		
TPO	Helium + X% Oxygen	Oxygen	-

2.8 GAS CHROMATOGRAPHY

Chromatography is still the most popular and powerful method for chemical species/components separation (Fig. 2-12). It is easy to apply this technique to the separation of multi-component samples on a small analytical scale.[16] Chromatography is primarily based on the rate at which different components of a mixture travel through a packed column or a capillary column, which has the stationary phase coating on its inner surfaces rather than being packed into the column (packed column), under the influence of a mobile phase (carrier gas), which is comprised of an inert gas e.g. helium, argon, nitrogen, etc. Gas chromatography (GC) is the interaction between the gaseous mobile phase and the stationery solid phase. Analytes must be volatile and sufficiently thermal stable 400°C. Analyte solubility depends only on its vapour pressure with the role of the mobile phase being purely mechanical. Aside from when polar gases are used, retention time of analytes is mainly achieved by changing the temperature where its solubility becomes an important factor. Nanogram (nanolitre) to microgram (microlitre) quantities are sufficient for qualitative and quantitative analysis. Operating pressures are kept at a minimum where possible to prevent building up pressure to destruct coating structure of the capillary column or packing of the packed column. The carrier gas continuously flows through the injection port, column and detector (Fig. 2-12). Flow rates are typically 2 to 50 $mL \cdot min^{-1}$ with high flow rates (higher pressure) applied for packed columns and low flow rates (lower pressure) for capillary columns. Due to higher separating power of capillary columns compared to packed columns, capillary columns are more widely used. A needle valve is used to maintain constant flow rates of carries gases. Liquid samples can also be injected into the GC by using a syringe. However, these liquids sample must be diluted to low concentrations for capillary

columns. The column is accommodated in an oven where the oven temperatures can be controlled delicately during analysis. Separated hydrocarbon components are detected using a more widely used flame ionisation detector (FID), where the effluent gas is mixed with H_2 and air, then pyrolysed, and burned in the flame. Within the flame, the hydrocarbon components of the sample stream undergo a complex ionisation that produces electrons and positive ions which are collected by an electrode causing current to flow through a measuring circuit. For non-hydrocarbon components, a TCD is also used in the analysis of gases components (carbon monoxide, carbon dioxide, argon, oxygen, nitrogen). Alternatively, a mass spectrometer (GC/MS) is coupled to further enhance identification of sample mixtures.[14]



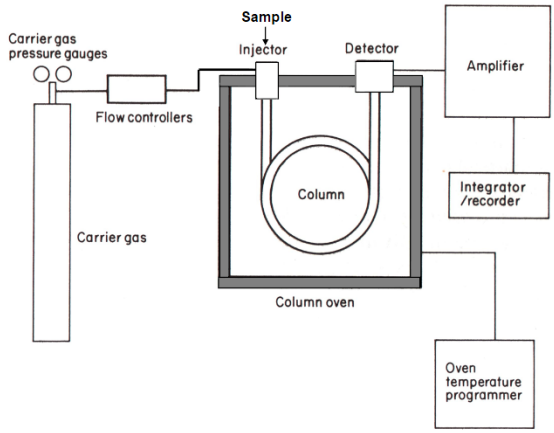


Fig. 2-12 A Perkin Elmer Autosystem XL Arnel Gas phase GC-FID (top); Working illustration of a GC (bottom). Figure reproduced from ref. 16.

On selecting a capillary column for the most efficient compound separation, four parameters must be considered:

i) Stationary phase. The general rule of thumb is to select the least polar phase required for separation. Non-polar stationary phases (methyl or phenyl) separate components predominantly by order of boiling point. Increasing amounts of phenyl or cyanopropyl groups causes separation to be more dependent on the differences between dipole moments or charge distributions. Polyethylene glycol phases can be used for even more polar components (alcohols or aldehydes) where separation depends on hydrogen bonding interactions.

ii) Column internal diameter. The smaller the diameter we select, the greater the efficiency that can be achieved.

iii) Film thickness. Thicker film column is needed when there is a large variation in sample concentration. This will reduce any broad overloaded peaks hence reducing compounds co-eluting. Thinner columns can be used if there is large variation in sample concentration but less likely for them co-eluting. As a rule, increasing the film thickness increases the retention of analytes, therefore requires a higher temperature for elution. Generally speaking, doubling the film thickness would result in an increase in elution temperature of approximately 15-20° under isothermal conditions. On the other hand, the increase in elution temperature is slightly less if a temperature program is used.

iv) Column length. Generally select the shortest column that provides good acceptable separation. If the maximum column length available is used but is still unable for separation then change either the stationary phase or internal diameter is

needed. As separation resolution is proportional to the square root of the column efficiency, then doubling the column length will only increase the column separation by about 40%.

2.9 HIGH PERFORMANCE LIQUID CHROMATOGRAPHY

High performance liquid chromatography (HPLC) is another powerful chromatography employed in this study (Fig. 2-13, top), which can separate and analyse chemical mixtures. Prototype of liquid chromatography (LC) originated in 1900s, known as 'classical column chromatography'. A glass cylinder was packed with a finely divided powder such as chalk, a sample was applied to the top of the column, and a solvent was poured onto the column. One drawback of classic LC was that the solvent was driven by gravity, the separation was very slow. On the other hand, if the solvent is driven by the vacuum, the plate height increases and the effect of the vacuum is annulled in a standard packed column. The limiting factor in LC was originally the size of the column packing. Once columns could be packed with particles as small as micro meter in scale, faster separations could be performed in smaller, narrower, columns. High pressure was required to force the mobile phase and sample through these new columns, and previously unneeded apparatus was required to maintain reproducibility of results in this new instruments. The use of high pressures in a narrow column allowed for a more effective separation to be achieved in much less time than was required for previous forms of LC.[17-18] This results the development of modern HPLC, where samples can be injected into the column automatically as well as the solvent (mobile phase).



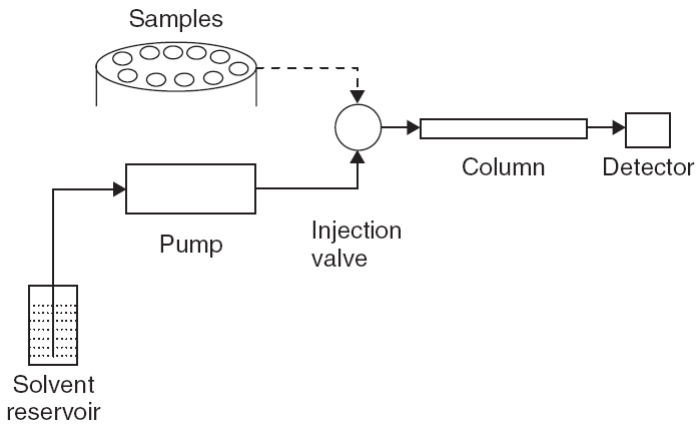


Fig. 2-13 A Perkin Elmer series 200 HPLC system (top); Schematic of an HPLC system (bottom).[19]

Figure reproduced from ref. 19.

A schematic of an HPLC system is shown in Fig. 2-13 (bottom), showing that the flow path of the solvent as it proceeds from the solvent reservoir to the detector (the solvent is usually referred to as the mobile phase or eluent). After injection of the sample, a separation takes place within the column, and separated sample components leave (are eluted or washed from) the column—with detection by a detector.[19]

The mobile phase in HPLC is usually a mixture of polar and non-polar liquid components whose respective concentrations are varied depending on the composition of the sample. When the solvent is passed through a very narrow bore

column, any contaminants or gas bubbles could plug the column or vary the retention times during repeated different trials.[17-18] This can easily be prevented by putting a filter and degassing the solvent to remove any dissolved gases, which could come out of solution mid-separation, and particulates. In the HPLC column, the components of the sample separate based on their differing interactions with the column packing. If a species interacts more strongly with the stationary phase in the column, it will spend more time adsorbed to the column's adsorbent and will therefore have a greater retention time.[17-18] In a typical analysis, the predominant HPLC mode in use today is reversed-phase chromatography, which characterises a non-polar column in collaboration with a polar mobile phase. Flow rates are typically 0.6 to 1 mL · min^{-1}, however, in some special cases a higher flow rate (~30 mL · min^{-1}) is used for preparative columns, with larger particles also give lower pressure drop that allow higher flow rates which increases the throughput of the columns.[19] In addition, the column is housed in a thermostatically controlled oven where temperatures can be finely controlled during analysis. Various detectors, such as refractive index (RI), UV/Vis, and electrochemical detectors are commonly used to identify separated components.

The separation efficiency of a chromatographic separation is measured using the concept of theoretical plates, which is a separation metric originated from fractional distillation**.** It assumes that there are a finite number of identical plates involved in a column. The number of theoretical plates and the height equivalent to a theoretical plate are related simply by the length of the column:[19]

$$\mathbf{N} = \frac{L}{H}$$

where **N** is the number of theoretical plates; L is the length of the column; H is the height equivalent to a theoretical plate, which is a measurement of column efficiency

per unit length of column. The width of an analyte peak can be used to measure the efficiency of the column in terms of retention time and peak width:

$$\mathbf{N} = 16\left(\frac{t_R}{W}\right)^2$$

where t_R is the retention time of the analyte, standing for the time duration between the injection of a sample and its elution from the column; W is the elution peak width. It is clearly seen that higher separation efficiency can be achieved when maximizing the number of theoretical plates. The plate height is related to the flow rate of the mobile phase, so for a fixed set of mobile phase, stationary phase, and analytes; separation efficiency can be maximized by optimizing flow rate as dictated by the van Deemter equation, which is an alternative expression derived from theoretical equations:[19]

$$H = A + \frac{B}{u} + Cu$$

where A represents the different possible paths that can be taken by the analyte through the stationary phase (eddy diffusion); B describes the longitudinal diffusion that occurs in the system; u is the mobile phase velocity; B/u term takes into account the diffusion of analyte molecules in the mobile phase caused by concentration gradients (longitudinal diffusion); C is a constant that describes the rate of adsorption and desorption of the analyte to the stationary phase; C · u is the mass transfer in the mobile phase. The separation between two chromatographic peaks is usually described in terms of their *resolution Rs* = (difference in retention times)/(average peak width):

$$R_s = \frac{2\left[t_{R_{(j)}} + t_{R_{(i)}}\right]}{W_i + W_j}$$

where *Wi* and *Wj* are the baseline widths *W* for peaks *i* and *j*, respectively. Better

separation (increased resolution) results from a larger difference in peak retention times and/or narrower peaks. *Rs* provides a quantitative evaluation on how well two elution peaks can be differentiated in a chromatographic separation.[19]

2.10 REFERENCES

1. J. W. Niemantsverdriet, *Spectroscopy in catalysis : an introduction*, 3rd completely revised and enlarged edn., Wiley-VCH, Weinheim, 2007.
2. I. Chorkendorff and J. W. Niemantsverdriet, *Concepts of Modern Catalysis and Kinetics*, John Wiley & Sons, 2003.
3. W. Oduro *Towards ultra-selective hydrogenation and hydrogenolysis: A nano engineering approach to heterogeneous catalyst design*. D.Phil thesis. University of Oxford, 2009.
4. W. Clegg, *Crystal structure analysis : principles and practice*, International Union of Crystallography; Oxford University Press, [Chester, England], New York, 2001.
5. H. Günzler and A. Williams, *Handbook of analytical techniques*, Wiley-VCH, Weinheim ; New York, 2001.
6. W. Zhou and Z. L. Wang, *Scanning microscopy for nanotechnology : techniques and applications*, Springer, New York, 2007.
7. V. I. Nefedov, *X-ray photoelectron spectroscopy of solid surfaces*, 1st English edn., VSP BV, Utrecht, 1988.
8. T. Vo-Dinh and G. Gauglitz, *Handbook of spectroscopy*, Wiley-VCH, Weinheim, 2003.
9. J. F. Watts and J. Wolstenholme, *An introduction to surface analysis by XPS and AES*, Wiley, New York ; Chichester, 2003.
10. Z. Xu, X. Huang and L. Wan, Zhejiang University Press; Springer, Hangzhou Berlin, New York, 2009.
11. I. Chorkendorff and J. W. Niemantsverdriet, *Concepts of modern catalysis and kinetics*, 2nd., rev. and enlarged edn., Wiley-VCH, Weinheim, 2007.

12. T. R. Crompton and Rapra Technology Limited., *Polymer reference book*, Rapra Technology Limited, Shrewsbury, 2006.

13. B. Shah, V. K. Kakumanu and A. K. Bansal, *J Pharm Sci-Us*, 2006, **95**, 1641-1665.

14. C. W. A. Chan, Ultraselective Nanocatalysts in Fine Chemical and Pharmaceutical Synthesis. D.Phil thesis. University of Oxford, 2012.

15. *Suite software for TPD/R/O 1110 Instruction manual*, ThermoQuest CE instruments, TMA-Milan, 1999.

16. H. Gunzler, A. Williams and Editors, *Handbook of Analytical Techniques, Volume 1*, Wiley-VCH, 2001.

17. D. A. Skoog, F. J. Holler and S. R. Crouch, *Principles of instrumental analysis*, 6th edn., Thomson Brooks/Cole, Belmont, CA, 2007.

18. J. Swadesh, *HPLC : practical and industrial applications*, 2nd edn., CRC Press, Boca Raton, Fla., 2001.

19. L. R. Snyder, J. J. Kirkland and J. W. Dolan, *Introduction to modern liquid chromatography*, 3rd edn., Wiley, Hoboken, N.J., 2010.

CHAPTER 3 - EXPERIMENTAL AND CHARACTERISATION

CHAPTER 3 - EXPERIMENTAL AND CHARACTERISATION 90

3.1 MODIFIED RANEY CATALYSTS 92

3.2 BIMETALLIC CATALYSTS 93

3.3 SUPPORTED OXIDE CATALYSTS 95

3.3.1 SYNTHESIS 95

3.3.2 CALCINATION 95

3.3.3 REDUCTION 96

3.4 PALLADIUM-IRON ALLOY 97

3.5 HYDROGENOLYSIS OF ETHYLENE GLYCOL 98

3.5.1 CATALYST TESTING 98

3.5.2 PRODUCT ANALYSIS 99

3.6 OXIDATION OF METHANE 100

3.7 CHARACTERISATIONS 102

3.7.1 TGA 102

3.7.2 XRD 102

3.7.3 TEM 103

3.7.4 XPS 103

3.7.5 EXAFS 103

3.7.6 TPD/R/O 104

3.7.7 PULSE CO CHEMISORPTION 105

3.8 REFERENCES.....106

3.1 MODIFIED RANEY CATALYSTS

Raney® Ni 2400, Raney® Ni 2800, Raney® Ni 3202, Raney® Ni 4200 and Raney® Cu were obtained from Aldrich without purification. Modified Raney® catalysts were prepared using a modified polyol process.[1-2] For the modified polyol process, the reduction of metal precursors can be catalysed in the presence of Raney Ni. Therefore, reaction temperatures lower than the self-reduction temperatures of metal precursors were used. Here, the Raney Ni provided a metallic surface to catalyse the deposition of a second metal from its precursor in solution. In a typical synthesis, Raney Ni was first dried under nitrogen in a tube furnace. Then, the dried Raney Ni powder was re-dispersed in diphenyl ether ($(C_6H_5)_2O$, ≥ 99%, Aldrich) contained in a 100 mL three necked round bottomed flask in a glove box. Doping of a second metal typically Rh, on the re-dispersed Raney Ni, was conducted by adding rhodium (III) acetylacetonate ($Rh(CH_3COCHCOCH_3)_3$, 97%, Aldrich) and 1,2-hexadecanediol ($CH_3(CH_2)_{13}CHOHCH_2OH$, 90%, Aldrich) at a 1 : 2 molar ratio to the diphenyl ether. The mixture was then purged with nitrogen for 15 minutes with magnetic stirring (300 rpm) before being heated at a constant rate to 250 °C, with the mixture then refluxed at 250 °C in a nitrogen atmosphere for 40 minutes. After the reduction, the mixture was cooled down to room temperature and the solution was then washed several times with a 1 : 1 mixture of hexane (C_6H_{14}, ≥ 97%, Sigma-Aldrich) and ethanol (C_2H_5OH, ≥ 99%, Sigma-Aldrich). The solid powder was then separated by centrifuge (Hettich Universal 320 Centrifuge, Fig. 3-1), with the resulting catalyst dried under a steady stream of nitrogen overnight and then re-dispersed in deionised (DI) water purified by a Milli-Q water purification system. A high performance liquid chromatography (HPLC, PerkinElmer Series 200 systems)

analysis of the rinse solutions was conducted to ensure the resulting catalyst was free from organic contamination before performing the catalyst testing.



Fig. 3-1 A Hettich Universal 320 Centrifuge.

3.2 BIMETALLIC CATALYSTS

Bimetallic catalysts were prepared using a wet impregnation method, a solid support was mixed with an aqueous solution containing an appropriate precursor salt as a slurry mixture, followed by solvent removal and reduction steps. In a typical synthesis, a slurry solution containing 0.5 g of activated carbon (type 87L, Johnson Matthey), and a mixture of 44.47 mg of rhodium (III) chloride ($RhCl_3$, 98%, Aldrich) and 23.76 mg of copper (II) nitrate trihydrate ($Cu(NO_3)_2 \cdot 3H_2O$, 99-104%, Sigma-Aldrich) with 3 : 1 (Rh : Cu) metal molar ratio dissolved in a 40 mL acetone (CH_3COCH_3, ≥ 99.5 %, Sigma-Aldrich) and DI water mixture at a 1 : 1 volume ratio. The mixture was then sonicated for 10 mins in an ultrasonic bath (Fisher Scientific FB15051 ultrasonic bath, Fig. 3-2), stirred overnight and then dried under nitrogen at room temperature. The dried powder was then reduced in a flow of 33% H_2/N_2 at a steady rate of 100 mL/min in a tube furnace (Carbolite type MTF 12/38/400, Fig. 3-3) at 673 K for 2 hours. The furnace was then cooled down to room temperature before

this 5wt% Rh/Cu (Rh:Cu=3:1) on active carbon was transferred into a glove box (Vacuum Atmospheres HE-63-P glove box, Fig. 3-4) for storage before the catalyst testing.[3]



Fig. 3-2 A Fisher Scientific FB 15051 ultrasonic bath.

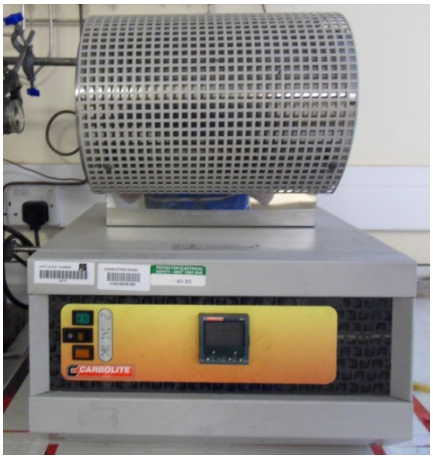


Fig. 3-3 A Carbolite type MTF 12/38/400 tube furnaces.

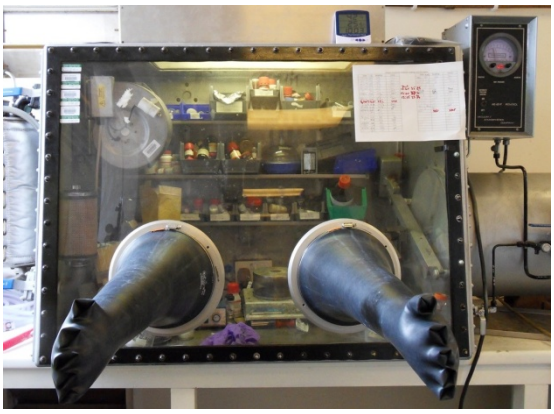


Fig. 3-4 A Vacuum Atmospheres HE-63-P glove box.

3.3 SUPPORTED OXIDE CATALYSTS

3.3.1 SYNTHESIS

Typical synthesis for 1 g of 5% Pd/Fe_3O_4 catalyst was carried out as follows: in a 500 mL beaker, 0.3309 g of palladium (II) nitrate solution ($Pd(NO_3)_2$, 15.11wt% Pd, Alfa Aesar) and 5.071 g of iron (III) nitrate nonahydrate ($Fe(NO_3)_3.9H_2O$, ≥98%, Sigma-Aldrich) were dissolved in a 200 mL DI water at room temperature under stirring (300 rpm).[4] Then, 1.0 M sodium carbonate solution (Na_2CO_3, ≥99.5%, Sigma-Aldrich) was added dropwise to the mixed solution until the pH of the final solution reached *ca*. 9.0. The pH was measured with a Mettler Toledo PHQ-180-050W pH meter. After stirring and aging for overnight at room temperature, the resulting precipitate was centrifuged 10 times at 5000 rpm for 10 min and washed with 200 mL of DI water between periods to remove Na^+ ions, air-dried at 110 ^oC overnight. The resulting powder was denoted as denoted as $Pd/Fe(OH)_x$.

3.3.2 CALCINATION

In order to decompose hydroxides (carbonates) to oxides, a calcination step is necessary. The dried catalyst ($Pd/Fe(OH)_x$) was gently grounded by pestle and mortar. Calcination of the dried and grounded catalyst was conducted in air atmosphere at a flow rate of 60 mL min^{-1}. The furnace was programmed (as seen in Fig. 3-5) as follows: (a) temperature was increased from 25 to 80 ^oC at 5 ^oC per min, (b) held at 80 ^oC for half an hour, (c) increased from 80 to 120 ^oC at 5 ^oC per min, (d) held at 120 ^oC for half an hour, (e) increased from 120 to 300 ^oC at 10 ^oC per min, and (f) held at 300 ^oC for next 2 h. The furnace was then air cooled back to room temperature. This yields the respective calcined catalyst, denoted as PdO/Fe_2O_3.

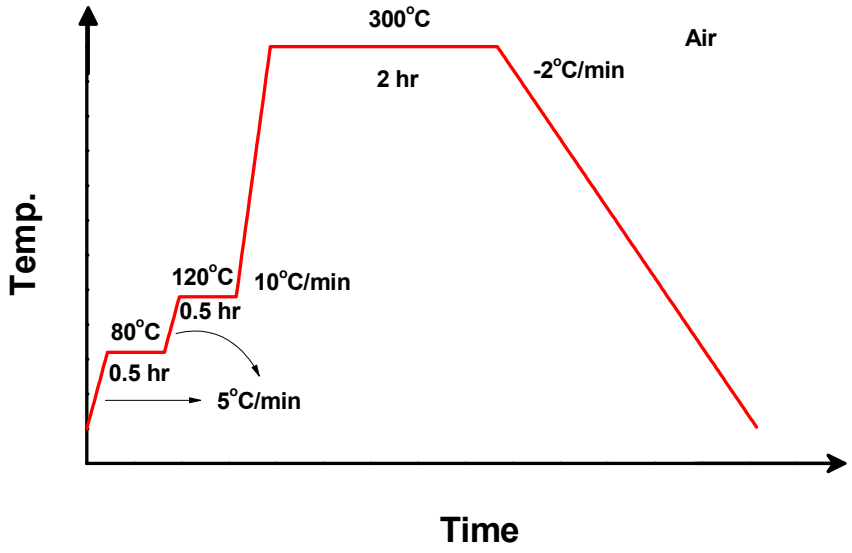


Fig. 3-5 Temperature profile for the calcination of Pd/Fe(OH)$_x$ catalyst.

3.3.3 REDUCTION

Reduction of the calcined catalyst was carried out in air atmosphere at a flow rate of 60 mL min^{-1}. The furnace was programmed (as seen in Fig. 3-6) as follows: (a) temperature was increased from 25 to 80 ^{o}C at 5 ^{o}C per min, (b) held at 80 ^{o}C for half an hour, (c) increased from 80 to 120 ^{o}C at 5 ^{o}C per min, (d) held at 120 ^{o}C for half an hour, (e) increased from 120 to 300 ^{o}C at 10 ^{o}C per min, and (f) held at 300 ^{o}C for next 2 h. The furnace was then air cooled back to room temperature and the powder was transferred into a glove box for storage before the catalytic testing The as-reduced catalyst was denoted as Pd/Fe_3O_4.

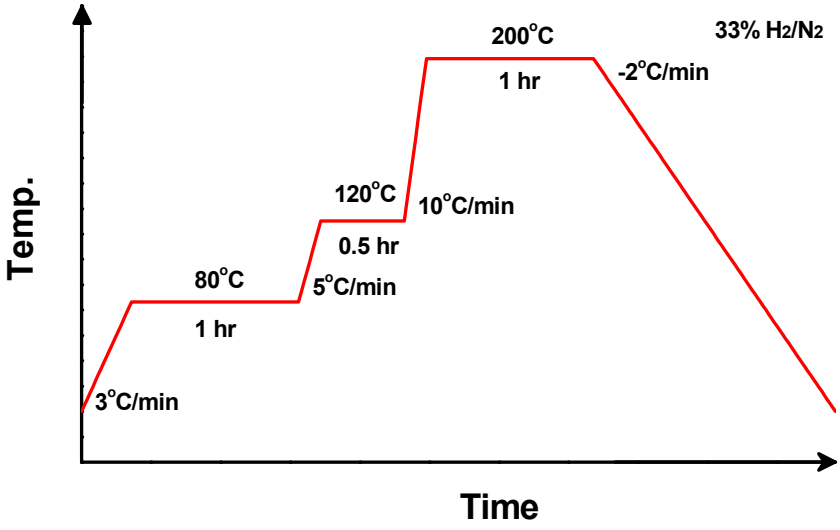


Fig. 3-6 Temperature profile for the reduction of PdO/Fe_2O_3 catalyst.

3.4 PALLADIUM-IRON ALLOY

Palladium-iron alloy (PdFe) catalyst was synthesised using a modified polyol process by reduction of palladium (II) acetylacetonate ($Pd(CH_3COCHCOCH_3)_2$, 99%, Aldrich) and thermal decomposition of iron (0) pentacarbonyl ($Fe(CO)_5$, > 99.99%, Aldrich) in the presence of oleic acid and oleylamine as the stablisers.[1, 5-6] An 8:1 molar ratio of $Fe(CO)_5$ to $Pt(acac)_2$ were used to gave $PdFe\text{-}Fe_3O_4$ mixed-phase particles.

In a typical synthesis, a mixture of 0.30 g of palladium (II) acetylacetonate (1.0 mmol, 99.99%, Alfa aser), 1.570 g (8.0 mmol) of $Fe(CO)_5$, 1.56 g of 1,2-hexadecanediol (6.0 mmol, 90%, Aldrich), 0.64 mL of oleic acid (2.0 mmol, 90%, Aldrich), and 0.64 mL of oleylamine (1.36 mmol, 70%, Aldrich) in 40 mL of dioctyl ether ($[CH_3(CH_2)_7]_2O$, 99%, Aldrich) in a 100 mL three necked round bottom flask were refluxed at 250 ^oC for 40 minutes in an inert environment by bubbling nitrogen gas through the reaction system and continuously stirred with a magnetic stirrer (300 rpm). Then the color of solution turned black. After cooling to room temperature, the

black solution was precipitated more than once by adding a 1 : 1 mixture of hexane (C_6H_{14}, ≥ 97%, Sigma-Aldrich) and ethanol (C_2H_5OH, ≥ 99%, Sigma-Aldrich) and then subjecting it to centrifugation (7000 rpm, 20 min). The supernatant was discarded, and the solid surfactant-stabilised PdFe-Fe_3O_4 sample was dried under a steady stream of nitrogen overnight.

3.5 HYDROGENOLYSIS OF ETHYLENE GLYCOL

3.5.1 CATALYST TESTING

Hydrogenolysis of ethylene glycol was performed in the liquid phase using a Parr 160 mL autoclave high pressure reactor (Fig. 3-7) fitted with a glass liner. An aqueous solution of ethylene glycol was used in order to further reduce viscosity. In a typical experiment, 30 mL of 0.85 M ethylene glycol solution ($C_2H_6O_2$, 99.8%, Sigma-Aldrich) and 0.50 g of catalyst were loaded in a glove box. The reactor was flushed with pure hydrogen (99.99%, BOC) 6 times to remove any traces of oxygen. The autoclave was pressurised to 20 bars of hydrogen at room temperature. The autoclave was linked with a Parr 4842 temperature controller. Then, it was heated to 195^oC and allowed to react for 24 hours with a constant stirring (200 rpm). After reaction the reactor was cooled to room temperature for analysis. Fig. 3-8 shows a schematic diagram showing the high pressure reactor designed for the catalyst testing.



Fig. 3-7 A Parr 160 mL pressure vessel.

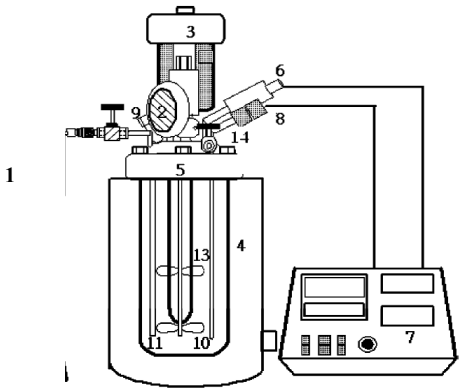


Fig. 3-8 A schematic diagram showing the high pressure reactor designed for the catalyst testing: 1, inlet valve; 2, pressure gauge; 3, motor; 4, heater; 5, extractor; 6, pressure detector; 7, temperature controller; 8, thermocouple; 9, safety rupture disk;10, internal string system; 11, inlet tube; 12, sample bottle; 13, cooling coil; 14, outlet valve.

3.5.2 PRODUCT ANALYSIS

After the allotted reaction time, the autoclave was cooled down to -60 ^{o}C in a dry ice/acetone bath. Here, the gas phase was analyzed by a Perkin Elmer Autosystem XL Arnel Gas phase GC-FID-Methanator in order to determinate the concentrations of CO, CH_4 and CO_2 in the reaction products. The liquid phase was analyzed by a Perkin Elmer 200 series HPLC equipped with a refractive index detector where 0.60 mL of 58 mM sucrose solution ($C_{12}H_{22}O_{11}$, ≥99.5%, Sigma-Aldrich) was added as an external standard to determine the concentrations of ethylene glycol, methanol and ethanol after the reaction. The mass balance of this typical catalytic batch reaction of over 95% was ensured.

3.5.2.1 CONDITIONS FOR GAS PHASE GC ANALYSIS

The components were separated and detected using a Perkin Elmer Arnel Autosystem XL GC equipped with an FID with a methanator. The column was carbowax 80-100 mesh packed column and N_2 gas as a mobile phase (18 psi). The

oven was programmed at an initial temperature of 180 ^{o}C for 0.5 min and then heated to 250 ^{o}C at a rate of 40 ^{o}C /min. The final temperature of 250 ^{o}C was held for 10 min.

3.5.2.2 CONDITIONS OF HPLC ANALYSIS

The products were separated on a 300 mm X 7.8 mm Aminex HPX-87H ion exclusion column at an oven temperature of 35 ^{o}C. The mobile phase was 0.025 M sulphuric acid prepared with Fisher HPLC grade water at a flow rate of 0.6 ml/min. Detection of the products based on the change in refractive index was made using a refractive index detector at a temperature of 35 ^{o}C.

3.6 OXIDATION OF METHANE

The catalytic activity of supported oxide catalyst for the oxidation of methane was tested on a self-built reactor system as illustrated in Fig. 3-9. The reactor was set up to control the reaction conditions of the reaction. The evolved gases were monitored by a GC-TCD/FID (Agilent 7890A GC system, Fig. 3-10). 0.20 g of calcined catalyst was sandwiched between two layers of quartz wool (Fisher Scientific) and inserted into a 6-mm-diameter stainless steel tube reactor (G). The reactor (G) was wound with a thermocouple that connected the reactor to the temperature-programmable furnace (J and F). The catalyst was pretreated with a gas stream of CH_4 at 20 mL/min at 200 °C for 1 h before testing. After the pretreatment, the testing started with a flow of methane/oxygen. A mixed stream of (A) CH_4 (99.99%, BOC) and (B) dilute O_2 (6.2% O_2 in N_2, BOC), controlled by a mass-flow controller C and D, respectively, was injected to the reactor at a flow rate of 36 mL/min. A cold trap was placed in an ice bath (K and L) to remove water produced in our apparatus setup, before reaching TCD. After passing through the cold trap, the remaining gas (CH_4, O_2 and N_2) and produced gas products reached the pre-calibrated

gas chromatography with a thermal conductivity detector (M). The quantity of each individual gas in the product could be determined and analysed using the computer (O). The detection limit of CO was 10 ppm due to the low sensitivity of the GC. A separated FID (N) was used to detect the CH_4 concentration. The catalytic performance of oxide supported catalysts was tested on the oxidation of CH_4 in dilute air from 200 to 500^oC. We derived the methane and oxygen conversions and product selectivity from product gas analysis (CH_4, O_2, CO, H_2, N_2, etc.) for each run using calibration. CH_4 conversion was defined by the differences in CH_4 concentration (obtained by FID) before and after the reaction.

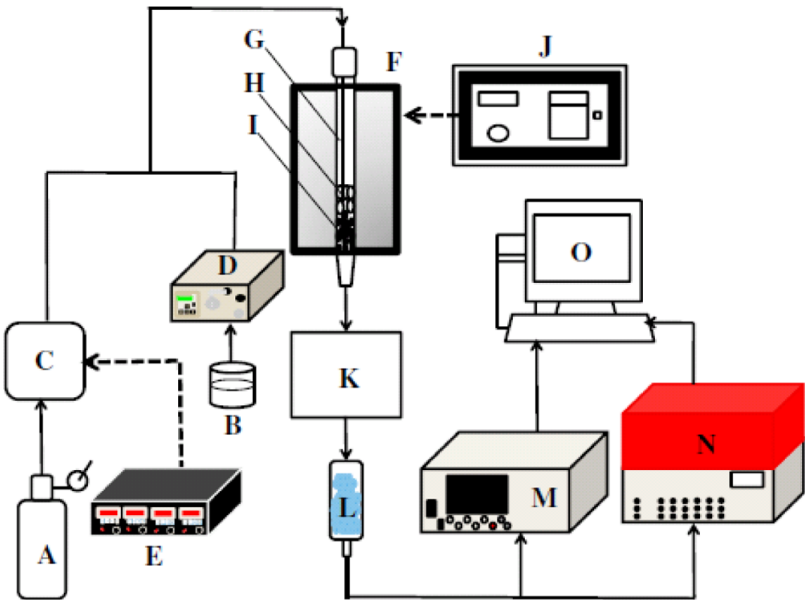


Fig. 3-9 A self-built reactor setup for methane oxidation.[7] A, inlet valve; B, pressure gauge; C, D and E, mass flow controller; E, extractor; F, furnace; G, 6-mm-diameter stainless steel reactor; H, thermocouple; I, powder mixture was sandwiched between quartz wool plugs; J, furnace temperature controller; K and L, ice bath; M, GC with a TCD; N, GC with a FID; O, computer. Figure reproduced from ref. 7.



Fig. 3-10 An Agilent 7890A GC system.

3.7 CHARACTERISATIONS

3.7.1 TGA

TGA was performed using a TA instruments Q50 thermogravimetric analyser. Specimens were loaded onto a platinum sample pan and heated from RT to 800 °C under air at a ramp rate of 10 °C/min and holding at the final temperature for 1 h.

3.7.2 XRD

Powder X-ray diffraction (PXRD) patterns were collected using a PANalytical X'Pert Pro diffractometer, operating in Bragg-Brentano focusing geometry and using $Cu_{K\alpha}$ radiation (λ = 1.5418 Å) from a generator operating at 40 kV and 40 mA (step size at 0.004°, time per step at 17.78 s, scan rate 0.000225°/s, total number of steps at 20000). The powder samples were dusted and pressed onto either a glass, an aluminium preparative slide or an air-tight sample holder prepared in a glove box. The XRD patterns were recorded within the angle range from 5 to 85° of 2θ. Calculation of the lattice parameter on the palladium samples are calibrated against the aluminum background peaks.

3.7.3 TEM

Transmission electron microscope images were obtained on a JEOL JEM-2200MCO aberration-corrected transmission electron microscope and operated at an accelerating voltage of 200 kV at the Department of Materials, University of Oxford with assistance from Dr. Neil Young. The samples were prepared by placing a drop of the sample dispersed in methanol onto a lacey carbon coated copper grid and dried in nitrogen at 85°C. Mean diameter was calculated by measuring at least 200 particles.

3.7.4 XPS

XPS characterisation for the iron oxide supported palladium samples were performed using a Thermo V. G. Scientific ESCALAB 250 with assistance from Dr. Jingping Hu. Al Kα (1486.6 eV) X-ray source and hemispherical electron energy analyser were used in XPS. Samples for XPS analysis were finely grounded using a pestle and mortar to ensure a homogeneous sample was obtained and the crystals were randomly distributed. The XPS spectra were fitted using a class of functional forms based on the Gaussian and Lorentzian functions using the XPS fitting programme CasaXPS.[8]

3.7.5 EXAFS

EXAFS measurement at the Pd K-edge (24530 eV), were performed on the B18 beamline at the Diamond Light Source (Diamond, UK) with assistance from Drs. Andrew Dent and Anna Kroner and my fellow student, Fenglin Liao in Tsang group to obtain information about the local structure of Pd catalysts (the nearest-neighbour interatomic distances and coordination number), which was then used to estimate the size of the Pd particles. The Diamond installation comprises a 3 GeV electron storage ring with typical currents of 200 mA. The B18 is a bending magnet beamline which has been designed to deliver monochromatic X-rays in the energy range of 2 to 35

keV. A Si (311) double crystal monochromator was used for energy selection with the resolution of 1 eV. X-ray absorption spectroscopy data were collected at the Pd K-edge at ambient temperature in transmission mode using optimized ionization chambers as detectors. Fluorescence spectra were acquired using I0 and a high count rate fluorescence 9-element Ge detector windowed on the Pd K-edge fluorescence peaks. Acquisition time of the XAS spectrum for each sample was about 40 minutes, 8-12 scans were collected for each sample. The EXAFS data analysis was performed using IFEFFIT 1 with Horae packages 2 (Athena and Artemes). All spectra were calibrated with Pd foil as the reference to avoid small energy shifts of the nano catalyst. The amplitude parameter was obtained from EXAFS data analysis of Pd foil (with known coordination number which were fixed during analysis) to be 0.84, which was used as a fixed input parameter in all fits to allow coordination number (CN) refinement. The k^3 -weighted spectra were Fourier transformed within the limits $2 < k < 15$ and $1<R<3$. In this work, we perform only a first shell data analysis under the assumption of single scattering. For the curve-fitting analysis, the empirical phase shift and amplitude functions for Pd-Fe bond and Pd-Pd bond were extracted from the data for PdFe alloy and Pd foil, respectively. Errors in the analysis were estimated by R factor.

3.7.6 TPD/R/O

TPR was performed using a Thermo Scientific TPD/R/O 1100. The preparative process and operation conditions were reported elsewhere.[7] In a typical characterisation, 25 mg of calcined catalyst sample was packed between two layers of quartz wool and insert into the TPR quartz tube with a thermocouple placed on the top layer in contact with the sample. In order to remove absorbed ambient gas molecules, the tube was inserted into the instrument for a helium (99.99%, BOC)

pretreatment process with a flow rate of 10 mL/min. The furnace temperature was then increased from 40 to 150 ^{o}C at 10 ^{o}C per min and held for 5 min before cooling. After the pretreatment, an analyse of reduction treatment was taken in a 5% H_2 in argon flowing through the TPR tube at 20 mL/min at a temperature ramp of 10 °C/min from 40 to 800 °C, then cooled down to room temperature.

3.7.7 PULSE CO CHEMISORPTION

Pulse Chemisorptions of PdO/Fe_2O_3 were performed using the same Thermo Scientific TPD/R/O 1100. The preparative and pretreatment methods were identical with the one mentioned in TPR (in 3.7.6), but the sample was additionally treated in a 5% H_2 in argon flowing through the TPR tube at 20 mL/min at either 40 or 200°C for 1 h, then cooled down to room temperature. Chemisorption analyses were taken by pulsing research grade CO (99.99%, BOC) onto the pretreated sample at room temperature to determine the size of palladium metal particles. CO pulses, with the volume of the injection loop 0.456 ccm, were injected at a series of 15-min intervals into the TPR tube. Ten pulses were then recorded per analyze and referenced to a blank run without adding any solid catalyst. A stoichiometry of metal to CO = 1 : 1 CO was taken to calculate the metal dispersion.[9]

3.8 REFERENCES

1. S. H. Sun, C. B. Murray, D. Weller, L. Folks and A. Moser, *Science*, 2000, **287**, 1989-1992.
2. M. Chen, J. P. Liu and S. H. Sun, *J Am Chem Soc*, 2004, **126**, 8394-8395.
3. S. C. Chou, C. T. Yeh and T. H. Chang, *J Phys Chem B*, 1997, **101**, 5828-5833.
4. B. T. Qiao, J. Zhang, L. Q. Liu and Y. Q. Deng, *Appl Catal A-Gen*, 2008, **340**, 220-228.
5. S. H. Sun, S. Anders, T. Thomson, J. E. E. Baglin, M. F. Toney, H. F. Hamann, C. B. Murray and B. D. Terris, *J Phys Chem B*, 2003, **107**, 5419-5425.
6. C. H. Yu, C. C. H. Lo, K. Tam and S. C. Tsang, *J Phys Chem C*, 2007, **111**, 7879-7882.
7. W. Y. Tong, A. West, K. Cheung, K. M. Yu and S. C. E. Tsang, *ACS Catal*, 2013, **3**, 1231-1244.
8. T. Fowowe, E. Hadzifejzovic, J. P. Hu, J. S. Foord and D. J. Caruana, *Adv Mater*, 2012, **24**, 6305-6309.
9. N. Mahata and V. Vishwanathan, *J Catal*, 2000, **196**, 262-270.

CHAPTER 4 - RANEY CATALYSTS FOR HYDROGENOLYSIS OF ETHYLENE GLYCOL

CHAPTER 4 - RANEY CATALYSTS FOR HYDROGENOLYSIS OF ETHYLENE GLYCOL 107

4.1 INTRODUCTION 108

4.2 EXPERIMENTAL METHODS 110

4.2.1 CATALYST SYNTHESIS 110

4.2.2 CATALYTIC TESTING 111

4.2.3 PRODUCT ANALYSIS 111

4.2.4 COMPUTATIONAL DETAILS 112

4.3 CATALYST CHARACTERISATION 113

4.3.1 TEM 113

4.3.2 PXRD 113

4.4 HYDROGENOLYSIS TESTING 115

4.4.1 RANEY Ni CATALYSTS FOR ETHYLENE GLYCOL HYDROGENOLYSIS 115

4.4.2 RANEY Cu CATALYSTS FOR ETHYLENE GLYCOL HYDROGENOLYSIS 120

4.5 DISCUSSION 121

4.6 CONCLUSION 130

4.7 REFERENCES 132

4.1 INTRODUCTION

Methanol is a basic building block for a wide variety of chemicals, many of which are commercially important as synthetic dyestuffs, resins, drugs, and perfumes. For example, a large quantity of methanol manufactured is used for the production of acetic acid, dimethylaniline for dyestuffs and formaldehyde for synthetic resins. It can also be used either directly or indirectly as a fuel. In recent years, methanol has been used for the production of dimethyl ether (DME) and olefins by the so-called methanol-to-olefins process (MTO),[1] or as a blend stock for motor fuels. Direct methanol fuel cells (DMFC) also allow the usage of methanol directly by electrochemical means. In addition, methanol is required as a key component for biodiesel production (approximately 10 % of methanol per litre of biodiesel). It has been proposed that methanol can be regarded as a chemical form of hydrogen carrier; when catalytically decomposed, it will generate in-situ hydrogen gas for mobile use.[2]

At present, methanol is typically manufactured from fossil fuels. It can be produced from natural gas based on the catalytic hydrogenation of synthesis gas (a mixture of carbon monoxide, carbon dioxide and hydrogen gases derived from incomplete catalytic combustion of natural gas) over a ternary CuO-ZnO-Al_2O_3 catalyst at 50–100 bar and 200–250 ^oC. Also, its production from coal via synthesis gas is increasing in locations where natural gas is expensive or not available.

However, the net emission of CO_2 to the atmosphere from fossil fuel based methanol synthesis is contributing significantly to the problem of climate change. As such, it is becoming increasingly important to shift the focus of methanol production from a dependence on fossil fuel to use of sustainable and renewable resources. Thus, the synthesis of this important platform chemical from renewable biomass as a greener resource is a desirable goal for the future.

Recent studies show to feed bio-gas, a mixture of methane and carbon dioxide resulting from the anaerobic decomposition of agricultural, domestic, and industrial sewage, to reformer for synthesis gas formation which can be adapted to current methanol production (synthesis gas route). For instance, the Netherlands based BioMCN uses crude glycerine to produce bio-methanol while Sweden based Chemrec AB uses black liquor from the paper mill process for its production. Generally, this route involves the complete breakdown of bulky biomass molecules in the presence of water to CO, CO_2 and H_2 prior to the reformation of bio-methanol. From an energy point of view, the complete cleavage of complex molecules (highly endothermic) followed by reassembling to form methanol (exothermic) is not an ideal approach compared to their direct conversion to methanol.

On the other hand, biological fermentation under mild conditions using delicate enzymatic pathways allows for the large scale selective production of bio-ethanol from complex biomolecules. However, no methanol is naturally produced by any biological process since methanol is highly toxic to microorganisms. It is, however, possible to produce methanol and ethanol with limited selectivity from the degradation of polyols by non-enzymatic chemical means.[3] Therefore, further investigation is needed to understand and to improve the selectivity towards these lower alcohols.

We are thus interested in exploring a non-syngas chemical activation of polyols (hydrocarbons) from biomass for methanol production. Ethylene glycol represents the simplest basic unit of polyols, making it a good model reactant for this study. Additionally, *Zhang et al.* have recently demonstrated that nickel promoted tungsten carbide can degrade cellulose into ethylene glycol with an impressive yield (61%)

within 30 minutes at 245 ^{o}C and 60 bar of H_2.[4] Ethylene glycol can also be produced at large scale from corn carbohydrates in pilot plants.[5]

Therefore, in this chapter we will examine the feasibility of ethylene glycol hydrogenolysis over the commercial catalysts Raney Ni,[6] Raney Cu[7] and supported Rh.[8] It is noted that introduction of a second metal to the first metal, forming an alloy or bimetallic structure is known to alter the electronic properties of metal catalysts resulting in changes in the adsorption strength of chemisorbed species. Thus, bimetallic catalysts were also briefly studied for this reaction in parallel with DFT modelling of the electronic properties for catalytic sites.

4.2 EXPERIMENTAL METHODS

4.2.1 CATALYST SYNTHESIS

Raney Ni 2400, Raney Ni 2800, Raney Ni 3202, Raney Ni 4200 and Raney Cu were obtained from Aldrich without further purification. Other catalysts were prepared mainly using two methods: wet impregnation and a modified polyol process. For the modified polyol process,[9-10] the reduction of metal precursors can be catalysed by the presence of Raney Ni. Therefore, reaction temperatures lower than the self-reduction temperatures of the metal precursors were used. Here, Raney Ni provided a metallic surface to catalyse the deposition of a second metal from its precursor in solution. In a typical synthesis, Raney Ni was first dried under nitrogen in a tube furnace. Then, the dried Raney Ni powder was re-dispersed in diphenyl ether ($(C_6H_5)_2O$) contained in a three necked round bottomed flask in a glove box. Doping of a second metal (typically Rh) on the re-dispersed Raney Ni was conducted by adding rhodium acetylacetonate ($Rh(CH_3COCHCOCH_3)_3$) and 1,2-hexadecanediol ($CH_3(CH_2)_{13}CHOHCH_2OH$) at a 1:2 molar ratio to the diphenyl ether. The mixture

was then purged with nitrogen for 15 minutes with magnetic stirring before being heated at a constant rate to 250 ^{o}C. The mixture was then refluxed under 250 ^{o}C in a nitrogen atmosphere for 40 minutes. After reduction, the mixture was cooled to room temperature and the resulting solution was washed several times with a 1:1 mixture of hexane and ethanol. The solid powder was then separated by centrifuge and the resulting catalyst dried under nitrogen before being then re-dispersed in water. HPLC analysis of the rinse solutions was conducted to ensure the resulting catalyst was free from organic contamination before performing the catalytic testing.

A simple wet impregnation was used to deposit a second metal from its precursor solution onto the solid powder followed by drying, calcination and pre-reduction.

4.2.2 CATALYTIC TESTING

The hydrogenolysis reaction was carried out in the liquid phase using a 160 mL autoclave high pressure reactor. In a typical experiment, 30 mL of ethylene glycol solution (0.85 M) and 0.50 g of catalyst were loaded in a glove box. The reactor was flushed with pure hydrogen to remove any trace of oxygen before pressurising to 20 bar at room temperature. It was then heated to 175 ^{o}C and allowed to react for 5 hours with constant stirring.

4.2.3 PRODUCT ANALYSIS

After the allotted reaction time, the autoclave was cooled to -60 ^{o}C in a dry ice/acetone bath. Here, the gas phase was analysed by a Perkin Elmer Autosystem XL GC fitted with a GC-FID-Methanator and a Stainless Steel Carbosphere 80/100 6ft x 1/8" column in order to determinate the concentration of CO, CH_4 and CO_2 in the reaction products. The liquid phase was analysed by a Perkin Elmer 200 series HPLC equipped with a refractive index detector where 0.60 mL of 58 mM sucrose solution

was added as an external standard to determine the concentrations of ethylene glycol, methanol and ethanol in the products. Conversion (%) is defined as the percent of ethylene glycol (mol) converted to all products. Selectivity (%) is defined as the moles of a specific product/moles of total products, where molecular stoichiometry has been taken into account. A mass balance of over 95% for a typical catalytic batch reaction was ensured.

4.2.4 COMPUTATIONAL DETAILS

All calculations were performed in the framework of DFT using the Vienna ab initio simulation package (VASP)[11-14]. The projector-augmented wave (PAW) potentials[15-16] were used to simulate the core electron interactions. The Perdew–Burke–Ernzerhof (PBE) functional[17-18] based on a generalised gradient approximation (GGA) was employed to evaluate the non-local exchange-correlation energy. A plane wave basis set with a cut-off energy of 350 eV was used. For structure optimisation, the ionic positions were allowed to relax until the forces were less than 0.05 eV/Å. Spin polarisation was included for all calculations.

The low coordinated Ni(211) edge surface was investigated by a periodic slab model with four layers of metal. A 2×4 surface unit cell (12.195×9.957 $Å^2$) and a 2×3×1 k-point grid determined by the Monkhorst-Pack method were utilised in this study. The bottom layer was fixed during all geometry optimisations. A vacuum layer of 15 Å along the z direction perpendicular to the surface (with the x and y directions being parallel to the surface) was employed to prevent spurious interactions between the repeated slabs. A second metal (M = Co, Cu, Rh, Sn) was introduced to study the modification effects on Ni(211)[19]. These dopant atoms were separately placed on the Ni(211) edge site in substitution of a single low-coordinated surface Ni atom.

4.3 CATALYST CHARACTERISATION

4.3.1 TEM

All Raney Ni and Cu catalysts were used as received. Typical TEM images shown in Fig. 4-1 suggest that micron sized islands with dark contrast contain many primary interconnected Ni particles of ill-defined shape.

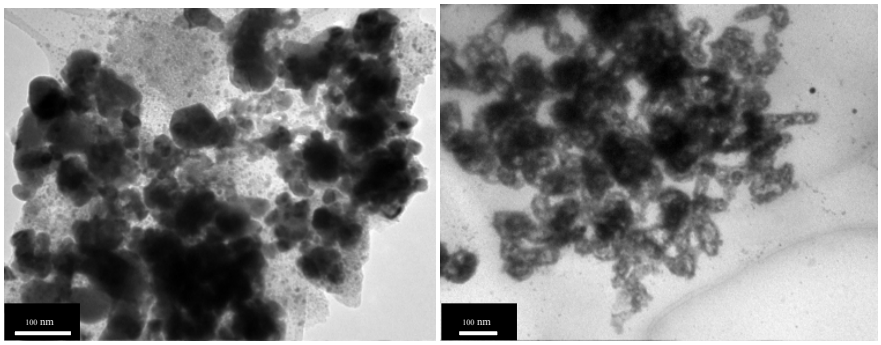


Fig. 4-1 TEM images of a typical Raney Ni2800 catalyst.

4.3.2 PXRD

Powder XRD in Fig. 4-2 indicates the presence of a Ni metal phase exclusively for all catalysts despite 20 wt% doping by various elements. It is noted that those peaks attributed to the Ni phase are clearly shifted to lower angles after the addition of a second metal. This could be due to strain imposed on the structurally non-relaxed Ni phase. However, the significant lattice expansions may also result from alloying of the second metal with Ni. Table 4-1 shows the predicted lattice constants for homogeneous alloys of given compositions according to Vegards's law. However, these values are considerably smaller than the measured values. This clearly suggests that the second metal does not form an extensive alloy structure with the Ni phase. A close examination of the XRD patterns clearly reveals that the Ni peaks become broadened, more non-Gaussian, and less symmetric upon doping with a second metal. This result indicates the second metal adopts the Ni phase, implying the deposition on

the Ni surface is highly dispersive and the impurities/layers added are pseudomorphic to the Ni phase. A summary is given in Table 4-2 describing the basic characteristics of these Raney catalysts according to the manufacturer, W.R. Grace and Co.

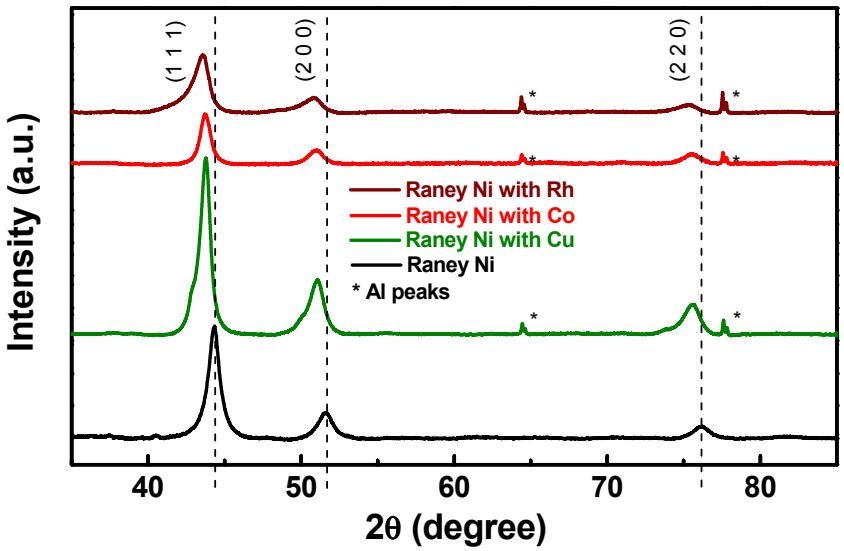


Fig. 4-2 Typical XRD patterns of Raney Ni impregnated with various surface elements showing no new phases (isomorphic deposition) but differences in Ni lattice strains (65° and 78° are holder peaks).

Table 4-1 Lattice constants for different metals on Raney Ni catalysts.

	Raney Ni 2800	**Cu on Raney Ni 2800**	**Co on Raney Ni 2800**	**Rh on Raney Ni 2800**
Lattice constant (Å) (1 1 1 plane)	3.543	3.585	3.584	3.604
% expansion	-	1.19	1.15	1.72
Alloy*	-	3.538	3.527	3.553

*Predicted by Vegards's law

Table 4-2 Catalyst specifications according to supplier.

Catalyst	Composition	ASP Range / microns	BET Surface Area (m^2/g)[20-21]
Raney Ni 2400	Ni(Al): Fe, Cr promoted	25 – 55	N.A.
Raney Ni 2800	Ni(Al)	45 – 90	80-100
Raney Ni 3202	Ni(Al): Mo promoted	20 – 55	70
Raney Ni 4200	Ni(Al)	20 – 50	78
Raney Cu 2900	Cu(Al)	35 – 75	82

4.4 HYDROGENOLYSIS TESTING

4.4.1 RANEY Ni CATALYSTS FOR ETHYLENE GLYCOL HYDROGENOLYSIS

The hydrogenolysis of ethylene glycol reaction was carried out with 30 mL of ethylene glycol solution (density of 0.85 M) over a series of Raney catalysts for the production of methanol. The results are summarised in Table 4-3.

As seen from Table 4-3, when the Raney catalysts were tested under the same reaction conditions, the best methanol selectivity (17.7%) at 2.1% ethylene glycol conversion was obtained over Raney Ni 2800. The catalytic activity was improved either by using comparative small Ni particles (as in case of Raney Ni 4200) or more significantly, by doping the Raney Ni catalyst with a transition metal (as in cases of Raney Ni 2400 and Raney Ni 3202). Despite comparable surface area, the activity of Raney Cu was much poorer compared to the Raney Ni catalysts under the same testing conditions. A prolonged (24 hours) reaction time with Raney Cu shows a good methanol selectivity (53.3%) but at a very low ethylene glycol conversion (0.14%).

Table 4-3 The catalytic performances of Raney catalysts for ethylene glycol hydrogenolysis; the last column represents the summation of iso-propanol, formaldehyde and acetone.

Catalyst	Conv. (%)	Selectivity (%)					
		CO	Methane	Ethane	Methanol	Ethanol	Others
Raney Ni 2400	56.8	0.0	83.7	5.5	8.2	2.5	0.1
Raney Ni 2800	2.1	0.2	78.3	1.8	17.7	1.9	0.1
Raney Ni 3202	26.7	0.0	76.8	6.8	9.5	6.6	0.3
Raney Ni 4200	7.5	0.1	81.1	5.3	11.8	1.6	0.1
Raney Cu 2900	<0.1	n.d.	n.d.	n.d.	n.d.	n.d.	n.d.
Raney Cu 2900[a]	0.1	9.3	12.8	0.0	53.3	14.6	10.0

Reaction conditions: 160 mL reactor; 2 mL catalyst slurry in water (supplied); 175 ^{o}C; 20 bar H_2; time= 2 hours. [a] 24hours

A series of ethylene glycol hydrogenolysis experiments were then conducted using the Raney Ni 2800 catalyst in order to study the effects of different reaction times and catalyst to reactant ratios.

Fig. 4-3 shows methane to be the major product at the shortest reaction time used (2 h) with a selectivity of 75%. However, at longer reaction times the methane selectivity is slightly increased at the expense of methanol, suggesting that a small extent of methane formation is contributed from sequential decomposition of methanol (further decomposition on the Ni surface at longer reaction time). The same effects of increasing the ethylene glycol conversion and methanol selectivity both were obtained by using longer reaction times and larger amount of catalyst. By extrapolation of the x-axis in Fig. 4-3b (reducing the extent of subsequent reactions

by minimising contact with the catalyst surface), the highest selectivity for methanol is shown to be around 20%. On the other hand, in spite of large variations in reaction times or catalyst amounts (> 4 fold), there was no major alteration to the methanol and methane selectivity. This implies that, under these reaction conditions, once methanol is produced, it is relatively stable against rapid degradation to methane with prolonged reaction time or excess contact with the Ni surface. This also suggests that most of the methanol and methane molecules were produced from parallel surface reactions on the catalyst surface. Thus, the predominant formation of methane may have originated directly from the degradation of ethylene glycol without going through a methanol intermediate. Clearly, Ni provides separate active sites for both the hydrogenolysis of ethylene glycol to methane and for the production of methanol molecules.

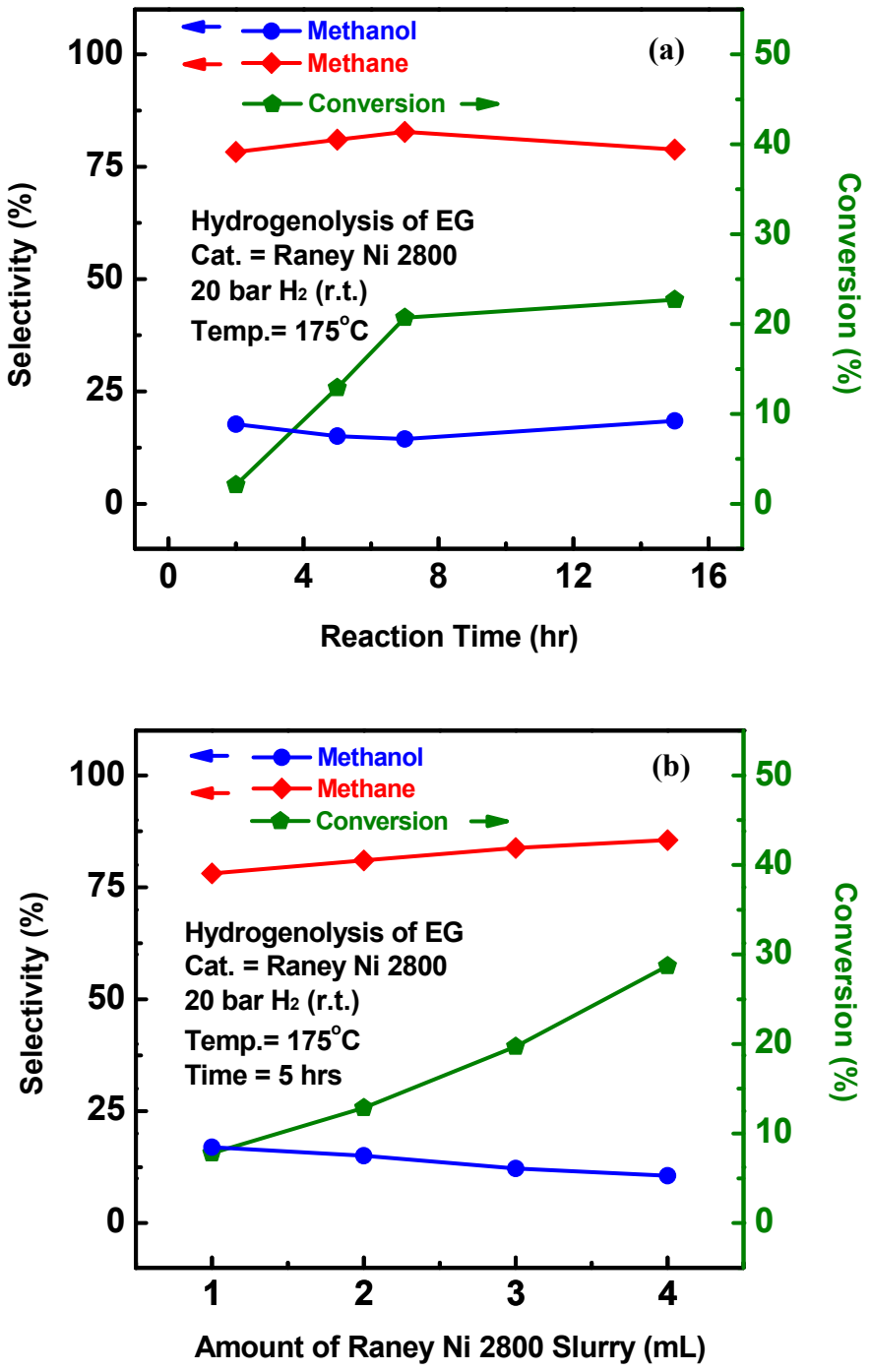


Fig. 4-3 The effect of reaction time (a) and catalyst amount (b) on selectivity and conversion at 175 ^{o}C and 20 bar of H_2

Nickel and modified nickel catalysts have been reported with good activities for biomass reforming for hydrogen production[22], for hydrogenation reactions[23-24] and for

alkane hydrogenolysis[25]. Here, Raney Ni catalysts are shown to be active for the conversion of ethylene glycol under hydrogen, but unfortunately methane is the major product. Since doping with transition metal impurities was previously demonstrated to enhance the activity significantly, it would be interesting to investigate the effect systematically modifying the Ni surface with a second metal has on catalytic activity and selectivity for this reaction. Therefore, a series of M-doped Raney Ni (where M = Cu, Co, Rh or Sn) bimetallic catalysts were synthesised and the catalyst testing results are summarised in Table 4-4.

It is interesting to note from Table 4-4 that the introduction of a second metal (Cu, Co, Rh or Sn) to the Raney Ni 2800 catalyst surface causes a significant alteration in the catalyst performance (activity and selectivity). When comparing with the Raney Ni 2800 catalyst, surface modification with Cu greatly suppressed the catalyst activity, as anticipated from the poor performance of Raney Cu but with no beneficial effect on selectivity towards methanol/ethanol. The catalytic activity of Raney Ni 2800 was maintained after both Co and Rh modification. However, only Rh modification offered an increased selectivity towards ethanol production while the Co modification offered no change in alcohol selectivity. It should be noted that Sn modification over Raney Ni 2800 suppressed activity but resulted in a significant improvement in ethanol selectivity at the expense of methane with only a slight drop in methanol selectivity.

Table 4-4 Catalytic performance of modified Raney Ni 2800 catalyst for hydrogenolysis of ethylene glycol.

Catalysts		Conversion	Selectivity (%)						Amount
Decorating Metal	Synthesis method	(%)	Methanol	Ethanol	Methane	Ethane	IPA	CO	(mL)
	C	12.9	15.0	1.8	81.0	1.5	0.6	0.1	2
20% Cu	P	6.2	5.3	0.9	86.3	7.1	0.2	0.1	2
20% Co	P	15.2	6.5	1.7	86.0	5.7	0.1	0.1	2
20% Rh	P	20.6	6.7	10.8	65.7	16.6	0.1	0.0	2
20% Sn	P	3.40	10.0	35.1	49.3	4.4	1.0	0.2	2

Catalyst synthesis method: C= commercial catalyst, P= polyol process. 175 ^{o}C; time= 5 hours; 20 bar H_2.

4.4.2 RANEY Cu CATALYSTS FOR ETHYLENE GLYCOL HYDROGENOLYSIS

As discussed previously, Raney Cu demonstrates a good selectivity towards alcohol formation (methanol and ethanol) but with very poor activity. Thus, it would be ideal to use a second metal to promote its catalytic activity as demonstrated in previous section.

According to Table 4-5, a 5% Rh-doped Raney Cu catalyst shows high selectivity towards methanol (39.6%) at slightly higher ethylene glycol conversion (0.3%) as compared to unpromoted Raney Cu (53.3% methanol selectivity with almost 0% conversion). In the case of 5% Ni-doped Raney Cu, 29.5% selectivity towards methanol at 0.4% conversion was obtained while in the case of 5% Ru-doped Raney Cu, 14.6% selectivity for methanol at 0.9% conversion was achieved. An attempt was also made to enhance the degree of mixing between Rh and Cu by pre-forming the required RhCu alloy nanoparticles using the polyol process. A high selectivity towards methanol and ethanol was achieved, reaching almost the same

levels as Cu (54% methanol selectivity at 0.4% conversion) when an extensive alloy catalyst was used.

Table 4-5 Catalytic performance of modified Raney Cu catalysts for hydrogenolysis of ethylene glycol.

Catalysts			Conversion (%)	Selectivity (%)			
Decorating Metal	Support	Synthesis method		Methanol	Ethanol	Methane	Others
	Raney Cu	C	< 0.1	n.d.	n.d.	n.d.	n.d.
	Raney Cu	C	0.1[b]	53.3	14.6	12.8	19.3
0.5% Ru	Raney Cu	P	0.5	14.0	7.6	60.4	18.0
1% Ru	Raney Cu	P	0.8	12.5	5.3	64.6	17.6
5% Ru	Raney Cu	P	0.9	14.6	7.5	61.2	16.7
5% Rh	Raney Cu	P	0.3	39.6	9.7	29.2	21.5
5% Rh	Raney Cu	P	0.3[a]	35.5	10.9	33.5	20.1
5% Rh	Raney Cu	P	0.9[b]	45.0	10.2	20.2	24.6
5% Ni	Raney Cu	P	0.4	29.5	8.7	42.8	19.0
10% Ni	Raney Cu	P	2.5[b]	24.5	5.3	57.9	12.3
5% Rh	Carbon	C	3.3	16.0	2.6	71.9	9.5
5% Rh/Cu[c] (Rh/Cu=3/1)	Carbon	P	0.4	54.0	10.6	10.9	24.5

Catalysts synthesis method: P= polyol process, W= wet impregnation. 175 ^{o}C; time= 5 hours; 20 bar H_2; 0.5g of catalyst used. a= 5 hr reducing time of polyol process, b=24 hr hydrogenolysis reaction, c= one step synthesis.

4.5 DISCUSSION

For any catalysis reaction, activity and selectivity may be explained by Sabatier's principle. This principle offers a qualitative guidance in chemical catalysis. It states that the interactions between the catalyst and the substrate molecule should be "just right"; that is, neither too strong nor too weak. If the interaction is too weak, the substrate will fail to bind to the catalyst and no reaction will take place. On the other hand, if the interaction is too strong, the catalyst gets blocked by substrate or product that fails to dissociate.[26]

Consequently, tuning the interaction of chemical species on catalyst metal surface is very important. If there is no adsorption between chemical species and catalysts, the catalysis will not progress further. The local chemisorption of specie with *d*-band electrons on metal surface will form bonding and antibonding state (see Fig. 4-4). The recent density function theory derived *d*-band centre model (please refer to appendix) proposed by Nϕrskov[19] can predict the binding strength of adsorbate on metal surface. If the *d*-band centre is far below the Fermi level (mainly dominant by sp bands), then the antibonding of adsorbate is filled and thus the adsorption is weak. If the *d*-band centre approaches the Fermi level, then antibonding state of adsorbate is high and empty. Thus, the adsorbate binds strongly on the surface. The change of *d*-band position can be influenced by strain (structural) and ligand effects. The discussion on the modification of *d*-band centre over different catalysts used in this study will be invoked.

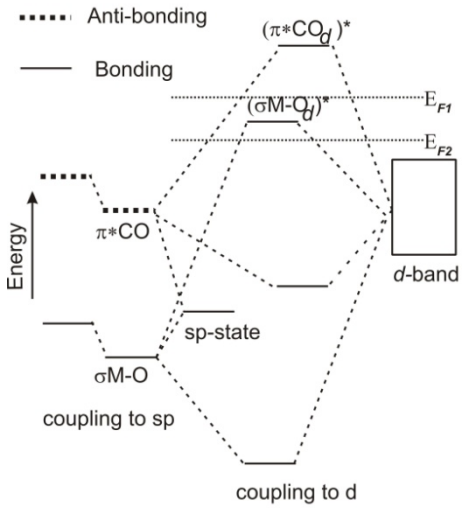


Fig. 4-4 Schematic illustration of the interactions between adsorbed alcohol (with M-O-C bonds) with electronic states of transition metal, E_{f2} refers to Fermi level of early transition metals which lie below the empty antibonding bands; E_{f1} refers to Fermi level of late transition and noble metals which lie above the filled antibonding bands.[27] Figure reproduced from ref. 27.

As stated previously, it is possible to use catalytic hydrogenolysis to convert hydrocarbon (polyols) molecules with a basic unit of (OHCH-CHOH) to smaller alcohols for use as a fuel. If hydrogenolysis can selectively cleave C-C bonds over C-O bonds, methanol will be favourably formed. Thus, the key challenge is activating C-C over C-O bonds to produce various small diols which can be converted to methanol at a high pressure of hydrogen (40 bar)[28-29]. A lack in fundamental understanding surrounding cleavage of the C-C bond on the surface poses a significant problem to solving this challenge as both reactions are favourable from a thermodynamic perspective. Both C-C and C-O bond cleavages require high temperature to overcome their activation barriers. However, the bond energies of both C-C and C-O are very similar (ΔH_{C-C} 348 kJ/mol and ΔH_{C-O} 360 kJ/mol), therefore, if the hydrogenolysis reaction is carried out under harsh conditions, it is less likely a high selectivity will be achieved as rupture of C-O bonds is unavoidable. Our research is aimed at developing a new nanocatalyst with a high specificity for the production of methanol, *via* catalytic hydrogenolysis of ethylene glycol as a model compound. To achieve this aim we need to gain a further understanding of ethylene glycol adsorption molecule on the surface, followed by the various mechanisms for further reactions.

As the simple schematic below illustrates, it is envisaged that ethylene glycol must compete with hydrogen for surface sites on Raney metal with the molecule adsorbing dissociatively through the two –OH groups (Fig. 4-5). The strength of chemisorptions, dependent on the electronic and geometric factors of the localised metal surface, will dictate the activity and distribution of products formed. As aforementioned, the hydrogenolysis of ethylene glycol gives us a range of products at different conversion over the Raney catalysts.

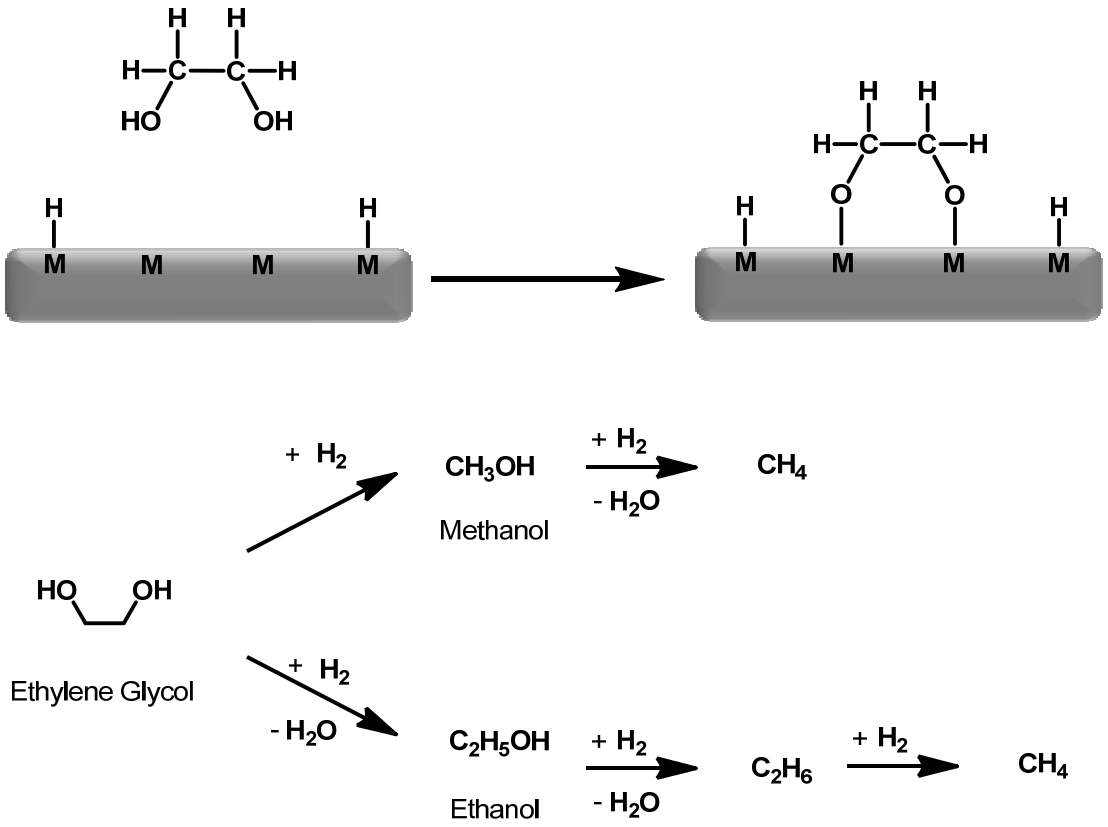


Fig. 4-5 A simple schematic diagram for adsorbed ethylene glycol for the hydrogenolysis of C-C on a transition metal M site (top)[30]; Typical pathway for the hydrogenolysis of ethylene glycol (bottom).

In the case of Raney Cu catalysts, their activity is much poorer compared to their Raney Ni counterparts (Table 4-3). This can be rationalised by referencing the activities given in Table 4-5 to d-band centre position. The high d-band centre of Ni clearly suggests a stronger bonding nature with the substrate molecule, leading to higher conversion. On the other hand Raney Cu catalysts, though having high surface areas on a per gram basis, do not activate ethylene glycol significantly due to a lower d-band centre position. However, excessive adsorption could prevent the molecules and/or fragments on surface from desorbing, leading to complete hydrogenolysis to the undesirable product methane. These results can be clearly seen from the testing of our Raney catalysts without modification.

It is well known that introduction of a second metal, even at impurity levels, will alter electronic properties and hence the adsorptivity and catalytic nature of the first metal. Our research was aimed at enhancing activity of Raney Cu catalysts while keeping their high methanol selectivity. In the case of active Raney Ni catalysts, enhancement in methanol selectivity at the expense of methane was required. As a result, modifications of both Raney Cu and Ni catalysts with second metal were conducted. In the case of 5% doping of Raney Cu catalysts, the order for methanol selectivity is as follows: Cu (53.3%) > Cu (Rh) (39.6%) > Cu (Ni) (29.5%) > Cu (Ru) (14.6%) with increasing conversions of 0%, 0.3%, 0.4% and 0.9% respectively. Thus, the activity and selectivity orders correlate fairly well with the calculated d-band centre positions due to 2nd metal modification (first column in Table 4-6). The lower d-band centre position of the (111) close packed Cu surface resulting from added impurities appears to favour increased methanol selectivity. Blending more active second metal will increase the d-band centre position with increasing activity but renders the methanol selectivity lower. The activity and selectivity orders can be rationalised using this argument except for the slightly higher selectivity and lower conversion than anticipated for the Ni promotion. However, in this case the sample might contain isolated small Ni particles/layers which do not contribute electronic perturbation of the Cu surface. Ni also has a very high d-band centre position itself (-1.29 eV), making it active for this reaction. This combination of 2nd metal surface modification with the activity contribution of the 2nd metal itself can explain this anomalous ranking of this sample.

In addition, RhCu was prepared by a co-reduction process where both Rh and Cu were reduced by the polyol process before dispersion onto a carbon support. This sample showed further improvement over those tested previously, achieving a

methanol selectivity of 54% at slightly higher conversion (0.4%). These improvements were attributed to better mixing between the Rh and Cu phases in the Rh/Cu bimetallic system. Despite the modifications the activity for the Raney Cu based system does not seem to be promoted to any significant extent by using second metals.

Table 4-6 d-band centre values (relative to Fermi level) for clean metals and metals with a surface impurity (in brackets).[19]

Element	eV	Element	eV	Element	eV	Element	eV
Cu	-2.67	Rh	-1.73	Ru	-1.41	Ni	-1.29
Cu(Rh)	-2.35	Rh(Cu)	-1.29			Ni(Rh)	-1.60
Cu(Ni)	-2.40					Ni(Co)	-1.10
Cu(Ru)	-2.09					Ni(Cu)	-1.10

In the case of Raney Ni catalysts modification, addition of a second metal (Table 4-4) did not result in drastic changes in methanol selectivity, but the conversion was greatly attenuated due to extensive coverage of the Ni surface by the added impurities. In this case, results could not be correlated with changes in d-band centre position of the (111) surface facet. It is well known that step sites are much more prominent on Raney Ni catalysts than conventional Ni catalysts.[19] Taking this into account, we have conducted the d-band centre calculations over a low coordinated Ni(211) surface step site as a representative site in a periodic slab model with four metal layers of a 2×4 surface unit cell (12.195×9.957 $Å^2$). A second metal (M = Co, Cu, Rh, Sn) was placed on the Ni(211) edge site, substituting for a single low-coordinated surface Ni atom, similar to the method used in a previous case.[8]

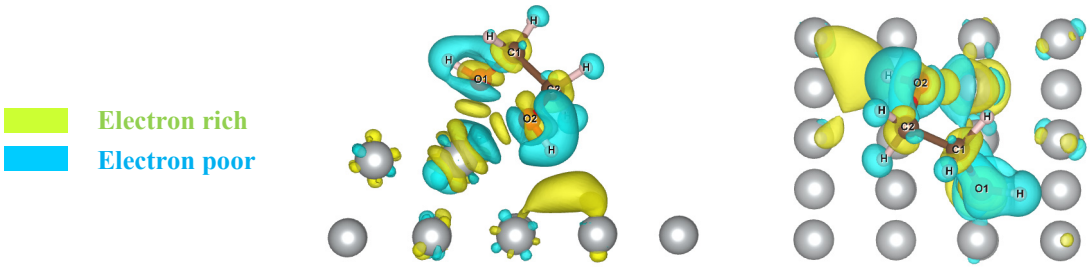


Fig. 4-6 Diagrams showing the calculated electron difference of adsorbed ethylene glycol on a Ni(211) step site with adsorption energy of -1.02 eV compared to the free state. (a) side view of adsorption; (b) top view of adsorption.

As shown in Fig. 4-6, the calculated electron difference for ethylene glycol before and after adsorption on a Ni(211) step site clearly suggests the adsorbed substrate molecule becomes electron deficient, inducing a breakdown of the structure. The strong adsorption energy (-1.02 eV) is expected to facilitate readily cleavage of the adsorbed substrate molecule. Table 4-7 shows that the further downshifted the d-band centre position of Ni(211) is due to the second metal modification, the lower the methanol selectivity. In addition, incorporation of a second metal, especially Rh or Sn, can greatly reduce the methane production in favour of other partially hydrogenated products (ethanol and ethane). This result indicates formation of methane is derived from excessive substrate adsorption until all C-C and C-O bonds have been cleaved. Thus, any surface coverage/blockage will reduce the average size of catalyst ensembles, leading to a reduction in methane production. However, one striking feature for both Raney systems is that methanol selectivity was the highest without modification. Blending a second metal can clearly change the electronic properties of these systems (through d-band centre position modifications) but the effect on methanol selectivity is marginal. This may suggest methanol is produced on unique surface sites totally independent from other partially hydrogenated products where an alteration in general electronic structure of the metal would not induce its adsorbed

form to convert to other products. This proposed mechanism is in agreement with the residence time study in Fig. 4-3. On the other hand, the changes in d-band centre appear to have a significant effect on other product distributions. In the case of Cu, where the adsorption of ethylene glycol is generally very weak (much lower d-band centre position), an upshift in d-band position caused by adding a second metal will enhance its adsorption leading to increased formation of all products apart from methanol. This leads to an overall lower selectivity for the methanol. In the case of Ni, excess adsorption due to an intrinsically high d-band centre results in ready conversion of most substrate molecules into other surface species on the Ni surface. Downshifting the d-band by adding a second metal allows for improved desorption of these species, and again leading to lower selectivity for methanol. For this discussion, we have mainly focused on selectivity and avoided a detailed analysis of changes in conversion for both cases due to the complex combined effects of d-band alteration and physical coverage of the surface by the second metal.

Table 4-7 Correlating d-band centre of (211) with methanol selectivity.

Raney Catalyst	d-band centre (relative to Fermi level) (eV)	Methanol selectivity (%)
Ni	-1.16	15.0
Sn on Ni	-1.33	10.0
Co on Ni	-1.35	6.5
Rh on Ni	-1.35	6.7
Cu on Ni	-1.38	5.3

It is evident from XRD and TEM that doping with a second metal does not seem to form an extensive homogeneous alloy structure (in disagreement with predictions from Vegards's law) nor a clear separate phase (separated particle of second metal). Instead, the shift in XRD peaks and non-Gaussian peak shapes imply

the second metal is highly dispersive on the Ni surface, giving a pseudomorphic surface coverage. On top of that, surface segregation effects may be involved in these catalyst materialsunder a reducing gas environment, especially in the Ni-Cu system. For example, in Ni-rich alloys, literature pointed out an observation of a strong surface segregation of Cu to the topmost layer which measured by atom probe.[31] It also pointed out that the surface concentration of Cu, which segregated to the surface, correlated well with the experimentally catalytic activity.[32-33] Therefore, the surface composition of these catalysts does not necessarily correspond to the bulk composition (PXRD), which may provide us insufficient information to understand active sites for a catalytic reaction.

The present trends in catalytic performance with respect to modifications of d-band positions using the model of surface impurities on bulk phases in Tables 4-6 and 4-7 are thus satisfactory. However, a simple direct attribution of catalytic performance to weight d-band centre position should be approached with caution since surface alloy formation at the interface, contribution from second metal atoms and cooperative contribution from bimetallic sites can also affect the catalytic results. Additional work should be carried out in this area in order to further understand these contributing effects.

Currently, we cannot fully explain why the elementary step(s) of converting ethylene glycol to methanol do not seem affected by changes in d-band centre position. This could be partially attributed to significant differences in adsorption time scale between the substrate and other product species on a specific site. Thus, a major advantage of using Raney catalysts instead of supported ones is that they provide a greater quantity of all metal sites as evidenced by the fact that methanol productivity per gram of catalyst containing specific sites is higher than for supported

catalysts (Table 4-8, last column). Further identification of the specific catalytic active sites and their modification methods will be key to improving methanol yield.

Table 4-8 Comparison between the catalytic performance of Cu, Ni and Rh metal catalyst for ethylene glycol hydrogenolysis.

Catalysts	Specific Catalytic Activity (mmol of ethylene glycol converted · g metal catalyst^{-1} · h^{-1})	Catalytic Activity per Gram Catalyst (mmol of methanol produced · g catalyst^{-1} · h^{-1})
Raney Cu 2900	0.017	0.090
Raney Ni 2800	0.440	0.132
5% Rh/Carbon	5.649	0.074

Reaction Condition: 175 ^{o}C; 5 hours; 20 bar H_2

4.6 CONCLUSION

There is a tremendous growing interest in utilising biomass for energy provision due to its carbon neutrality. Here, we employ ethylene glycol as a model compound for catalytic activation, which represents a basic unit for complex hydrocarbon molecules (polyols). In this chapter, hydrogenolysis of ethylene glycol in hydrogen over modified Raney Ni and Cu catalysts to produce methanol has been studied. This work provides information essential to the development of new catalysts for hydrocarbon conversion to methanol, a novel but important reaction for converting biomass to a transportable form of energy. In this study, modification of electronic structure, and hence adsorption properties, of Raney catalysts has mainly been achieved by blending with second metal(s). It has been shown that the activity and selectivity of this reaction can be significantly affected by this approach. In contrast, no effect on methanol selectivity was observed despite significant variation in d-band centre position which strongly affected the selectivity of all other products. This result suggests methanol is produced at an intrinsic rate on specific sites independent

from the rest of the surface where d-band alteration will not influence the conversion to other products.

4.7 REFERENCES

1. M. Stocker, *Microporous and Mesoporous Materials*, 1999, **29**, 3-48.
2. G. A. Olah, *Angewandte Chemie-International Edition*, 2005, **44**, 2636-2639.
3. P. Gallezot, *Catalysis Today*, 2007, **121**, 76-91.
4. N. Ji, T. Zhang, M. Y. Zheng, A. Q. Wang, H. Wang, X. D. Wang and J. G. G. Chen, *Angewandte Chemie-International Edition*, 2008, **47**, 8510-8513.
5. CCM Data & Business Intelligence. (2013). Retrieved November 05, 2013, from http://www.cnchemicals.com/PressRoom/PressRoomDetail_c_925.html.
6. A. Perosa and P. Tundo, *Industrial & Engineering Chemistry Research*, 2005, **44**, 8535-8537.
7. S. R. Schmidt, S. K. Tanielyan, N. Marin, G. Alvez and R. L. Augustine, *Topics in Catalysis*, 2010, **53**, 1214-1216.
8. I. Furikado, T. Miyazawa, S. Koso, A. Shimao, K. Kunimori and K. Tomishige, *Green Chemistry*, 2007, **9**, 582-588.
9. S. H. Sun, C. B. Murray, D. Weller, L. Folks and A. Moser, *Science*, 2000, **287**, 1989-1992.
10. M. Chen, J. P. Liu and S. H. Sun, *Journal of the American Chemical Society*, 2004, **126**, 8394-8395.
11. G. Kresse and J. Hafner, *Physical Review B*, 1993, **47**, 558-561.
12. G. Kresse and J. Hafner, *Physical Review B*, 1994, **49**, 14251-14269.
13. G. Kresse and J. Furthmuller, *Computational Materials Science*, 1996, **6**, 15-50.
14. G. Kresse and J. Furthmuller, *Physical Review B*, 1996, **54**, 11169-11186.
15. P. E. Blochl, *Physical Review B*, 1994, **50**, 17953-17979.
16. G. Kresse and D. Joubert, *Physical Review B*, 1999, **59**, 1758-1775.

17. J. P. Perdew, K. Burke and Y. Wang, *Physical Review B*, 1996, **54**, 16533-16539.

18. J. P. Perdew, K. Burke and M. Ernzerhof, *Physical Review Letters*, 1997, **78**, 1396-1396.

19. A. Ruban, B. Hammer, P. Stoltze, H. L. Skriver and J. K. Norskov, *Journal of Molecular Catalysis a-Chemical*, 1997, **115**, 421-429.

20. P. Azadi, K. M. Syed and R. Farnood, *Applied Catalysis A-General*, 2009, **358**, 65-72.

21. http://www.sigmaaldrich.com/catalog/product/aldrich/221678.

22. G. W. Huber, J. W. Shabaker and J. A. Dumesic, *Science*, 2003, **300**, 2075-2077.

23. A. Saadi, R. Merabiti, Z. Rassoul and M. M. Bettahar, *Journal of Molecular Catalysis A-Chemical*, 2006, **253**, 79-85.

24. E. van Ryneveld, A. S. Mahomed, P. S. van Heerden, M. J. Green and H. B. Friedrich, *Green Chemistry*, 2011, **13**, 1819-1827.

25. R. Burch and A. R. Flambard, *Journal of Catalysis*, 1982, **78**, 389-405.

26. G. Rothenberg, *Catalysis : concepts and green applications*, Wiley-VCH, Weinheim, 2008.

27. H. Y. Ma, G. C. Wang, Y. Morikawa and J. Nakamura, *Sci China Ser B*, 2009, **52**, 1427-1433.

28. C. H. C. Zhou, J. N. Beltramini, Y. X. Fan and G. Q. M. Lu, *Chemical Society Reviews*, 2008, **37**, 527-549.

29. R. D. Cortright, R. R. Davda and J. A. Dumesic, *Nature*, 2002, **418**, 964-967.

30. E. P. Maris, W. C. Ketchie, M. Murayama and R. J. Davis, *Journal of Catalysis*, 2007, **251**, 281-294.

31. Y. S. Ng, T. T. Tsong and S. B. Mclane, *Phys Rev Lett*, 1979, **42**, 588-591.

32. T. Sakurai, T. Hashizume, A. Kobayashi, A. Sakai, S. Hyodo, Y. Kuk and H. W. Pickering, *Phys Rev B*, 1986, **34**, 8379-8390.

33. J. H. Sinfelt, D. J. C. Yates and J. L. Carter, *J Catal*, 1972, **24**, 283-296.

CHAPTER 5 – SUPPORTED OXIDE CATALYSTS FOR HYDROGENOLYSIS OF ETHYLENE GLYCOL

CHAPTER 5 – SUPPORTED OXIDE CATALYSTS FOR HYDROGENOLYSIS OF ETHYLENE GLYCOL 135

5.1 INTRODUCTION 137

5.2 OBJECTIVES 139

5.3 SYNTHESIS OF CATALYSTS 139

5.3.1 SYNTHESIS OF METAL OXIDE CATALYSTS BY CO-PRECIPITATION 139

5.3.2 HANDLING OF PRE-REDUCED Pd/Fe_3O_4 SAMPLES. 140

5.3.3 CATALYST TESTING AND PRODUCT ANALYSIS 140

5.4 CHARACTERISATIONS OF METAL SUPPORTED OXIDE CATALYSTS 141

5.4.1 XRD 141

5.4.2 TPR 147

5.4.3 TEM AND HAADF-STEM 149

5.4.4 XPS 153

5.4.5 CO CHEMISORPTION 155

5.4.6 EXAFS 155

5.5 CATALYTIC TESTING 159

5.5.1 HYDROGENOLYSIS OF ETHYLENE GLYCOL 159

5.5.2 METAL-SUPPORT INTERACTION: A MECHANISTIC STUDY OF C-C AND C-O BOND CLEAVAGE 166

5.5.3 KINETICS STUDY 170

5.6 DISCUSSION 173

5.7 CONCLUSION 175

5.8 REFERENCES.....176

5.1 INTRODUCTION

The global distribution of natural resources (oil, gas, coal) for energy and chemical provisions is uneven, giving rise to severe political and economic issues in some regions. With an ever increasing world population, dwindling natural reserves and prevalent green house gas problems,[1-4] these non-renewable routes of energy production are unlikely to remain dominant for long periods of time. However, the switch to renewable resources poses huge scientific and technological challenges, and the current trend is to manage and diversify these non-renewables for cleaner and more efficient utilisation.[4] Catalytic production of methanol is very important as this high energy density liquid can be used as a transportation fuel with good volatility (for combustion engines or fuel cells devices), and as a key platform chemical in further synthesis.[3] Given the fact that long-term energy security is a key global challenge, the strategic importance of methanol is expected to rise.[3] Currently, methanol is synthesised on a large scale using natural gas from an energy inefficient process, which requires an indirect, thermally-intensive and endothermic step to completely break down methane to CO/H_2 before re-assembly to form methanol by the ex-ICI process.

From both an energetic and resource diversification standpoint, it would be ideal to synthesise methanol *directly* from different carbon containing resources without any reorganisation steps. As such, we are interested in exploring an alternative non-syngas route utilising ethylene glycol, which is easily available from biomass or fossil fuels for methanol production. At present, ethylene glycol is produced from fossil resources, mainly from an oil cracking process *via* ethylene, but it can also be made from gas and coal.[5] The gradual depletion of fossil resources and emerging environmental concerns have triggered new developments in the synthesis

of ethylene glycol from biomass as a potentially renewable process i.e. a multi-tonnes scale pilot plant synthesis from corn carbohydrates,[6] from carbohydrates by engineered enzymes,[7] and as a new synthetic step from cellulose over carbide catalysts,[5, 8] etc.

Although at present there is no economic incentive to convert the more costly ethylene glycol to methanol, the increasing legislative and economic pull toward methanol utilisation may change this position should the science and technology for this process become available. As demonstrated in chapter 4, the first key technical challenge for this new catalytic process is identifying a catalytically active surface for efficient C-C cleavage followed by C-H formation to form methanol without further conversion to thermodynamically more stable products such as methane or carbon oxides. Thus, a new catalyst for hydrogenolysis of ethylene glycol is required to obtain a high alcohol selectivity.

In chapter 4, we demonstrated that a series of commercial catalysts, including Raney Ni, Raney Cu and supported Rh, with larger quantities of exposed metal sites on a per gram basis show higher activity for the hydrogenolysis of ethylene glycol. This could alter the electronic properties of the metal component, hence altering the adsorption strength of chemical species on the surface. The introduction of an appropriate support material may dramatically enhance activity and selectivity of the active metal phase. Thus, supported catalysts were also briefly studied for this reaction in parallel with DFT modelling of the electronic properties of the catalytic sites.

In this chapter, we extend the study of ethylene glycol hydrogenolysis over a range of supported metal catalysts to achieve a more viable and economically attractive conversion of ethylene glycol to methanol and ethanol.

5.2 OBJECTIVES

The aim of this chapter is to synthesise a range of metal supported catalysts for ethylene glycol hydrogenolysis. By adding a high surface area metal oxide into our catalytic system, we expect to achieve a more selective route for methanol production with moderate conversion of ethylene glycol. It is believed that the oxide support plays an important role in heterogeneous catalysis. As discovered by recent advances, oxide supports act as structural and electronic promoters to improve catalyst activity and selectivity. As discussed in chapter 1, the co-precipitation method has been widely employed to achieve supported metal catalysts with a stoichiometric mixture of well-defined mixed crystallites. Therefore, catalysts in this work were prepared using the co-precipitation technique. The catalytic performance of different metals or oxides combinations for ethylene glycol hydrogenolysis were also scrutinised in order to understand and tailor the nature of metal-support interaction(s) for the selective cleavage of C-C over the C-O bond. It should be noted that selectivity differences towards C-C or C-O cleavage may depend on the electronic and geometric properties of active sites and the nature of ethylene glycol adsorption. As a result, discussion of reaction mechanisms for C-C and C-O bond cleavage, with reference to electronic properties of the catalyst surface, takes place at the end of this chapter.

5.3 SYNTHESIS OF CATALYSTS

5.3.1 SYNTHESIS OF METAL OXIDE CATALYSTS BY CO-PRECIPITATION

A typical synthesis for 1 g of 5% Pd/Fe_2O_3 catalyst was carried out as follows: 0.3309 g of $Pd(NO_3)_2$ solution from Alfa Aesar (15.11wt% Pd) and 5.071 g of $Fe(NO_3)_3 \cdot 9H_2O$ from Sigma Aldrich were dissolved in 200 mL deionised water at

room temperature under stirring. Then, 1.0 M Na_2CO_3 solution was added dropwise until the pH of the final solution reached *ca*. 9.0. After stirring and aging overnight at room temperature, the resulting precipitate (denoted as $Pd/Fe(OH)_x$) was filtered, washed with 200 mL deionised water each for ten times, air-dried at 110 ^oC overnight, gently grounded by pestle and mortar and calcined in air at 300 ^oC for 2 hours. [9] The calination temperature was set at 300^oC as the minimal decomposition temperature of $Pd/Fe(OH)_x$ was determined by TGA to be ca. 200^oC. The dried calcined powder (denoted as PdO/Fe_2O_3) was then pre-reduced in a stream of 33% H_2/N_2 at a steady flow rate of 60 mL/min in a tube furnace at 200 ^oC for 1, 5, 48 or 72 hours. The furnace was then cooled to room temperature and the powder transferred to a glove box for storage before catalytic testing. The as-reduced catalyst was denoted as Pd/Fe_3O_4. A typical co-precipitation technique was adopted for the synthesis of 5% Pd on various oxide supports (ZnO, Ga_2O_3, CeO_2 and Al_2O_3). Each sample was aged, dried and calcined in an identical manner.

5.3.2 HANDLING OF PRE-REDUCED Pd/Fe_3O_4 SAMPLES.

Early experiments suggested the pre-reduction treatments (temperature and duration) have a significant effect on the initial catalytic activity of the samples (induction time). As a result, all pre-reduced samples were handled and transferred with extreme care and without contact with air. For example, the transfer of samples for XPS, TEM, XRD, and EXAFS studies was conducted in an inert gas using a glove bag and/or air-tight sample holders (XRD and EXAFS) before analyses.

5.3.3 CATALYST TESTING AND PRODUCT ANALYSIS

The hydrogenolysis reaction and product analysis were detailed in chapter 4. The mass balance of over 95% was ensured for a typical catalytic batch reaction.

5.4 CHARACTERISATIONS OF METAL SUPPORTED OXIDE CATALYSTS

5.4.1 XRD

Fig. 5-1 shows XRD patterns for 5% Pd supported on different metal oxides, including Fe_2O_3, ZnO, Ga_2O_3, CeO_2 and Al_2O_3. All XRD profiles were collected after samples were calcined in air at 300°C, followed by reduction in 33% H_2/N_2 at 300°C. It can be clearly seen that after reduction all oxides display distinctive phases. A distinguishable Pd(111) peak is only observed for Ga_2O_3, CeO_2 and Al_2O_3 samples. Based on the Scherrer equation and the Pd(111) diffraction peak, the average crystallite size of Pd on Ga_2O_3, CeO_2 and Al_2O_3 were estimated to be approximately 12, 27 and 5 nm, respectively. It is interesting to note that no Pd peak is observed for Fe_2O_3 and ZnO supported catalysts, indicating the supported Pd remained highly dispersed in the Fe_2O_3 and ZnO catalysts even after reduction, possibly due to a strong interaction between Pd and the two supports.

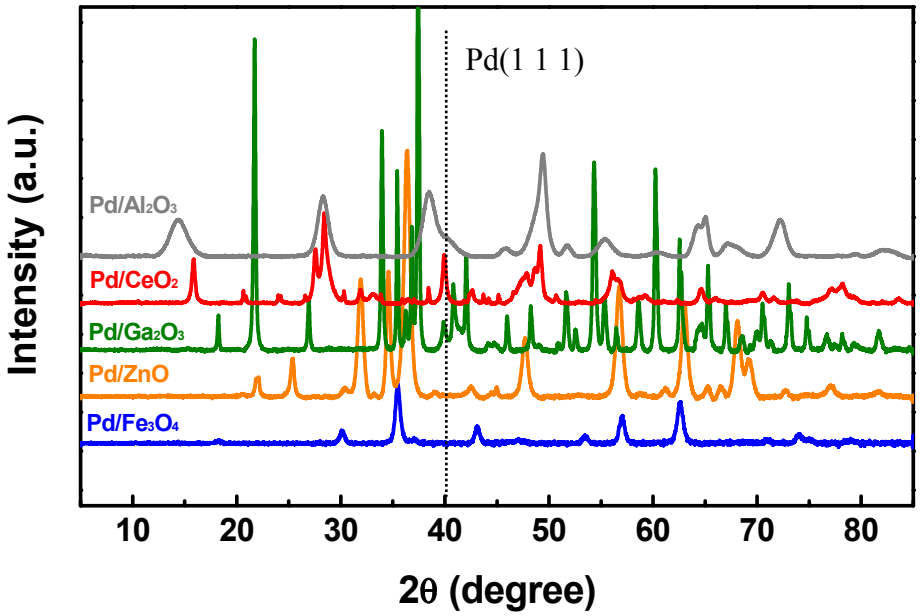


Fig. 5-1 PXRD profiles for a series of metal oxide (Fe_3O_4, ZnO, Ga_2O_3, CeO_2 and Al_2O_3) supported Pd catalysts which have been calcined in air at 300 °C followed by reduction in dilute H_2 (at H_2:N_2 molar ratios of 1:2) at 200 °C.

Similarly, XRD patterns of Fe_2O_3 and metals (including Pd, Rh, Ni, Pt and Ag) supported on Fe_2O_3 after their calcination in air at 300^oC, followed by reduction in 33% H_2/N_2 at 200^oC are shown in Fig. 5-2a and 5-2b, respectively. Bare Fe_2O_3 in Fig. 5-2a displays clear Fe_2O_3 phases (black curve). On the other hand, it is rather surprising there was no discernible Fe_2O_3 phase observed for the supported metal catalysts even though all samples were calcined at high temperature. The absence of Bragg peaks for Fe_2O_3 in these XRD patterns suggests the Fe_2O_3 was amorphous in nature. The structure and properties of amorphous Fe_2O_3 reviewed by Machala et al. have recently attracted a considerable attention.[10] In contrast, Fig. 5-2b shows a characteristic Fe_3O_4 phase (a 'reduced Fe_2O_3' phase) but no Pd peak is observed. Both Fig. 5-2a and b imply the formation of a strong material interaction between iron oxide and the supported metals, resulting in the destruction of iron oxide structure.

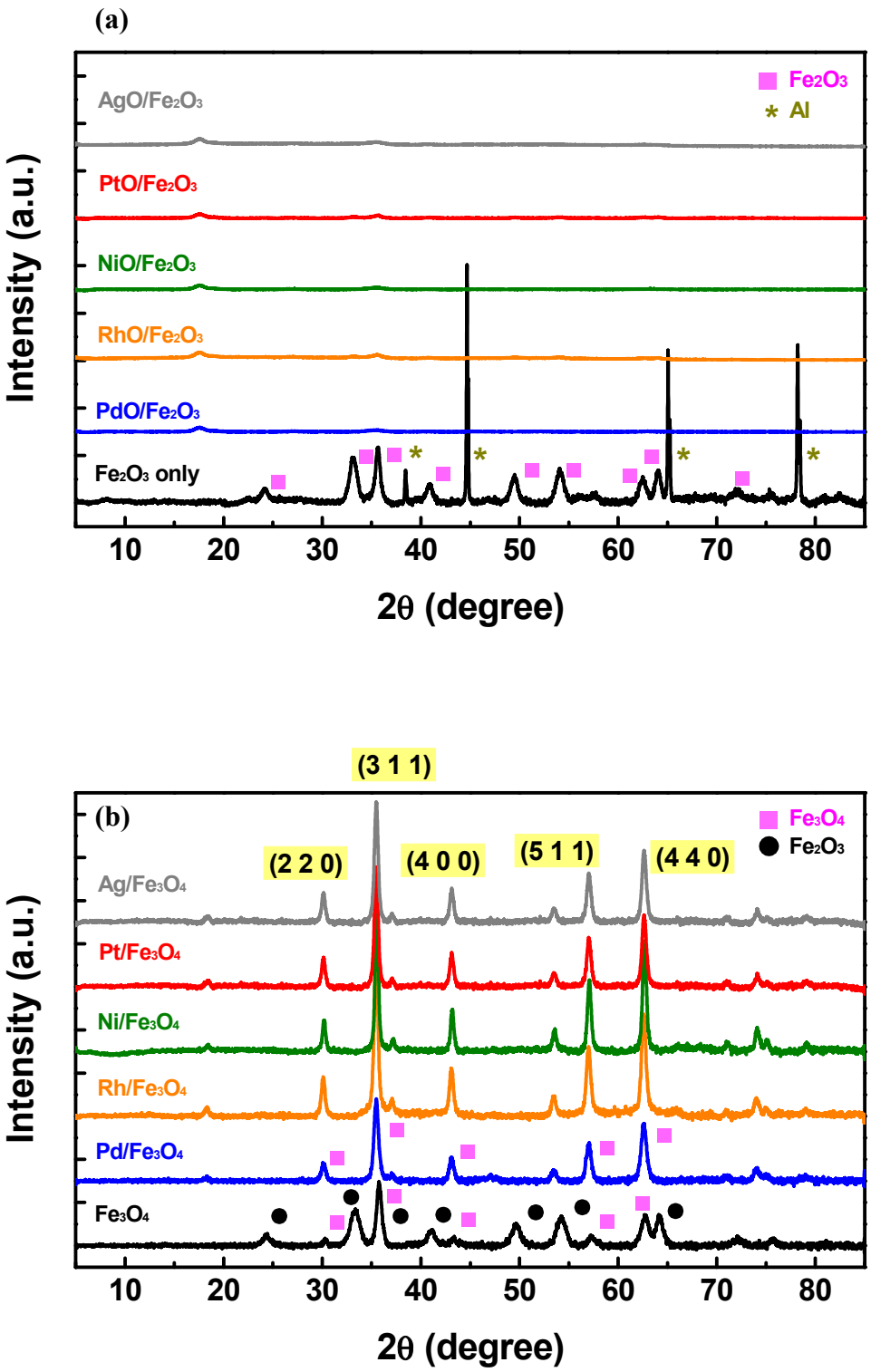


Fig. 5-2 (a) PXRD profiles for Fe_2O_3 and Fe_2O_3 supported metal oxides (including Pd, Rh, Ni, Pt and Ag) calcined in air at 300 ^oC; (b) PXRD profiles for Fe_3O_4 and Fe_3O_4 supported metals (including Pd, Rh, Ni, Pt and Ag) reduced in dilute hydrogen (at H_2:N_2 molar ratios of 1:2) at 200 ^oC.

Fig. 5-3a shows the XRD pattern for Pd/Fe_3O_4 (pre-reduced 1h), which gives a 'reduced Fe_2O_3' phase (small Fe_3O_4 phases are difficult to distinguish from Fe_2O_3 phases with air exposure, and are not easy to be seen and are hence termed 'reduced Fe_2O_3') but with no Pd peak observed, indicative of extremely small Pd containing particles on the reduced iron oxide surface below the detection limit of this technique. On the other hand, two additional broad diffraction peaks marginally differentiable from the background, shown at 40.76 degrees and 47.09 degrees (see Fig. 5-3b), were observed after the sample was tested for ethylene glycol hydrogenolysis over a prolonged time of 72 hours (deliberately inducing a small degree of sintering). According to the database (JCPDS 88-2335, 65-3253), diffraction peaks for Pd(111) and Pd(200) are located at 40.01 and 46.54 (2θ degrees) and PdFe(111) and PdFe (200) peaks at 40.79 and 47.27 (2θ degrees), respectively. Thus, the two peaks observed are a closer match with those of PdFe than Pd. In addition, XRD peaks for our PdFe synthesised *via* a polyol process (ca. 4.6 nm, the black curve in Fig. 5-3b)[11] also fit well with these two peaks. In addition, the calcined PdO/Fe_2O_3 gave an amorphous iron oxide structure, indicative of a sol-gel-like chemistry through hydrolysis during the co-precipitation of palladium and iron nitrates. The Pd still maintained an atomically dispersed level in the Fe-O-Fe network (as illustrated in Fig. 5-4). Furthermore, no Pd peaks were observed on the iron oxide surface for the pre-reduced Pd/Fe_3O_4 sample (blue curve).

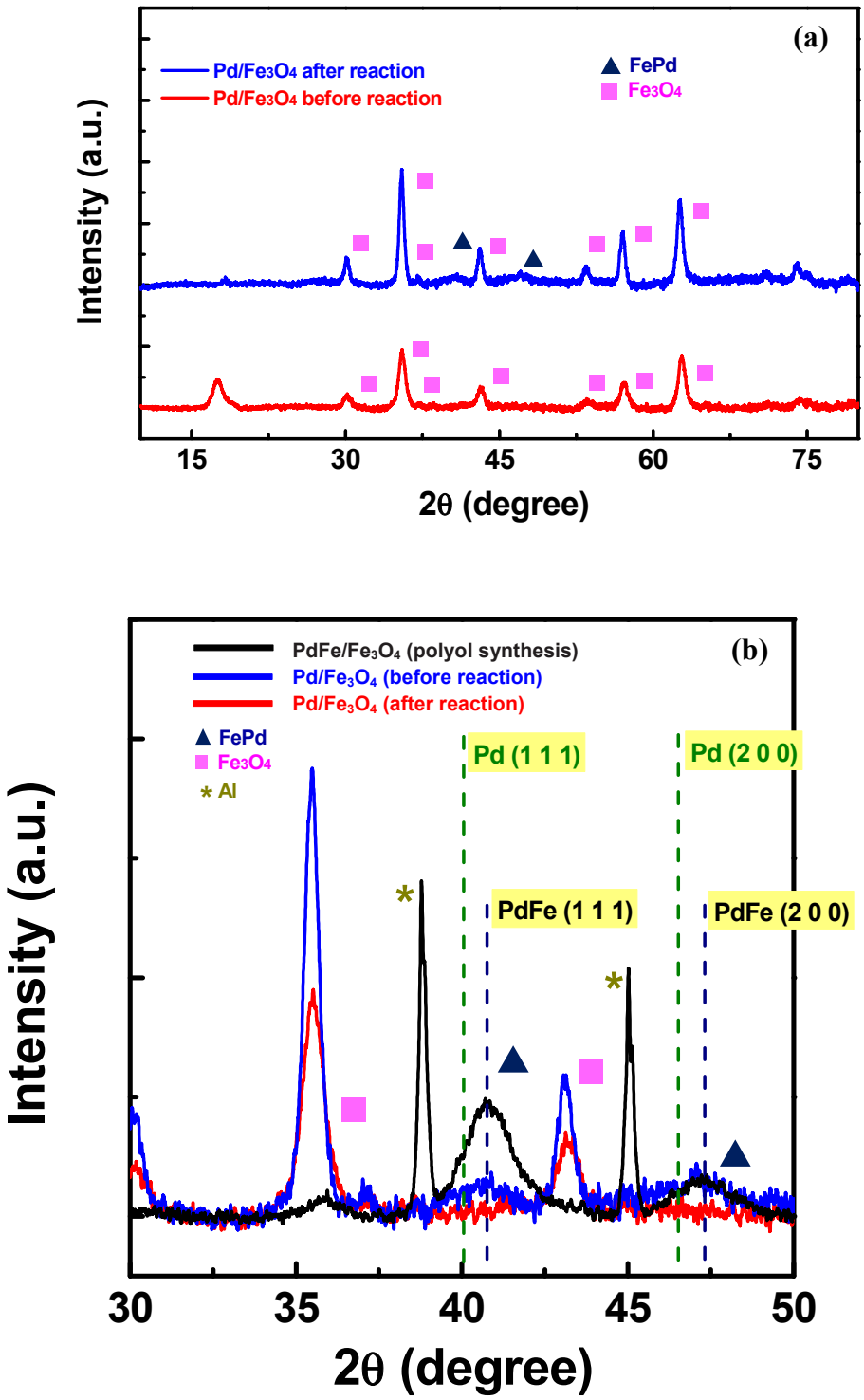


Fig. 5-3 (a) PXRD patterns for Pd/Fe_2O_3 before and after hydrogenolysis of ethylene glycol at 195 ^oC, 20 bar H_2 (RT) (the high and broad peak at 17^o in Pd/Fe_2O_3 before reaction was derived from the air-tight sample holder); (b) Enlarged XRD region to show two small peaks formed after reaction corresponding to PdFe rather than Pd.

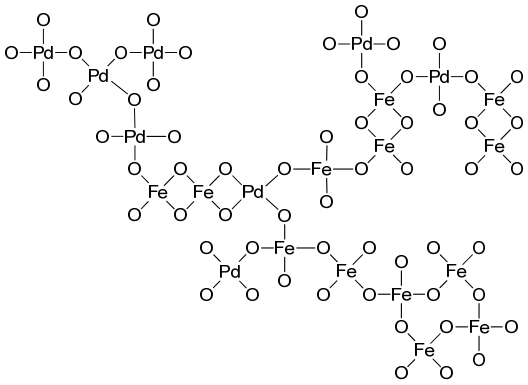


Fig. 5-4 The envisaged co-precipitated network of -Pd-O-Fe- created after hydrolysis and cross-condensation between Pd and Fe precursors in water.

Corresponding in-situ XRD profiles for the calcined 5% PdO/Fe_2O_3 catalyst reduced under a flowing stream of hydrogen is presented in Fig. 5-5. The gradual growth of the Fe_3O_4 phase with increasing reduction temperature, combined with no formation of crystallite Pd, further indicates a distinctive transformation from an amorphous Pd-O-Fe structure to atomically dispersed Pd supported on iron oxide, in agreement with the aforementioned envisaged network structure.

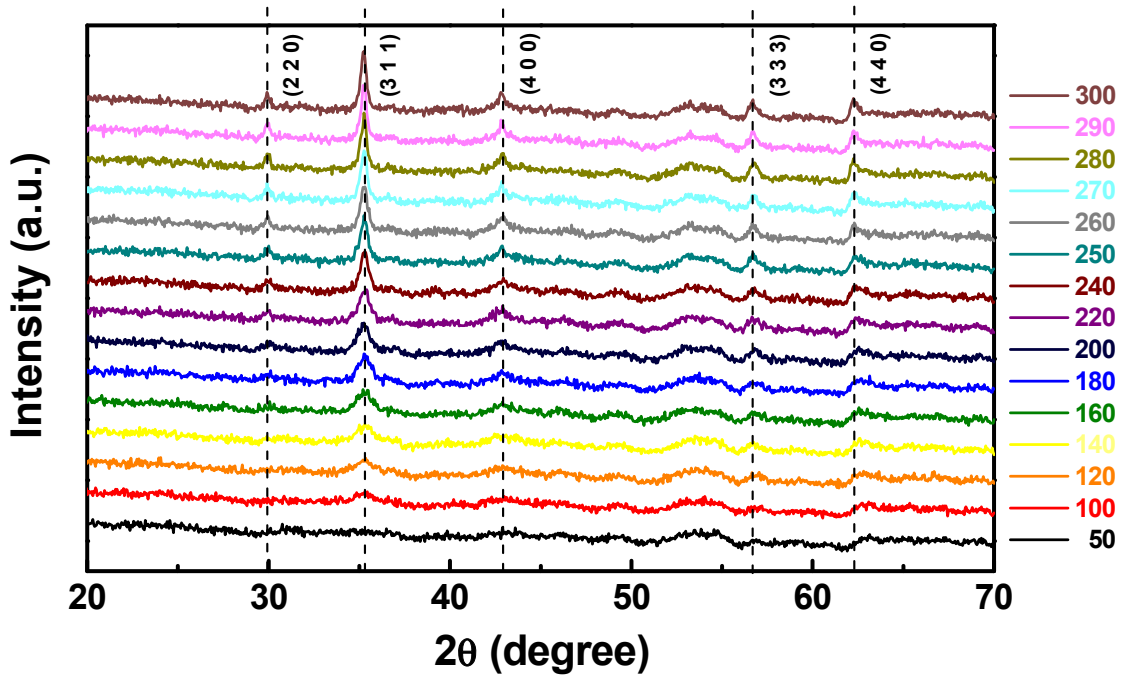


Fig. 5-5 In-situ XRD profile for 5% PdO/Fe_2O_3 in dilute H_2.

5.4.2 TPR

Hydrogen temperature-programmed reduction (TPR) presented in Fig. 5-6a indeed shows no reduction of Fe_2O_3 until the temperature is about 340 ^oC where some surface reduction by gaseous hydrogen occurred. The hydrogen reduction of bulk Fe_2O_3, involving much slower diffusion of lattice oxygen, requires a higher activation energy, hence it takes place at a higher temperature (broad peak with the maximum at 600 ^oC). It is interesting to note that the presence of Pd appears to more readily catalyse the reduction of surface oxygen from Fe_2O_3, forming a defective surface and shifting the reduction temperature to around 130 ^oC. This implies a catalysed reduction of some Fe^{3+} to primarily Fe^{2+} to form the 'Fe_3O_4' phase, but also to Fe^0 associated with Pd^0 to produce PdFe in hydrogen under our pre-reduction/testing conditions. Fig. 5-6b clearly shows an absence of the typical hydrogen evolution peak for β-Pd hydride[12] (pure Pd particles should readily take up hydrogen to form hydride at room temperature) as compared to alumina supported Pd at around 70 ^oC (negative peak) in the second TPR profile of the same Pd/Fe_3O_4 sample without exposure to air. These results are consistent with the formation of highly dispersive PdFe clusters in the sample.

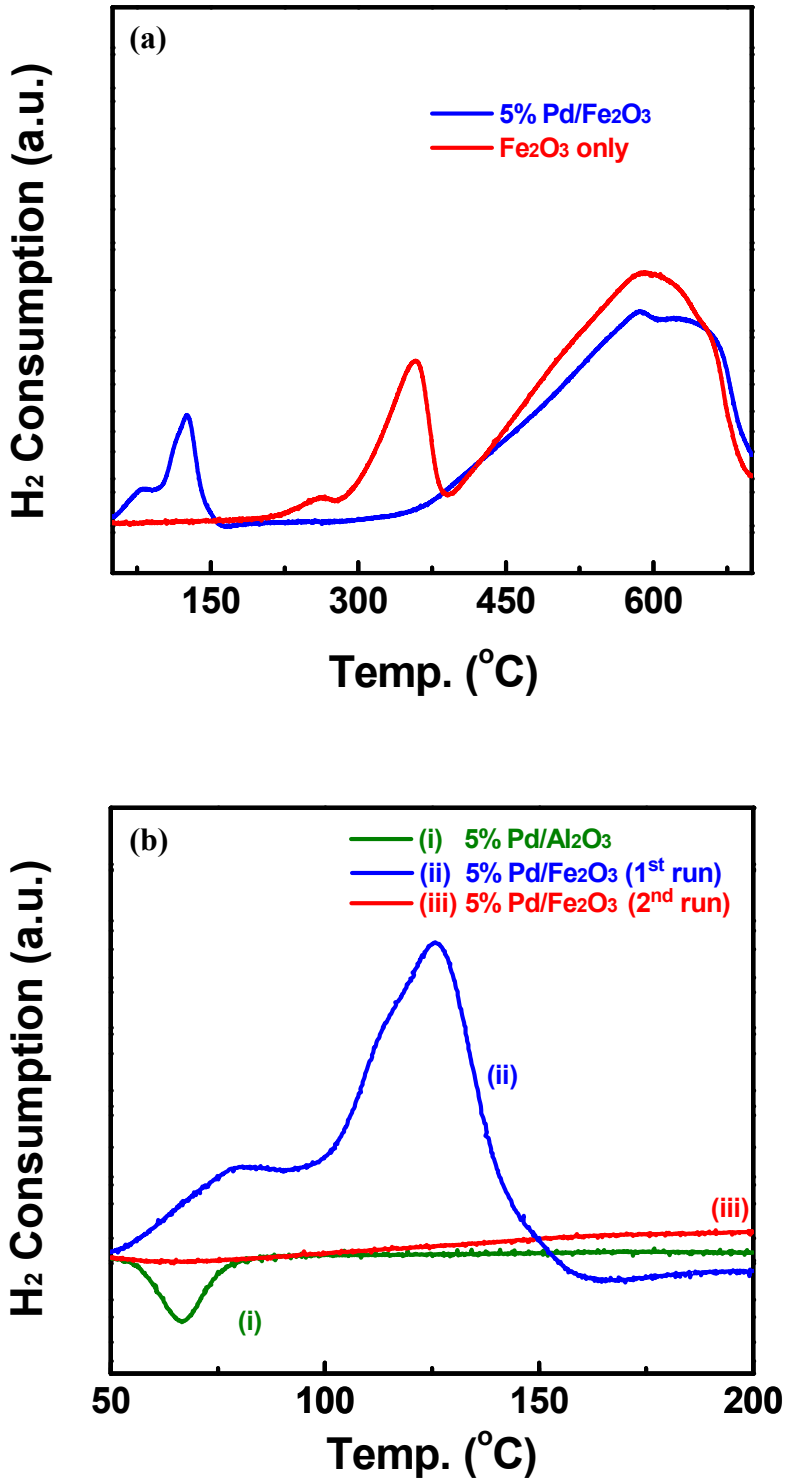


Fig. 5-6 (a) H_2–TPR profiles for Fe_2O_3 and PdO/Fe_2O_3; (b) 1st and 2nd repeated TPR profiles for PdO/Fe_2O_3 in H_2 after temperature programmed heating was terminated at 200 °C as compared to the TPR profile for PdO/Al_2O_3.

5.4.3 TEM AND HAADF-STEM

As seen from the XRD and TPR studies, iron oxide tends to interact with Pd during the preparation process to form an amorphous Pd-O-Fe network. The co-precipitated catalyst shows a highly dispersed structure and forms surface PdFe. Given these results, it is desirable to investigate the influence of preparation method on the catalyst structure. Thus, the interactions between Pd and Fe_2O_3 were compared by using different preparation methods, and the resulting effects were probed by TEM. Fig. 5-7a and 5-8b are TEM images of 5% Pd/Fe_3O_4 obtained by precipitation of palladium nitrate with Na_2CO_3 on commercial Fe_3O_4 and co-precipitation of palladium and iron nitrate with Na_2CO_3, respectively. Both synthesised samples were treated in an identical manner.

Lattice resolution can be seen for the Fe_3O_4 and the small dark features approximately 5 nm in diameter are the Pd particles. Larger Pd particles are observed for Pd precipitated on commercial Fe_3O_4, with the average size of about 4.12 nm (Fig. 5-7a). In contrast, the Pd particles in co-precipitated catalysts shown in Fig.5-7b are smaller and only visible near the edge of the cluster. This highlights the importance of co-precipitation where hydrolysis and cross-condensation between Pd and Fe precursors creates the close network of -Pd-O-Fe-, resulting in reduction of Fe^{3+} ions in close proximity to Pd and the production of surface PdFe particles.

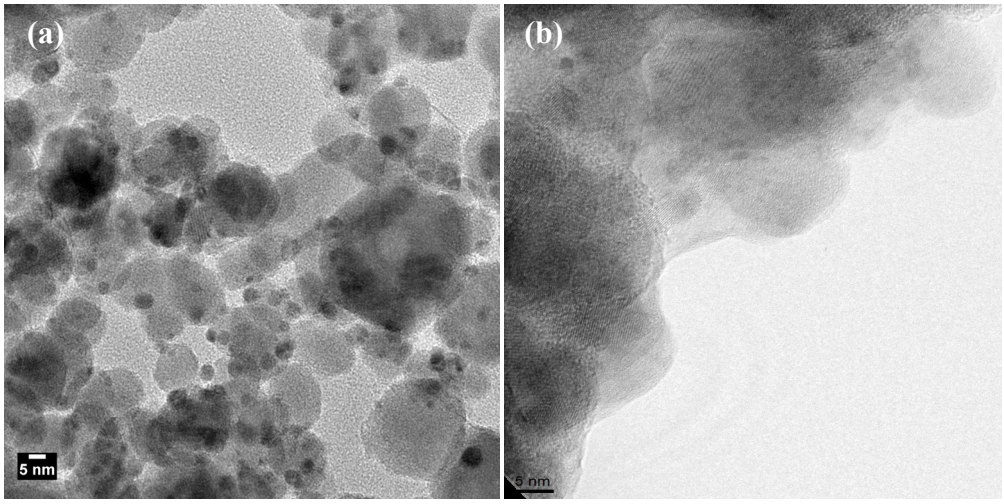


Fig. 5-7 TEM micrographs of 5% Pd/Fe_3O_4 obtained by: (a) precipitation of palladium nitrate on commercial Fe_3O_4; (b) co-precipitation of palladium and iron nitrate; both samples were reduced in 33% H_2/N_2 at 200 °C.

High-angle annular dark field scanning transmission electron microscopy (HAADF-STEM) was used to acquire a detailed microscopic view to determine morphology of the Pd/Fe_3O_4 catalyst particles after pre-reduction. Using a JEOL JEM-2200MCO aberration corrected transmission electron microscope, a large number of small metal particles in the observable thin areas of Fe_3O_4 were revealed. The metal particles ranged in size from *ca.* 0.5 to 2.5 nm in diameter, with particles of 0.5-1.5 nm being the most commonly measured size (as shown in Fig. 5-8). Energy dispersive X-ray spectroscopy confirms the particles consist predominantly of Pd and Fe, although any Fe content could not be unambiguously determined due to the underlying iron oxide support. The direct visualisation of extremely small metal clusters (groups of atoms), and occasionally even single atoms around the edges of the clusters, on the reduced Fe_3O_4 surface under higher magnification could be made.

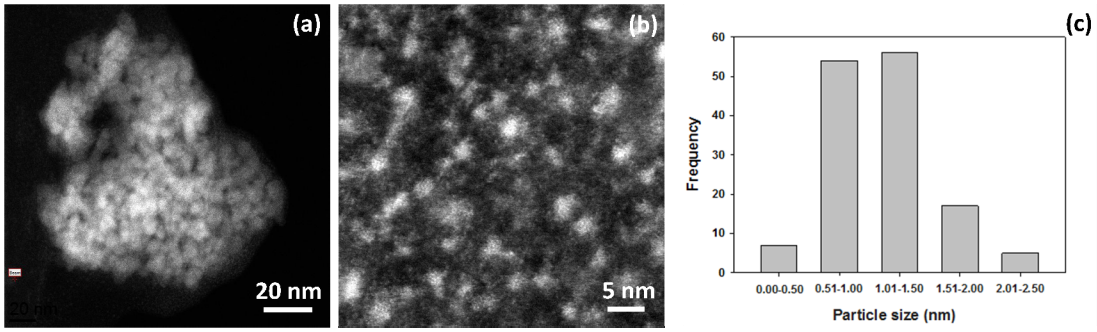


Fig. 5-8 (a) HAADF-STEM image showing an aggregate of nanoscale Pd/Fe_3O_4 catalyst particles. (b) Higher magnification HAADF-STEM image of a thin area, revealing the catalyst surface is covered in nanoscale clusters of metal atoms. (c) Histogram reporting the size distribution of particles in (b). Features such as irregular monolayer clusters and single atoms have not been included here due to ambiguity in defining their size due to mobility under the beam and varying background contrast from the uneven underlying support.

Fig. 5-9a shows typical small particles of Pd around 1-2 nm in size, the structure and shape of the particles are very irregular and individual atoms around the particle perimeter can be seen. In Fig. 5-9b, the image contrast level has been increased to aid identification of small metal atom clusters on the surface, such as those highlighted within the marked circle. An intensity line profile as marked in Fig. 5-9a is plotted in Fig. 5-9c and suggests a group of three isolated adatoms, each with a reproducible half peak width of 1.1 ± 0.1 Å. However, we were unable to ascertain whether Pd or Fe or mixed adatoms were produced based only on this microscopic study. The contrast level relative to the support and that of single adatoms suggests the particles consist generally of one or two layers of metal atom clusters. Fig. 5-9d and 5-9e show further representative areas of the catalyst with an unusually high density of ultra-small metal clusters composed of atom groups on the Pd/Fe_3O_4 surface. Zhang and co-workers have recently reported dispersed single Pt atoms on

iron oxide using a preparation method similar to this work, where they attributed the observed high activity for CO oxidation to these single metal sites on the catalyst.[13-14] Although we cannot discount single metal site catalysis of this hydrogenolysis, more complex steric requirements for adsorption and catalysis of ethylene glycol on metal sites is expected.[15] Additionally, there are no literature reports of homogeneous single metal site catalysts activating ethylene glycol to methanol in hydrogen. In addition, the need for extensive pre-reduction time (long activation time), and the formation of corresponding high density PdFe clusters on surface before the detection of methanol, support the proposal of PdFe clusters as the active species responsible for methanol production.

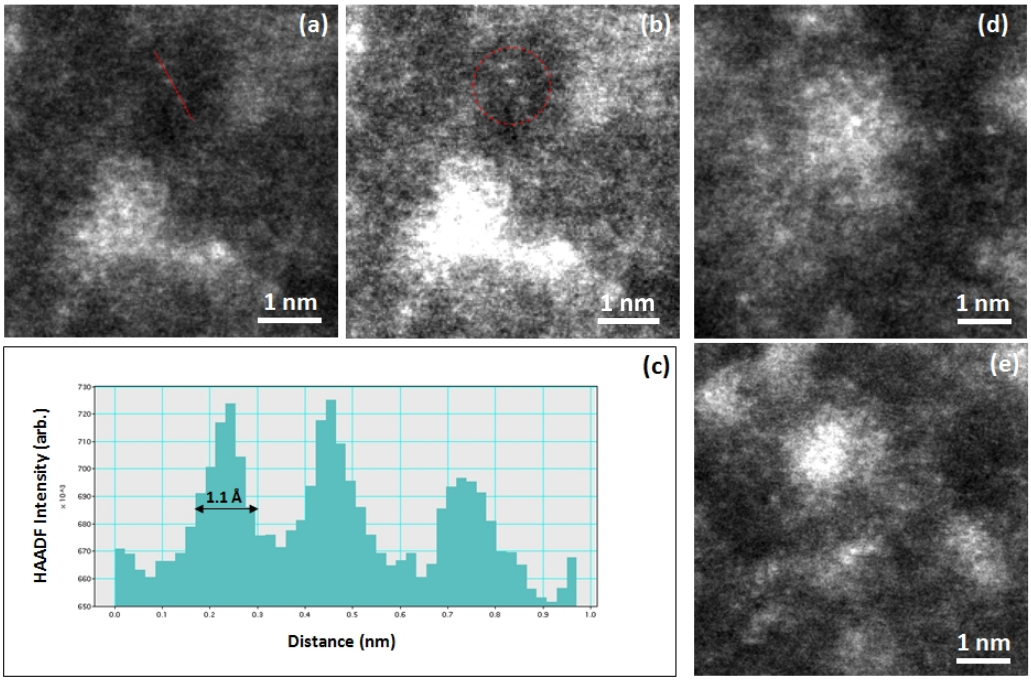


Fig. 5-9 HAADF-STEM imaging of the Pd/Fe_3O_4 catalyst. (a) Typical area of the specimen containing irregular atomic clusters with three distinctive surface adatoms. (b) The same raw data as Fig. 5-9a with the image contrast enhanced to highlight the three single adatoms. The circle highlights the three single adatoms on the Fe_3O_4 surface. (c) Line profile along the line marked in Fig. 5-9a, showing three distinct isolated atoms, each with a half peak width of 1.1 Å. (d) and (e) represent typical irregular groups of atom clusters found in the catalyst material.

5.4.4 XPS

The surface electronic structure of the catalyst was investigated by XPS. In order to correlate the quantity of methanol production with the number of PdFe clusters on the catalyst surface, samples were tested for ethylene glycol hydrogenolysis over different durations (with different methanol selectivities) and then carefully quenched and analysed by XPS. Fig. 5-10 indicates the binding energies of Pd and Fe are both shifted to higher values (referenced to literature values), indicative of 'PdFe' alloy-like formation.[16-19] Unfortunately, there was no clear correlation between the shift in binding energy of Fe $2p_{3/2}$ (Fig. 5-10a) and methanol selectivity due to interference from the bulk iron oxide background. On the other hand, the progressive binding energy shift of Pd $3d_{5/2}$ from 335.16 eV (pure Pd) to the converging value of 336.17 eV shown in Fig. 5-10b (matched with the values for the PdFe sample (*ca.* 4.6 nm) and the extensively hydrogen pre-reduced sample), shows a clear correlation between the increasing amount of surface PdFe and increasing methanol selectivity.[17]

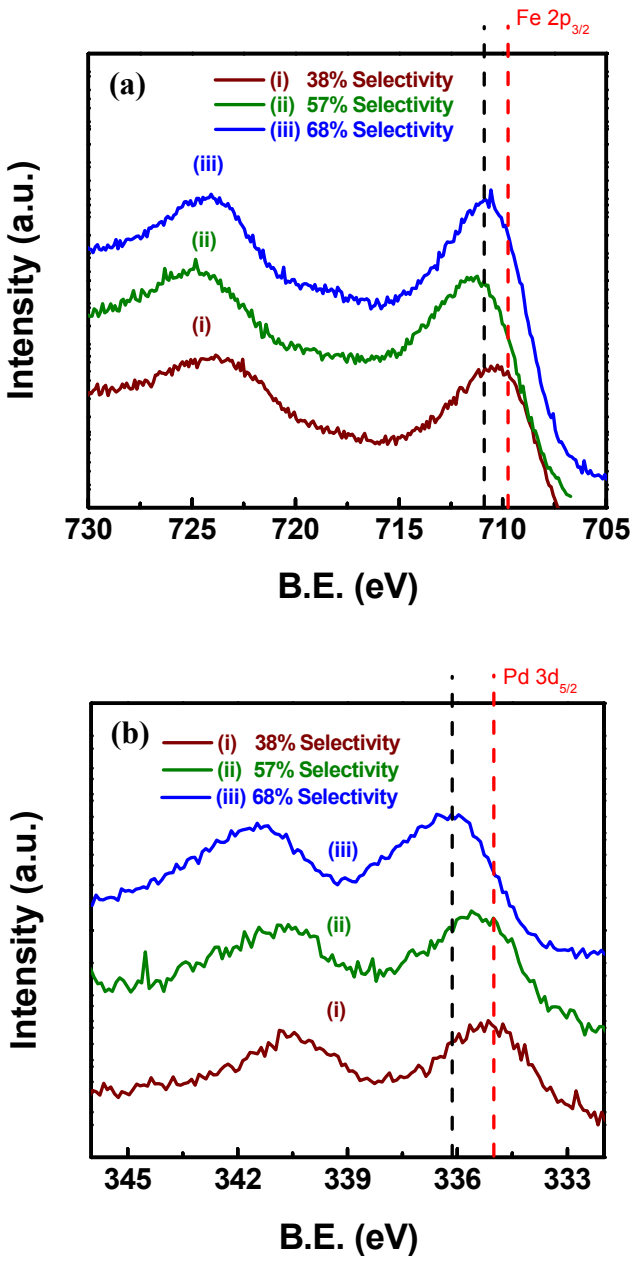


Fig. 5-10 XPS spectra of Pd/Fe_3O_4 catalyst at different hydrogen pre-reduction times (1, 5 and 48 h). The spectra are evaluated at 195 °C for 24 h (corresponding to different alcohol selectivities). All spectra were calibrated to an adventitious C 1s peak at 284.5 eV with the application of electron shower gun to reduce charging effects of the samples. (a) Fe $2p_{3/2}$ region. The dash lines correspond to literature values for the binding energies of Fe $2p_{3/2}$ (red) and the Fe $2p_{3/2}$ in a PdFe alloy (black) (NIST database);[20] (b) Pd $3d_{5/2}$ region. The dash lines correspond to literature values for the binding energies of Pd $3d_{5/2}$ (red) and Pd $3d_{5/2}$ in a PdFe alloy (black) (NIST database).[20]

5.4.5 CO CHEMISORPTION

In heterogeneous catalysis, the degree of dispersion of active metal particles on the support (or particle size of supported metal) is an important factor affecting activity. As a result, active metal surface area was evaluated using pulse CO chemisorption, as shown in Table 5-1. The resulting CO uptake was then used to calculate the particle size and metal surface area.[21-22] Samples were pretreated with hydrogen either at 40 ^{o}C or 200 ^{o}C (to simulate reaction conditions). A clear inverse relationship between Pd metal loading and Pd dispersion (from 0.415 to 0.073) was observed.

Table 5-1 CO adsorption characteristics for Pd/Fe_3O_4 catalysts with different Pd loading. Particle size measurement taken from CO chemisorption was estimated by applying the formula $d = (1.12/D)$ nm and assuming a stiochiometric CO/Pd ratio.[21, 23]

Pd loading (%)	CO Uptake ($\mu mol\ g^{-1}\ cat$)	Dispersion, D	Metal area (m^2) $g^{-1}\ cat$	$g^{-1}\ Pd$	Particle Size, d (nm)	Pre-reduction temp. (^{o}C)
1	38.99	0.415	1.85	185.0	2.7	40
	27.89	0.297	1.32	132.0	3.8	200
5	135.33	0.288	6.42	128.4	3.9	40
	82.61	0.176	3.92	78.4	6.4	200
10	68.70	0.073	3.26	32.6	15.3	200
20	209.44	0.111	9.93	49.7	10.1	40

5.4.6 EXAFS

We then carried out EXAFS characterisation at the Pd K edge (24350 eV) of 5% Pd/Fe_3O_4, both before (poor methanol selectivity) and after (good methanol selectivity) extensive reduction as compared with a commercial 5% Pd/C catalyst. We were particularly interested in estimating the size of Pd containing particles based on

analysis of coordination number (CN) derived from EXAFS data, which should be more representative than TEM (regional analysis) and XRD (small size escapes detection). Based on the refined parameters included in Table 5-2 it is noted that commercial Pd/C with 2 nm Pd particles gives a CN of *ca.* 8.0 at a Pd-Pd distance of 2.73 Å from the first shell analysis. This result is consistent with detailed size estimates of supported Pd particles from a recent EXAFS study conducted alongside with multiple other multiple techniques including gas adsorption, TEM and XRD.[24] Similarly, the derived CN of *ca.* 3.5 reflects the four fold symmetry (square planar) of -PdO_4- in our non-reduced gel form, again conforming with the proposed network structure. Interestingly, we observe an extremely low average CN for Pd-Pd distance in the sample after pre-reduction within the acceptable R- and D-W factors. According to Agostini et al.'s model (cubooctahedral shape of Pd was assumed)[24] and calibration curve, such a small CN corresponds to Pd particles smaller than ca. 1 nm, indicating they are metallic clusters (or groups of adatoms). Strikingly, we are also able to directly observe a Pd-Fe distance (CN = 1.0) of 2.59 Å and a shorter, distorted Pd-Pd distance (CN = 1.9) of 2.66 Å after reduction, confirming the formation of 'PdFe' clusters. The low CN derived from the EXAFS data is indicative of extremely small particle size, matching with observations from the aforementioned HAADF-STEM. Additionally, as shown in Table 5-1, our CO chemisorption measurements after extensive reduction at 200 ^{o}C (82.61 μmol g^{-1} cat.) clearly reflect attenuation of the CO uptake value as compared to the same sample with reduction at 40 ^{o}C (135.33 μmol g^{-1} cat. with only the formation of Pd^{0}). This matches with literature observations describing the dilution and electronic effects of Pd and Fe atoms on CO molecules on the 'PdFe' surface.[25] It should be noted that these small 'PdFe' containing clusters on the oxide surface could be very different from a

thermodynamically stable PdFe alloy with defined structure, stoichiometry and morphology. The spent Pd/Fe_3O_4 sample (sample after the hydrogenolysis of ethylene glycol) was also examined. Although the spent sample was handled and transferred with extreme care (in a glove box) without contacting air, it was not easy to eliminate air oxidation during the washing step. Thus, a Pd-O distance (CN = 0.76) of 1.76 Å was clearly observed. There was an increase in CN to *ca.* 8.6 for Pd in the spent sample, suggesting an aggregation of particles. In addition, a CN (2.9) for Pd-Fe species was also identified, considerably larger than for the fresh form (CN = 1.0), which further illustrates a significant degree of particle sintering during the hydrogenolysis reaction.

Table 5-2 EXAFS characterisation of Pd/Fe_2O_3 before and after pre-reduction.

	Scattering pair	CN*	Bond length (Å)	R-factor (%)	Ef (eV)	DW factor ($\sigma^2 x10^{-3}$ Å^2)	k-range
Pd/C	Pd-Pd	8.0 (3)	2.73 (1)	2.6	-7.6	6.1 (3)	2-17
Pd/Fe_2O_3 (before pre-reduction)	Pd-O	3.5 (2)	2.01 (1)	1.3	-4.5	2.8 (6)	2-16
Pd/Fe_3O_4 (fresh, after pre-reduction)	Pd-Fe	1.0 (2)	2.59 (1)	1.6	-7.4	5.1 (4)	2-12
	Pd-Pd	1.9 (2)	2.66 (1)			7.3 (6)	
	Pd-Pd	2.4 (2)	2.75 (1)			3.6 (3)	
Pd/Fe_3O_4 (spent, after pre-reduction)	Pd-Pd (in Pd phase)	5.0 (5)	2.75 (1)	2.4	-4.5	0.8 (1)	1.4-3.4
	Pd-O (oxide phase)	0.7 (1)	1.76 (1)			0.1 (1)	
	Pd-Fe (in PdFe)	1.3 (2)	2.75 (4)			0.1 (1)	
	Pd-Pd (in PdFe)	0.7 (1)	2.72 (3)			0.1 (1)	
	Pd-Fe (in $PdFe_3$)	1.6 (3)	2.55 (2)			0.9 (1)	

EXAFS fitting results Pd/C commercial catalyst, calcined PdO/Fe_2O_3 and Pd/Fe_3O_4 before and after reaction (all fitted in combined k^{1-3} weighting). The amplitude reduction factor ($S0^2$) value for palladium was fixed at 0.84 to determine the structural parameters for each bond pairs.

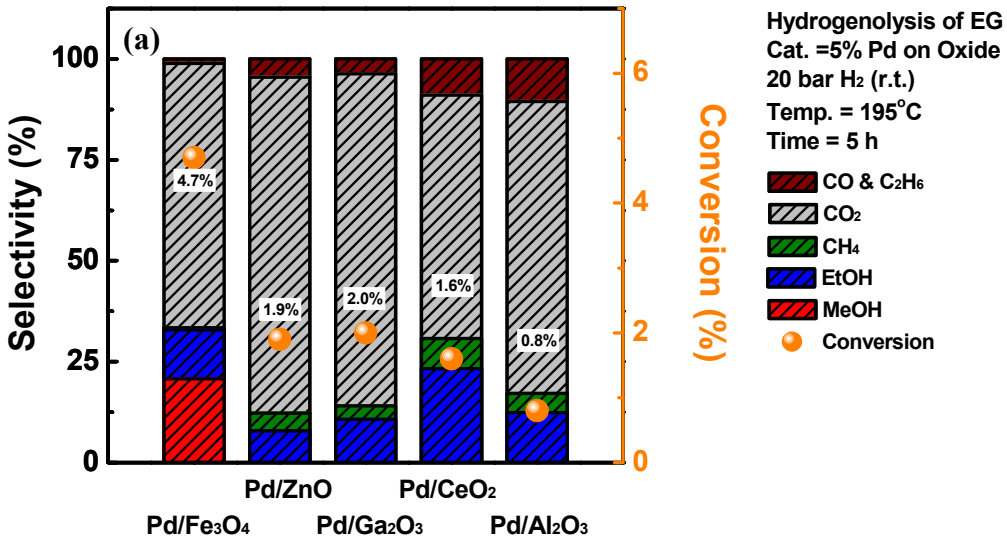
*The lower coordination number errors were due to statistical errors in the phase shifts being non-perfect and limitations in the spherical electron wave calculation, whereas a greater uncertainty of ± 0.5 atom is expected.

5.5 CATALYTIC TESTING

5.5.1 HYDROGENOLYSIS OF ETHYLENE GLYCOL

As shown in Fig. 5-11a, the conversion of ethylene glycol in aqueous solution is generally low over all Pd containing catalysts under a high pressure of hydrogen, presumably because the metal surface is primarily covered with water molecules and adsorbed hydrogen (this will later be confirmed by kinetics study). However, once ethylene glycol is activated on the surface, the main product is carbon dioxide (C-C bond cleavage followed by C-O bond formation). Various activities for ethanol production from the hydrogenolysis of ethylene glycol (C-O bond cleavage followed by C-H formation) were observed for the different samples. It is interesting to note that highly dispersed Pd (no visible Pd peak from XRD) on iron oxide was the only sample which showed discernible activity for methanol production (C-C cleavage followed by C-H formation), but with little methane formation. The other samples, ZnO, Ga_2O_3, CeO_2, and Al_2O_3, containing larger sizes of Pd particles (Pd peaks were visible by XRD) on other oxide supports yielded no methanol (and small quantity of ethanol), but with a good degree of methane production. In addition, we always get finer Pd particles when we are working with iron oxide than when we work with the other oxides under identical preparation conditions for the co-precipitation process. Perhaps, an extremely well-dispersed Pd (only can be seen on Fe_3O_4) acted as the active site, providing higher adsorption energy to the substrate for breaking C-C bond. Thus, iron oxide appears to be the essential component for methanol production. We then screened a number of metals supported on iron oxide produced by co-precipitation. As shown in Fig. 5-11b, the two most promising catalysts Rh/Fe_3O_4 and Pd/Fe_3O_4 showed relatively high selectivity towards the lower alcohols (methanol and ethanol). However Rh, being a metal of stronger adsorptive properties than Pd

according to its d-band centre position,[26-27] gave higher conversion but with methane as the primary product. It is noted that metals with stronger intrinsic adsorptive properties are well known to catalyse methane production from hydrocarbons/alcohols with exhaustive hydrogenolysis on their surface.[28] The combination of small Pd particles and iron oxide clearly demonstrates a synergetic effect for the production of methanol and ethanol as meta-stable products, surprisingly giving higher selectivity with prolonged testing time in our batch reactor configuration.



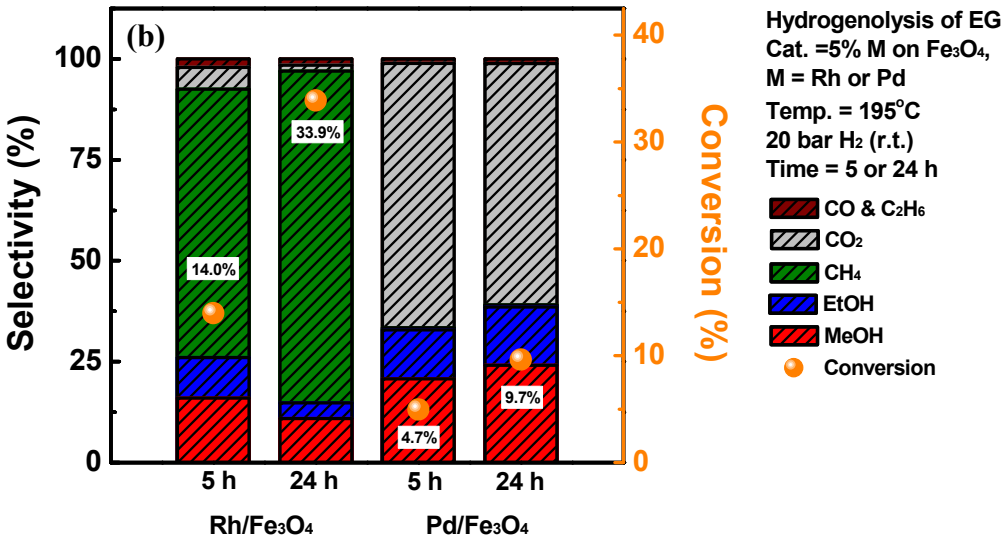


Fig. 5-11 (a) Catalytic performances of 5% Pd supported on different oxides (prepared by co-precipitation) for hydrogenolysis of ethylene glycol (pure 4.0 nm Pd and 4.6 nm PdFe showed no activity for alcohol production); (b) Comparison of 5% Pd and 5% Rh on iron oxide for hydrogenolysis of ethylene glycol.

Fig. 5-12a shows a further improvement in cumulative selectivity to over 50% for the two lower alcohols after the catalyst was tested in a batch reactor for 72 h. Time-fraction analysis in Fig. 5-12b clearly suggests the catalyst initially gave higher ethylene glycol conversion but was mainly selective for CO_2. But, within the period of 24 to 72 h, at least 80% selectivity (with methanol selectivity >50%) towards the two lower alcohols was achieved at about 4.3% conversion. The CO_2 produced during the reaction could be due to the aqueous reforming reaction of ethylene glycol ($C_2H_6O_2 + 2H_2O \rightarrow 2CO_2 + 5H_2$) under our reaction conditions[2, 29]. On the other hand, ethylene glycol may reduce surface iron oxide in the presence of Pd. Our evidence suggests the latter reaction plays an important part in the initial production of large quantities of CO_2. We thus conclude there must be a deep reduction of Pd/Fe_2O_3 by ethylene glycol (self-oxidised to CO_2) assisted by Pd to give PdFe nanoparticles and clusters during the induction period which accounts for the poor initial alcohol selectivity. Extensive reduction of Fe_2O_3 by hydrogen should not take place under our pre-reduction or testing conditions.[30]

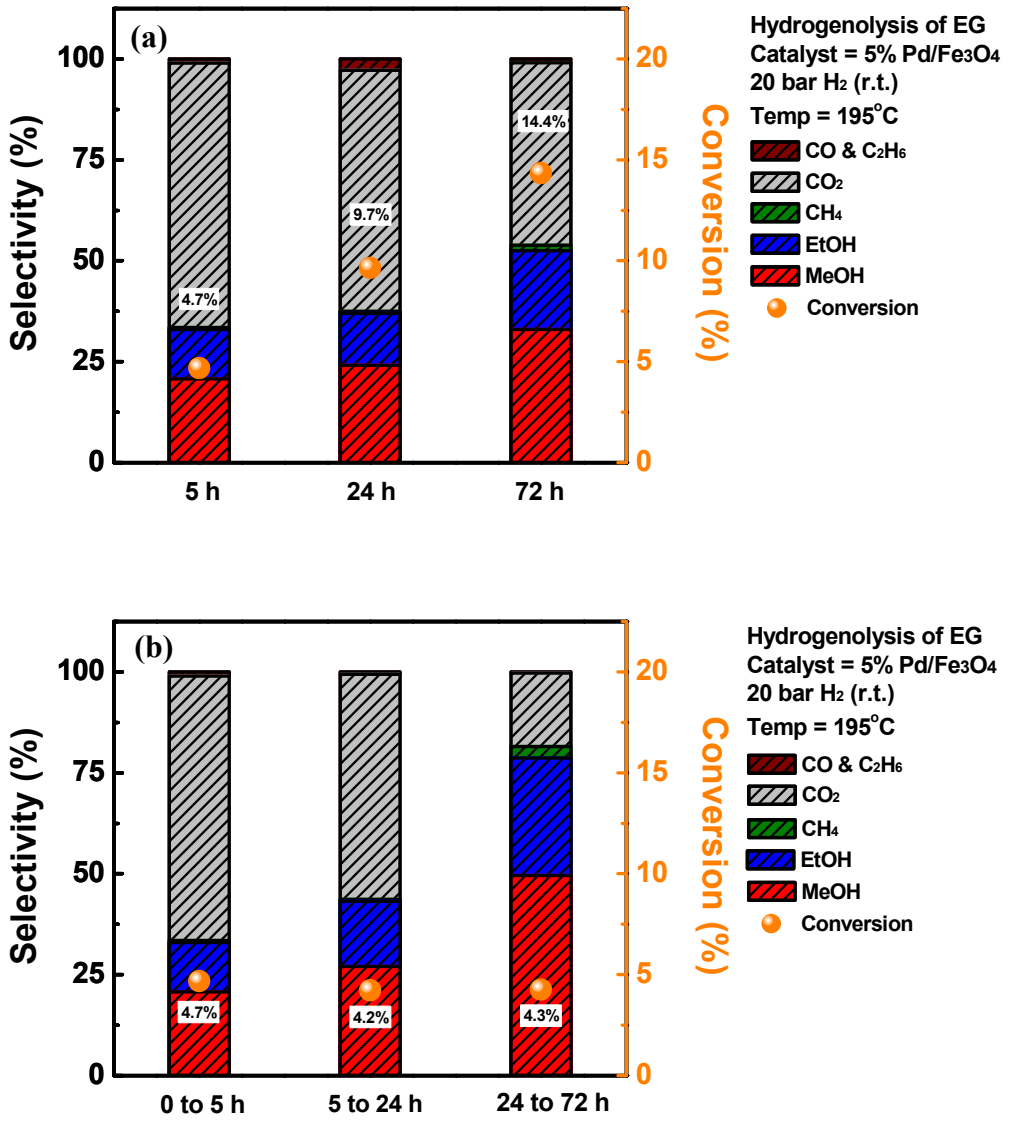


Fig. 5-12 (a) Change of gross selectivity over 5% Pd/Fe_2O_3 versus time in batch-wise hydrogenolysis of ethylene glycol; (b) Time-fraction selectivity over 5% Pd/Fe_2O_3 at different periods in batch-wise hydrogenolysis of ethylene glycol.

Fig. 5-13 shows catalytic performance for re-testing of the used sample, which confirms the catalyst indeed required an initial long induction period for extensive reduction to reach a steady state in order to achieve high alcohol selectivity. Once it was conducted, the catalyst became selective without the need for any further induction. Also, when the catalyst was pre-reduced in hydrogen for a longer duration

(72h) or at a higher temperature, the alcohol selectivity immediately reached a steady state of above 75% with no additional induction. The optimum temperature was around 195 ^{o}C, and gives the same alcohol yield with repeated testing. On the other hand, a significant decrease in alcohol selectivity was observed when repeated testing was carried out at a higher temperature of 215 ^{o}C. This may suggest these highly dispersed PdFe were susceptible to sintering, resulting in reduced activity for alcohol production.

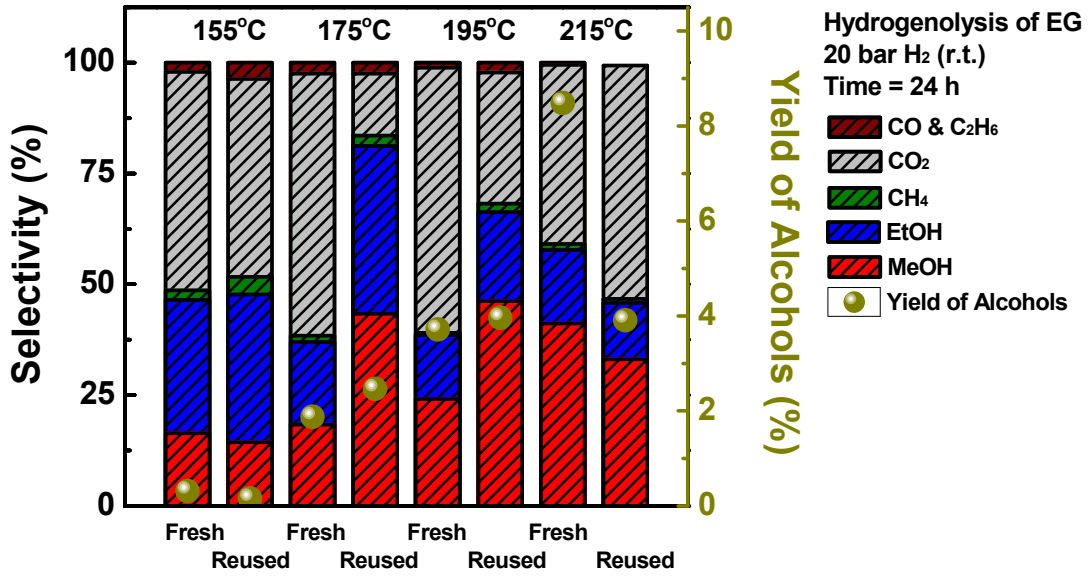


Fig. 5-13 Catalytic performance for hydrogenolysis of ethylene glycol over fresh (pre-reduced in H_2 at 200 ^{o}C for 1 h) and spent Pd catalysts under different temperatures.

As far as we are aware, decent conversion of ethylene glycol or related polyols to lower alcohols, especially to methanol at high selectivity, has not been reported before this work. At present, the methanol/ethanol ratio obtained is above 2:1 and the methanol selectivity could be optimised further. However, for fuel applications there may be no need to separate the two alcohols. The superb catalytic selectivity for this

reaction clearly reflects the unusual behaviour of Pd/Fe_3O_4. It is important to investigate the reason(s) for the interesting metal-support interaction observed in yielding methanol at prolonged induction time.

Furthermore, it is interesting to investigate the mechanism of ethylene glycol hydrogenolysis by combining the effects of metal dispersion/particle size and catalytic performance as shown in Fig. 5-14. Here, there is no obvious change in methanol selectivity when the loading of Pd metal increases from 1 wt% to 20 wt%, while the corresponding CO uptake value increases 2.5 times and the size of Pd increased 3.75 times (Table 5-1). This shows the Pd/Fe_3O_4 active site for breaking C-C bonds is not be affected by the changing Pd particle size or, more specifically, that the active site for methanol production is not on the Pd particle, but PdFe. On the other hand, a step change in ethanol selectivity (the major product of C-O cleavage) of 60.1% was seen over the 20% Pd/Fe_3O_4 where the Pd particle size increased to 10.1 nm (CO chemisorption for the sample pre-reduced at 40 ^oC given in Table 5-1), suggesting C-O cleavage took place on terrace sites of Pd or PdFe. The XRD also agrees well with the size change for Pd (ca. 6 nm calculated from the Scherrer equation) in the 20% Pd/Fe_3O_4.

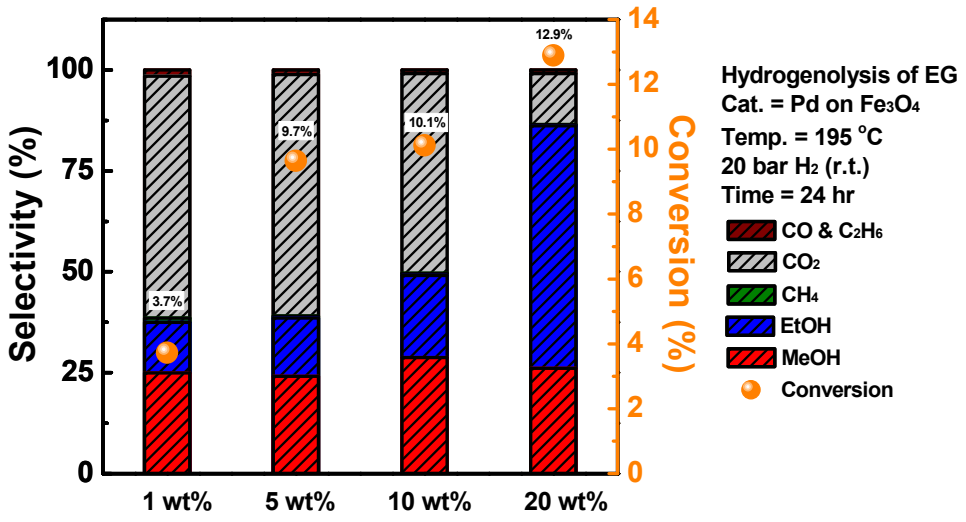


Fig. 5-14 Catalytic performance for hydrogenolysis of ethylene glycol over Pd/Fe_3O_4 with different Pd metal loadings.

The corresponding methanol productivities per gram of catalyst and per gram of Pd over Pd/Fe_3O_4 with different Pd metal loading (ranging from 1 to 20%) were calculated based on the results from Fig. 5-15 and are listed in Table 5-3. An inverse relationship between specific catalytic activity (second column in Table 5-3) and increased metal loading was observed, indicating a lower dispersion of Pd (surface Pd) on iron oxide was obtained at higher loading. This trend corresponds well with the measured CO uptake. Not surprisingly, the catalysts (1% Pd loading) with highest Pd dispersion demonstrated the highest catalytic activity for methanol production, producing 3.1 mmol of methanol per gram of Pd metal per hour. Although PdFe has been identified as the active site for methanol production in the hydrogenolysis of ethylene glycol, there was no characterisation technique available to quantify the number of PdFe active sites or PdFe effective surface area on the Pd/Fe_3O_4 catalyst. Thus, the turn over frequency (mmol of methanol production / metal surface area / unit time) for the catalyst could not be obtained.

Table 5-3 Specific catalytic activity and per gram based catalytic activity for the hydrogenolysis of ethylene glycol over Pd/Fe_3O_4 with different Pd metal loadings.

Catalysts	Specific catalytic activity (mmol of ethylene glycol converted · g metal catalyst^{-1} · h^{-1})	Catalytic activity per gram catalyst (mmol of methanol produced · g catalyst^{-1} · h^{-1})	Catalytic activity per gram Pd (mmol of methanol produced · g Pd^{-1} · h^{-1})
1% Pd/Fe_3O_4	7.933	0.031	3.10
5% Pd/Fe_3O_4	4.105	0.076	1.52
10% Pd/Fe_3O_4	2.153	0.092	0.92
20% Pd/Fe_3O_4	1.371	0.133	0.66

5.5.2 METAL-SUPPORT INTERACTION: A MECHANISTIC STUDY OF C-C AND C-O BOND CLEAVAGE

In previous sections, we reported a unique metal-support interaction within a Pd/Fe_3O_4 sample prepared by co-precipitation at controlled pH in aqueous solution. The catalyst was extensively characterised using XRD, TPR, TEM, STEM, XPS, CO chemisorption and EXAFS. All evidence suggests atomically dispersed Pd in a sol-gel like matrix formed during the co-precipitation step can be chemically "glued" to bulk Fe-O-Fe networks. Upon controlled reduction, we showed this material can produce a supported metal phase with extremely high dispersion, ranging from small metal PdFe clusters (sub-nano) down to individual atoms, on a defective iron oxide surface with strong metal-support interaction even after heat treatments. As a result, ethylene glycol can be converted to methanol and ethanol over this catalyst surface.

Although an active catalyst for methanol production from ethylene glycol has been demonstrated, the elementary step(s) of ethylene glycol conversion to methanol are not clear. We will thus refocus our study toward understanding these steps in

order to selectively control the relative cleavage of C-C and C-O bonds in ethylene glycol hydrogenolysis. It is known that an alteration in general metal electronic structure (i.e. different in the d-band centre position, please refer to appendix) can induce different degrees of adsorptive strengths for a substrate, resulting in conversion to a range of products. Accordingly, a range of metals supported on iron oxide, including Ni, Rh, Pd, Pt and Ag, were synthesised in an identical manner and tested for this reaction.

As seen in Fig. 5-2, amorphous Fe_2O_3 phases were observed in all supported metal catalysts after calcination and no corresponding metal peaks were identified from XRD after reduction (Fig. 5-2b). The conversion of ethylene glycol over the supported metal catalysts is generally small (Fig. 5-15), except for Rh/Fe_3O_4 which gave a conversion of 33.9%.

It is well accepted that the d-band centre position of a metal affects the degree of substrate molecule adsorption, where the higher the d-band centre, the stronger the adsorption.[26-27] By plotting the product selectivities against d-band centre position (Fig. 5-16), three volcano relationship curves (methane, methanol and ethanol) are clearly observed. As the d-band centre positions of Ni and Rh are higher than for other metals, they have stronger predicted adsorption strengths. It is indeed seen that these two metals produce methane and carbon dioxide as the main products due to extensive hydrogenolysis of C-C and C-O. Although Ni was expected to give the highest ethylene glycol conversion and methane selectivity due to its d-band position, the results do not support this assertion. We attribute this to the smaller quantity of Ni particles produced from the stable $NiFe_2O_4$ spinel structure precursor as previously discussed. In order to obtain methanol as the partial hydrogenolysis product, the catalyst must possess an appropriate adsorptive strength in order to cleave only the C-

C bond but not the C-O bond before hydrogenation. Indeed, Fig. 5-16 shows the intermediate d-band centre position of Pd relative to the five metal/iron oxide catalysts can provide proper adsorptive energy for the hydrogenolysis of ethylene glycol to methanol with simultaneous C–C bond cleavage and C–H formation (as illustrated in Fig. 5-17). For a metal surface with a lower d-band centre position and weaker adsorptive properties, such as Pt, the activity for C-C bond cleavage is not strong, and as a result, the catalyst only allows for the selective cleavage of the C-O bond followed by hydrogenation to produce ethanol (C–O cleavage followed by C–H formation). In the case of Ag with the lowest d-band centre position, its adsorptive ability is so weak that there is almost no catalytic activity for ethylene glycol conversion. We proposed the correlation between activity/selectivity of metal catalysts with d-band centre position can provide a clear direction for selective C-C and C-O cleavages in bio-fuel conversion.

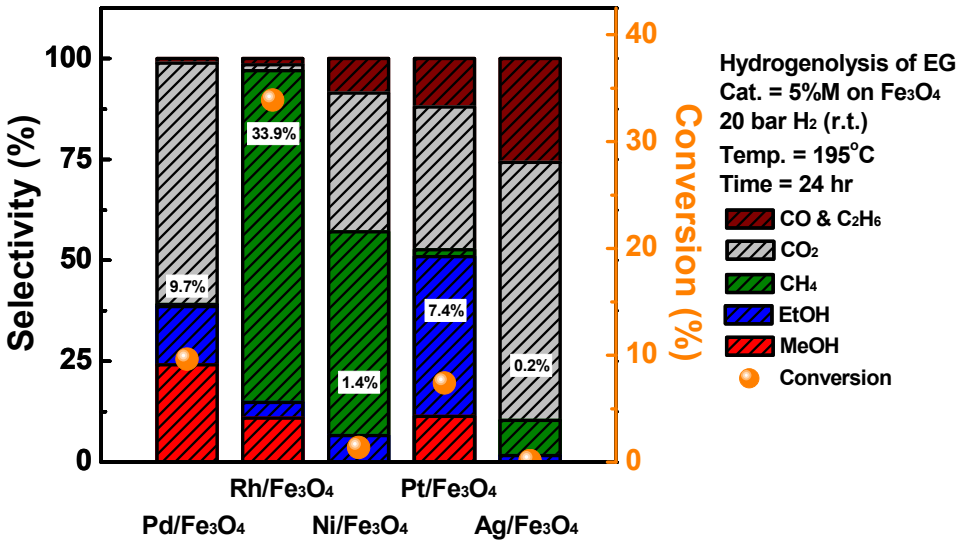


Fig. 5-15 Plot of selectivities for ethylene glycol hydrogenolysis over different metal catalysts supported on iron oxide.

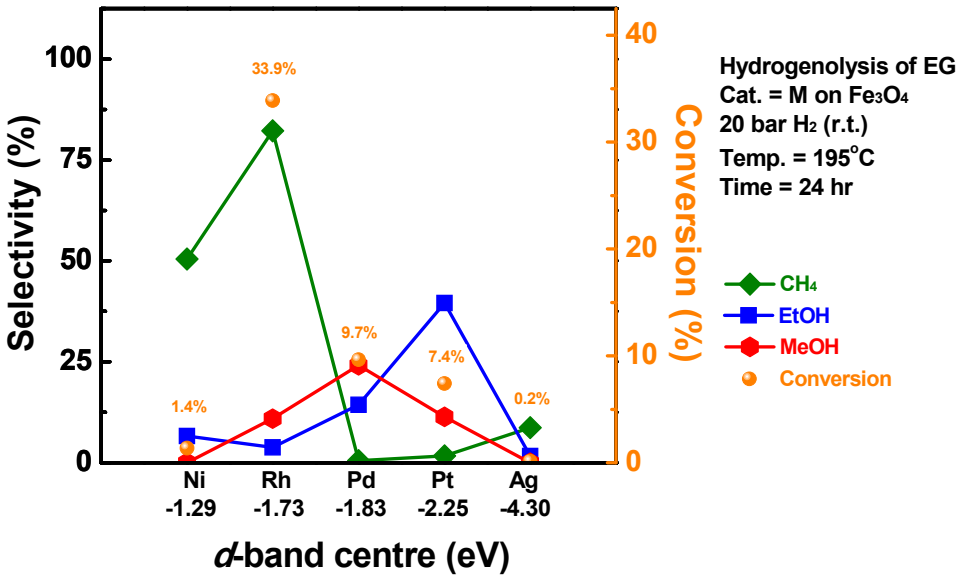


Fig. 5-16 Plot of selectivities for ethylene glycol hydrogenolysis over different metal catalysts (supported on iron oxide). A volcano relationship between product selectivity and *d*-band centre position can be clearly seen.

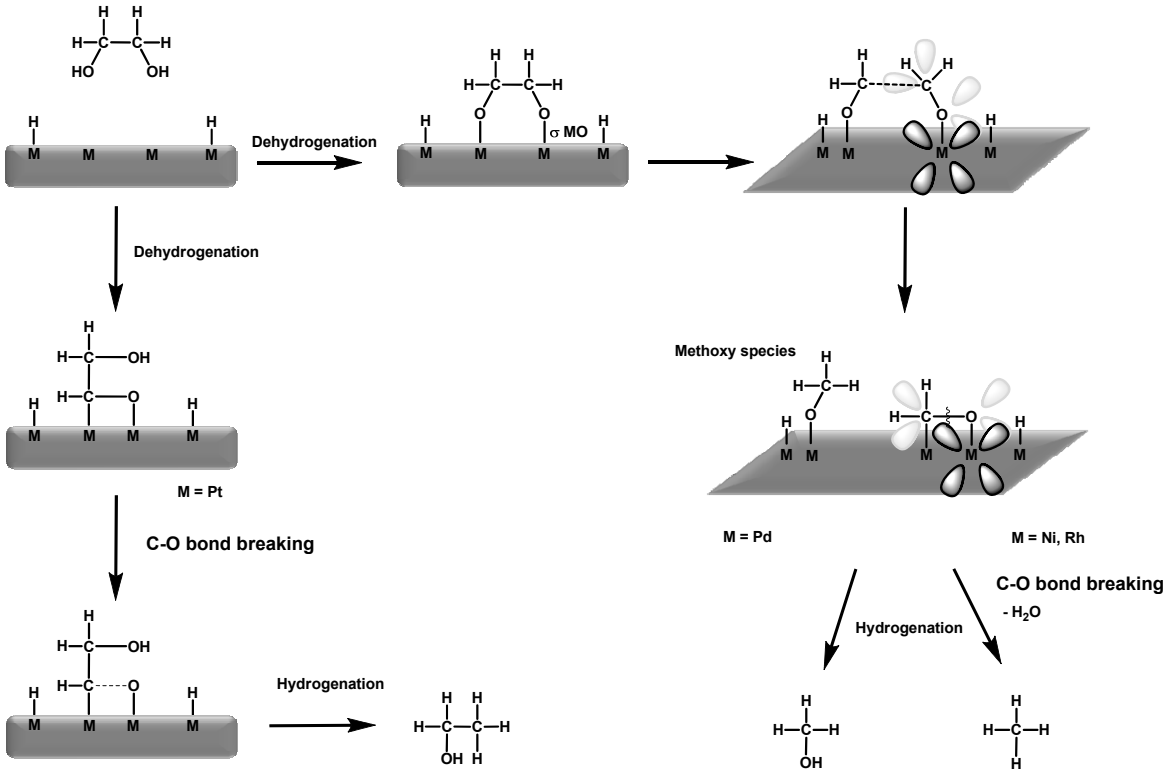


Fig. 5-17 A schematic diagram describing the adsorbed ethylene glycol for the hydrogenolysis of ethylene glycol on a transition metal M.[31]

5.5.3 KINETICS STUDY

In previous sections 5.5.1 and 5.5.2, we identified an effective Pd/Fe_3O_4 catalyst for the hydrogenolysis of ethylene glycol to methanol. The effects of Pd particle size, oxide support and different doping metals on iron oxide catalysts were examined. Although the proposed reaction for methanol production is thermodynamically feasible, the knowledge of kinetics for this catalysed reaction is rather limited. However, it is of significant importance if we want to further evaluate this process for economic viability. It is well known that reaction kinetics are influenced by various parameters, such as temperature, pressure, substrate concentration, etc.[32] It is generally understood that if a catalytic reaction is governed by diffusion (mass transport) limitation, its apparent activation should be less than 25 kJ mol^{-1}, indicating the reactant diffuses slowly from the bulk phase through the boundary layer to the external catalyst surface. Higher apparent activation energy (> 25 kJ mol^{-1}) implies the reaction is governed by a truly chemical step.

The reaction for methanol production from the hydrogenolysis of ethylene glycol is given by Eq. 5-1.

$$C_2H_6O_2 + H_2 \rightleftharpoons 2CH_3OH \qquad \text{Eq. 5-1}$$

A kinetic study on the rate of methanol production as a function of ethylene glycol concentration and hydrogen pressure was therefore carried out. The rate equation is given by Eq. 5-2,

$$r = \frac{d[CH_3OH]}{dt} = k\,[C_2H_6O_2]^{m} \cdot [H_2]^{n} \qquad \text{Eq. 5-2}$$

where k is the rate constant for this reaction. The rate constant is independent of substrate concentration (concentration of ethylene glycol or pressure of hydrogen in our case) but dependent upon reaction temperature. As a result, the rate constant for our batch reactor configuration is derived at 195 ^{o}C for 24 h. Fig. 5-18a clearly shows

an increase in hydrogen pressure results in a decrease in methanol production. According to Henry's Law, the availability of dissolved hydrogen in solution depends linearly on the applied pressure. This result suggests the H_2 substrate could be a limiting factor such that ethylene glycol and hydrogen may compete for the same metal sites. At elevated H_2 pressures, the rate of methanol production from ethylene glycol is greatly suppressed (n = -1). On the other hand, there is a linear relationship between activity and ethylene glycol concentration (m = +1), as shown in Fig. 5-18b. Linear fitting for the ln *k* vs 1/T plot gave a slope of $-E_a/R$, where R is the gas constant equal to 8.314 J K^{-1} mol^{-1}. The apparent activation energy for methanol production is determined to be 96 kJ mol^{-1} according to the Arrhenius plot presented in Fig. 5-18c. This high activation energy clearly suggests there is no mass transport limitation in the hydrogenolysis of ethylene glycol to methanol over Pd/Fe_3O_4. This is consistent with the temperature study where a rise in temperature gives an exponential enhancement in rate for methanol production.

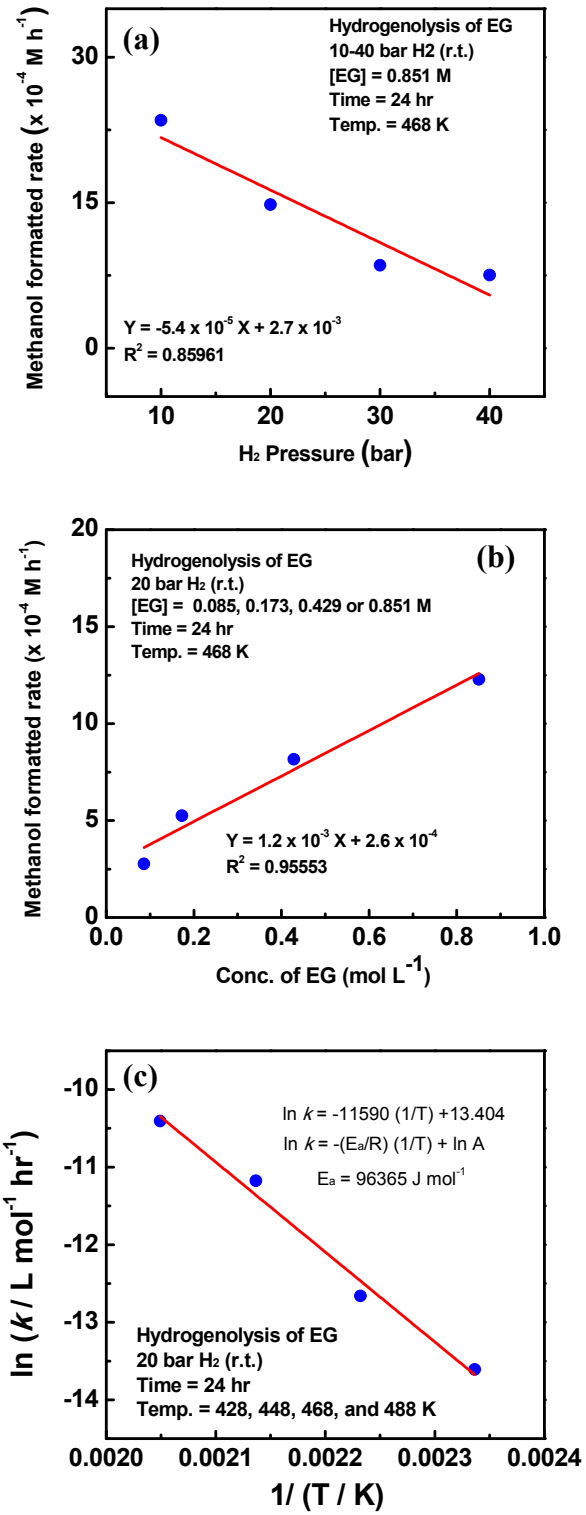


Fig. 5-18 A kinetic study to evaluate the orders of reaction with respect to substrates with derived apparent activation energy over Pd/Fe_3O_4: (a) A plot showing the decrease in methanol production at increasing hydrogen pressure; (b) A plot showing the increase in methanol production at increasing ethylene glycol concentration; (c) A plot of ln *k* against 1/T for the Pd/Fe_3O_4 catalyst.

5.6 DISCUSSION

This work clearly demonstrates that methanol can be synthesised with high selectivity at moderate conversion by the direct hydrogenolysis of biomass derived ethylene glycol over Pd/Fe_3O_4, opening up a new pathway for activation of other carbon-containing resources (biomass and oil) from natural gas using the syn-gas route. From a mechanistic viewpoint, conversion of ethylene glycol to methanol or ethanol requires C-C or C-O bond breakage with C-H formation over the catalytically active site(s) on Pd/Fe_3O_4 in a highly cooperative and concerted manner, otherwise extensive surface adsorption and degradation of the substrate and intermediates on large metal catalyst surfaces will lead to the more thermodynamically stable CO_2 or CH_4 formation.[15] It is important to eliminate or substantially reduce the formation of these stable products through the use of extremely well-dispersed Pd containing clusters/atoms. We observe that a Pd/Fe_3O_4 catalyst prepared by simple co-precipitation displays an unusual material interaction, long described as a 'strong metal-support interaction', which could not be achieved by other oxides. Our evidence suggests the formation of extremely dispersed PdFe clusters and adatoms on iron oxide surface during catalysis. Their presence undoubtedly indicates a degree of chemical species exchange and reconstruction at the interface between the metal and oxide support, giving a kind of 'chemical definition' of this metal-support interaction. The observed atomic levels of dispersion on iron oxide are surprising given the various heat pre-treatments. It is believed a sol-gel like chemistry, through hydrolysis and cross condensation during the co-precipitation of iron and palladium nitrates, plays a crucial role in the dispersion,[33] as shown in Fig. 5-4. However, C-C bond in ethylene glycol cannot easily be broken over other oxides due to relatively larger Pd particles (Fig. 5-1). Moreover, the formation of small but catalytically active PdFe

clusters at high surface concentration can offer enhanced activity/selectivity due to electronic modification of the Pd band-like structure.[26, 34] The thermal refractory nature of the alloy clusters can also reduce their surface mobility under our moderate testing conditions, otherwise large particles would have been obtained. The formation of these small PdFe clusters or sub-nanoparticles is expected to be extremely important for methanol production in the new synthetic step. Recent DFT calculations clearly suggest the kinetic adsorption of C-O bonds from ethylene glycol are more favourable than both C-H and C-C adsorptions over extended (111) metal surfaces.[15] The bidentate nature of adsorbed ethylene glycol forces the C-O bonds into an angle more perpendicular to the plane of the surface than is seen for C-O bonds in the case of monoalcohols on a flat metal surface. This facilitates activation of C-O bonds but destabilises the approach of α H in C-H or α C in C-C at the other end of the molecule to the terrace metal sites, giving undesirable cleavages. On the other hand, relaxation of the steric constraints on small clusters/sub-nano metals would therefore facilitate C-C activation, leading to scissoring of the molecule followed by C-H formation to methanol on their low coordination sites. In addition, surface oxygen vacancies are expected to be formed simultaneously with Fe^{3+} reduction in close proximity to the formed PdFe clusters from the support surface (refer to the TPR) due to the maintenance of electrical neutrality, which will assist adsorption of ethylene glycol.[35] Since ethylene glycol is the simplest representative of biomass-derived polyols, selective cleavage of C-C in other biomass molecules to form methanol over the small surface PdFe clusters could be achieved. In light of this work it would be interesting to investigate the recently reported 'special metal-support interactions' of Au and Ag clusters on a wide range of exciting catalysis in literature.[14, 36-37]

5.7 CONCLUSION

In conclusion, we report a *new* process for catalytic production of methanol over Pd/Fe_3O_4 with a strong and unique metal-support interaction. Further studies are warranted to optimise methanol productivity and evaluate catalyst stability under industrially applicable conditions, but this novel catalytic capability has the potential to open up a new route for converting other carbon containing natural resources to methanol apart from the established natural gas process *via* the syngas route. As a result, ethylene glycol produced from oil, coal and especially biomass with its stronger environmental incentives, can be used to produce this strategically important chemical. In addition, the combined selectivity to methanol/ethanol of 80% with the rest of CO_2 and H_2 co-products from aqueous reforming may also allow reduction or elimination of the need for expensive hydrogen gas input (hydrogen is balanced for this product distribution), rendering the catalytic process promising at this stage.

Finally, although the presently high cost of ethylene glycol does not support this new methanol synthesis route, the price of a chemical and feasibility of a synthetic route are based on the market pull and availability of new science and technology. For example, the traditional route to produce ethylene glycol from oil cracking via ethylene is becoming more expensive with dwindling oil supplies. As a result, this has triggered recent developments of some new processes including a new syn-gas route to ethylene glycol, coal-based production of ethylene glycol, and new renewable processes based on biomass. There is evidence that the demand for methanol as both fuel and platform chemical will become higher in the future regarding energy security and environment, which may form a further market pull for the conversion of ethylene glycol to methanol.

5.8 REFERENCES

1. D. E. Bloom, *Science*, 2011, **333**, 562-569.
2. R. D. Cortright, R. R. Davda and J. A. Dumesic, *Nature*, 2002, **418**, 964-967.
3. G. A. Olah, *Angew Chem Int Edit*, 2005, **44**, 2636-2639.
4. J. Tollefson, *Nature*, 2011, **473**, 134-134.
5. H. R. Yue, Y. J. Zhao, X. B. Ma and J. L. Gong, *Chem Soc Rev*, 2012, **41**, 4218-4244.
6. CCM Data & Business Intelligence. (2013). Retrieved November 05, 2013, from http://www.cnchemicals.com/PressRoom/PressRoomDetail_c_925.html.
7. R. E. Osterhout, P. Pharkya, and A. P. Burgard, *United States Pat. Appl.*, 20110312049, 2011.
8. N. Ji, T. Zhang, M. Y. Zheng, A. Q. Wang, H. Wang, X. D. Wang and J. G. G. Chen, *Angew Chem Int Edit*, 2008, **47**, 8510-8513.
9. B. T. Qiao, J. Zhang, L. Q. Liu and Y. Q. Deng, *Appl Catal a-Gen*, 2008, **340**, 220-228.
10. L. Machala, R. Zboril and A. Gedanken, *J Phys Chem B*, 2007, **111**, 4003-4018.
11. C. H. Yu, C. C. H. Lo, K. Tam and S. C. Tsang, *J Phys Chem C*, 2007, **111**, 7879-7882.
12. C. W. A. Chan, Y. L. Xie, N. Cailuo, K. M. K. Yu, J. Cookson, P. Bishop and S. C. Tsang, *Chem Commun*, 2011, **47**, 7971-7973.
13. B. T. Qiao, A. Q. Wang, X. F. Yang, L. F. Allard, Z. Jiang, Y. T. Cui, J. Y. Liu, J. Li and T. Zhang, *Nat Chem*, 2011, **3**, 634-641.
14. X. F. Yang, A. Wang, B. Qiao, J. Li, J. Liu and T. Zhang, *Acc Chem Res*, 2013.

15. M. Salciccioli, W. T. Yu, M. A. Barteau, J. G. G. Chen and D. G. Vlachos, *J Am Chem Soc*, 2011, **133**, 7996-8004.

16. K. Noack, H. Zbinden and R. Schlogl, *Catal Lett*, 1990, **4**, 145-156.

17. A. D. Romig and J. I. Goldstein, *Metall Trans A*, 1978, **9**, 1599-1609.

18. S. L. Zhang and J. R. Zhang, *Phys Status Solidi B*, 1994, **182**, 421-427.

19. M. P. Felicissimo, O. N. Martyanov, T. Risse and H. J. Freund, *Surf Sci*, 2007, **601**, 2105-2116.

20. NIST X-ray Photoelectron Spectroscopy Database 20, V. 4.1, 2012.

21. N. Mahata and V. Vishwanathan, *J Catal*, 2000, **196**, 262-270.

22. X. Y. Zhang, E. Y. Long, Y. L. Li, L. J. Zhang, J. X. Guo, M. C. Gong and Y. Q. Chen, *J Mol Catal a-Chem*, 2009, **308**, 73-78.

23. J. R. Anderson, *Structure of metallic catalysts*, Academic Press, London ; New York, 1975.

24. G. Agostini, R. Pellegrini, G. Leofanti, L. Bertinetti, S. Bertarione, E. Groppo, A. Zecchina and C. Lamberti, *J Phys Chem C*, 2009, **113**, 10485-10492.

25. F. Boccuzzi, E. Guglielminotti, F. Pinna and M. Signoretto, *J Chem Soc Faraday T*, 1995, **91**, 3237-3244.

26. A. Ruban, B. Hammer, P. Stoltze, H. L. Skriver and J. K. Norskov, *J Mol Catal a-Chem*, 1997, **115**, 421-429.

27. K. Tedsree, C. W. A. Chan, S. Jones, Q. A. Cuan, W. K. Li, X. Q. Gong and S. C. E. Tsang, *Science*, 2011, **332**, 224-228.

28. R. Burch and A. R. Flambard, *J Catal*, 1982, **78**, 389-405.

29. J. W. Shabaker, G. W. Huber, R. R. Davda, R. D. Cortright and J. A. Dumesic, *Catal Lett*, 2003, **88**, 1-8.

30. G. Neri, A. M. Visco, S. Galvagno, A. Donato and M. Panzalorto, *Thermochim Acta*, 1999, **329**, 39-46.

31. E. P. Maris, W. C. Ketchie, M. Murayama and R. J. Davis, *J Catal*, 2007, **251**, 281-294.

32. G. C. Bond, *Heterogeneous catalysis : principles and applications*, 2nd edn., Clarendon Press, Oxford, 1987.

33. IUPAC-NIST Solubility Database, V., NIST Standard Reference Database 106, 2007.

34. J. R. Kitchin, J. K. Norskov, M. A. Barteau and J. G. Chen, *Phys Rev Lett*, 2004, **93**.

35. T. L. Chen and D. R. Mullins, *J Phys Chem C*, 2011, **115**, 13725-13733.

36. M. D. Hughes, Y. J. Xu, P. Jenkins, P. McMorn, P. Landon, D. I. Enache, A. F. Carley, G. A. Attard, G. J. Hutchings, F. King, E. H. Stitt, P. Johnston, K. Griffin and C. J. Kiely, *Nature*, 2005, **437**, 1132-1135.

37. Y. Lei, F. Mehmood, S. Lee, J. Greeley, B. Lee, S. Seifert, R. E. Winans, J. W. Elam, R. J. Meyer, P. C. Redfern, D. Teschner, R. Schlogl, M. J. Pellin, L. A. Curtiss and S. Vajda, *Science*, 2010, **328**, 224-228.

CHAPTER 6 – OXIDATION OF METHANE FOR HYDROGEN AND CARBON DIOXIDE PRODUCTION

CHAPTER 6 – OXIDATION OF METHANE FOR HYDROGEN AND CARBON DIOXIDE PRODUCTION 179

6.1 INTRODUCTION 180

6.2 OBJECTIVES 184

6.3 CHARACTERISATIONS OF CATALYSTS 185

6.3.1 PXRD 185

6.3.2 TPR 186

6.3.3 STEM 189

6.4 THERMODYNAMIC CALCULATIONS 190

6.5 CATALYTIC TESTING 193

6.5.1 Rh ON Fe_2O_3 193

6.5.2 OTHER METALS ON Fe_2O_3 197

6.5.3 Rh ON OTHER OXIDE SUPPORTS 198

6.5 DISCUSSION 201

6.6 CONCLUSION 205

6.7 REFERENCES 206

6.1 INTRODUCTION

Methane is the main component of natural gas and considered one of the notorious greenhouse gases. A high level of methane emission or leakage from oil or gas field can seriously threaten our living environment.[1] On the other hand, the total reserve of natural gas in our world is quite abundant when compared to oil (Fig. 6-1).[2] However, gaseous methane itself is not convenient for storage or transportation, especially for direct fuel applications. As a result, a new catalytic technology to utilise methane to substitute petrol has been regarded for a long time as an important area of research. Methanol, synthesised from methane, has been regarded as a perfect candidate as according to the Nobel Laureate, George Olah.[3-4] There are several natural resources, such as coal and biomass, the carbon of which can also be used for the methanol production, but they are more difficult to process than natural gas/methane and the excess of C/H ratios rendering a high carbon emissions. At present, more than 90% of methanol is produced from natural gas. As we discussed in the first chapter, current methanol production process from natural resources undergoes a two-step process which is operated at high pressure and temperature: i) Production of syn-gas (a mixture of CO and H_2) by reforming of methane or gasification of coal/biomass (Eq. 6-1) and ii) Production of methanol from syn-gas (Eq. 6-2).

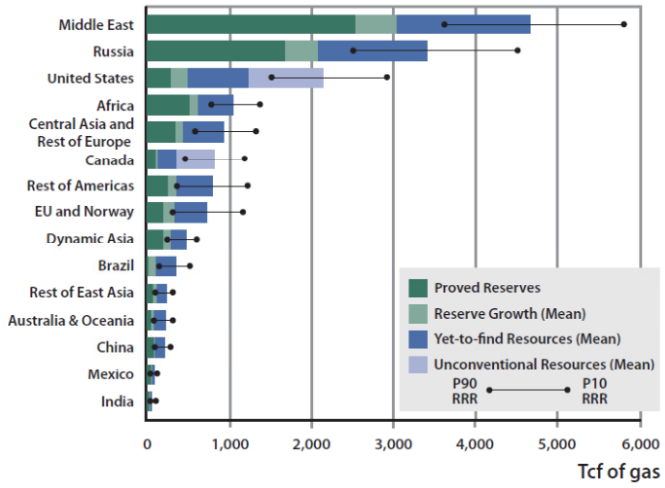


Fig. 6-1 Proved reserves of NG, reserved growth, estimated undiscovered resources, and unconventional resources in the US and elsewhere in the world.[5] Figure reproduced from ref. 5.

$CH_4 + H_2O \rightleftharpoons CO + 3H_2$ ΔG_{298K} = 142 kJ mol^{-1} ΔH_{298K} = 206 kJ mol^{-1} Eq. 6-1

$CO + 2H_2 \rightleftharpoons CH_3OH$ ΔG_{298K} = -29 kJ mol^{-1} ΔH_{298K} = -91 kJ mol^{-1} Eq. 6-2

$CH_4 + \frac{1}{2}O_2 \rightleftharpoons CH_3OH$ ΔG_{298K} = -116 kJ mol^{-1} ΔH_{298K} = -126 kJ mol^{-1} Eq. 6-3

$CH_4 + 2O_2 \rightleftharpoons CO_2 + 2H_2O$ ΔG_{298K} = -801 kJ mol^{-1} ΔH_{298K} = -801 kJ mol^{-1} Eq. 6-4

It has been argued that this two-step process is a thermal-intensive process (Eq. 6-1) and hence is energetically inefficient. For that reason, a question of whether we could produce methanol directly from methane oxidation was posed (Eq. 6-3).[6] The direct oxidation of methane has been in practise for more than hundred years, but the main reaction produces CO_2 and water as the primary products (Eq. 6-4).[7] Decent methanol selectivity was observed only when applying a high pressure (above 100 atm).[8-9] Nevertheless, during the period of 1905 to 1980 less attention was paid on this topic due to the low cost of crude oil and abundant other natural reserves. Moreover, a poor methanol selectivity and activity was obtained over a wide range of materials worldwide from many laboratories.[6-7, 10] Despite a huge research activity in methane activation in 80s there were only few significant improvements reported in

methane conversion and methanol selectivity.[11-13] Presumably, the high dissociation energy of the C-H bond of methane (438 kJ mol^{-1}) than those of C-H (437 kJ mol^{-1}) and O-H (385 kJ mol^{-1}) bonds of CH_3OH renders the methanol product more susceptible to be attacked. Therefore the simultaneous oxidation of methanol is inevitable for the methane activation under the same conditions, leading to the deep oxidation to CO and CO_2. Therefore, a much lower temperature (50 ^oC) was recently employed to oxidise methane by H_2O_2 over supported AuPd nanoparticles.[14] Although the demonstrated activity was very low, (at less than 0.02 % methane conversion) more than 50% selectivity towards methanol was obtained.[14] Although a good knowledge on the mechanism of methane activation has been elucidated, a breakthrough in heterogeneous catalysis for the directly partial oxidation of methane to methanol has not been achieved yet.

Previously attempts have tried to lower the energy input and produce more efficient catalytic approach via bio- and homogeneous catalysis. Biological conversion of methane to methanol has been widely studied.[15-17] Methanotrophs, an important group of methane-oxidising bacteria, digest methane to produce CO_2 through metabolism which produces energy with methanol as the metabolite. Utilising methanotrophs has enabled extracellular methanol to be produced with the concentration of 1 g/L.[18] The active site on methane monooxygenases (MMO) in methanotrophs for methanol production was identified[19] and recently a biomimetic tricopper complex derived from MMO structure has been synthesised and been shown to be an efficient catalyst to oxide methane to methanol at room temperature.[20] For a non-biocatalysis system, Periana et al. employed an organometallic platinum catalyst to catalytically oxidise methane to methanol derivative with more than 70% yield in a sulfuric acid solution.[21] The biological or homogeneous oxidation of

methane to methanol provides a high selectivity towards methanol and can be operated under mild conditions, which sounds an ideal and attractive alternative in terms of energetic point of view. However, a lot of effort is needed regarding how to scale up the current small scale enzymatically catalytic methanol production to an industrial level but maintaining the enzymatic activity.[16] Nevertheless, the employment of an industrially more desirable heterogeneous catalytic system has not yet been successful. Re-examination of existing process and consideration of an alternative approach is thus necessary.

By considering the thermodynamic equilibrium of the system, we propose a new approach. This comprises of two reaction steps, which can provide an overall exothermic practice for methanol production without involving the syn gas route. The two reaction steps are shown as follows (Eqs. 6-5 & 6-6):

$CH_4 + O_2 \rightleftharpoons CO_2 + 2H_2$ ΔG_{298K} = -343 kJ mol^{-1} ΔH_{298K} = -319 kJ mol^{-1} Eq. 6-5

$CO_2 + 3H_2 \rightleftharpoons CH_3OH + H_2O$ ΔG_{298K} = -9 kJ mol^{-1} ΔH_{298K} = -50 kJ mol^{-1} Eq. 6-6

The idea is to activate the methane molecule to give thermodynamically more stable products as CO_2 and H_2 at low temperature without producing syn gas (CO/H_2) at high temperature. These products can be directly used for the feed stream following synthesis of methanol without the large temperature discrepancy between the previous syngas production process and corresponding methanol synthesis. Two anticipated advantages for the process are proposed: firstly, the combined overall reactions are exothermic hence without inputting intensive thermal energy per mole of methanol synthesised. Secondly, methanol synthesis from CO_2 and H_2 has been demonstrated at large scale for commercial applications.

It is well known that the thermal decomposition of methane to produce H_2 is one of the conventional hydrogen production processes (Eq. 6-7)

$CH_4 \rightleftharpoons C + 2H_2$ ΔH_{298K} = 74.4 kJ mol^{-1} Eq. 6-7

Without the assistance of catalysts, it would require a high temperature (high thermal energy input) to achieve a reasonable H_2 yield.[22] Catalytic methane cracking over transition metal catalysts can substantially reduce the reaction temperature down to 500-650 ^oC.[23-26] The process has been identified as a CO/CO_2-free process, which is a benefit for some industries, especially for fuel cell applications, preventing the Pt-based catalyst being poisoned by CO.[27-28] However, inevitable carbon deposition on the surface of catalysts would lead to catalyst deactivation. Therefore, a regeneration process, either by steam-gasification or air oxidation, is required to remove the deposited carbon to regenerate the deactivated catalyst.[29] Previous research revealed that the regenerated catalyst showed a very low activity compared to fresh one.[25] This was attributed to a less active metal phase formed after the regeneration.[30] Recent progress in methane catalytic cracking research has been summarised by a number of publications, which all pointed out that the rapid catalyst deactivation must be overcome to achieve economical competitiveness (methane steam reforming).[28, 31] It is thus promising to combine methane catalytic cracking (Eq. 6-7) and regeneration step into a single catalytic process (Eq. 6-5).

6.2 OBJECTIVES

This chapter is to extend the idea of non-syn-gas approach for methanol synthesis by direct methane oxidation. This aims to demonstrate the possibility of using direct oxidation of methane to CO_2 and H_2, which act as carbon and hydrogen sources for methanol synthesis, with no CO formation over a well-dispersed catalyst at low reaction temperature. A range of co-precipitated synthesis catalysts were therefore prepared for this reaction. It is necessary to use highly dispersed catalysts

for methane activation owing to the fact that methane is quite stable. Supported versions of a similar catalyst (Pd on Fe_2O_3) was extensively characterised as shown in chapter 5 in this thesis. The material was shown to display a unique metal-support interaction for the high dispersion of active metal (Pd) on iron oxide in an atomic scale. Here, we believe the development of a new process to economically convert methane is of high importance. Therefore, selective activation of methane to CO_2 and H_2 over a highly dispersed active metal (Rh) on a Fe_2O_3 support was first attempted.

6.3 CHARACTERISATIONS OF CATALYSTS

6.3.1 PXRD

The average crystallite sizes of metal supported on Fe_2O_3 were examined using PXRD as shown in chapter 5. All samples showed amorphous Fe_2O_3 with no detection of metal phase, indicating well-dispersed metal particles on the iron oxide support. Here we presented the PXRD of a commercial 5% Rh/C catalyst before and after the methane oxidation (Fig. 6-2). Although we observed a slight shift of Rh peak to lower diffraction angle, the severe peak broadening renders the shift almost 'invisible' from the XRD. This shift may suggest a lattice expansion of Rh structure resulting from the deposited carbon produced from methane decomposition.

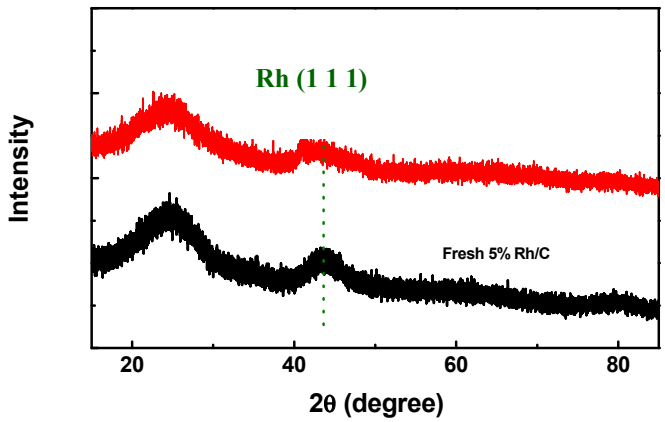


Fig. 6-2 PXRD patterns of the 5% Rh/C catalyst before and after oxidation of methane.

6.3.2 TPR

Fig. 6-3 shows the H_2-TPR profile of a range of Fe_2O_3 supported catalysts calcined at 300 °C in air. It was evident that the TPR pattern of bare Fe_2O_3 (brown curve) showed two reduction steps, consisting of the first reduction peak of Fe_2O_3 to Fe_3O_4 at 300 ^oC and the second peak at 600 ^oC attributed to the reduction of Fe_3O_4 to Fe^o.[32-33] We observed various degrees of peak shifts of the first reduction peak caused by H_2 over the metal doped Fe_2O_3 catalysts, indicating different interactions between the support and metals. In addition, a third peak was observed over some samples (Rh, Ag and Pt) owing to the reduction of introduced metal oxide, such as RhO, AgO and PtO.

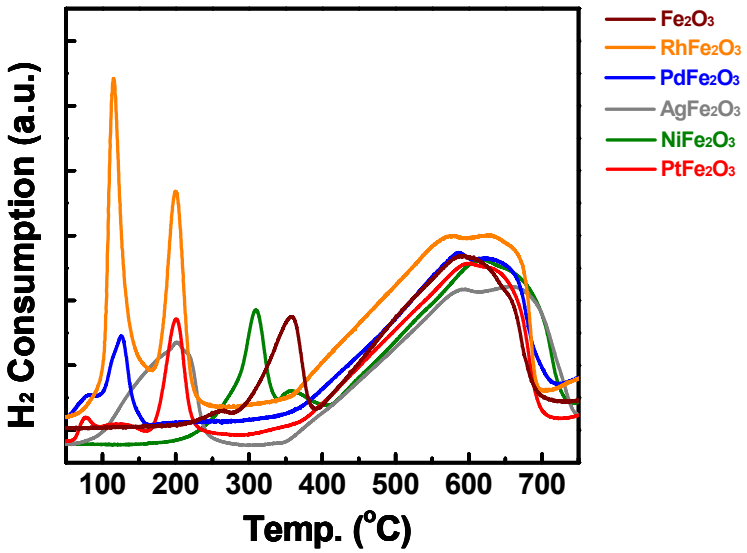


Fig. 6-3 H_2-TPR profiles of calcined Fe_2O_3 and 5% M/Fe_2O_3 (M = Rh, Pd, Ag, Ni or Pt).

A similar study of the methane-TPR was applied for the same batch of preparative catalysts. Fig. 6-4 displays their methane-TPR profiles which enable us to identify the activity of methane cracking over these samples. It is clear that methane displayed a strong reducing power for the iron oxide reduction. For the methane-TPR

pattern over bare Fe_2O_3 (brown), two peaks were observed at 450 and 650 ^oC, corresponding to the reductions of Fe_2O_3 and Fe_3O_4, respectively. The patterns shown in Fig. 6-4 were similar to those exhibited in H_2-TPR. The difference in intensity is due to their difference in thermal conductivity between detecting gases (H_2 or CH_4) and carrier gases (Ar). It is clearly seen that in the methane-TPR pattern there is a negative signal generated after the temperature ramping to 350 ^oC, indicating the production of a new gaseous compound of a high thermal conductivity with respect to Ar over Rh/Fe_2O_3 catalyst (orange curve). Upon reviewing our reactants (5% methane in argon) and the intensity of the signal, production of H_2 gas was concluded due to its highest thermal conductivity (later confirmed by the GC-TCD detector). It is interesting to note that Rh on iron oxide was the only sample that showed an activity for methane cracking. With negative peaks shown after the reduction of rhodium oxide (ca. 350 ^oC) indicative of the methane cracking happening on the surface of Rh metal.[34] The negative peak did not level off before the end of ramping, revealing that the deposited carbon produced by methane cracking did not cover the whole metal surface and the catalyst was not totally deactivated. Thus, the carbon produced from the methane cracking must be somehow oxidised by the catalyst to produce carbon oxides simultaneously. This is consistent with previous reports that Rh catalyst has a low capacity for carbon generation.[35] Additionally, it is evident that Rh is a better dehydrogenation catalyst than Pd, Ag, Cu and Ag according to Fratesi et al.'s calculations.[36] Obviously, CH_4 could be used for the reduction of rhodium and then it would further be decomposed to produce H_2 and carbon oxides on the metal surface. However, a part of generated H_2 could be consumed for the iron oxide reduction (H_2-TPR). In order to obtain a clear profile of methane decomposition/hydrogen

production, a comparative study of methane-TPR profiles over other non-oxide supported metals, including Rh, Ag, and Pd, would be necessary.

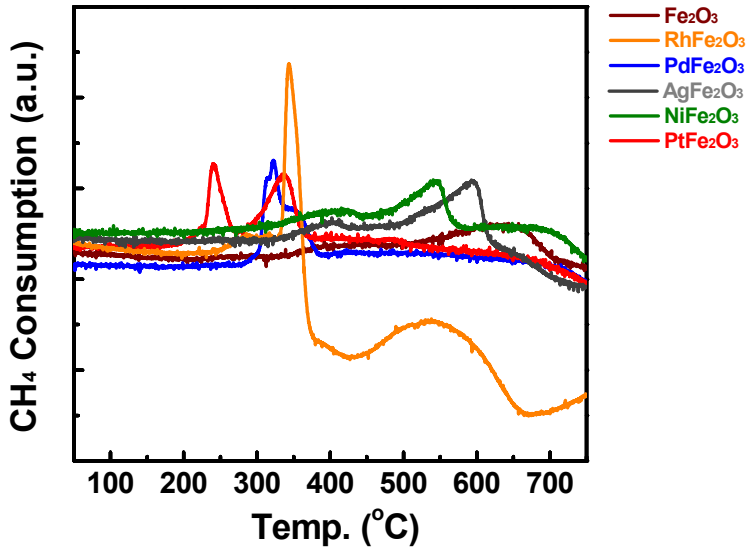


Fig. 6-4 CH_4-TPR profiles of calcined Fe_2O_3 and M/Fe_2O_3 (M = Rh, Pd, Ag, Ni or Pt).

Fig. 6-5 shows other methane-TPR profiles over non-metal oxides supported catalysts as compared to the orange curve which represents the methane-TPR of Rh/Fe_2O_3. It demonstrates that many transition metals have the ability to crack methane at different temperatures, for example, the negative peak on Rh/graphite, Pd/graphite and Pt/graphite catalysts began at 340, 410 and 500 ^oC, respectively. In the case of graphite supported catalysts, the order for methane activation is as follows: Rh > Pd > Pt, which is in line with literature results for methane activation over these metals.[37-38] Again, Rh seems to be the most active metal for methane cracking with the H_2 evolvement at and from 340 ^oC. It is thought that the absence of negative peak for methane-TPR over the other Fe_2O_3 supported catalysts (Pd, Ag, Ni and Pt) was probably attributed to the in-situ H_2 consumed for the reducible support reduction.

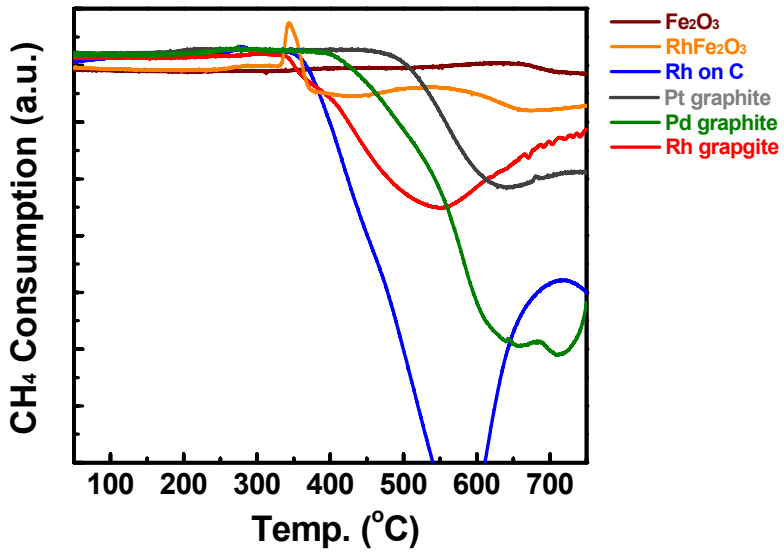


Fig. 6-5 Methane-TPR profiles of calcined Fe_2O_3, Rh/Fe_2O_3, Rh/C, Pt/graphite, Pd/graphite and Rh/graphite (all metal loadings are 5%).

6.3.3 STEM

HAADF-STEM was used to examine the morphology and size of the iron oxide supported Rh catalyst after a pre-reduction with hydrogen at 200 ^{o}C (Fig. 6-6). The Rh particles (bright dots) are clearly observed on the iron oxide support in Fig. 6-6 (a), revealing the Rh particles are well-dispersed. This corresponds well with our XRD patterns. In addition, the Rh particles were on average 2.2 nm in diameter. Lattice fringes of iron oxide particles are clearly seen from Fig. 6-6 (b), as those highlighted within the marked circle.

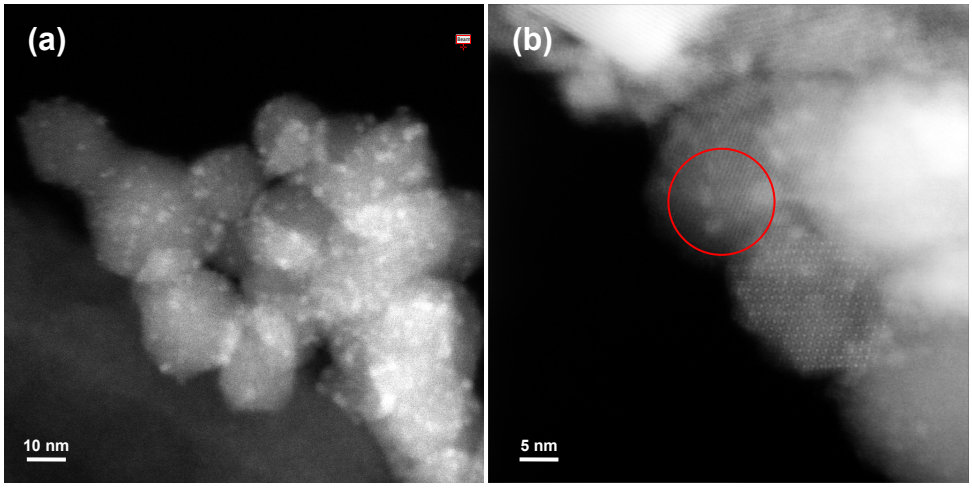


Fig. 6-6 HAADF-STEM imaging of Rh/Fe_3O_4 catalyst. (a) Typical morphology of Rh/Fe_3O_4 catalyst; (b) Higher magnification image of Rh particles distributed on the surface of iron oxide. The lattice fringes of the iron oxide are clearly demonstrated.

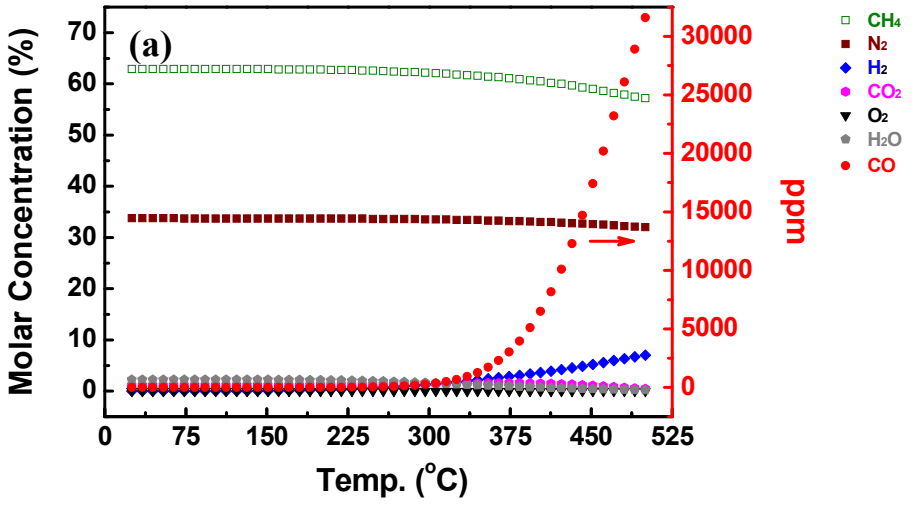
6.4 THERMODYNAMIC CALCULATIONS

It is important to understand the operating temperature window to activate methane and prevent an extensive production of CO from CO_2 by the reverse water gas-shift reaction (RWGSR, Eq. 6-8). From the equilibrium point of view, it is also essential to predict the CO contents during the operation of the partial oxidation of methane. Theoretical calculations were performed using HSC Chemistry 5.11 package to estimate the gas composition in thermodynamic equilibrium, where only the intrinsic properties of the gas species were considered. Based on our preliminary experiment, $CH_4(g)$ and $O_2(g)$ were considered as the reactants (with N_2 as an diluent) and $H_2(g)$, $CO_2(g)$, $CO(g)$ and $H_2O(g)$ were recognised as the exclusive products. Different CH_4 to O_2 ratios, ranging from 30:1 to 3:1, were then applied and O_2 was set as the limiting reactant. The results of the calculations are shown in Fig. 6-7. It is clearly seen that oxygen was used up, and the RWGSR started to take off when the temperature was above 300 ^oC,[39] indicating the products (CO_2 and H_2) could be consumed above this temperature. On the other hand, at a higher temperature

equilibrium composition of methane steam reforming can be achieved (Eq. 6-1). Therefore, for the production of H_2/CO_2, it is important to operate the reaction at a low temperature to avoid steam reformation and reversed water gas equilibria by rendering the conditions under a kinetically controlled regime. Unfortunately, we observed from the calculation that the amount of methane did not really change in the gas composition until the temperature reached 200 ^oC. On the other hand, the CO content dramatically increased when the temperature was much higher than 400 ^oC where the steam reformation and shift equilibria appear to be operating efficiently. As a consequence, we believe that the ideal operating temperature for methane oxidation to CO_2/H_2 will be located between 200 to 400 ^oC. In the next section, comparison of the calculated results with those experimental results obtained over the 5%Rh/Fe_2O_3 was made. .

$$CO_2 + H_2 \rightleftharpoons CO + H_2O \qquad \Delta H_{298K} = 41.1 \text{ kJ mol}^{-1} \qquad \text{Eq. 6-8}$$

$$CH_4 + H_2O \rightleftharpoons CO + 3H_2 \qquad \Delta H_{298K} = 206 \text{ kJ mol}^{-1} \qquad \text{Eq. 6-1}$$



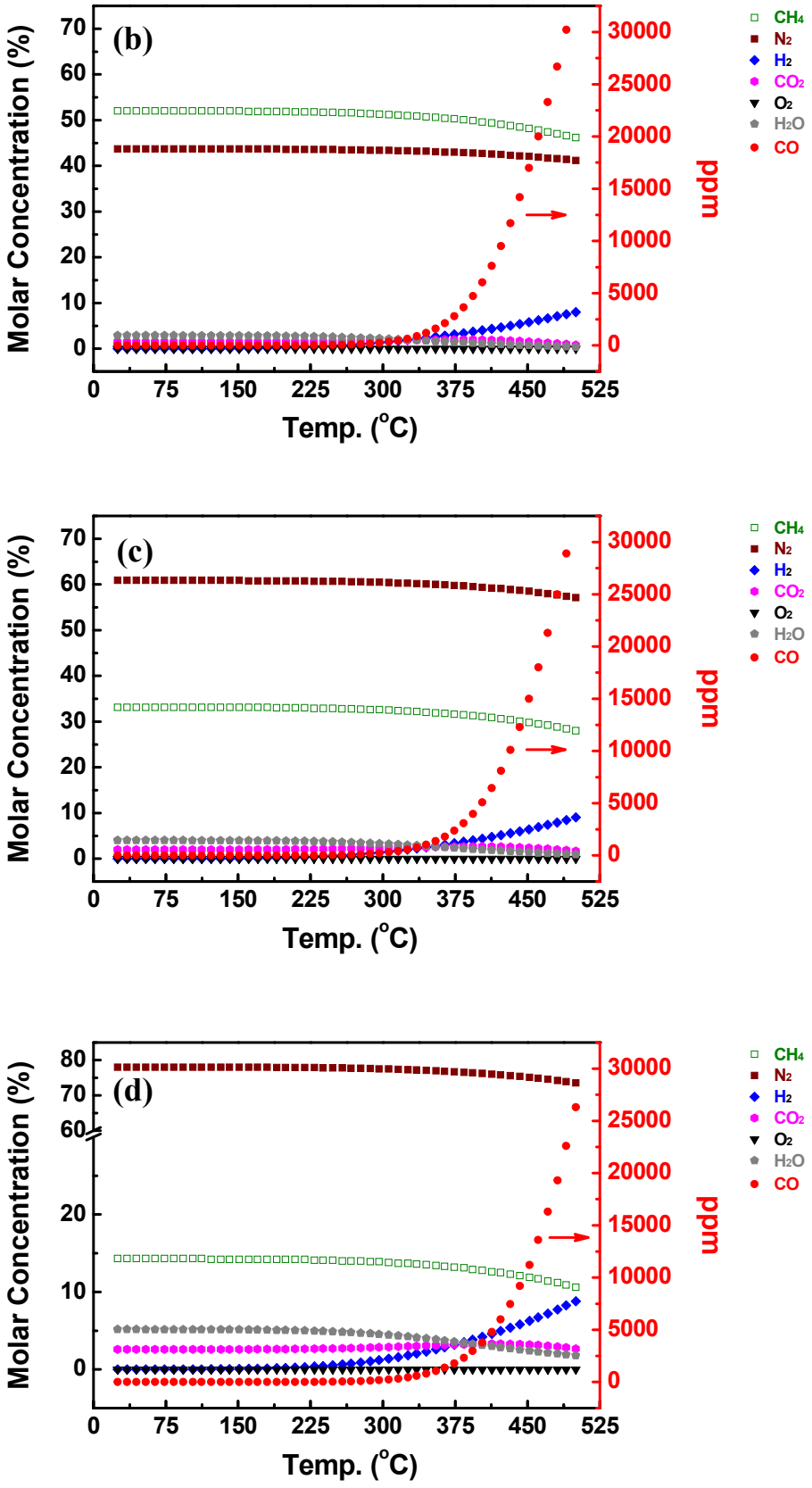


Fig. 6-7 Thermodynamic equilibrium product compositions. A plot of thermodynamic equilibrium product compositions as a function of temperature. (a) CH_4:O_2 = 30:1; (b) CH_4:O_2 = 18.6:1; (c) CH_4:O_2

= 10:1; (d) CH_4:O_2 = 3:1; (calculations performed with the HSC Chemistry 5.11 software).

6.5 CATALYTIC TESTING

6.5.1 Rh ON Fe_2O_3

The reaction was carried out by passing a mixture of CH_4 and O_2 feed stream (36 mL min-^{1}) through a fresh 0.2 g 5% Rh/Fe_2O_3 catalyst with pre-reduction in CH_4. Fig. 6-8 shows the temperature-dependent catalytic performance with feed streams with different CH_4/O_2 ratio. A general trend clearly reveals that the experimental data significantly deviated from the equilibrium values. It can be seen that no methane is converted until the temperature reaches 250 ^{o}C which may be the minimum activation energy for the dehydrogenation of CH_4 over this type of catalyst. There was no CO produced below 300 ^{o}C (CO is not detectable below the detection limit of 1 ppm). On the contrary, at above the temperature, the CO selectivity was dramatically increased in line with aforementioned thermodynamic calculations. Additionally, CO_2 was only generated above 250 ^{o}C. A more important fact is that no H_2 was observed before O_2 was totally consumed, indicating that the elementary steps for methane total combustion were very important on the catalyst surface in producing gaseous hydrogen (Eq. 6-4). Presumably, the adsorbed hydrogen atoms -oxygen atoms recombination rate on surface was much faster and can readily take place than that of hydrogen atoms -hydrogen atoms recombination to form dihydrogen if there are excess of surface oxygen over the Rh catalysts. Thus, for the generation of hydrogen gas, the supply of oxygen must be limited such that the surface oxygen species can be quickly scavenged by the carbonaceous species (C or CO) to form CO_2, leaving the hydrogen for recombination to form dihydrogen from the controlled methane oxidation over this catalyst.

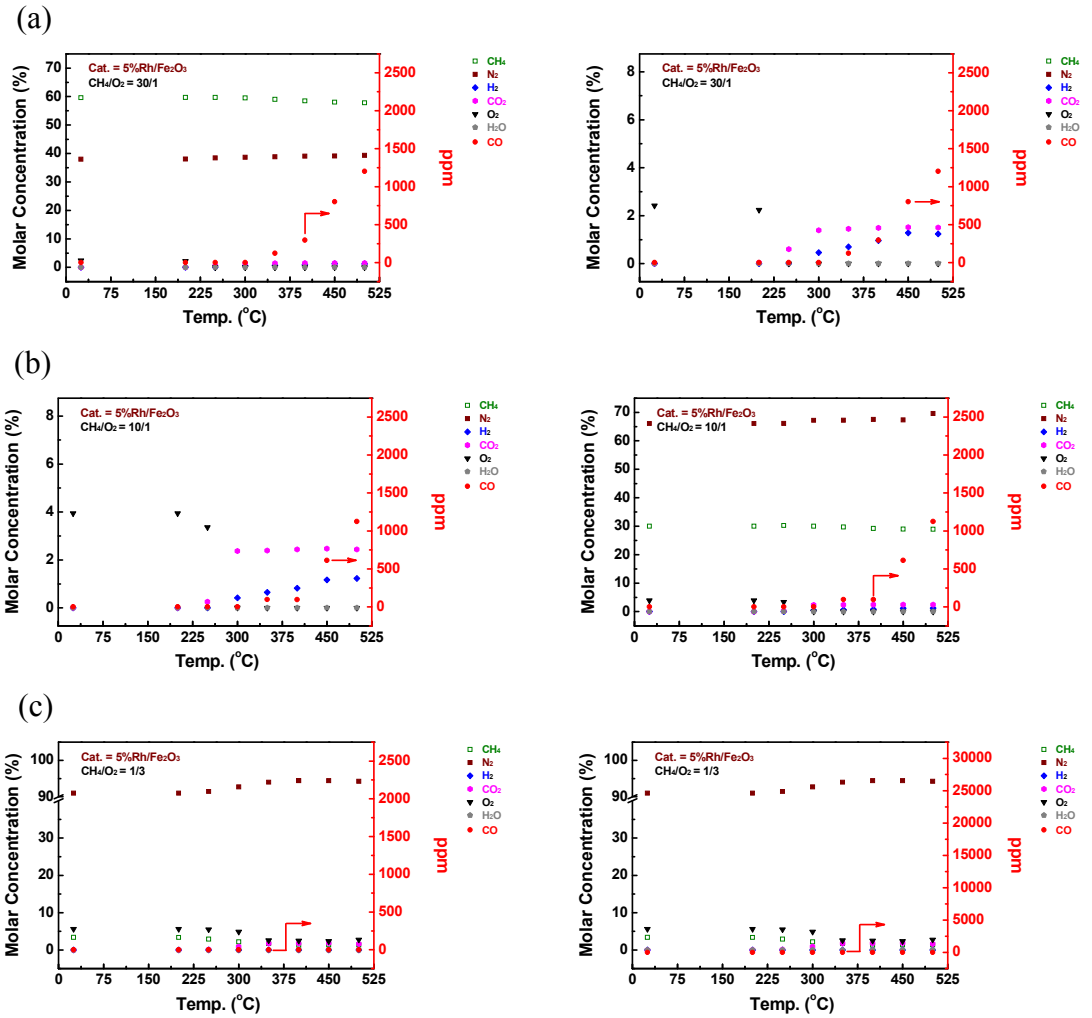


Fig. 6-8 Temperature-dependent catalytic performance with different feed ratios of CH_4/O_2 over 5%Rh/Fe_2O_3 catalysts. (a) CH_4:O_2 = 30:1; (b) CH_4:O_2 = 10:1; (c) CH_4:O_2 = 1:3; (left) full scale gas composition change with temperature; (right) enlarged region to show a clear gas composition of H_2, CO and CO_2.

During the testing of the catalysts in some cases, we observed a large deviation in carbon, hydrogen or oxygen mass balances, which indicated the involvements of other side reactions. In order to understand the main reasons for the poor mass balances for some species, we have to review the definitions for methane conversion and products selectivity carefully. For example, we defined that CH_4 conversion as the molar concentration difference in CH_4 (obtained by TCD) before and after the

reaction. H_2 selectivity was defined as the mole fraction of hydrogen from methane to form molecular hydrogen.[40] A similar definition for CO_2, and CO selectivity was used based on the methane input according to the following equations:

$$H_2 \text{ selectivity (\%)} = \left[\frac{\text{moles of } H_2 \text{ produced}}{\text{moles of } CH_4 \text{ consumed} \times 2}\right] \text{ x } 100$$

$$CO_2 \text{ selectivity (\%)} = \left[\frac{\text{moles of } CO_2 \text{ produced}}{\text{moles of } CH_4 \text{ consumed}}\right] \text{ x } 100$$

$$CO_2\text{* selectivity (\%)} = \left[\frac{\text{moles of } CO_2 \text{ produced}}{\text{moles of } O_2 \text{ consumed}}\right] \text{ x } 100$$

$$CO \text{ selectivity (\%)} = \left[\frac{\text{moles of } CO_2 \text{ produced}}{\text{moles of } CH_4 \text{ consumed}}\right] \text{ x } 100$$

$$CO\text{* selectivity (\%)} = \left[\frac{\text{moles of CO produced}}{\text{moles of } O_2 \text{ consumed} \times 2}\right] \text{ x } 100$$

Table 6-1 summarises the CH_4 conversions and the selectivity towards different products (including H_2, CO_2 and CO) at different feed ratios of CH_4/O_2. Given the fact that the O_2 was the limiting reactant, the methane conversion increased with decreasing CH_4 to O_2 ratio. O_2 was used up at 300 ^oC only with the CH_4/O_2 feed ratio > 10 (Fig. 6-8 (b)). As a result, no H_2 was observed when CH_4/O_2 ratio = 1/3. It was however, using the above definitions, that H_2 balance did not seem to reach 100% (CH_4/O_2 = 30 or 10 in Table 6-1), indicating that some molecules containing hydrogen atoms were not accountable. Since we did not monitor the water molecules formed, which could be produced by oxygen-hydrogen reaction, leading to the deviations in the mass balance of oxygen and hydrogen. Thus, such oxygen and hydrogen unbalances could be used as a mean to gauge the extent of hydrogen combustion reaction over this catalyst. Similarly, we also noted that carbon was not balanced due to carbon deposition on catalyst surface in some cases, particularly over Pd containing catalysts. This deviation can therefore be used as a means to monitor the degree of carbon deposition during our pretreatment/prereduction process. Notice that CO_2* selectivity can also be defined based on the consumption of O_2. In the

situation when both the calculated CO_2 and CO_2* selectivity matched each other, we can conclude that the mass balance was acceptable.

According to Eq. 6-5, the produced H_2 to CO_2 ratio should be at 2 to 1 only if this single methane oxidation reaction has taken place. However, we hardly obtained such high H_2/CO_2 ratios from our different testing conditions, indicative of the presence of other parallel reactions being taking place simultaneously. The highest ratio of i.e. H_2/CO_2*= 1.7 was obtained when we used much higher CH_4/O_2 ratios. Under this situation, it is anticipated that when methane molecule is activated on the catalyst surface to produce adsorbed hydrogen and carbon atoms, the surface oxygen atoms from the limited oxygen supply will be mainly used to oxidise carbon atoms to produce CO_2. This would leave the formation of dihydrogen at a greater quantity with only a small degree of oxygen atoms used to oxidise the hydrogen atoms for the production of water. However, when excess oxygen at lower CH_4/O_2 ratios was used a much lower H_2/CO_2* ratio was obtained. According to Au and Wang, the CH_4 molecule should be firstly activated on catalyst surface to form hydrogen and carbon atoms and then the carbon atoms will react with oxygen on the same metal surface sites to form CO.[34] Thus, we further envisage that such adsorbed CO on metal surface is quite stable (back donation of electrons from metal to CO to form a strong surface specie) which is rather immobile on Rh surface, giving CO/H_2 in the absence of an active oxide support. However, in using reducible metal oxide support, i.e. iron oxide surface, as in our case, the surface oxygen must be activated on the oxide support and transferred to Rh at the interface to form CO_2.[41] Under a lower CH_4/O_2 feed ratio, the high concentration of surface oxygen species on iron oxide will not only migrate to oxidise the CO at the interface, the higher coverage of surface oxygen on the oxide support will also encourage the more mobile hydrogen atoms spilling over from metal

surface to the oxide support surface via a fast hydrogen conduction on surface –OH groups. This will eventually lead to a rapid combustion of hydrogen resulting in a lower H_2/CO_2. Conversely, the hydrogen atoms from Rh may find it difficult to reach the iron oxide surface in the opposite direction to reach the surface oxygen on the oxygen deficient oxide surface to cause combustion at the higher CH_4/O_2 feed ratios (reducing conditions). This will lead to a high concentration of hydrogen atoms build-up on Rh surface for the dihydrogen formation. The proposed mechanism of methane activation over a Rh/Fe_2O_3 catalyst is summarised in Fig. 6-9.

Table 6-1 Catalytic performances for methane activation over Rh/Fe_2O_3 catalysts at different methane to oxygen ratios.

Sample	CH_4/O_2	CH_4 conversion at 300 ^{o} (%)	Selectivity at 300 ^{o}C (%)					CO (ppm)
			H_2	CO_2	CO_2*	CO	CO*	
5% Rh/Fe_2O_3	30	2.7	13.9	59.7	60.6	0.0	0.0	0.0
	10	5.7	11.9	133.9	60.2	0.0	0.0	0.0
	0.3	35.4	0.0	74.2	63.1	0.0	0.0	0.0

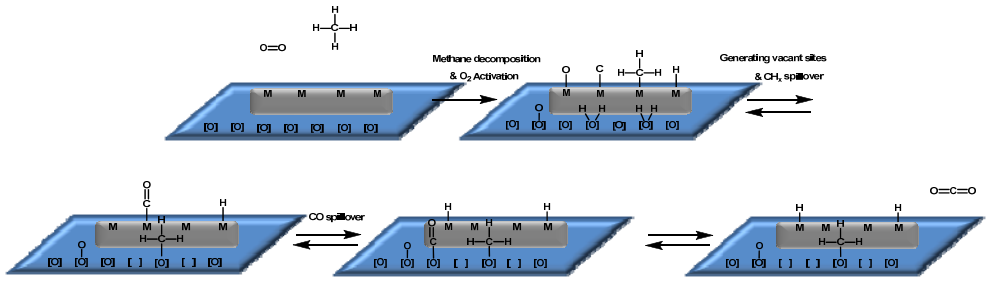


Fig. 6-9 A schematic diagram to describe the adsorbed methane for the production of H_2 and CO_2 on a iron oxide supported Rhodium.

6.5.2 OTHER METALS ON Fe_2O_3

Table 6-2 displays the CH_4 conversions and the selectivity at 300 ^{o}C towards H_2, CO_2 and CO at a mixed stream of CH_4/O_2 = 30 over Fe_2O_3 supported metals, including Rh, Pd, Ag, Ni and Pt. The results are in agreement with the methane-TPR,

showing that Rh was the most active catalyst. Ashcroft et al., demonstrated that Rh has the highest activity for methane partial oxidation.[35] Furthermore our investigation are in line with the proposed dehydrogenation rate of methanol: Rh > Pt > Cu > Pd > Ag.[42] Conversely, Ni is known as an active metal for methane cracking, but no methane conversion over our allergic 'Ni/Fe_2O_3' was observed. It is possible that the active metal phase for methane cracking was not formed from our stable $NiFeO_4$ spinel catalyst precursor.[28]

Table 6-2 Catalytic performances for methane activation over a range of Fe_2O_3-supported metal catalysts at a methane to oxygen ratio = 30.

Sample	CH_4:O_2	CH4 conversion at 300 ^{o} (%)	Selectivity at 300 ^{o}C (%)					CO (ppm)
			H_2	CO_2	CO_2*	CO	CO*	
5% Rh/Fe_2O_3	30	2.7	13.9	59.7	60.6	0.0	0.0	0.0
5% Pd/Fe_2O_3		0.5	0.0	181.8	66.9	0.0	0.0	0.0
5% Ag/Fe_2O_3		0.1	0.0	68.4	16.3	0.0	0.0	0.0
5% Ni/Fe_2O_3		0.6	0.0	102.6	44.8	0.0	0.0	0.0
5% Pt/Fe_2O_3		2.2	1.3	59.2	57.3	0.0	0.0	0.0

6.5.3 Rh ON OTHER OXIDE SUPPORTS

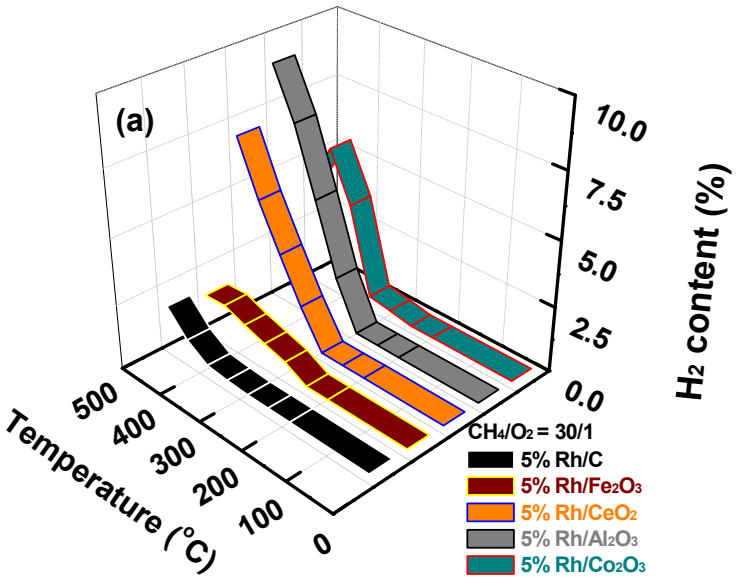
Methane-TPR and the previous catalytic results both show that Rh was the most effective amongst the five metals studied for the methane cracking. It would be interesting to elucidate the effect of different supports for Rh for this reaction. The supports examined included carbon, Fe_2O_3, CeO_2, Al_2O_3 and Co_2O_3. Their catalytic performances at 300 ^{o}C are shown in Table 6-3. It is obvious from Table 6-3 that the CH_4 conversions are in general low over all the Rh-containing catalysts under the limiting oxygen conditions. The highest conversion of 2.9% was obtained over

Rh/Co_2O_3 at 300 ^oC. If we calculate the conversion in term of oxygen consumption, it can go up to 87.8%, which means around 88% of methane was converted to CO_2 in the feed stream of CH_4/O_2 = 30/1. The carbon was not balanced over this catalysis study but higher than expected due to carbon deposition during our pre-treatment step. Rh/Fe_2O_3 and Rh/Co_2O_3 were the only two samples that gave decent selectivity towards hydrogen. The highest hydrogen selectivity was observed over Rh/Fe_2O_3. Presumably the iron oxide and in part cobalt oxide acted as a 'moderate' oxygen provider at reducing conditions which can oxidise CO on metal surface to CO_2 but leaving most hydrogen atoms on metal surface for the dihydrogen formation (poor hydrogen spillover on the oxygen deficient oxide support). The rest metal oxide supports either provided more active surface oxygen for hydrogen combustion on catalyst surface (good hydrogen spillover surface), giving lower H_2/CO_2 or provided no oxygen (inert oxide supports) which led only to the syngas formation. Given the fact that there is no active oxygen supply from the inert carbon support (Rh/C) that could react with the adsorbed hydrogen, Rh/C catalyst indeed showed the lowest CO_2 selectivity.

Table 6-3 Catalytic performances for methane activation over different supported Rh catalysts at a methane to oxygen ratio = 30.

Sample	$CH_4:O_2$	CH_4 conversion at 300 ^{o} (%)	Selectivity at 300 ^{o}C (%)					CO (ppm)
			H_2	CO_2	CO_2*	CO	CO*	
5% Rh/C	30	2.2	0.0	66.0	39.1	0.0	0.0	0.0
5% Rh/Fe_2O_3		2.7	13.9	59.7	60.6	0.0	0.0	0.0
5% Rh/CeO_2		0.6	0.0	223.5	96.2	0.0	0.0	0.0
5% Rh/Al_2O_3		0.3	0.0	194.1	62.3	0.0	0.0	0.0
5% Rh/Co_2O_3		2.9	7.4	113.1	76.0	0.0	0.0	0.0

Fig. 6-10 shows a detailed temperature-dependent catalytic performance over different supported Rh catalysts. Not surprisingly, all catalysts could activate oxygen above 250 ^{o}C (Fig. 6-10 (a) and (b)), indicating that any hydrogen produced may be burned off. The content of CO, thermodynamically favourable product, was increased above 350 ^{o}C; however, the observed values deviated far beyond the equilibrium, suggesting that CO production is greatly suppressed (from over 25000 to less than 4000 ppm). A very low level of CO (961 ppm) was produce over the 5% Rh/Fe_2O_3 even at 500 ^{o}C. In addition, the RWGSR was encouraged above 400 ^{o}C, therefore, decreased CO_2 and H_2 content were observed over all catalysts except Rh/Fe_2O_3 and Rh/Co_2O_3. At temperatures higher than 300 ^{o}C, the H_2 contents (as syngas) over Rh/CeO_2, Rh/Al_2O_3 and Rh/Co_2O_3 catalysts were significantly boosted.



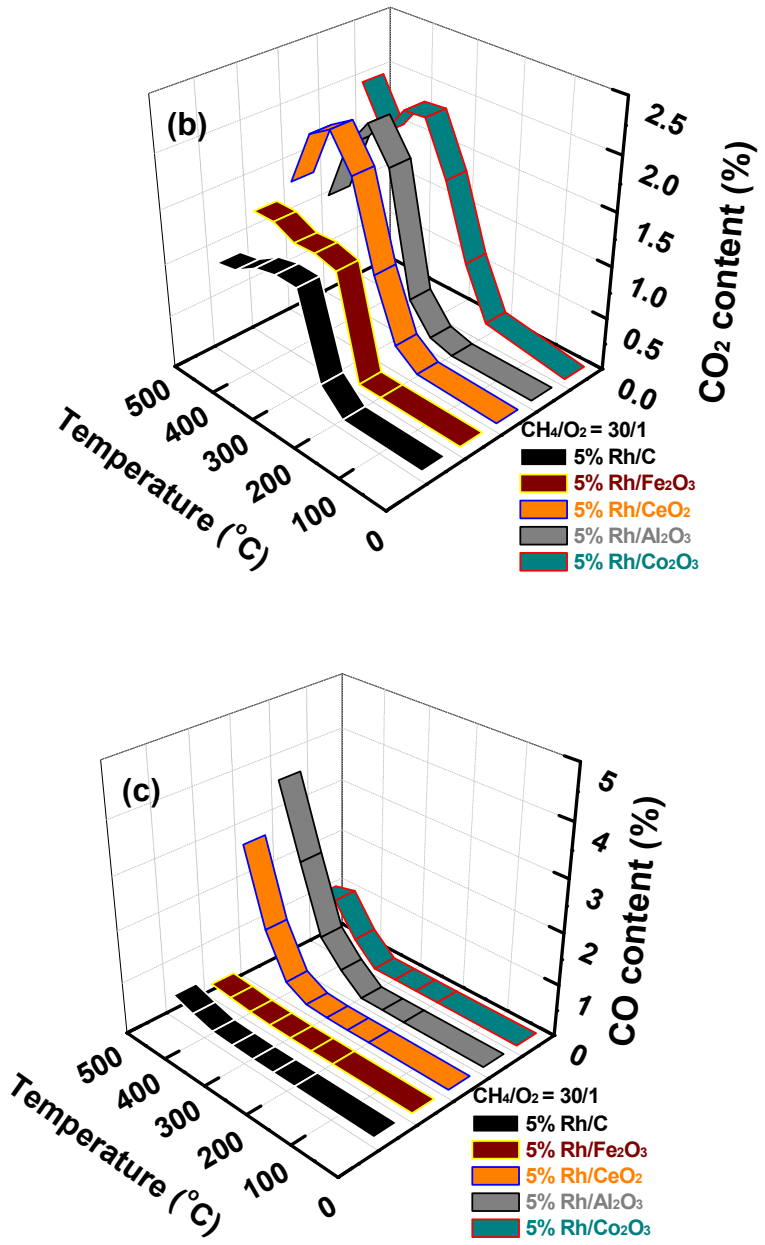


Fig. 6-10 Temperature-dependent catalytic performance over 5%Rh/C, 5%Rh/Fe_2O_3, 5%Rh/CeO_2, 5%Rh/Al_2O_3 and 5%Rh/Co_2O_3 catalysts at a gas feed ratio of CH_4/O_2 = 30. (a) H_2 content; (b) CO_2 content; (c) CO content.

6.5 DISCUSSION

It is noted that Rh has a stronger intrinsic adsorptive property and therefore it can activate/dehydrogenate methane easily. This is reinforced by the methane-TPR results, where Rh supported on Fe_2O_3 was able to activate methane at a low

temperature. Additionally, we can determine the catalytic activity for methane cracking over graphite supported metal catalysts given is: Rh > Pd > Pt. Methane catalytic cracking to hydrogen production and methane partial oxidation have been widely studied.[28] Green and co-workers have studied POM over Al_2O_3 supported on transition metal catalyst.[35] They identified Rh and Ir were the most effective catalysts (Ir = Rh > Ni > Pd > Ru), and no carbon deposition was observed. In addition, Tsang et al. has summarised recent developments for partial oxidation of methane to syngas over various metals, such as Rh, Pd, Pt, Ru, Ni, Co and Fe.[43] Rh revealed the best activity among transition metals. In addition, Iron group metals (Fe, Co and Ni) are known to have the highest activity for hydrocarbon cracking.[28] But they have the disadvantage of carbon accumulation. A similar trend of metal activity was found for methane steam and dry reforming, where Rh demonstrated the highest activity than other metals but with no carbon deposition.[44-45] Our investigations are in line with these observations. Consequently, Rh not only provides a lower activation energy for methane activation but also gives an active surface for the facile recombination of carbon and dissociated oxygen to form syngas at relatively low temperature. Furthermore, it is thought that the active Rh can support a faster rate of recombination of adsorbed hydrogen (Rh-H reacts with Rh-H) before the hydrogen combustion (Rh-H reacts with Rh-O), leaving the activated carbon atoms, from the methane, to react with oxygen to form CO. It is also apparent from our experiments that H_2 was not produced until O_2 over the Rh/Fe_2O_3 was totally consumed. Therefore, there was no H_2 observed in a lower CH_4/O_2 ratio in a practical case ($CH_4:O_2$ = 1:3), suggesting that highly reactive [O] coverage on the oxide support may destroy the adsorbed hydrogen atoms favourably to form water. Thus, oxygen starving conditions (high CH_4/O_2 ratios) can only be used over this catalyst in order to produce a high level of

dihydrogen content. Under such conditions, carbon deposition over catalysts can unfortunately become favourable. This can explain a general decrease in conversion observed at higher temperature over the non-Rh metals. Interestingly, this did not happen over all the Rh based catalysts. Notice that Rh/Fe_2O_3 was the only Fe_2O_3 supported catalyst which gave a viable hydrogen amount at a high CH_4/O_2 ratio (CH_4/O_2 = 30), despite the fact that the CO_2 to H_2 ratio produced was not at 1/2 according to the stoichiometry but at around 4 (Table 6-3). This clearly suggests that a substantial amount of hydrogen was still oxidised to water by the active oxygen. Thus, a more delicate control in oxygen through tailoring the surface coverage or nature of oxygen mobility on the catalyst surface must be required to produce CO_2 but not destroying the hydrogen.

Previous literature suggested that a minimal interaction between the active metal and support can increase the conversion for methane cracking.[46] But this is not the case for the selective methane oxidation, where an oxidation step is incorporated with the methane cracking. The use of appropriate oxide support is very important in heterogeneous catalysis. It not only acts as a dilution but provides active sites for molecular oxygen activation and controlled surface oxidation reactions. In our case, it is found that Fe_2O_3 could contribute to disperse and stabilise metal to their clusters or even atoms forms, as apparently observed from our XRD and STEM. This provides a higher activity over iron oxide supported catalysts rather than other oxide supports are used. Zhang and co-workers noted that single Pt atoms dispersed on iron oxide using a similar preparative method.[47] In addition, Wu et al. has reported a similar feature of "atomically dispersed Pd" on iron oxide.[48] Apart from the advantage of high dispersion, it is believed that the combination of Rh and iron oxide can provide a unique feature for the production of H_2/CO_2 reaction. For example, Chen et al.

recently reported that using this type of catalyst, the interface-confined surface oxygen vacant sites together with the metal are active for dioxygen activation, producing reactive dissociated oxygen atoms to oxidise the CO to CO_2. As a result, they demonstrated that ethanol molecule can be selectively converted into hydrogen gas and CO_2 at low temperature over the rhodium-iron oxide catalyst on solid aluminium oxide .[41] It clearly demonstrates that with the help of reducible iron oxide (Fe_xO_y), the in-situ formed CO on metal can be catalysed by the vacant oxygen sites of iron oxide to proceed WGSR to CO_2, which increases the hydrogen production and prevents coking.

Eriksson et al. reported that in the partial oxidation of methane over rhodium catalysts under a temperature programmed reaction conditions, H_2, CO and CO_2 were produced above 320, 340 and 300 ^oC, respectively.[49] They compared two different oxidants, namely O_2 versus water vapour and discovered that the gas composition of products was altered significantly when water vapour was added. This is due to the introduction of the WGSR, which resulted to give a lower CO content. In our system, 5% Rh/Fe_2O_3 is the easiest reducible oxide among four oxides supported Rh we examined. It is expected that the water vapour was easily produced during the reduction of iron oxide by evolved hydrogen (generated by methane cracking). The resulting water vapour could also increase the ignition temperature further and reduced the combustion reaction of methane to produce hydrogen. Here, such an exciting role of the support is highlighted.

On the basis of these accounts, we believe that Rh on Fe_2O_3 contributes an important ensemble for the activation of methane to CO_2 and H_2 in our study. This is achieved at low temperature where a kinetically controlled regime operates, which

leads to the decrease in RWGSR. Further optimisation of this catalyst in formulation and under different reaction conditions is on-going.

6.6 CONCLUSION

In conclusion, we report an approach for selective CO_2 and H_2 co-production by the direct methane oxidation over a 5% Rh/Fe_2O_3 catalyst without any detectable CO (below detection limit of 1 ppm). A 2.7% conversion of methane with selectivity ratio of $CO_2/H_2 = 4$ in a mixed gas feed stream of $CH_4/O_2 = 30$ at 300 ^oC is obtained. The reaction is operated in a kinetically controlled regime at 300 ^oC, where CO formation from RWGSR is greatly suppressed. Different supported Rh catalysts have been examined in order to elucidate the interaction(s) between the Rh metal and oxide supports. It is evident that the Rh/Fe_2O_3 acts as an interesting bifunctional catalyst for this reaction. First, this catalyst gives a high dispersion of Rh which is expected to deliver a higher surface energy with enhanced activity. The Rh metal surface provides catalytically active sites for dissociation of methane to adsorbed hydrogen and carbon atoms effectively, and active oxygen on metal surface catalyses the carbon atoms to CO. On the other hand, the surface oxygen from Fe_2O_3 will transfer to the metal-support interface to form CO_2 for the WGSR. Although the best working conditions for this catalyst have yet to be optimised, it is believed that the combination of engineering approaches such as recycling unreacted methane or using membrane separation technology, this product stream may be applied directly as a feedstock to supply for methanol production or proton exchange membrane for fuel uses.

6.7 REFERENCES

1. J. Tollefson, *Nature*, 2013, **493**, 12-12.
2. *BP Statistical Review of World Energy, June*, 2012.
3. G. A. Olah, *Angew Chem Int Edit*, 2005, **44**, 2636-2639.
4. G. A. Olah, A. Goeppert and G. K. S. Prakash, *Beyond oil and gas : the methanol economy*, Wiley-VCH ;John Wiley, Weinheim Chichester, 2006.
5. L. Bromberg and W. K. Cheng, *Methanol as an alternative transportation fuel in the US: Options for sustainable and/or energy-secure transportation*, Cambridge, 2010.
6. H. D. Gesser, N. R. Hunter and C. B. Prakash, *Chem Rev*, 1985, **85**, 235-244.
7. N. R. Foster, *Appl Catal*, 1985, **19**, 1-11.
8. W. A. Bone, *Nature*, 1931, **127**, 473-508.
9. D. M. Newitt and A. E. Haffner, *Proceedings of the Royal Society of London. Series A.*, 1932, **134**, 591-604.
10. Q. Zhang, D. He and Q. Zhu, *J Nat Gas Chem*, 2003, **12**, 81-89.
11. N. R. Hunter, H. D. Gesser, L. A. Morton, P. S. Yarlagadda and D. P. C. Fung, *Appl Catal*, 1990, **57**, 45-54.
12. G. S. Walker, J. A. Lapszewicz and G. A. Foulds, *Catal Today*, 1994, **21**, 519-526.
13. C. J. Jones, D. Taube, V. R. Ziatdinov, R. A. Periana, R. J. Nielsen, J. Oxgaard and W. A. Goddard, *Angew Chem Int Edit*, 2004, **43**, 4626-4629.
14. M. H. Ab Rahim, M. M. Forde, R. L. Jenkins, C. Hammond, Q. He, N. Dimitratos, J. A. Lopez-Sanchez, A. F. Carley, S. H. Taylor, D. J. Willock, D. M. Murphy, C. J. Kiely and G. J. Hutchings, *Angew Chem Int Edit*, 2013, **52**, 1280-1284.

15. Whittenb.R, K. C. Phillips and Wilkinso.Jf, *J Gen Microbiol*, 1970, **61**, 205-&.

16. D. Park and J. Lee, *Korean J Chem Eng*, 2013, **30**, 977-987.

17. R. S. Hanson and T. E. Hanson, *Microbiol Rev*, 1996, **60**, 439-471.

18. J. L. Vega, E. C. Clausen and J. L. Gaddy, *Abstr Pap Am Chem S*, 1988, **196**, 71-Fuel.

19. R. Balasubramanian, S. M. Smith, S. Rawat, L. A. Yatsunyk, T. L. Stemmler and A. C. Rosenzweig, *Nature*, 2010, **465**, 115-U131.

20. S. I. Chan, Y. J. Lu, P. Nagababu, S. Maji, M. C. Hung, M. M. Lee, I. J. Hsu, P. D. Minh, J. C. H. Lai, K. Y. Ng, S. Ramalingam, S. S. F. Yu and M. K. Chan, *Angew Chem Int Edit*, 2013, **52**, 3731-3735.

21. R. A. Periana, D. J. Taube, S. Gamble, H. Taube, T. Satoh and H. Fujii, *Science*, 1998, **280**, 560-564.

22. Z. Q. Bai, H. K. Chen, W. Li and B. Q. Li, *Int J Hydrogen Energ*, 2006, **31**, 899-905.

23. M. G. Poirier and C. Sapundzhiev, *Int J Hydrogen Energ*, 1997, **22**, 429-433.

24. R. Aiello, J. E. Fiscus, H. C. zur Loye and M. D. Amiridis, *Appl Catal A-Gen*, 2000, **192**, 227-234.

25. M. S. Rahman, E. Croiset and R. R. Hudgins, *Top Catal*, 2006, **37**, 137-145.

26. M. A. Ermakova and D. Y. Ermakov, *Catal Today*, 2002, **77**, 225-235.

27. R. J. Farrauto and C. H. Bartholomew, *Fundamentals of industrial catalytic processes*, 2nd edn., Wiley, Hoboken, N.J., 2006.

28. A. M. Amin, E. Croiset and W. Epling, *Int J Hydrogen Energ*, 2011, **36**, 2904-2935.

29. J. L. Figueiredo, J. J. M. Orfao and A. F. Cunha, *Int J Hydrogen Energ*, 2010, **35**, 9795-9800.

30. F. C. Schouten, O. L. J. Gijzeman and G. A. Bootsma, *Surf Sci*, 1979, **87**, 1-12.

31. H. F. Abbas and W. M. A. W. Daud, *Int J Hydrogen Energ*, 2010, **35**, 1160-1190.

32. K. Otsuka, T. Kaburagi, C. Yamada and S. Takenaka, *J Power Sources*, 2003, **122**, 111-121.

33. P. Fabrizioli, T. Burgi, M. Burgener, S. van Doorslaer and A. Baiker, *J Mater Chem*, 2002, **12**, 619-630.

34. C. T. Au and H. Y. Wang, *J Catal*, 1997, **167**, 337-345.

35. A. T. Ashcroft, A. K. Cheetham, M. L. H. Green and P. D. F. Vernon, *Nature*, 1991, **352**, 225-226.

36. G. Fratesi, P. Gava and S. de Gironcoli, *J Phys Chem C*, 2007, **111**, 17015-17019.

37. R. L. Martins, M. A. Baldanza, M. M. V. M. Souza and M. Schmal, *Stud Surf Sci Catal*, 2004, **147**, 643-648.

38. P. Ferreira-Aparicio, A. Guerrero-Ruiz and I. Rodriguez-Ramos, *Appl Catal A-Gen*, 1998, **170**, 177-187.

39. C. S. Chen, W. H. Cheng and S. S. Lin, *Appl Catal A-Gen*, 2003, **238**, 55-67.

40. J. C. Brown and E. Gulari, *Catal Commun*, 2004, **5**, 431-436.

41. L. W. Chen, C. K. S. Choong, Z. Y. Zhong, L. Huang, T. P. Ang, L. A. Hong and J. Y. Lin, *J Catal*, 2010, **276**, 197-200.

42. A. C. Lausche, J. S. Hummelshoj, F. Abild-Pedersen, F. Studt and J. K. Norskov, *J Catal*, 2012, **291**, 133-137.

43. S. C. Tsang, J. B. Claridge and M. L. H. Green, *Catal Today*, 1995, **23**, 3-15.

44. Rostrupn.Jr, *J Catal*, 1973, **31**, 173-199.

45. J. R. Rostrupnielsen and J. H. B. Hansen, *J Catal*, 1993, **144**, 38-49.

46. Y. Echegoyen, I. Suelves, M. J. Lazaro, R. Moliner and J. M. Palacios, *J Power Sources*, 2007, **169**, 150-157.

47. B. T. Qiao, A. Q. Wang, X. F. Yang, L. F. Allard, Z. Jiang, Y. T. Cui, J. Y. Liu, J. Li and T. Zhang, *Nat Chem*, 2011, **3**, 634-641.

48. C. T. Wu, K. M. K. Yu, F. L. Liao, N. Young, P. Nellist, A. Dent, A. Kroner and S. C. E. Tsang, *Nat Commun*, 2012, **3**.

49. S. Eriksson, M. Nilsson, M. Boutonnet and S. Jaras, *Catal Today*, 2005, **100**, 447-451.

CHAPTER 7 - CONCLUSION AND FUTURE PERSPECTIVE

CHAPTER 7 - CONCLUSION AND FUTURE PERSPECTIVE.....210

7.1 CONCLUSION AND FUTURE WORK.....211

7.2 FUTURE PERSPECTIVE 212

7.1 CONCLUSION AND FUTURE WORK

As shown in previous chapters, we have explored an alternative non-syngas route to utilise ethylene glycol that is easily accessible from biomass or fossil fuels for the methanol production. We have demonstrated that the modification of electronic structure of Raney catalysts by d-band centre position alteration can affect their adsorption properties. As consequence, the activity and selectivity of these catalysts are greatly influenced in ethylene glycol hydrogenolysis reaction. Moreover, we have shown that methanol is produced on specific surface sites independent from the other sites at intrinsic rate and would not be converted to other products by the d-band alteration.

We have also demonstrated that a simple co-precipitation could produce highly dispersed sub-nano PdFe clusters on a defective iron oxide surface. This catalyst dramatically increases the selectivity to methanol for the hydrogenolysis of ethylene glycol compared to the modified Raney catalysts. The surface PdFe clusters derived from a strong metal-support interaction are shown to provide active sites for the methanol production. Therefore, future work should be focused on using different synthesis approach to increase the amount of PdFe alloy on a support surface, and investigating the correlation between the degree of alloying of PdFe and the catalytic activity, especially in methanol selectivity, of ethylene glycol hydrogenolysis. We will further extend our study on hydrogenolysis of other polyols, e.g. glycerol, glucose, and sucrose, which fit with a more general scenario of biomass, for methanol production.

We have then extended this preparative method to synthesise a high dispersed Rh metal on iron oxide and used it for selective CO_2 and H_2 production from a direct methane-oxygen oxidation reaction. This catalyst is not only demonstrated to be

highly selective for CO_2/H_2 production but also shows no activity for CO production. It is found that the Rh surface provides catalytically active sites for the dissociation of methane to adsorbed hydrogen and carbon atoms which readily combine with active oxygens at the metal-support interface to form CO_2 selectively to yield the H_2/CO_2 gas mixture. At this stage, Rh seems not to be a good candidate for producing high yield H_2 for following methanol synthesis, however, our investigation of small amount hydrogen production over Rh catalysts matches with currently used three-way catalyst, opening up a new application of this catalyst, especially in applying to a methane (natural gas) engine for reducing NOx level in exhaust gas. On top of that, more characterisations (XPS and EXAFS) of the most effective catalyst, Rh/Fe_2O_3, should be done to understand the active composition for methane activation.

7.2 FUTURE PERSPECTIVE

It is clearly evident that heterogeneous catalysis plays an important role in modern chemical industries. With the continuous market growth of chemicals, the need for new catalysis reactions is expected to rise in order to meet the industrial demands. The activity in searching new catalytic reactions and new catalysts can be reflected by the vigorous activity of the global leading catalyst, chemical, oil and gas companies such as Johnson Matthey, BASF, DuPont, Royal Dutch Shell, BP, and Exxon Mobil, which continue to expand their patents portfolio in these areas. This provides a promising future in the research on heterogeneous catalysis.

Furthermore, the gradual depletion of the fossil resources and the emerging environmental concerns encourage us to develop new alternative routes such as presently demonstrated in this thesis: the methanol synthesis from biomass. Although some countries are exploring the use of shale gas (an alternative to natural gas) for

energy uses, which may put back the agenda for developing our cleaner methanol route perhaps for decades. Given the fact that the long term energy security is the key global challenge, the strategic position and demand for methanol as both fuel and platform chemical of methanol are expected to rise. Thus, I believe the research for renewable biomass for catalytic methanol production will definitely continuous to grow in the foreseeable future.

CHAPTER 8 – APPENDIX

CHAPTER 8 – APPENDIX 214

8.1 DENSITY FUNCTIONAL THEORY OF METAL SURFACES[1] 215

8.2 A SIMPLE MODEL FOR d-BAND THEORY[3] 216

8.3 REFERENCES.....219

8.1 DENSITY FUNCTIONAL THEORY OF METAL SURFACES[1]

Density functional theory (DFT) calculation provides guidance for experimental chemists to understand trends in adsorption energies between metal and substrates, and predict reactivity across transition metals to design experiments in the heterogeneous catalysis. Among the DFT, the *d*-band model is an approximate description of bond formation on a metal surface (Fig. 8-1).[2] It forms a description of chemical bonding between metal *s* and *d* states, the adsorbate states. The model works to a first approximation by projecting the adsorbate valence states onto the metal *s* states, giving rise to its downshift and broadening because all transition metal *s* states are diffuse and broad. The second projection is the metal *d* states, where significant differences arise from the position of the metal. This leads to the formation of their bonding and antibonding states. The difference in chemical bonding is explained by the degree of filling of the adsorbate antibonding states relative to the Fermi level, as antibonding states are always above the metal *d* states. The centre of *d* states relative to the Fermi level is the first indicator to the strength of the surface chemical bond.

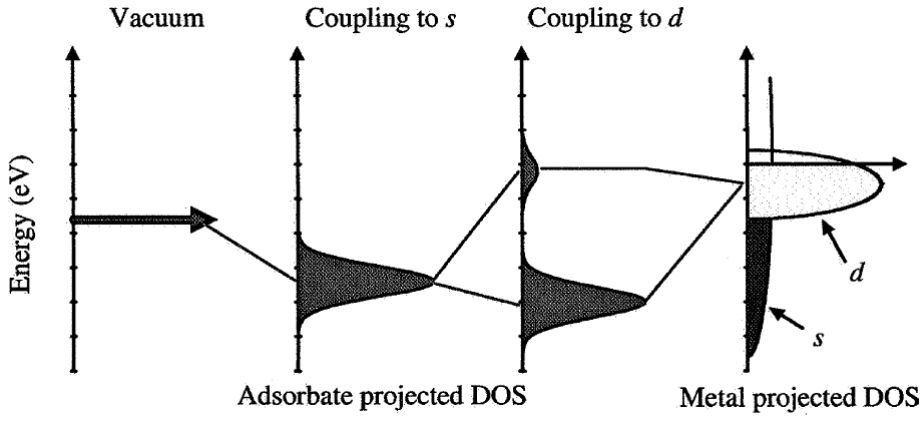


Fig. 8-1 Illustration of bond formation between an adsorbate and the *s* and *d* states on a metal surface.

Figure reproduced from ref. 1.

8.2 A SIMPLE MODEL FOR d-BAND THEORY[3]

Here we use a one-electron description of the quantum mechanics of atoms to describe the interaction between the electron and a metal surface to simplify the system. A one-electron state in an atom or molecule outside a metal surface will interact with all the valence states of the surface atoms. These states form a band or several bands of states. Figure 8-2 shows a typical density of states (DOS) for a transition metal. Because all the transition metals have one *s* electron in the metallic state, here, the broad *s* band is half filled. On the other hand, the *d* states are seen to form much narrower bands. The occupancy of the *d* bands varies along the transition metals as they shift through the Fermi level (ε_F). The narrow *d* bands are a consequence of the small coupling matrix element V_{dd} between the localised *d* states.

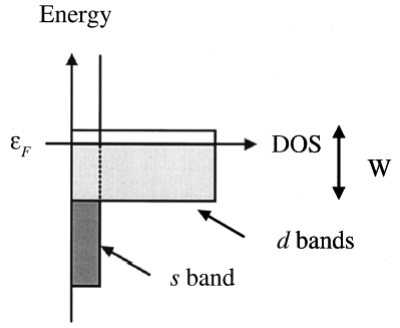


Fig. 8-2 Schematic illustration of the DOS of a transition metal, showing the broad *s* band and the narrow *d* bands (width *W*) around the Fermi level, ε_F. Figure reproduced from ref. 2.

Fig. 8-3a illustrates the interaction of an adsorbate state with a broad *s* band of a metal. Since *d* bands are narrow, the interaction of an adsorbate state with the *d* electrons of a surface often gives rise to bonding and antibonding states demonstrated in Fig. 8-3b. The broadening adsorbate state limited with a single resonance is often referred to "weak chemisorption," whereas when there are split-off bonding and antibonding states which refer to "strong chemisorptions".[4]

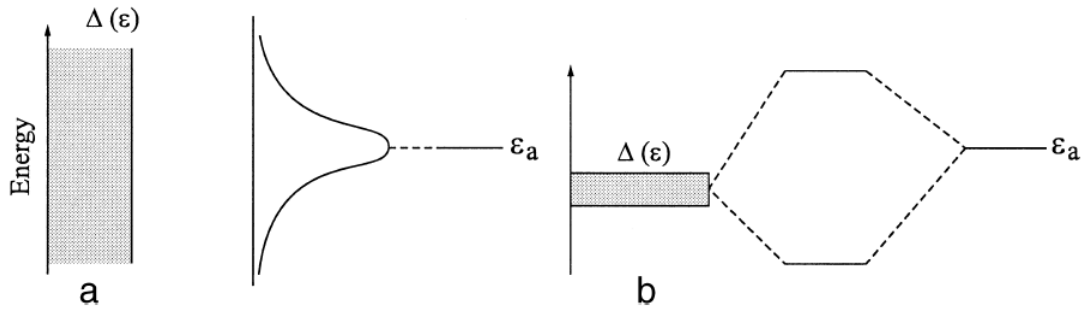


Fig. 8-3 The local DOS at an adsorbate for: (a) a broad surface band; (b) a narrow metal band. (a) corresponds to the interaction with a metal *s* band and (b) is representative of the interaction with a transition metal *d* band. Figure reproduced from ref. 3.

Figure 8-4 shows the result of a model calculation whereby a single adsorbate level is coupled by a matrix element V to a band of states. In the calculation, V is kept fixed as the band is shifted up in energy. The filling of the band is kept fixed so that as the centre of the band (ε_d) is shifted up toward the Fermi level, the band width W decreases. When the band is low and broad, as shown on the left-hand side of the figure, only a single resonance can be seen at the bottom of the band. As ε_d shifts up, a distinctive antibonding state appears above the band. These antibonding states stay above the Fermi level, therefore they are empty, and the bond becomes increasingly stronger as the number of empty antibonding states increases. The model calculation illustrates the progressive change between "weak" and "strong" chemisorptions which also illustrates a general principle about bonding at a surface: When antibonding states are shifted up through the Fermi level (stay above and become empty) which forms strong bonding. On the contrary, weak bonding occurs if bonding states are shifted down through the Fermi level and become filled.

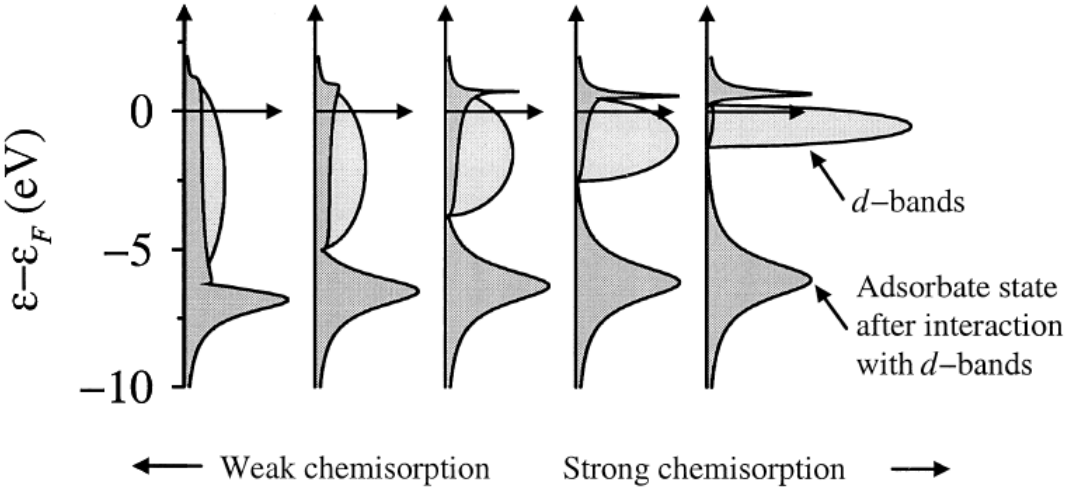


Fig. 8-4 The local DOS projected onto an adsorbate state interacting with the *d* bands at a surface. The strength of the adsorbate–surface coupling matrix element *V* is kept fixed as the center of the *d* bands ε_d is shifted up toward the Fermi energy ($\varepsilon_F = 0$) and the width *W* of the *d* bands is decreased to keep the number of electrons in the bands constant. As ε_d shifts up, the antibonding states are emptied above ε_F and the bond becomes stronger. Figure reproduced from ref. 2.

Apart from the filling of *d* bands (increases towards the right of the periodic table), other factors contributing to the surface bonding include: i) metal cohesive energy, increases down the periodic table; ii) coupling matrix element, V, estimated by linear muffin-tin orbitals theory, the value of which increases down the group and left of the periodic table as the *d* states are more tightly bound. Applying the *d* band model can rationalise why Cu and Ag are less active metals due to their fully filled *d* band, leading to a completely filled adsorbate antibonding states resulting in net Pauli repulsions in the dissociation of ethylene glycol and molecular hydrogen during hydrogenolysis reaction. [5-6]

8.3 REFERENCES

1. C. W. A. Chan, *Ultraselective Nanocatalysts in Fine Chemical and Pharmaceutical Synthesis.* DPhil thesis, University of Oxford, 2012.
2. A. Nilsson, L. G. M. Pettersson, B. Hammer, T. Bligaard, C. H. Christensen and J. K. Norskov, *Catal Lett*, 2005, **100**, 111-114.
3. B. Hammer and J. K. Norskov, *Adv Catal*, 2000, **45**, 71-129.
4. B. I. Lundqvist, O. Gunnarsson, H. Hjelmberg and J. K. Norskov, *Surf Sci*, 1979, **89**, 196-225.
5. B. Hammer and J. K. Norskov, *Nature*, 1995, **376**, 238-240.
6. A. Ruban, B. Hammer, P. Stoltze, H. L. Skriver and J. K. Norskov, *J Mol Catal a-Chem*, 1997, **115**, 421-429.